

Optimal Control for Minimum Thrust Demand in Extended Formation Flight

FG van Wyk

Department of Electric & Electronic Engineering
Stellenbosch University

Supervisor: Prof. T. Jones

Report submitted in fulfillment of the requirements for the degree Masters in
Engineering in the Department of Electrical & Electronic Engineering at the
Stellenbosch University

MEng (Electric & Electronic Engineering)

March 2016

Declaration

By submitting this thesis electronically, I declare that the entirety of the work contained therein is my own, original work, that I am the sole author thereof (save to the extent explicitly otherwise stated), that reproduction and publication thereof by Stellenbosch University will not infringe any third party rights and that I have not previously in its entirety or in part submitted it for obtaining any qualification.

.....

Date

Copyright © 2016 Stellenbosch University

All rights reserved

Acknowledgments

In the spirit of successfully compiling this thesis, I would like to express my sincere gratitude to those who made it possible:

- Prof. Thomas Jones for his guidance, explanations, ideas and expertise. His dedication and insight helped me to successfully meet the project objectives, and he taught me a great deal about problem solving.
- Mr. Japie Engelbrecht for his invaluable insights on flight mechanics and formation flight, but even more for creating this research opportunity and communicating with all the involved parties of this project.
- The NAC for financial support in the form of a study bursary. I hope that this work will contribute value.
- Jordan Adams, Drewan Sanders and Prof. Chris Redelinghuys for sharing their expertise on aerodynamics and flight mechanics, which created the theoretical foundation for this thesis. Jordan also invested a great deal of time to make sure I grasped the concepts which fell outside my field of study.
- My formation flight and lab buddy, Evert Trollip, for his technical assistance, dedication and words of motivation. He played a big role in the compilation of this project, from the deciphering of technical papers to the deeper understanding of flight mechanics.
- All the van Wyks for their emotional and financial support. Each one of them contributed a great deal of wisdom and motivation to back me in this endeavor. Your commitment in this time will always be remembered.
- Finally to a special lady. Klara, thank you for dealing with the day to day highs and lows of this project. You helped me create and maintain a healthy balance throughout this work and together we discovered the life lessons hidden in our research goals. I'm excited to see how we practice and grow this wisdom in the future.

Abstract

The research drive behind this formation flight thesis is to increase the flight efficiency of commercial aircrafts. Previous research has shown that formation flight holds significant fuel savings for the follower aircraft. Due to the longevity of the wingtip vortices, fuel savings at extended formations (more than ten wingspans in longitudinal separation) are plausible, making formation flight viable for commercial use.

In formation flight, the forces and moments acting on the follower aircraft are directly related to the position of the follower relative to the leader's displaced wingtip vortices. The upwash created by the leader's vortices produces an additional lift benefit on the follower in the outer wake. As a result, the follower lowers its angle of attack and reduces the aircraft's induced drag, creating a more efficient flight condition. However, this non-uniform upwash also produces a large rolling moment on the follower aircraft.

In this thesis, two commercial aircraft models were implemented in simulation: a leader in isolated flight, and a follower with the wake interaction aerodynamics of the leader aircraft. A second-order engine model with non-linearities was included to increase the aircraft model fidelity. For the isolated aircraft, airspeed, altitude and cross-track controllers were developed. By remapping and augmenting these conventional aircraft controls, follower station keeping was achieved. However, flying deep in the wake induced large rolling moments on the follower, which required high aileron settings. A complementary filter system was designed to reduce aileron demand by inducing sideslip on the follower to counter the wake-induced rolling moment. This filter system modified the aileron control signal to pass high-frequency information to the ailerons and low-frequency commands to other control surfaces. This method proved successful, as a small rudder or differential thrust setting could be applied to induce sideslip of less than 1.5° , and reduce aileron trim while effectively regulating formation-hold.

The complementary filter system enabled the follower aircraft to stably fly deep in the wake and achieve more efficient flight conditions. However, flying at the optimum separation is challenging, as the wingtip vortex location will be unknown in a real world application. Measuring the wingtip vortex location also comes with additional complexities and thus a controller dedicated to minimizing thrust demand was developed. By applying small circular perturbations to the follower aircraft's lateral and vertical formation-hold controllers, the aircraft was exposed to the gradients of the wake. This controller decreased thrust by minimizing the follower's pitch angle through integral control of the gradient information. By optimizing the lateral and vertical separation, the follower converged to the most efficient separation and effective extremum-seeking control was achieved in light turbulence. In moderate turbulence, the perturbation signal observable in the optimization objective disappeared in the turbulence noise, and extremum seeking was unsuccessful for higher levels of turbulence.

A mean thrust reduction of 26% was obtained on the follower aircraft at one wingspan lateral and zero vertical separation in light turbulence. This saving translates to a 24% decrease in fuel flow, confirming the economic significance of formation flight.

Opsomming

Vorige navorsing toon dat formasievlug 'n beduidende bydrae kan lewer tot brandstofbesparing vir 'n volgervliegtuig. Die verlengde leeftyd van 'n vliegtuig se nasleurvortekse maak dit moontlik om by meer as tien vlerkspanne se longitudinale skeidingsafstand steeds hoë vlakke van brandstofbesparing te bereik. Die navorsingsdryfkrag agter hierdie formasievlugprojek is hoofsaaklik daarop gerig om meer effektiewe vlug vir kommersiële vliegtuie voor te stel.

In formasievlug is die kragte en momente wat op die volgervliegtuig inwerk direk gekoppel aan die volger se posisie ten opsigte van die voorste vliegtuig se verplaaste nasleurvortekse. Die opwaartse lugvloei wat geskep word deur die voorste vliegtuig se nasleurvortekse skep 'n addisionele opwaartse krag op die volger. As gevolg van hierdie ekstra krag kan die volger sy aanvalshoek verminder, wat dus 'n afname in geïnduseerde weerstand skep. In formasie verminder die weerstand, en 'n meer ekonomiese vlugkondisie kan behaal word. Ongelukkig veroorsaak hierdie nie-uniforme lugstroom ook 'n sterk rolmoment op die volgervliegtuig.

In hierdie tesis is twee kommersiële vliegtuigmodelle geïmplementeer: die voorste vliegtuig in geïsoleerde vlug, en die volger in die nastroom van die voorste vliegtuig. 'n Tweede-order enjinmodel is ook ontwikkel om by te dra tot 'n meer verteenwoordigende vliegtuigmodel. Om die vliegtuig in geïsoleerde toestande te evalueer, is konvensionele lugspoed, hoogte en laterale-afstandbeheerders ontwerp en gesimuleer. Deur bloot hierdie konvensionele beheerders minimaal aan te pas kon formasiehoubeheer effektief toegepas word. Hoe dieper die volgervliegtuig egter in die nasleur van die voorste vliegtuig inbeweeg, hoe groter word die rolmoment wat op die volger geïnduseer word, tot dit die rolroer-beheeroppervlakte versadig. Om hierdie versadigingsprobleem aan te spreek is 'n komplementêre filtersisteem ontwikkel wat die rolroer-beheersein filter om hoëfrekwensie-informasie na die rolroer te voer en laëfrekwensie-informasie aan die roerbeheer te stuur. Dit induseer 'n syglip op die volgervliegtuig, wat 'n teenrolmoment veroorsaak. Hierdie metode was suksesvol omdat lae roer of differensiële enjinkrag 'n klein glyhoek kon induseer, wat drasties die vlak van rolroer-beheer verminder het.

Die komplementêre filterstelsel stel die volgervliegtuig in staat om stabiel diep in die nasleur van die voorste vliegtuig te vlieg, tot by die posisie waar die minimum stukrag benodig word. Om die volgervliegtuig by hierdie optimale posisie te laat vlieg, skep addisionele komplikasies omdat die presiese posisie van die nasleurvortekse nie maklik gemeet kan word nie. Dus is 'n beheerder ontwikkel wat toegewy is aan die minimering van die volgervliegtuig se enjin-stukragverbruik.

'n Aanpasbare, nie-lineêre terugvoerbeheerder is geïmplementeer om die volgervliegtuig na die optimale posisie in die nasleur te stuur. Deur klein sirkelvormige beheerseine aan die volger se laterale en vertikale formasiehoubeheerders te voer, kon die volger in die nasleur rondbeweeg word op 'n wyse wat die gradiënt-informasie van die nasleur ontgin. Hierdie gradiënt-informasie is gemeet deur die volger se verandering in aanvalshoek te evalueer. Die informasie is geïntegreer om die volgende skatting vir die optimale posisie aan die vertikale en laterale formasiehoubeheerders te verskaf. Hierdie minimum-soekbeheerder kon suksesvol die minimum enjinstukrag-posisie in die nasleur opspoor en volg in ligte turbulensie. In matige turbulensie kon hierdie soekbeheerder nie funksioneer nie omdat die perturbasie seín verdwyn

in die reis vanaf die hoë vlakke van atmosferiese steurings.

'n Gemiddelde enjinstukrag besparing van 26% was bereik deur die volgervliegtuig by die optimale posisie in die nasleur te laat vlieg (een vlerkspan in laterale verplasing en nul in vertikale verplasing). Hierdie enginekrag besparing verteenwoordig 'n 24% besparing in brandstof vloei deur die volgervliegtuig. Hierdie eerste skatting tot die brandstof besparing van formasievlug bevestig die ekonomiese potensiaal wat formasie vlug kan bied.

Contents

Declaration	ii
Acknowledgements	ii
Abstract	iii
Opsomming	iv
1 Formation Flight Overview and Project Outline	1
1.1 Introduction	1
1.2 Current Developments	1
1.3 Research Collaboration	2
1.4 Literature Review	2
1.4.1 Aircraft Wake and Wingtip Vortices	3
1.4.2 Benefits and Challenges of Extended Formation Flight	4
1.4.3 Aerodynamic Modeling of Formation Flight Airframes	6
1.4.4 Flight Controllers and Extremum-Seeking Control in Formation Flight	7
1.5 Problem Statement	9
1.6 Project Objectives	9
1.7 Project Overview and Methodology	10
2 Turbofan Engine Model	12
2.1 Literature Review: Modeling A Turbofan Engine	12
2.1.1 Two-Spool Turbofan Engine Dynamics	12
2.1.1.1 Shaft Dynamics: Effect Of Inertia	13
2.1.1.2 Pressure And Temperature Dynamics	15
2.1.2 Turbofan Engine Simulation Projects	16
2.1.3 Concluding The Engine Literature Review	17
2.2 Deriving A Thrust Model From EMUCT Using Linear Bisection	18
2.2.1 Parameter Fitting Algorithm	19
2.2.2 Convergence of the Parameter Identification Algorithm	22
2.3 Determining And Validating The Engine Model	23
2.3.1 The Thrust Gain Schedule	23

2.3.2	The Second-Order Engine Model Parameters	24
2.3.3	Fuel Flow Model	27
2.4	Concluding The Engine Model	28
3	Mathematical Models	29
3.1	Conventional Axis Systems	29
3.1.1	Body Axis	30
3.1.2	Stability and Wind Axes	30
3.1.3	Inertial Axis	31
3.2	Aircraft Model Sign Conventions	31
3.3	Six Degrees of Freedom Equations of Motion	32
3.3.1	Aircraft Kinetics	32
3.3.2	Aircraft Kinematics	33
3.4	Aircraft Forces and Moments	34
3.4.1	Gravitational Model	34
3.4.2	The Higher-Order Boeing 747 Thrust Model	35
3.4.2.1	Thrust Distribution Model	35
3.4.2.2	The Forces And Moments Produced by Engine Thrust	36
3.4.2.3	Thrust Model Simulation	38
3.5	Control Actuators	39
3.6	Aerodynamic Model for Isolated Flight	39
3.7	Relative Formation Separation	41
3.8	Formation Aerodynamic Interaction Model	42
3.8.1	Approximate Aerodynamic Interaction Model.	43
3.8.2	Aerodynamic Interaction Model Limitations	46
3.9	Atmospheric Turbulence Model	48
3.10	Concluding the Mathematical Modeling	49
4	Trim and Linear Dynamic Analysis	51
4.1	Trim Analysis	51
4.1.1	Isolated Flight Trim Analysis	52
4.2	Formation Flight Trim Analysis	54
4.3	Aircraft Model Linearization	57
4.3.1	Linearizing About Trim	58
4.3.2	Isolated Flight Linear Aircraft Model	59
4.3.3	Linear Follower Aircraft in Formation	62
4.4	Trim and Linearization Conclusion	67

5	Conventional Flight Aircraft Controllers	68
5.1	Longitudinal Control	68
5.1.1	DQ Control: Pitch Rate Damper and Normal Acceleration Control . .	69
5.1.1.1	DQ Control: Design	70
5.1.1.2	DQ Control: Specifications and Closed-Loop Response . . .	71
5.1.2	Climb Rate Control	75
5.1.2.1	Climb Rate Control: Design	75
5.1.2.2	Climb Rate Control: Specifications and Closed-Loop Response	76
5.1.3	Auto-Thrust Control	77
5.1.3.1	Auto-Thrust Control: Design	78
5.1.3.2	Auto-Thrust Control: Specifications and Closed-Loop Response	79
5.1.4	Altitude Control	81
5.1.4.1	Altitude Control: Design	81
5.1.4.2	Altitude Control: Specifications and Closed-Loop Response .	83
5.1.5	Concluding the Longitudinal Control	86
5.2	Lateral Control	87
5.2.1	DPDR Controller	87
5.2.1.1	DPDR Controller: Design	88
5.2.1.2	DPDR Controller: Specifications and Closed-Loop Response	89
5.2.2	Cross-Track Controller	91
5.2.2.1	Cross-Track Controller: Design	92
5.2.2.2	Cross-Track Controller: Specifications and Closed-Loop Re- sponse	94
5.2.3	Concluding the Lateral Control	96
5.3	Control Anti-Windup	96
5.4	Conventional Control Under Turbulent Conditions	97
5.5	Concluding the Conventional Flight Controls	98
6	Formation-Hold Control	101
6.1	Formation-Hold by Conventional Control Augmentation	102
6.1.1	Longitudinal Formation-Hold	103
6.1.1.1	Longitudinal Formation-Hold: Control Design	103
6.1.1.2	Longitudinal Formation-Hold: Specifications and Response .	104
6.1.2	Vertical Formation-Hold	105
6.1.2.1	Vertical Formation-Hold: Control Design	105
6.1.2.2	Vertical Formation-Hold: Specifications and Response	106
6.1.3	Lateral Formation-Hold	107
6.1.3.1	Lateral Formation-Hold: Design	108

6.1.3.2	Lateral Formation-Hold: Specifications and Response	109
6.1.4	Formation-Hold Control Authority Problem	112
6.2	Complementary Filter Control	114
6.2.1	Sideslip Formation-Hold Control	114
6.2.1.1	Sideslip Formation-Hold Control: Design	115
6.2.1.2	Sideslip Formation-Hold Control: Specifications and Response	116
6.2.2	Sideslip and Differential Thrust Formation-Hold Control	118
6.2.2.1	Sideslip and Differential Thrust Formation-Hold Control: De- sign	119
6.2.2.2	Sideslip and Differential Thrust Formation-Hold Control: Spec- ifications and Response	120
6.3	Formation-Hold Control Under Turbulent Conditions	123
6.4	Formation Flight Efficiency Analysis	126
6.5	Concluding Formation-Hold Control	127
7	Extremum Seeking in Formation	129
7.1	Literature Review	129
7.2	Optimization Objective and Assumption Evaluation	133
7.3	Extremum-Seeking Controller	135
7.3.1	Extremum-Seeking Design Procedure	136
7.3.1.1	Phase Synchronization	137
7.3.1.2	Pitch Angle Observer	138
7.3.1.3	Logic Control	138
7.3.2	Extremum-Seeking Control Specification	140
7.4	Extremum-Seeking: Simulation Results	142
7.5	Extremum Seeking Under Turbulent Conditions	146
7.6	Extremum Seeking Conclusion	150
8	Concluding Optimal Formation Flight Control	151
8.1	Conclusion	151
8.2	Limitations and Recommendation for Future Work	153
	References	159
A	Model Parameters and Control Gains	160
A.1	Aircraft Attributes	160

B	Extended Simulation Results	163
B.1	Conventional Control Under Turbulent Conditions	163
B.2	Formation-Hold Flight Controls Under Turbulent Conditions	165
B.2.1	No Complimentary Filter Active	165
B.2.2	Rudder Complimentary Filter Active	167
B.2.3	Rudder and Differential Thrust Complimentary Filter Active	169
B.3	Extremum-Seeking Controller	171
B.3.1	Extremum-Seeking Controller With A 20s Perturbation Period	171
B.3.2	Extremum-Seeking Controller With A 30s Perturbation Period	173
B.3.3	Extremum Seeking Control In Turbulent Conditions	174

List of Figures

1.1	Aircraft wake with wingtip vortices inducing upwash and downwash	4
1.2	Follower aircraft in wake of leader and exposed to upwash of leader's wingtip vortices	5
1.3	Lift benefit and rolling moment induced on follower aircraft by wingtip vortices of leader	5
1.4	Horseshoe vortex representation [1]	7
1.5	Project methodology	11
2.1	Turbofan engine modules	13
2.2	Analogy of shaft dynamics by two-disk system	14
2.3	EMUCT Engine Model Inputs and Outputs	18
2.4	Second-Order EMUS engine model with thrust controller	19
2.5	Linear bisection algorithm for model parameter optimization	21
2.6	Cost function convergence for model parameter optimization using linear bisection	22
2.7	Parameter convergence using the linear bisection algorithm	22
2.8	Steady-state correlation between the EMUCT and EMUS models for a range of fuel flow commands	24
2.9	EMUS model gain schedule	24
2.10	Correlation between EMUCT and EMUS models for step inputs up to 2% steady-state settling time for a range of fuel flow commands	25
2.11	Second-order model parameter fitting values over a range of thrust step inputs around 44.25 kN trim thrust	26
2.12	Second-order EMUS model for acceleration and deceleration combination	26
2.13	EMUS poles and zeros for both acceleration and deceleration transfer functions	27
2.14	EMUS model thrust output validated with EMUCT thrust output data	27
2.15	The EMUCT fuel flow model versus the EMUS fuel flow model for various step inputs in fuel command	28
3.1	Mathematical model system overview	29

3.2	Body, wind, stability and inertial axis representation	30
3.3	Sign conventions of the aircraft model	31
3.4	Six degrees of freedom model	32
3.5	Higher-order thrust model diagram	35
3.6	Engine placement and alignment variables of the Boeing 747 aircraft	37
3.7	Thrust model output as actuated by T_h command with no δ_T applied	38
3.8	Thrust model output as actuated with constant T_{hc} and δ_{Tc} applied	39
3.9	Formation flight separation and effective separation	41
3.10	Wake-induced incremental aerodynamic coefficients ($\xi = -10, \eta = 0 : 2, \zeta = -1 : 1$)	45
3.11	Wake-induced aerodynamic coefficients at zero vertical separation ($\xi = -10, \eta = 0 : 2, \zeta = 0$)	46
3.12	Induced drag and rolling moment incremental coefficient comparison between the approximate and numerical method over an elliptical wing for $\zeta = 0$ by Bizinos et al. [2]	47
3.13	Lift and rolling moment incremental coefficient comparison between wind tunnel data, vortex lattice code, and the approximate and numerical integration methods $\zeta = 0$ by Bizinos et al. [2]	48
4.1	Sideslip trim equilibrium of moments achieved with ailerons countering the sideslip-induced rolling moment	53
4.2	Sideslip trim equilibrium of forces achieved by roll angle countering the sideslip induced side force	54
4.3	Calculated follower trim for $\zeta = 0$ and $\beta_T, \delta_{TT} = 0$	55
4.4	Calculated follower trim for $\zeta = 0$ and $\delta_{AT}, \delta_{TT} = 0$	56
4.5	Calculated follower trim for $\zeta = 0$ and $\delta_{AT}, \delta_{RT} = 0$	57
4.6	Boeing 747 aircraft poles as calculated and compared to Heffley data [3]	60
4.7	Linear versus non-linear system response for small control input step in the longitudinal system	61
4.8	Linear versus nonlinear system response for small control input step in the lateral system	62
4.9	Pole movement over lateral separation with the follower at $\zeta = 0$ and $\eta = 1$ to 1.4, where red represents $\eta = 1$ and blue represents $\eta = 1.4$	64
4.10	Pole movement over vertical separation with the follower at $\eta = 1$ and $\zeta = -0.2$ to 0.2, where red represents $\zeta = -0.2$ and blue represents $\zeta = 0.2$	65
4.11	Longitudinal linear vs. non-linear model states for small step input	66
4.12	Lateral linear vs. non-linear model states for small step input	67

5.1	Aircraft longitudinal control diagram for isolated flight	69
5.2	DQ law: pitch rate damper and normal acceleration control diagram	70
5.3	Longitudinal dynamics plant and closed-loop DQ controller poles	73
5.4	DQ controller normal acceleration unit step response	73
5.5	DQ controller longitudinal linear vs. non-linear aircraft for unit step normal acceleration command	74
5.6	DQ controller elevator actuator response for unit step normal acceleration command.	74
5.7	Climb Rate control diagram	75
5.8	Climb rate proportional (P) controller: a) system open-loop and closed-loop poles and b) unit step response for climb rate	76
5.9	Climb rate proportional (P) controller: a) elevator actuator response and b) thrust response for a unit step response in climb rate	77
5.10	Airspeed control concept	78
5.11	Aircraft auto-thrust control diagram	78
5.12	Auto-thrust proportional integral controller: a) climb rate plant to auto-thrust controller closed-loop system poles and b) response for unit step input	80
5.13	Auto-thrust proportional integral (PI) controller: a) elevator actuator response and b) thrust response for a unit step response in airspeed	80
5.14	Aircraft altitude proportional (P) control diagram	81
5.15	Aircraft altitude proportional integral derivative (PID) control diagram	82
5.16	Auto-thrust plant to altitude proportional (P) controller closed-loop system poles	83
5.17	Altitude proportional (P) controller response for: a) unit step input and b) coupling between lateral states and altitude control	84
5.18	a) Altitude proportional (P) controller plant poles to proportional integral derivative (PID) control system closed-loop poles b) PID control root locus design	85
5.19	a) Altitude P and PID controller response for unit step input and b) coupling between lateral states and altitude state with PID control	85
5.20	Auto-thrust proportional integral (PI) controller: a) elevator actuator response and b) thrust response for a unit step response in airspeed	86
5.21	Integrator windup protection for controller integrators	87
5.22	Lateral DPDR control diagram	88
5.23	a) Lateral aircraft plant to DPDR controller closed-loop system poles and b) roll response for one degree step in roll command	90
5.24	a) DPDR controller sideslip response and b) control aileron and rudder demand for one degree step in roll command	90

5.25 DPDR controller: a) sideslip response, b) roll angle response and c) aileron and rudder response for one degree step in sideslip command	91
5.26 Aircraft cross-track control diagram	92
5.27 Aircraft cross-track control diagram	93
5.28 a) DPDR plant to cross-track velocity closed loop system poles and b) cross-track velocity unit step response	95
5.29 a) Cross-track velocity plant to cross-track separation proportional controller closed loop system poles, b) cross-track separation response c) aileron and rudder response for cross-track unit step command	95
5.30 Integrator windup protection for controller integrators	96
5.31 Altitude anti-windup in PID controller	97
6.1 Formation flight systems overview	101
6.2 Formation-hold longitudinal control augmentation on follower aircraft	102
6.3 Formation-hold lateral control augmentation on follower aircraft	102
6.4 Longitudinal formation-hold control design	103
6.5 Experimentally determining the critical parameter for Ziegler-Nichols controller tuning	104
6.6 Longitudinal formation-hold proportional controller response for a unit step command in longitudinal separation for various gains where $\eta = 1$ and $\zeta = 0$	105
6.7 Formation-hold vertical control design	105
6.8 Vertical formation-hold controller pole movement for ζ between -0.2 and 0.2, from red to blue, with $\eta = 1$ and $\xi = 10$	106
6.9 Vertical formation-hold controller for $\eta = 1$ and $\xi = 10$: a) small step response for vertical separation from $\zeta = 0$ to $\zeta = 0.1$ and b) large step response for vertical separation from $\zeta = -1$ to $\zeta = 0$	107
6.10 Formation-hold lateral control design.	108
6.11 Lateral formation-hold control by expanding the cross-track with a PID controller	109
6.12 PID control: a) root locus design and b) step response in isolated flight	110
6.13 Lateral formation-hold controller pole movement for η from 1 to 1.4, moving from red to blue with $\zeta = 0$ and $\xi = 10$	111
6.14 Lateral formation-hold controller for $\zeta = 0$ and $\xi = 10$: a) small step response for lateral separation from $\eta = 1$ to $\eta = 1.1$ and b) large step response for vertical separation from $\eta = 2$ to $\eta = 1$	111
6.15 Formation-hold control response when flying from the outer wake to the optimum separation ($\eta = 1, \zeta = 0$) for: a) formation separation parameters and b) thrust and differential thrust control perturbation	112

6.16	Formation-hold control response when flying from the outer wake to the optimum separation ($\eta = 1, \zeta = 0$) for: a) control surface deflection and b) follower aircraft attitude	113
6.17	Formation-hold lateral control with complementary filter system	114
6.18	Countering the wake-induced rolling moment by applying: a) ailerons or b) rudder through the complementary filter system	115
6.19	Complementary filter system to mix aileron authority to rudder	115
6.20	Aileron to rudder complementary filter design	116
6.21	Formation-hold control with sideslip complementary filter active. Response for flying from the outer wake to the optimum separation ($\eta = 1, \zeta = 0$) for: a) formation separation and b) follower thrust perturbation	117
6.22	Formation-hold control with sideslip complementary filter active. Response for flying from the outer wake to the optimum separation ($\eta = 1, \zeta = 0$) for: a) control surface deflection and b) follower aircraft attitude	118
6.23	Countering the wake induced rolling moment by applying: a) ailerons or b) differential thrust through the complementary filter system.	119
6.24	Complementary filter system to mix aileron authority to rudder and differential thrust	119
6.25	Rudder-to-differential thrust complementary filter design	121
6.26	Formation-hold control with sideslip and differential thrust complementary filter active. Response for flying from the outer wake to the optimum separation ($\eta = 1, \zeta = 0$) for: a) formation separation and b) follower thrust perturbation	121
6.27	Formation-hold control with sideslip and differential thrust complementary filter active. Response for flying from the outer wake to the optimum separation ($\eta = 1, \zeta = 0$) for: a) control surface deflection and b) follower aircraft attitude	122
6.28	Formation-hold control with rudder complementary filter system and without the complementary filter system under moderate turbulence fly at the optimum separation	125
6.29	Formation flight a) thrust and b) fuel response at $\eta = 1$ and $\zeta = 0$ in light turbulence	126
7.1	Extremum-seeking control scheme as proposed by Krstić [4]	130
7.2	Formation flight extremum seeking as proposed by Binetti [5]	132
7.3	a) Follower trim pitch angle in the wake and b) wake-induced change in follower pitch angle trim	133
7.4	Gradient maps for the follower pitch angle in the wake	134
7.5	Proposed extremum-seeking control scheme for optimal fuel consumption in formation flight	135

7.6	Lateral extremum-seeking control loop architecture	136
7.7	Lateral extremum-seeking control loop architecture	137
7.8	Wake map logic partitions	139
7.9	Formation flight state machine	140
7.10	Extremum-seeking controller band-pass and low-pass filter design	141
7.11	Extremum-seeking control flight path with regard to lateral and vertical separation, with a perturbation frequency period of 30 seconds and an amplitude of about $0.02b$	143
7.12	Extremum-seeking controller response for formation separation and attitude, with a perturbation frequency of 30 seconds and an amplitude of about $0.02b$	143
7.13	Extremum-seeking controller follower inputs for the control surfaces and thrust, with a perturbation frequency of 30 seconds and an amplitude of about $0.02b$	144
7.14	Extremum-seeking control band-pass and low-pass filter output for vertical optimization, with a perturbation frequency period of 30 seconds and an amplitude of about $0.02b$	146
7.15	Extremum-seeking controller performance under light turbulence with a perturbation period of 30 seconds and an amplitude of about $0.02b$	147
7.16	Extremum seeking controller performance under light turbulence with a perturbation period of 30 seconds and an amplitude of about $0.02b$	148
7.17	Extremum seeking controller performance under light turbulence where the optimum location shifted at 700 seconds from $\eta = 1, \zeta = 0$ to $\eta = 1, \zeta = 0.2$	149
B.1	Conventional controller performance under turbulent conditions	163
B.2	Conventional controller actuator performance under turbulent conditions	164
B.3	Cross-track controller performance under turbulent conditions	164
B.4	Conventional controller actuator performance under turbulent conditions	165
B.5	Formation-hold control: a) lateral separation, b) vertical separation and c) longitudinal separation in turbulence with no complimentary filters active	165
B.6	Formation-hold control: a) roll angle response, b) pitch angle response and c) sideslip angle response in turbulence with no complimentary filters active	166
B.7	Formation-hold control: a) aileron actuator response, b) rudder actuator response and c) elevator actuator response in turbulence with no complimentary filters active	166
B.8	Formation-hold control thrust response in turbulence with no complimentary filters active	167
B.9	Formation-hold control: a) lateral separation, b) vertical separation and c) longitudinal separation in turbulence with rudder complimentary filters active	167

B.10 Formation-hold control: a) roll angle response, b) pitch angle response and c) sideslip angle response in turbulence with rudder complimentary filters active	168
B.11 Formation-hold control: a) aileron actuator response, b) rudder actuator response and c) elevator actuator response in turbulence with rudder complimentary filters active	168
B.12 Formation-hold control thrust response in turbulence with rudder complimentary filters active	169
B.13 Formation-hold control: a) lateral separation, b) vertical separation and c) longitudinal separation in turbulence with rudder and differential thrust complimentary filters active	169
B.14 Formation-hold control: a) roll angle response, b) pitch angle response and c) sideslip angle response in turbulence with rudder and differential thrust complimentary filters active	170
B.15 Formation-hold control: a) aileron actuator response, b) rudder actuator response and c) elevator actuator response in turbulence with rudder and differential thrust complimentary filters active	170
B.16 Formation-hold control: a) thrust response and b) differential thrust response in turbulence with rudder rudder and differential thrust complimentary filters active	171
B.17 Extremum-seeking control flight path with regard to lateral and vertical separation with a perturbation frequency period of 20 seconds and an amplitude of about $0.015b$	171
B.18 Extremum-seeking controller response for formation separation and attitude with a perturbation frequency of 20 seconds and an amplitude of about $0.015b$	172
B.19 Extremum-seeking controller follower inputs for the control surfaces and thrust with a perturbation frequency of 20 seconds and an amplitude of about $0.015b$	172
B.20 Extremum-seeking control flight path with regard to lateral and vertical separation with a perturbation frequency period of 30 seconds and an amplitude of about $0.02b$	173
B.21 Extremum-seeking controller response for formation separation and attitude with a perturbation frequency of 30 seconds and an amplitude of about $0.02b$	173
B.22 Extremum-seeking controller follower inputs for the control surfaces and thrust with a perturbation frequency of 30 seconds and an amplitude of about $0.02b$	174
B.23 Extremum-seeking controller performance under light turbulence with a perturbation period of 30 seconds and an amplitude of about $0.02b$	174
B.24 Extremum-seeking controller performance under light turbulence with a perturbation period of 30 seconds and an amplitude of about $0.02b$	175

List of Tables

3.1	Sign conventions and aircraft model parameters	32
4.1	Straight and level flight trim in isolated flight	53
5.1	Longitudinal system DQ controller design specification	72
5.2	The standard deviation of conventional controllers under turbulent conditions normalized to aircraft wingspan	98
6.1	The standard deviation over 15 minutes for the formation-hold controllers under turbulent conditions with rudder and differential thrust filter active and $\xi = 10$	123
6.2	The standard deviation for the various formation-hold controllers under turbulent conditions with $\eta = 10$, evaluating the application of the complementary filter system	124
7.1	Extremum-seeking logic control boundary values	142
A.1	Boeing 747 aerodynamic coefficient parameters for isolated flight	160
A.2	Boeing 747 physical parameters	161
A.3	Boeing 747 wake characteristics	161
A.4	Aircraft actuator parameters	162

Nomenclature

Acronyms

CF6-80	Turbofan engine produced by General Electric, a common choice for the Boeing 747
CG	Center of Gravity
EMUCT	Engine Model University of Cape Town. Turbofan engine model of a CF6-80 engine as derived by Sanders et al. [6]
EMUS	Engine Model University Stellenbosch. Engine actuator model as derived for this thesis
GSP	Gas Turbine Simulation Program by The National Aerospace Laboratory
HPF	High pass filter
LPF	Low pass filter
MAC	Mean Aerodynamic Cord
MIMO	Multiple Input Multiple Output
P	Proportional
PID	Proportional integral derivative control system
SISO	Single Input Single Output

Coordinate Vector

\bar{V}, α, β	Aircraft freestream velocity magnitude, angle of attack and sideslip in polar coordinate representation
Φ, Θ, Ψ	The Euler 3-2-1 attitude parameters of the body axis system with respect to inertial axis space

L, M, N	Roll, pitch and yaw moments in the subscripted axis system. If the subscript is not included, the body axes is implied
N, E, D	Coordinates of the position vector in the inertial axis
P, Q, R	Roll, pitch and yaw rate in the body axis
U, V, W	Axial, lateral and normal velocity in the body axis
X, Y, Z	Axial, lateral and normal force vector in the subscripted axis system. If the no subscript is included, the body axes is implied

Modeling

\mathcal{R}	Aspect ratio
\bar{c}	Mean aerodynamic chord
\bar{V}_s	Speed of sound
$\delta_A, \delta_E, \delta_R$	Aileron, elevator and rudder control deflections
η_T	Tailplane setting angle.
μ	Vortex core radius normalized by wingspan, $\frac{r_c}{b}$
σ	Downwash influencing factor
τ	Moment influencing factor
θ_e, ψ_e	Engine tilt angle, for upward tilt and inboard tilt respectively
ξ, η, ζ	Axial, lateral and vertical separation between the leader and follower aircraft normalized to the aircraft wingspan
ζ_f	Double the tailfin height normalized by wingspan, $\frac{b_f}{b}$
ζ_v	Tailfin root displacement above wing normalized by wingspan, $\frac{z_v}{b}$
a_1	Tailplain lift coefficient slope
a_i, a_o	Engine placement distance for inboard and outboard engines respectively in the subscripted direction
a_x, a_y, a_z	Separation distance between the leader and the follower aircraft
b	Aircraft wingspan

b_f	Double the tailfin height
b_h	Tailplain span
b_v	Bound vortex span, $\frac{\pi}{4}b$
b_{fv}	Tailfin bound vortex height
b_{hv}	Tailplain bound vortex span
c_f	Tailfin chord
C_L, C_D	Lift and drag dimensionless aerodynamic coefficients in the subscripted axis
C_l, C_m, C_n	Rolling, pitching and yawing moment dimensionless aerodynamic coefficients in the subscripted axis
C_X, C_Y, C_Z	Axial, normal and side force dimensionless aerodynamic coefficients in the subscripted axis
c_{l_α}	Two-dimensional wing lift coefficient gradient
g	Gravitational constant.
h	Perpendicular distance from vortex filament to influence point
I_{xx}, I_{yy}, I_{zz}	Aircraft principle moments of inertia about the respective body axis
m	Aircraft mass constant
q	Dynamic pressure
r_c	Vortex core radius
S	Wing surface area
t	Time
t^*	Time separation between leader and follower aircraft
T_h, δ_T	Thrust and differential thrust
$T_{so}, T_{si}, T_{po}, T_{pi}$	The four engines of the aircraft model; starboard outer, starboard inner, port outer and port inner respectively.
v_a, ω_a	Atmospheric disturbance linear and angular velocities
W_f	Engine fuel flow rate

z_v Tailfin root displacement above wing

Subscripts

0 Steady in isolated flight

B Body axis system

c Command or reference signal

E Inertial axis system.

j Leader aircraft

k Follower aircraft

S Stability axis system

T Parameter value at trim

W Wind axis system

LP Linearization point.

Superscripts

* Effective separation

A Aerodynamic

G Gravity

T Thrust

Symbols

ω_n Natural frequency

ζ_n System damping

Chapter 1

Formation Flight Overview and Project Outline

1.1 Introduction

Migratory birds flying in v-shape formation have always been a mesmerizing sight. Closer analysis of this natural phenomenon of formation flight estimates that a flock of 25 birds can increase their flight range by 70% when compared to a bird in lone flight [7]. Yet not much attention has been paid to this method of flying by the general aviation community. One can argue that this is largely due to the increased pilot workload and risks associated with flying in close formation [8]. Because of these risks, formation flight is mostly only considered for military and air-show purposes. However, formation flight extending in downstream longitudinal separations of at least ten wingspans is considered less hazardous [9], possibly making this form of formation flight a commercially viable option. This mode of flight takes advantage of the persistence of the lead aircraft's wake, which results in wingtip vortices propagating up to 40 wingspans downstream. The circulation of these vortices produces an upwash in the outer wake, which can be utilized by the follower aircraft to reduce its induced drag. With increasing air traffic, environmental concerns and raising fuel prices, more focus should be placed on advanced techniques for reducing the fuel demand on commercial aircraft.

1.2 Current Developments

The Federal Aviation Administration (FAA) estimates that the number of passengers making use of commercial airliners will increase by two thirds over the period 2013 to 2033, while past data shows that airliners find it more challenging to maintain profitability with the current rise in fuel costs [10]. This rise in demand, environmental concerns and the increase in running costs are creating a demand for developing more economical air transport. Since formation flight shows estimated savings in fuel consumption of between 10% and 40%, it is

becoming an attractive option to cater to the high industry demands [11].

In recent years, more researchers have been looking into formation flight controllers to explore the potential of formation flight's promising economical benefits. There has already been successful implementations of close formation flight autopilot controllers on military aircraft [12]. Other studies predict that extended formation flight, suitable for commercial purposes, can offer significant reductions in induced drag of approximately 30% [9].

1.3 Research Collaboration

This thesis was compiled under a research collaboration between Stellenbosch University and the University of Cape Town. One of the aims of this collaboration is to investigate the simulation and control of extended formation flight conditions for commercial aircraft. The research collaboration is also investigating the economic benefits of formation flight, as well as the safety and ride comfort implications of such a system.

In a previous study by Bizinos et al. [13], an aerodynamic model was derived to calculate the induced forces and moments experienced by the wingman aircraft flying in the wake of the leader. This aerodynamic model was used by Buchner et al. [14] to analyze the stability and performance of the trailing aircraft's flight control systems. It was found that a trimmable region exists which can potentially produce added fuel savings. Other research projects that focus on passenger comfort and safety consideration in extended formation flight are currently being conducted by other researchers under this collaboration.

This thesis focuses on the design and simulation of a flight controller for commercial aircraft that optimizes fuel consumption during extended formation flight. This research builds on the aerodynamic wake model as derived by Bizinos [13].

1.4 Literature Review

The prospect of an increasing demand on commercial transport, as discussed in Section 1.2, has generated extensive research on the modeling, economical benefits and design feasibility of formation flight for commercial use. This thesis was conducted with the primary focus on designing and simulating a flight controller that optimizes fuel consumption during echelon formation of two identical commercial aircraft. In order to establish a clear understanding of the current research developments in this field, a brief literature review will be provided in this section, focusing on the following research areas:

- Aircraft wake and wingtip vortices
- Benefits and challenges related to formation flight
- Modeling of the aerodynamic interaction of formation flight
- Flight controllers and extremum seeking control in formation flight

1.4.1 Aircraft Wake and Wingtip Vortices

Before attempting to model and control an aircraft in the wake of another, it is essential to investigate the predominant aerodynamics in the wake of an aircraft. This section will discuss the expected aerodynamic effects, their causes and the expected interactions induced on follower aircraft.

In all forms of fixed-wing flight, wingtip vortices form due to the differential pressure between the bottom and top surfaces of the wing. The pressure drives fluid around the wingtip, resulting in a strong vortex. This pressure difference produces a span-wise flow toward the wingtip on the bottom surface, as well as toward the fuselage on the top surface, as a function of the angle of attack and airspeed. The difference in flow direction at the wing's trailing edge creates a free shear layer or vortex sheet [15]. Following the wing's trailing edge, this vortex sheet begins to roll up, spiraling into two well-defined, counter-rotating wingtip vortices. Within the range of 10 wingspans downstream of the wing's trailing edge, the vortex roll-up can be considered complete [16]. This region is known as the near-field wake. The far-field wake follows and stretches from 10 to 100 wingspans downstream. In this region, the wingtip vortex pair propagates through the atmosphere without undergoing any major change, although atmospheric turbulence and stratification have a significant influence on the longevity of this region. The far-field wake is followed by a region where rapid vortex decay occurs and vortex circulation diffuses [13].

It is in this far-field wake where the benefits of formation flight are most prominent. Figure 1.1 illustrates an aircraft generating a counter-rotating vortex pair as generated from the aircraft wingtips. This vortex pair, more than ten wingspans downstream, produces a downwash region in line with the aircraft, and an upwash region on either side of the outer wake. The upwash and downwash are effects of the vortex circulation. Although vortices are generally undesirable as they create this downwash, which increases the induced drag on the wing, they are accompanied by the same amount of upwash, which can in fact be beneficial to the second wing flying in the upwash region further downstream [17].

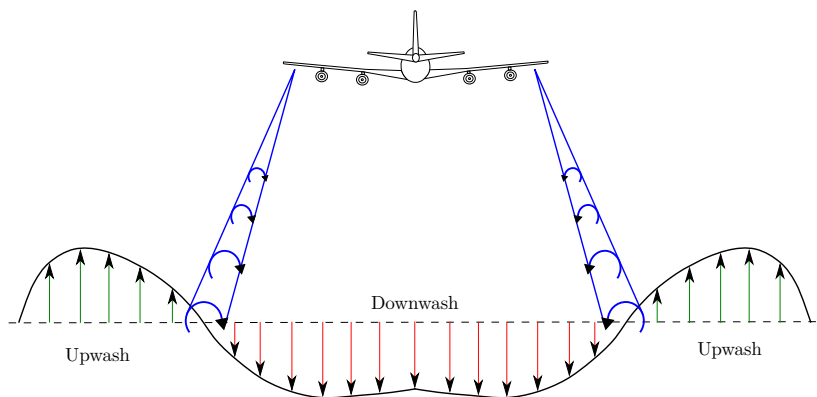


Figure 1.1: Aircraft wake with wingtip vortices inducing upwash and downwash

It is in these upwash regions where formation flight is most beneficial. The following section will further investigate the benefits and challenges related to flying a follower aircraft in the far-field wake.

1.4.2 Benefits and Challenges of Extended Formation Flight

Extended formation flight can be defined as the aerodynamic interaction between two aircraft in the far-field wake, as described in Section 1.4.1. Throughout the literature, aircraft placement in formation also indicates that an optimal separation exists, where the lift-to-drag ratio is maximized for the follower aircraft [2, 5, 11]. The far-field wake can be considered constant with regard to longitudinal spatial offset or separation, since the vortex decay between 10 and 40 wingspans downstream is negligible [9]. When considering the lateral and vertical separation between the leader and follower in echelon formations, the lateral separation most dominantly influences the formation lift benefit on the follower, since the follower aircraft can easily move from an upwash region to a downwash region [18]. In Figure 1.2, the wake lift profile is illustrated. The follower aircraft can increase its lift benefit by moving deeper into the wake's upwash region, up to the point where the follower crosses the leader's wingtip vortex and moves into the downwash region. This lift benefit produces a significant reduction in induced drag, and as a result, the follower aircraft can fly at a lower angle of attack. Due to the reduced drag, the follower aircraft can lower its thrust demand and increase fuel savings. A flight test in close formation of two F18 aircraft resulted in a reduction in fuel flow of 14 % [19]. In another flight test of two DO-28 aircraft, the follower reduced its peak thrust application by 20% or more, and achieved an average reduction over the test period of 10%, thereby confirming the importance of optimum separation tracking [20].

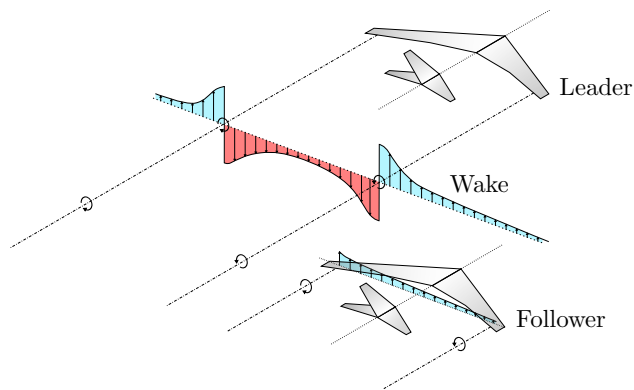


Figure 1.2: Follower aircraft in wake of leader and exposed to upwash of leader's wingtip vortices

Unfortunately, the lift benefit on the follower aircraft is not the only effect of the leader's vortex circulation flowing over to the follower's wing surface. The stability derivatives change not only in lift and drag, but also in moments and a side-force with variation in vertical and lateral separation [13, 21, 22]. Of these secondary effects, the rolling moment is the most dominant due to the non-uniform nature of the lift profile on the follower aircraft, as illustrated by Figure 1.3. The follower aircraft is rolled in the opposite rotation from the nearest wingtip vortex, causing the follower to bank and turn out of the wake if aileron demand is not increased to counter the rolling moment and consequently maintain straight and level flight.

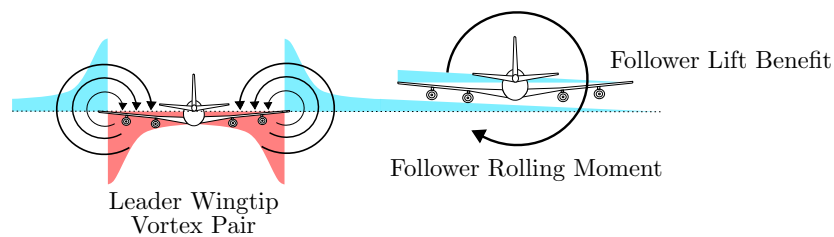


Figure 1.3: Lift benefit and rolling moment induced on follower aircraft by wingtip vortices of leader

Since flying at the optimum location in the wake can be a daunting and hazardous task for pilots to perform, autonomous flight controllers are proposed. These controllers are implemented to stabilize the follower in formation, and to utilize the possible fuel savings to a maximum while countering the unwanted effects, such as the large rolling moment induced by the wake. In order to design a formation flight controller for this thesis, a model of the aerodynamic wake-induced effects on the follower was required. The next section investigates the aerodynamic modeling of the wake in more detail.

1.4.3 Aerodynamic Modeling of Formation Flight Airframes

Research on the aerodynamic effects of the wake has received much attention in recent years, not only for the purposes of formation flight, but also due to the safety concerns relating to persistent wake interaction. The most troubling of these concerns is cases where the strong wakes of larger aircraft can endanger smaller aircraft during takeoff and landing in the same airspace. Various wind tunnel tests have been conducted to investigate and better understand the wakes of different aircraft and their interaction effects on follower aircraft. For analytical applications such as feasibility studies and system design, mathematical wake models are generally more useful for simulation purposes. Of these wake models, the most common are models using lift line theory and vortex lattice methods. However, practical comparisons often indicate that most of these analytical approaches overestimate the effects of the wake [13, 21, 23].

Throughout the development of aerodynamics and fluid mechanics, various vortex velocity profiles have been proposed. The earliest work that was derived was what is well-known today as the Rankine vortex; followed by the Lamb-Oseen vortex profile in the 1920s. The work that followed these models was largely based on empirical relations derived from measured data. Four frequently used vortex profiles, that include viscous effects are the Burnham-Hallock, Kurylowich, Wickelmans and modified Benz vortex profiles which can be implemented analytically [13, 23].

With regard to modeling the wake of the leader aircraft, the single horseshoe vortex method for a fixed-wing aircraft offers a simple yet close approximation for the two counter-rotating, fully rolled-up trailing vortices. This method also shows reasonable agreement with experimental data [2] and vortex lattice code [21]. The horseshoe vortex with a circulation strength, such as the Burnham-Hallock profile, consists of a bound vortex over the wing with a span of $\frac{\pi}{4}b$, where b is equal to the wingspan, and two trailing vortices extending to infinity as seen in Figure 1.4. In most models, the effects of the fuselage and tailfin of the aircraft are negligible. In simplified models, the vortices resulting from the tailplane of the aircraft are also considered insignificant when compared to the main wing at extended downstream separations, and are therefore also excluded from the wake model [13, 23].

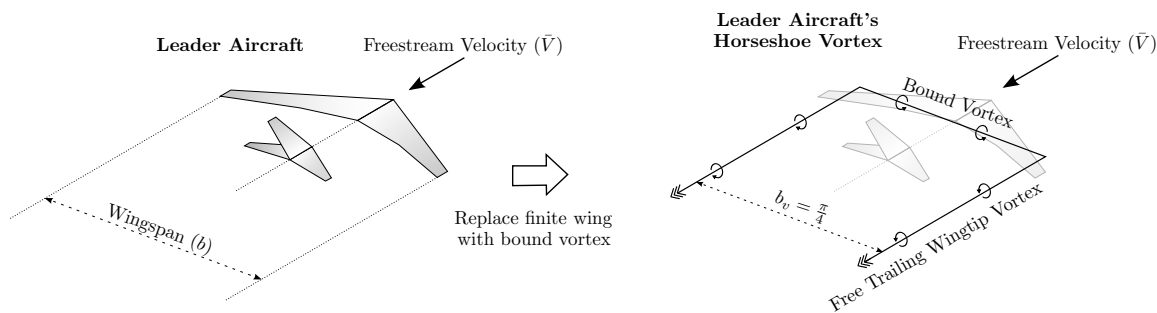


Figure 1.4: Horseshoe vortex representation [1]

Deriving an aerodynamic interaction model can be a complex analysis, and thus for the purposes of this study a completed single horseshoe model will be used to reduce the complexity of the work. The wake model as derived by Bizinos et al. [13] meets the desired criteria, as it is scalable, simple to reproduce, and gives the wake-induced forces as aerodynamic coefficients defined as functions of lateral and vertical separation. More detail on the Bizinos model implementation, its assumptions and limitations is provided in Section 3.8.

1.4.4 Flight Controllers and Extremum-Seeking Control in Formation Flight

In formation flight, the follower aircraft are constantly faced with the challenges of station keeping in unconventional airflow. This requires the follower aircraft to trim control surfaces unconventionally to maintain straight and level flight. In order to hold constant separation, it is vital to communicate information between the leader and follower aircraft. In this section, a brief review is provided of some of the existing formation flight controllers for station keeping and extremum seeking.

Formation-hold or station-keeping controllers have been designed and implemented successfully in research. In a paper by Hanson et al. [12], an overview of the NASA Dryden Flight Research Center Autonomous Formation Flight Project is given, with a successful flight demonstration of precision autonomous station keeping in formation of two F/A-18 aircraft. In this project, the relative position estimate between the leader and the follower was established by communicating the blended inertial navigation (INS) and global positioning system (GPS) measurements across an air-to-air telemetry link. The follower aircraft was also equipped with an experimental precision formation flight autopilot responsible for vertical and lateral station keeping. This experimental system became unstable when flying the follower in the vortex where maximum drag reduction was observed. The inner-loop control system of the F-18 aircraft was preserved, while extending the outer loops with a position command autopilot implementing proportional and integral control loops.

Although formation-hold is useful, the ultimate goal of this thesis is to go one step further and locate the "sweet-spot" in the wake with regard to fuel consumption. This is a challenging prospect, mainly due to the fact that the optimum relation to the vortex core is known to move in the wake as the weight or trim angle of attack of the leader aircraft changes [24]. Through thorough investigation it seems that limited work has been done on autonomously flying the follower aircraft at the optimal separation. One reason for this is the vortex detectability problem: it is challenging, expensive and in some cases impractical to measure the exact location of the vortex in real time during flight. More research has focused on developing technology that detects wake hazards in airspace surrounding airport runways, but unfortunately much of this wake detection instrumentation is still heavy and expensive [25]. For ground measurement, radar, lidar, large microphone and sonar arrays have been configured to perform successful detection of wake hazards [26, 27]. Despite significant advances made in wake hazard detection, these systems are primarily designed for ground use, and only limited sensor systems have been developed for in-flight use. Airborne lidar has been tested, but is still considered impractical for commercial use due to cost and weight concerns. Some of the more practical research proposes locating the optimum by sensing the vortex using noisy pressure measurements distributed along the follower aircraft's wing [28, 29]. This method can improve wake observability, although sensing in static formations remains problematic as relative motions between the aircraft improve wake observability [25].

While vortex sensing through instrumentation can become a viable solution through further developments, it does require the installation of possibly expensive and complicated sensor arrays. As an alternative, some researchers have proposed extremum-seeking control schemes measuring induced drag savings as a function of the decreasing angle of attack or pitch angle, or by optimizing more complex cost functions [5, 8, 30]. The pitch angle as a performance measurement objective is considered a good practical approach, since it is measured more easily than angle of attack, especially in the unconventional airflow of the wake. However, locating the optimum still requires perturbing the follower in the wake to sense the wake gradient. Conical scan methods have been applied successfully to track the optimum separation and minimize the follower's pitch angle in simulation [5]. Effective extremum seeking in the wake has been confirmed through flight testing, with the noisy fuel flow measurement as performance objective [30]. The movement of a superimposed dither signal may cause additional discomfort for passengers but this phenomenon is considered outside the scope of this project.

1.5 Problem Statement

Previous research has established that there exists a strong economical benefit in formation flight [5, 9, 14]. Recent work by Bizinos et al. [13] has proposed that commercial airliners take advantage of this flight mode to reduce engine thrust demand by 10% or more. However, to optimize this benefit, the follower aircraft must maintain formation at a specific location with regard to the leader vortex. This can be challenging, since the vortex location changes for different leader aircraft weights or trim angles of attack [24]. This uncertainty creates a need for performance optimization by measurement of an efficiency objective.

Finding and maintaining the optimum location is a daunting concept for pilots and requires high workload. Measuring the location of the vortex in the wake also proves difficult and expensive [25]. For these reasons, an autopilot needs to be developed which can perform station keeping and optimization objectives to maximize efficiency. The field of autonomous formation flight has produced research on advanced control systems, such as the work of Brodecki et al. [8], Binetti et al. [5] and Brown et al. [30]. These advanced optimum-seeking controllers have been applied to military aircraft in simulation and in formation flight testing. Thus the question is asked: How can we design an autopilot system to stably fly a follower aircraft deep in the wake, while seeking the optimum separation?

1.6 Project Objectives

In this project, a controller scheme to locate and maintain the optimal separation in extended formation with regard to power efficiency, as described in Section 1.5, had to be designed and implemented in simulation. In order to test this design, a number of mathematical models and auxiliary flight controllers had to be designed and implemented which could operate coherently. With a clear scope of the problem, the project objectives were defined as follows:

- Develop a commercial turbofan engine model that captures the thrust dynamics and fuel usage estimation with increased accuracy for a given set of ambient conditions.
- Assemble a thrust model that represents the engine placement on the aircraft, capable of producing balanced and differential thrust.
- Create a non-linear model of a commercial aircraft in isolated flight, with the thrust model included.
- Design conventional altitude, airspeed and heading controllers for the commercial aircraft model.

1.7 Project Overview and Methodology

- Include a model for the aerodynamics of the wake-induced forces and moments on the follower aircraft.
- Implement a formation-hold autopilot capable of flying the follower aircraft deep inside the wake, while maintaining stability and not pushing the ailerons' trim close to saturation.
- Design and implement an extremum-seeking algorithm for optimum fuel savings in formation flight.
- Evaluate this extremum-seeking controller in formation flight through simulation.

All the models and simulations in this project were constructed and evaluated using MATLAB and Simulink.

1.7 Project Overview and Methodology

Conventionally for autopilot design, an aircraft is modeled in isolated flight by identifying the forces and moments acting on the aircraft as a rigid body. These forces and moments are then applied to a six degrees of freedom model, which calculates the aircraft kinematics and kinetics, yielding the various system states of the aircraft. These include position, orientation, velocity and angular velocities. The aircraft states are measured and fed back in conventional aircraft control design to alter the aircraft airspeed, altitude and heading. The conventional controllers apply a command to the aircraft control actuators, which generally include a thrust setting and aileron, rudder and elevator deflections.

With the focus on formation flight, both a leader and a follower aircraft in right echelon formation are modeled. A wake aerodynamic interaction model is included on the follower aircraft. Aside from the extended aerodynamic model of the follower, the follower model is similar to that of the leader. The leader aircraft is initialized at cruise in straight and level flight. The aim is to develop an autopilot on the follower which can automatically position itself at the optimum formation separation.

1.7 Project Overview and Methodology

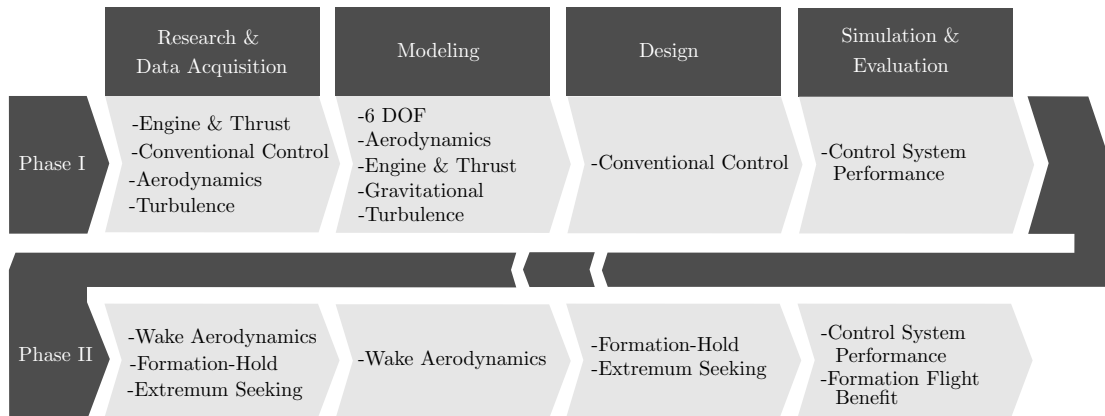


Figure 1.5: Project methodology

A project methodology was proposed to meet the objectives as stated in Section 1.6. Figure 1.5 illustrates the project methodology, which was divided into two phases: isolated flight and formation flight. These two phases were subdivided into four development stages, which included research, modeling, design and simulation or evaluation. In Phase I, the isolated flight phase, a single aircraft model was developed with conventional controls for the aircraft model. This phase served as a baseline with which to compare the performance of the follower in the wake. In Phase II, the follower aircraft and wake model were included to simulate a formation scenario, which in turn included the wake-induced forces and moments on the follower. For this formation flight model, a formation-hold and extremum-seeking controller was developed to autonomously fly the follower to the most efficient formation separation. With the developed models and controllers in place, a performance analysis was conducted.

In the chapters to follow, mathematical models will be described for all the models listed in Figure 1.5. A higher-fidelity, second-order engine model will also be implemented to more accurately capture the aircraft thrust dynamics and approximate fuel consumption if possible. A trim and linear dynamic analysis will be presented, which can be used in the linear control design procedures to calculate control gain and analyze stability. The conventional and formation-hold controllers will be discussed in more detail, followed by a proposed extremum-seeking controller. Finally, a performance analysis under turbulent conditions for all controllers will be provided to conclude the design and simulation of an extremum-seeking formation flight controller which maximizes flight efficiency with regard to thrust application.

Chapter 2

Turbofan Engine Model

One of the objectives of this thesis was to increase the thrust dynamic simulation fidelity on the aircraft. In order to achieve this, a higher-order engine model was proposed to provide a more realistic response for the engine dynamics. In the proposed engine model, a fuel flow estimation was also included. Since the drive towards formation flight is to take advantage of the economical benefits, a fuel savings estimation can greatly contribute towards this objective.

In the sections to follow, a short literature review on turbofan engine modeling will be conducted; a linear bisection parameter identification algorithm will be presented to match a second-order model to a high-fidelity commercial aircraft engine model; and the proposed system will be analyzed.

2.1 Literature Review: Modeling A Turbofan Engine

In recent years, the safety, economical, optimization and design advantages of simulating a turbofan engine with high accuracy has motivated the aviation community to invest in developing advanced simulation models for turbofan engines. In this section, turbofan engine modeling from a control-engineering perspective will be investigated, and some developed models will be discussed briefly.

2.1.1 Two-Spool Turbofan Engine Dynamics

When modeling a turbofan engine for control engineering, it is common practice to treat the engine stages as holistic modules. Thus the thermodynamic and fluid-mechanic properties are considered the same within a module [31]. For a two-spool turbofan engine common to Boeing 747 aircraft, the system can be divided into the following modules, as seen in Figure 2.1:

- Engine fan and bypass

2.1 Literature Review: Modeling A Turbofan Engine

- Low and high pressure compressors
- Combustion chamber
- High and low pressure turbines
- Outlet nozzle
- High and low pressure spools

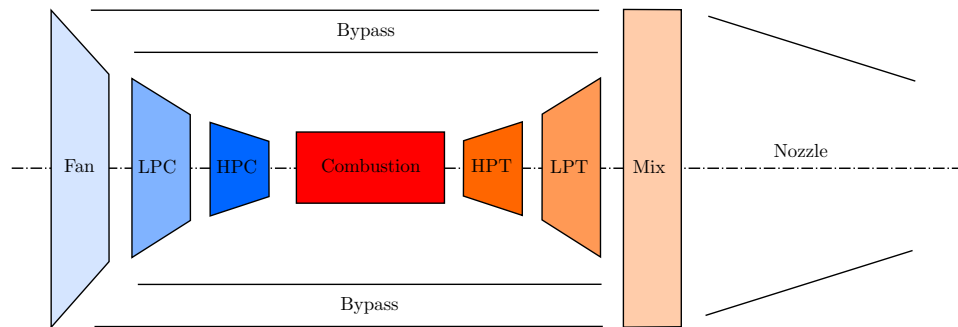


Figure 2.1: Turbofan engine modules

In simplified modeled engines a lumped-parameter approach is used to capture the dominant engine dynamics and reduce the engine model complexity. In a gas turbine engine there are mainly three types of dynamics at work. These are: the shaft, pressure, and temperature dynamics. These dynamic effects will be discussed to better understand the physics of the engine.

2.1.1.1 Shaft Dynamics: Effect Of Inertia

Of the three engine dynamic effects at work, the shaft dynamics represent the simplest form and yet the most important dynamic behavior of a gas turbine engine. Shaft dynamics, in their simplest form, can be represented by a two-disk system, as in Fig. 2.2, where two round disks are connected by a shaft [31]. The acceleration of this combined rigid body can be based on the principles of Newtonian mechanics, shown in Equation 2.1, where $\dot{\omega}$ is the angular acceleration of the body, ΔQ is the differential torque exerted on the disks and I is the mass moment of inertia of the combined body.

$$\dot{\omega} = \frac{\Delta Q}{I} \quad (2.1)$$

2.1 Literature Review: Modeling A Turbofan Engine

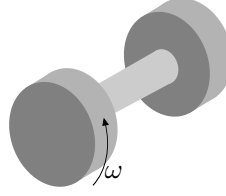


Figure 2.2: Analogy of shaft dynamics by two-disk system

For a turbofan engine, the angular acceleration $\dot{\omega}$ is substituted with the shaft acceleration \dot{N} , and the differential torque ΔQ can be expressed as a function of both shaft speed N and fuel flow rate W_f [31]. After substitution, Equation 2.2 gives the shaft dynamic equation:

$$\dot{N} = \frac{f(N, W_f)}{I} \quad (2.2)$$

To linearize the shaft dynamics Equation 2.2, the Taylor series expansion of the function f at a steady-state operating point is obtained, and only the first-order terms are retained. Equation 2.3 gives the linearized shaft dynamics equation.

$$\dot{N} = \left(\frac{1}{I}\right) \left(\frac{\partial Q}{\partial N} \Delta N + \frac{\partial Q}{\partial W_f} \Delta W_f\right) \quad (2.3)$$

For the linear shaft dynamics of a two-spool engine, such as the General Electric CF6-80, the equations can be derived by extending the single-spool system in Equation 2.3 to a two-spool system, as in Equation 2.4.

$$\begin{aligned} \dot{N}_1 &= \frac{1}{I_1} \left(\frac{\partial Q_1}{\partial N_1} \cdot \Delta N_1 + \frac{\partial Q_1}{\partial N_2} \cdot \Delta N_2 + \frac{\partial Q_1}{\partial W_f} \cdot \Delta W_f \right) \\ \dot{N}_2 &= \frac{1}{I_2} \left(\frac{\partial Q_2}{\partial N_1} \cdot \Delta N_1 + \frac{\partial Q_2}{\partial N_2} \cdot \Delta N_2 + \frac{\partial Q_2}{\partial W_f} \cdot \Delta W_f \right) \end{aligned} \quad (2.4)$$

In these equations, the change in shaft torque ($\Delta Q, \Delta Q_1$ and ΔQ_2) is a function of mass flow rate, the specific heat of the gas at a constant pressure and the change in temperature between modules [31, 32]. Furthermore, the output equation of any engine variable y can be simplified and expressed as a function of fuel flow rate and shaft speed, as given by Equation 2.5.

$$\Delta y = \frac{\partial y}{\partial N_1} \cdot \Delta N_1 + \frac{\partial y}{\partial N_2} \cdot \Delta N_2 + \frac{\partial y}{\partial W_f} \cdot \Delta W_f \quad (2.5)$$

Equations 2.4 and 2.5 can be written in the following matrix notion of a state space system, given by Equation 2.6:

2.1 Literature Review: Modeling A Turbofan Engine

$$\begin{aligned}
 \begin{bmatrix} \dot{N}_1 \\ \dot{N}_2 \end{bmatrix} &= \mathbf{A} \cdot \begin{bmatrix} N_1 \\ N_2 \end{bmatrix} + \mathbf{B} \cdot W_f = \begin{bmatrix} \frac{\partial Q_1}{\partial N_1} & \frac{\partial Q_1}{\partial N_2} \\ \frac{\partial Q_2}{\partial N_1} & \frac{\partial Q_2}{\partial N_2} \end{bmatrix} \begin{bmatrix} N_1 \\ N_2 \end{bmatrix} + \begin{bmatrix} \frac{\partial Q_1}{\partial W_f} \\ \frac{\partial Q_2}{\partial W_f} \end{bmatrix} W_f \\
 y &= \mathbf{C} \cdot \begin{bmatrix} N_1 \\ N_2 \end{bmatrix} + D \cdot W_f = \begin{bmatrix} \frac{\partial y}{\partial N_1} & \frac{\partial y}{\partial N_2} \end{bmatrix} \begin{bmatrix} N_1 \\ N_2 \end{bmatrix} + d \cdot W_f
 \end{aligned} \tag{2.6}$$

Now that a state space system for the shaft dynamics is available, the frequency-domain representations can be obtained through Equation 2.7.

$$\frac{Y(s)}{W_f(s)} = \mathbf{C}(s\mathbf{I} - \mathbf{B})^{-1}\mathbf{B} + \mathbf{D} = \frac{k(s + \mathbf{z}_1)}{(s + \mathbf{r}_1)(s + \mathbf{r}_2)} \tag{2.7}$$

This transfer function represents a second-order dynamic system, where k is the gain constants, \mathbf{z}_1 is a zero and \mathbf{r}_1 and \mathbf{r}_2 are the two system poles. Depending on the output y selected, the zero and gain constant will change. However, the poles will remain the same [31], particularly for shaft speeds and engine pressure ratios. Thus in Equation 2.1 to Equation 2.7, the primary engine dynamics, i.e. the shaft dynamics due to inertial effects, have been simplified to be approximated by a second-order dynamic system.

2.1.1.2 Pressure And Temperature Dynamics

Although the shaft dynamics are most dominant in engine transient behavior, pressure and temperature changes also contribute to engine dynamics. In a jet engine, there exist numerous chambers holding volumes of gas. Each of these volumes is capable of storing thermal energy and gas masses. The mass stored in a volume causes the pressure in the volume to change, corresponding to the change in temperature due to the thermodynamic relationship between these properties [31].

For a two-spool engine, the largest gas pockets should be accounted for, which normally refer to the spaces between the engine modules. The change in pressure is relatively proportional to the difference in mass or mass flow and the change in temperature at a specific density. The most simplified model for change in pressure can be defined as the time integral of the difference in mass flow rate for a specific volume [31], where ideal gas behavior at a nominal operating condition is assumed.

As for the temperature dynamics, there are two types at work in a jet engine. The first is the change of temperature associated with a direct change in the thermodynamic state of the gas in a volume. The second is the change in temperature associated with the heat transfer between the surrounding metal parts of the engine's hot sections and the gas flow. Changes

2.1 Literature Review: Modeling A Turbofan Engine

in the first temperature dynamics can be caused by work input or the extraction of the heat caused by chemical reactions. These changes in temperature are very fast compared to the changes in metal temperatures or heat-soak effects [31].

Although the temperature changes caused by metal-heating effects are slow, visible and large, they are not considered to be of particular interest at cruise flight, since the engine is considered to be applied at a stable temperature and pressure operating point, with relatively small changes in acceleration and deceleration.

2.1.2 Turbofan Engine Simulation Projects

High-fidelity engine simulation models have been developed by industry leaders and researchers to investigate and improve engine designs. The National Aerospace Laboratory (NLR) has developed a Gas Turbine Simulation Program (GSP) [33] for the purpose of off-line component-based modeling for a wide range of gas turbines. Over 35 engines from aerospace and industrial applications have been modeled for analysis in GSP. GSP can perform both steady-state and transient simulations of any kind of gas turbine configuration by establishing an engine component model arrangement. GSP is a powerful tool for performance prediction and off-design analysis. The software is specifically capable of performing sensitivity analysis on variables such as: ambient flight conditions, installation losses, engine and control system malfunctioning, component deterioration and exhaust gas emissions. Since this software is trusted in the turbofan machinery industry, the data generated from the software can be used for model validation. The GSP software comes with a sample model of a General Electric CF6-80, a common selection for the Boeing 747.

The University of Cape Town has recently developed a high-fidelity engine model of a CF6-80. This engine model (Engine Model University of Cape Town - EMUCT) was developed and obtained through the work of Sanders et al. [6], where they investigated the effects of atmospheric turbulence on fuel consumption in extended formation flight. This engine model was implemented in MATLAB Simulink and the results extensively validated with GSP software. In this study, it was of high importance to accurately model transient behaviors due to the demand of dynamic throttling under turbulent conditions of formation flight.

For the EMUCT model, a thermodynamic, component-based approach was taken to model the engine. This approach is known as the Inter-Component Volume Method, and allowed for the inclusion of volume and rotary dynamics. This meant that each component was modeled mathematically based on the thermodynamic operation of the specific component,

2.1 Literature Review: Modeling A Turbofan Engine

including: intake, fan, compressors, combustors, turbines, and nozzles. The compressors and turbines, which are the rotary components, were also modeled based on steady-state characteristic maps as obtained from GSP simulations. The implemented fuel input controller included slew rates and saturation values for fuel flow rate. These constraints prevent combustion flame-out, and keep the rotary components within operation boundaries that are proportional to the current operation point of the engine. It is also stated in this study that the acceleration and deceleration of the engine shafts will differ due to the hysteresis in the engine's dynamics. Thus the modeling of a truly representative controller for the engine model was found to be too complex for the scope of this work, and simplified approaches were implemented to keep the engine model functional within the component constraints. As a result the fuel flow model transients in this study can be considered conservative.

In the work of Sanders et al. [6], the EMUCT model was validated against the GSP CF6-80 model. The error in design point calculation was found to be much less than 5%, with the combustion model showing the largest deviations. However, it was further found that these errors have a minimal effect on overall thrust (less than 1%). As for transient condition the EMUCT model performed exceptionally well. The EMUCT model showed an error of only 0.47% for the total thrust dynamic responses. Thus it can be concluded that the design point calculations and transient behavior of the EMUCT model are valid and a good data source for model validation.

2.1.3 Concluding The Engine Literature Review

In writing this thesis, it was challenging to find engine model data representative of engine thrust dynamics and fuel consumption. The best available option was to use the work of Sanders et al. [6] to generate engine model transients for the desired engine operating condition. Although the EMUCT model matches industry accepted simulation models for a Boeing 747 engine, its simulation speeds made it impractical to use in this thesis. Thus, a lower-fidelity model had to be developed which treated the entire engine as a single module. Implementing a lower-order engine model means that an decrease in overall model fidelity or accuracy is to be expected.

While studying the literature on turbofan engines, the dominant dynamics of twin-spool engines were identified. The work of Jaw [31] stated that the shaft dynamics represent the most dominant transient behaviors. By simplifying the system and reducing it to a two-disk representation, as shown by Figure 2.2, the shaft dynamics could be reduced to a second-order system. Since the pressure and temperature dynamics can be considered relatively constant at cruise conditions, and since shaft speed is a close indicator of engine thrust, it was assumed

2.2 Deriving A Thrust Model From EMUCT Using Linear Bisection

that a second-order system would be sufficient to model the engine thrust.

2.2 Deriving A Thrust Model From EMUCT Using Linear Bisection

In the work of Sanders et al. [6], a representative, simplified model of a General Electric CF6-80 engine was derived. Since the CF6-80 engine is one of the standard engine choices for the Boeing 747, it was decided to develop an engine model (Engine Model University of Stellenbosch - EMUS) based on data from this EMUCT model. For this project, the EMUS model was created with the primary objective to capturing the thrust and fuel flow dynamics. Data was generated by treating the EMUCT model as a black-box for a range of fuel flow command W_{fc} , as seen in Figure 2.3, with altitude (D) and airspeed (\bar{V}_T) conditions. The output engine thrust T_h and actual fuel flow W_f were recorded.

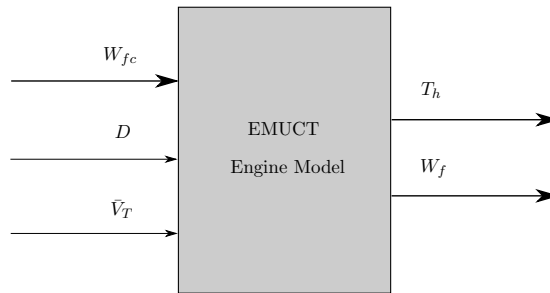


Figure 2.3: EMUCT Engine Model Inputs and Outputs

Through a brief literature review, it was found that the engine thrust dynamics could be simplified to a second-order transfer function, as described in Section 2.1. However, on examining the EMUCT model data, it was decided to include gain scheduling and a slew rate limiter as shown in Figure 2.4 to more accurately track the performance of the high-fidelity EMUCT model. An open-loop setpoint controller was also augmented to the engine model to calculate the fuel flow command for a given thrust input, in order to produce the desired steady-state thrust output.

2.2 Deriving A Thrust Model From EMUCT Using Linear Bisection

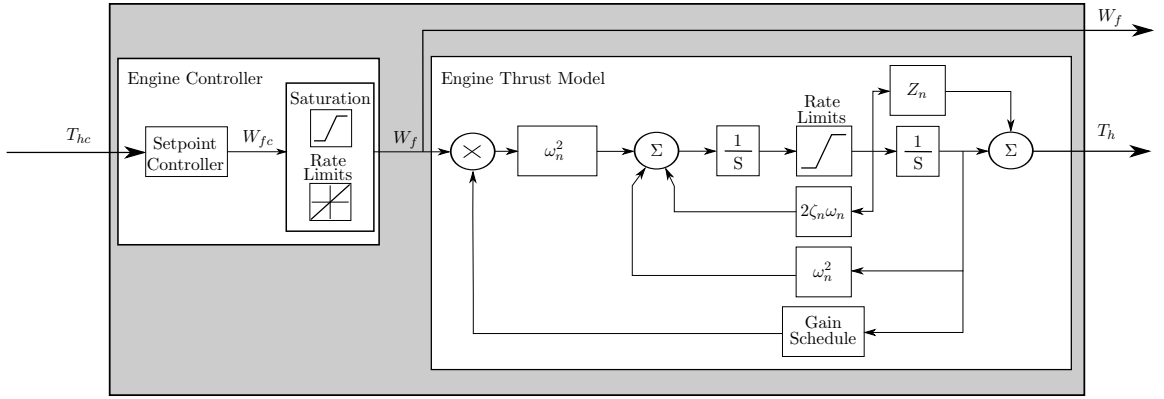


Figure 2.4: Second-Order EMUS engine model with thrust controller

2.2.1 Parameter Fitting Algorithm

To find the best match of EMUS model parameters for the EMUCT model, an algorithm was developed based on the principles of linear bisection. This algorithm was used to determine the gain schedule which minimizes steady-state error, and to find the second-order transfer function model parameters which best match the transient response for thrust output. For both cases, the linear bisection algorithm described in Figure 2.5 was used whereas the parameter matrix (\mathbf{P}) is defined in Equation 2.8.

$$\begin{aligned}
 \mathbf{P} &= K_{gain} \quad \text{for determining the gain schedule} \\
 \mathbf{P} &= \begin{bmatrix} \omega_n \\ \zeta_n \\ Z_n \end{bmatrix} \quad \text{for best matching the second-order parameters}
 \end{aligned} \tag{2.8}$$

The following process was followed to determine the engine model parameters which best match the EMUCT data:

1. Define the initial conditions for altitude, airspeed and trim thrust.
2. Select a range of input fuel flow rates.
3. Run the EMUCT model and record fuel flow and thrust output data for a range of fuel flow rate inputs.
4. Run a linear bisection algorithm to find a gain schedule which matches the steady-state thrust output.
5. Match the fuel flow rate limits.
6. Match the acceleration and deceleration of thrust rates and set up the thrust rate limiters.

2.2 Deriving A Thrust Model From EMUCT Using Linear Bisection

7. Run a linear bisection algorithm to best fit the EMUS engine model parameters to the EMUCT transient thrust output for the range of fuel flow rate inputs.
8. Calculate the average of the model parameter results for the different input settings to best fit the thrust range as defined.
9. Run the engine thrust model for a set of fuel flow rate inputs and determine the values for the setpoint controller.

Figure 2.5 gives a simplified general case of the linear bisection algorithm used to derive a model for the engine thrust dynamics. The algorithm starts by simulating the EMUCT model for a defined i number of fuel flow rate commands (W_{fc}), for which all thrust (T_{hEMUCT}) and fuel flow (W_{fEMUCT}) data is recorded. The EMUS model is initialized, after which the step size (ΔP) is set to a large initial size. During the outer loop of fuel command iterations, the model parameters (\mathbf{P}) are estimated for all the predefined number of fuel flow rate commands. By iterating the inner loop m time, the model parameters are estimated to the best fit the EMUCT data for the specific fuel command. All parameter combinations for positive, negative and half-step sizes are simulated, and a least squares cost function is used to find the best parameter combination. This results in 4^n possible combinations, where n is the number of model parameters in \mathbf{P} . Thus 4^n number of cost function results are evaluated with the minimum cost defined as the optimum parameter fit. The parameter values and step sizes are adjusted accordingly, and the iteration is repeated as the step size decreases. After acceptable convergence, which is usually in less than ten iterations, the parameter values are stored and the fuel command is adjusted. The result of this algorithm is a set of parameters $\mathbf{K_P}$ for a combination of fuel flow rate command inputs. An average of these parameters is taken over the most likely range of fuel flow rate commands for the defined flight condition to give the best fit model for the EMUCT data.

2.2 Deriving A Thrust Model From EMUCT Using Linear Bisection

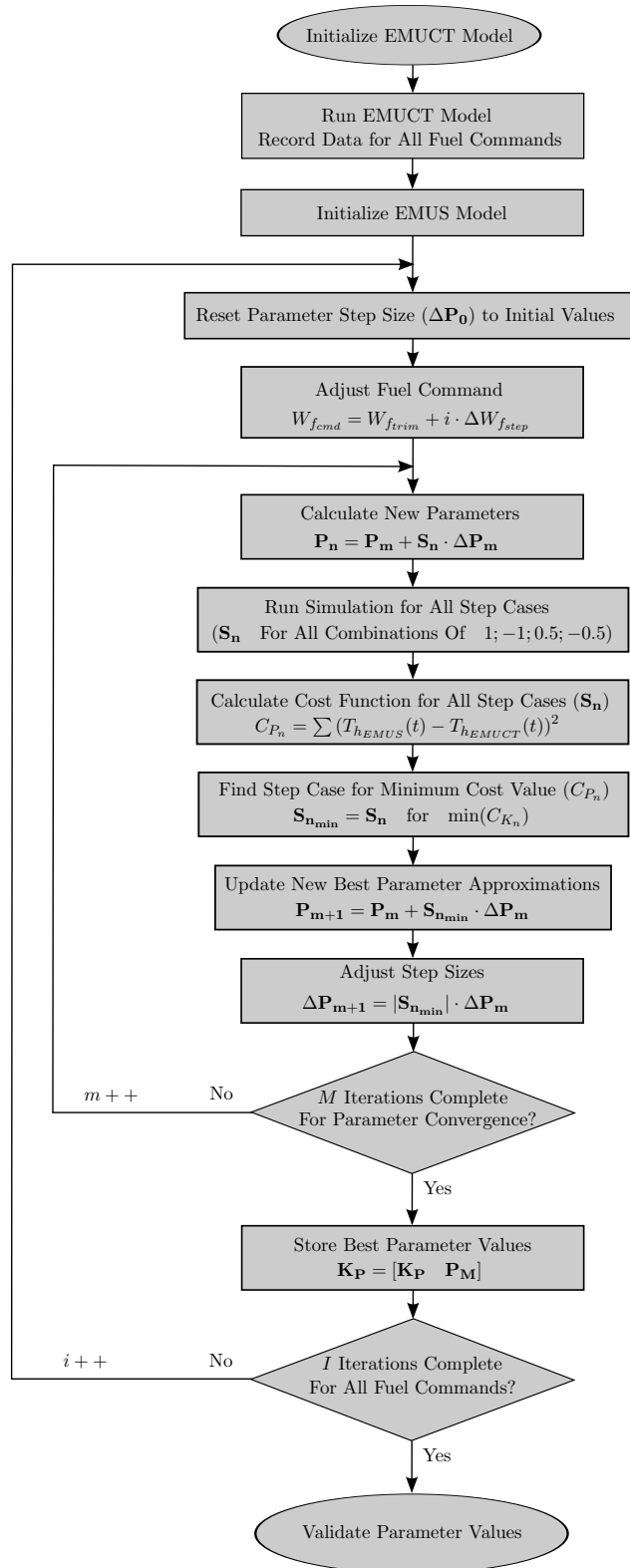


Figure 2.5: Linear bisection algorithm for model parameter optimization

2.2 Deriving A Thrust Model From EMUCT Using Linear Bisection

2.2.2 Convergence of the Parameter Identification Algorithm

The linear bisection parameter identification algorithm, as discussed in Section 2.2.1, was applied successfully. Figure 2.6 shows how the algorithm of Figure 2.5 converges over 15 iterations. In Figure 2.6, the gain value approaches zero, since the final value of the EMUCT model can be matched closely by the EMUS model. However, the second-order model parameters do not lead to an exact match due to higher-order dynamics present in the EMUCT model, which are impossible to accurately represent with only second-order systems.

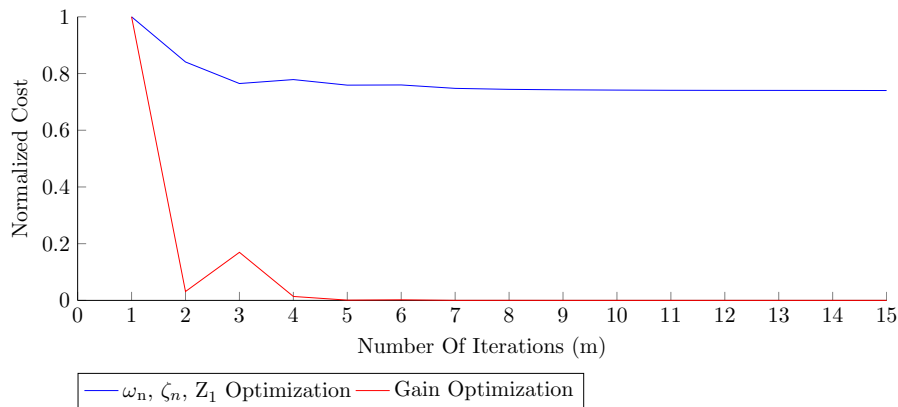


Figure 2.6: Cost function convergence for model parameter optimization using linear bisection

Figure 2.7 shows how the actual parameter values converge to a single specific value as the step size decreases during convergence. This figure shows parameter value convergence for the gain values (Figure 2.7a) and the natural frequency, damping and zero (Figure 2.7b) of the second-order model for a defined fuel flow command.

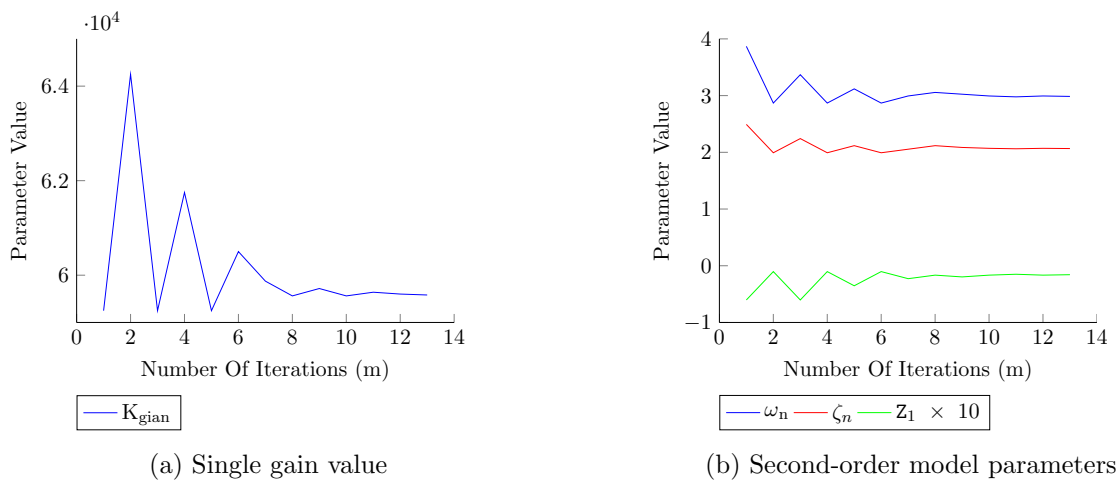


Figure 2.7: Parameter convergence using the linear bisection algorithm

2.3 Determining And Validating The Engine Model

In this section, the model structure and estimation algorithm were defined, and algorithm convergence was demonstrated. Next, the EMUS model parameters were determined and validated against the EMUCT model data.

2.3 Determining And Validating The Engine Model

Three tests were conducted to show that the EMUS model outputs correspond to the EMUCT model outputs for thrust and fuel flow dynamics. The first test evaluated the correlation between the models at a steady-state condition for various fuel flow input commands. The second, evaluated the transient correlation between the models for step inputs of fuel flow commands, and the third showed that the EMUS fuel flow rate output matches the EMUCT values.

2.3.1 The Thrust Gain Schedule

The algorithm in Figure 2.5 was used to determine the gain schedule for the EMUS model. The gains were matched for EMUCT steady-state values at various fuel flow command inputs. Figure 2.8 shows the simulation results with the error at steady state (e_{ss}), as calculated with Equation 2.9 with t at a time when the simulation has reached a steady-state condition.

$$e_{ss} = \left| \frac{T_{h_{EMUCT}}(t) - T_{h_{EMUS}}(t)}{T_{h_{EMUCT}}(t)} \right| \times 100 \quad (2.9)$$

It was observed that the EMUS gain schedule values closely match the EMUCT steady-state values for a range of fuel flow rate inputs. The steady-state error (e_{ss}) was found to be less than 0.01%, as seen in Figure 2.8. Thus the EMUS gain schedule could be determined with high accuracy.

2.3 Determining And Validating The Engine Model

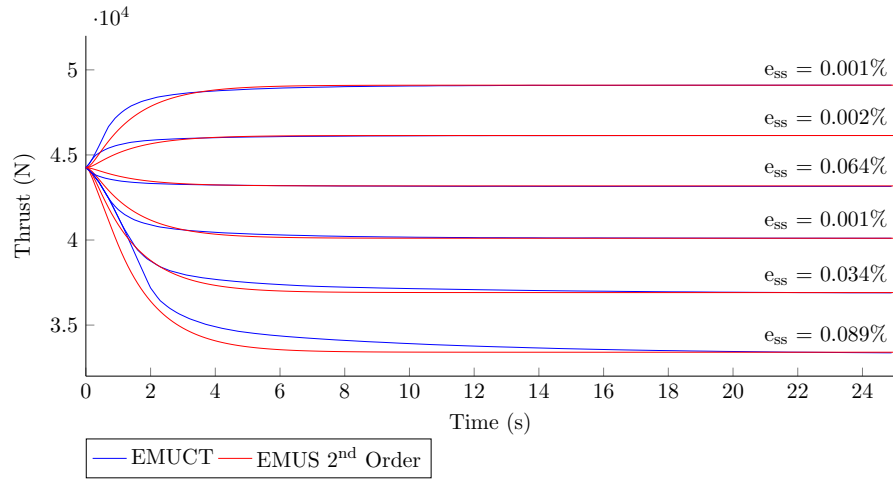


Figure 2.8: Steady-state correlation between the EMUCT and EMUS models for a range of fuel flow commands

The identified gain schedule is illustrated by Figure 2.9, where the gain schedule is given as a function of output thrust.

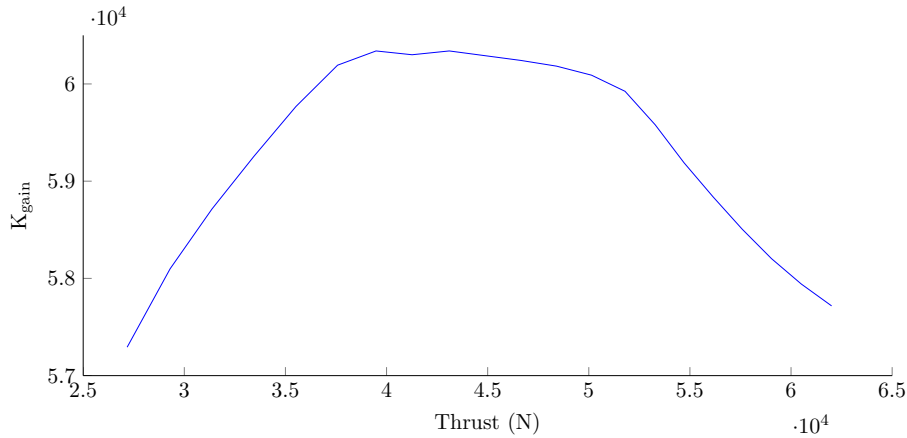


Figure 2.9: EMUS model gain schedule

2.3.2 The Second-Order Engine Model Parameters

The algorithm described in Figure 2.5 was applied to determine the EMUS model parameters, which include the natural frequency (ω_n), the damping (ζ_n) and a zero (Z_n). An error percentage was determined by calculating the mean error up to the time when the thrust output settles at 2% of the steady-state value ($t_{ss2\%}$). This error percentage was calculated by finding the mean error, as given by Equation 2.10, for time (t) from zero to $t_{ss2\%}$, following a step command in the fuel flow rate.

2.3 Determining And Validating The Engine Model

$$e_{ss2\%} = \frac{1}{t_{ss2\%}} \int_{t=0}^{t=t_{ss2\%}} \left| \frac{T_{h_{EMUCT}}(t) - T_{h_{EMUS}}(t)}{T_{h_{EMUCT}}(t)} \right| dt \times 100 \quad (2.10)$$

Figure 2.10 shows the correlation between the EMUCT model and the EMUS model for a range of step command fuel flow rate inputs. At each input value, the model parameters are adjusted by the algorithm in Figure 2.5 for optimum fitting. As a result, a range of poles and zeros was obtained which matches the EMUS and EMUCT thrust output. The error was found to be less than 1% for all calculated parameters, which is an excellent result for matching the second-order system to the high-fidelity EMUCT model.

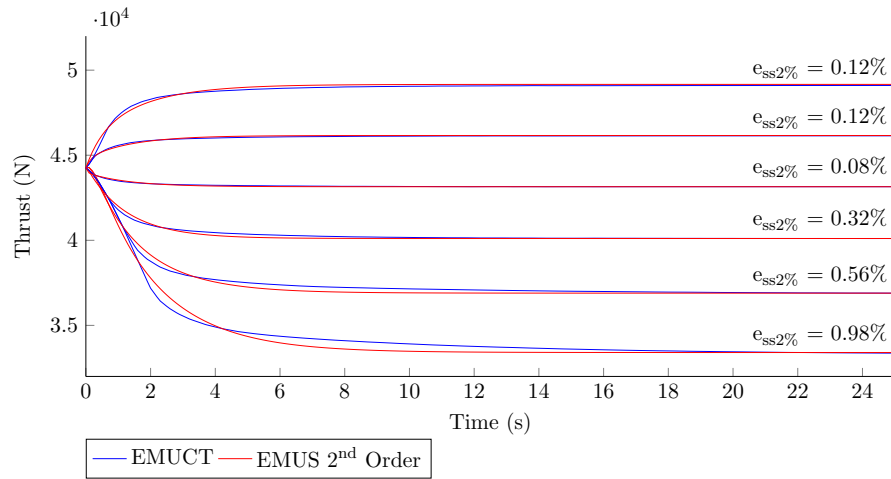


Figure 2.10: Correlation between EMUCT and EMUS models for step inputs up to 2% steady-state settling time for a range of fuel flow commands

Figure 2.10 shows the EMUS model parameters as adjusted for each step command to optimally fit the EMUCT data. Figure 2.11 shows how the parameters change for thrust step inputs about engine trim thrust. This figure demonstrates the non-linearity of the engine.

2.3 Determining And Validating The Engine Model

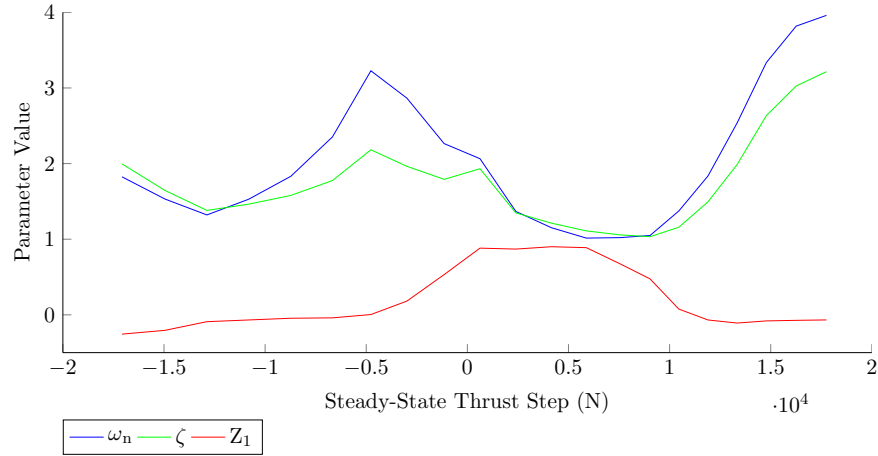


Figure 2.11: Second-order model parameter fitting values over a range of thrust step inputs around 44.25 kN trim thrust

In Figure 2.11, a large difference in model parameters can be observed between acceleration and deceleration behavior, as the positive thrust steps give an entirely different range or model parameter values than the negative thrust steps. For this reason a dual model engine was created, and the EMUS model will switch transfer function parameters between engine acceleration and deceleration. Figure 2.12 shows how the model parameters change based on a conditional statement for thrust increase ($\dot{T}_h > 0$) and thrust decrease ($\dot{T}_h < 0$).

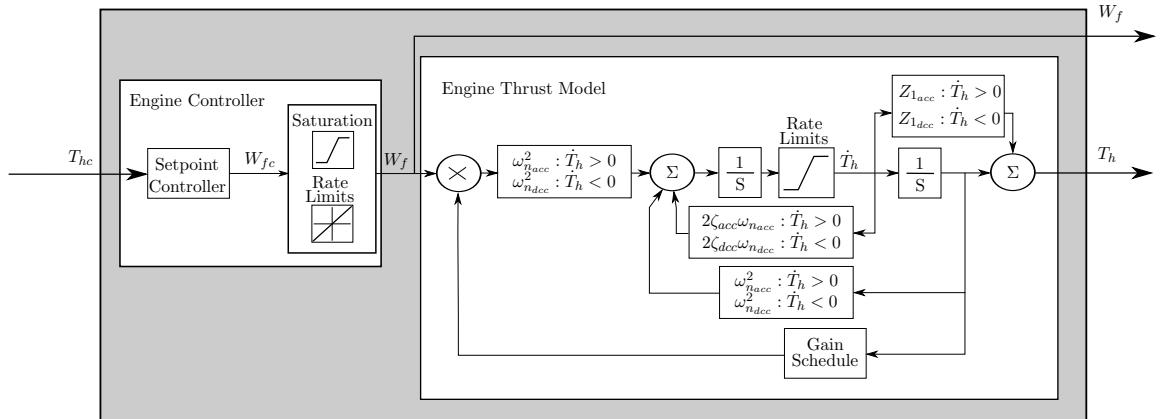


Figure 2.12: Second-order EMUS model for acceleration and deceleration combination

For the model in Figure 2.12, the model parameters were determined by taking the mean for both the acceleration and deceleration ranges in Figure 2.11 separately (positive steps for accelerations and negative steps for decelerations). Figure 2.13 shows the selected average poles and zeros for the acceleration and deceleration models.

2.3 Determining And Validating The Engine Model

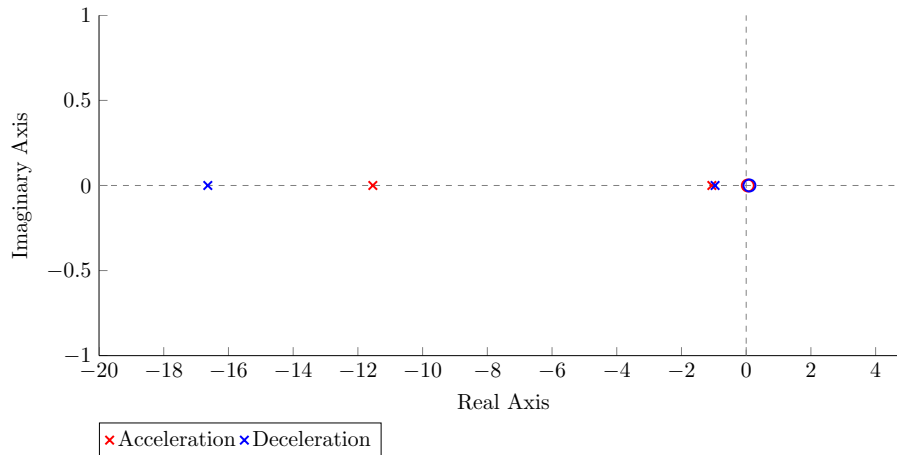


Figure 2.13: EMUS poles and zeros for both acceleration and deceleration transfer functions

With all the model parameters defined, the EMUS model could be validated against the EMUCT, model as seen in Figure 2.14. It was found that the EMUS model matches the EMUCT model very closely near the design point flight condition. Equation 2.10 was used to find the mean error up to 2% settling time for various step commands. The mean model parameters in Figure 2.11 were selected to best fit the EMUCT data near trim thrust.

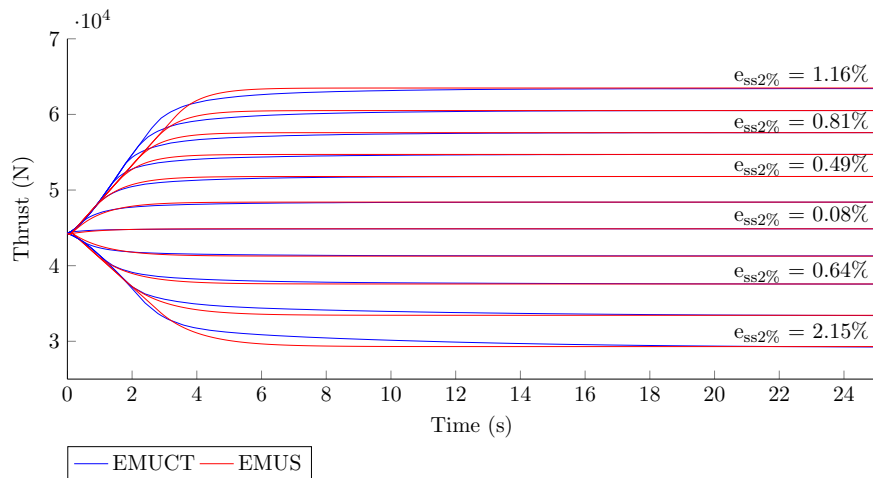


Figure 2.14: EMUS model thrust output validated with EMUCT thrust output data

From Figure 2.14 it can be concluded that the EMUS thrust output, closely correlates with the EMUCT model thrust output with a mean transient response error of less than 1% for most step responses near the operating point of 12.1 km and Mach 0.8.

2.3.3 Fuel Flow Model

The same fuel flow model was used for the EMUS model, as proposed by the EMUCT model. This model was implemented by Sanders et al. [6] to reduce the work of modeling fuel flow actuators and the implementation of complicated engine controllers. Saturation and rate

2.4 Concluding The Engine Model

limiting constraints were applied to keep all engine components in a safe operating range within the flight envelope. Since the EMUS thrust model was based on the performance of the EMUCT model, it was decided to use the same simplified fuel flow model so that the fuel usage would correspond to the thrust output.

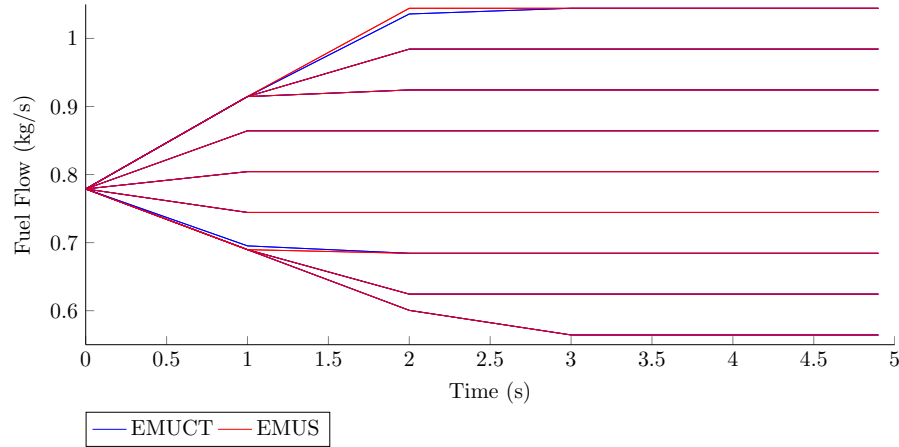


Figure 2.15: The EMUCT fuel flow model versus the EMUS fuel flow model for various step inputs in fuel command

Figure 2.15 shows the correlation between the EMUCT and the EMUS fuel flow models. From Figure 2.15 it can be observed that the EMUS model closely matches the EMUCT fuel flow model, extending the engine model to provide a fuel flow estimate.

2.4 Concluding The Engine Model

In this chapter, a representative second-order model for a turbofan engine was presented. This model was developed for a popular commercial aircraft engine, the General Electric CF8-60, at cruise conditions of an altitude of $\pm 12\,192$ m and Mach 0.8. In order to achieve this, a literature review on turbofan engine modeling for control design purposes was conducted and a high-fidelity simulation model validated by industry software was obtained. A linear bisection parameter matching algorithm was then used to fit the second-order model to the thrust output of the high-fidelity model. A simplified fuel flow estimation model was also included as represented by the high-fidelity model.

This turbofan engine model was then implemented on the aircraft model as a thrust actuator. The following chapter includes the thrust forces and moments equations, which utilize this engine model actuator to generate a more representative aircraft thrust dynamic response.

Chapter 3

Mathematical Models

The modeling of an aircraft takes into consideration all the external forces and moments applied to the body. In this thesis, both the leader and the follower aircraft are considered to be rigid bodies. The forces and moments will comprise of thrust, gravity, conventional aerodynamic and wake aerodynamic loads. The realistic description of the aircraft's forces and moments together with the aircraft's equations of motion result in an accurate simulation representation. In this chapter, the mathematical aircraft and formation model composition will be discussed.

Figure 3.1 shows all the modeled systems and their relationships. In simulation, the leader and follower aircraft are connected by state communication, in which some of the leader's states are made available to the follower to calculate the formation separation for control purposes. A turbulence model is also included in order to analyze the formation and optimal-seeking controller performance in turbulent conditions.

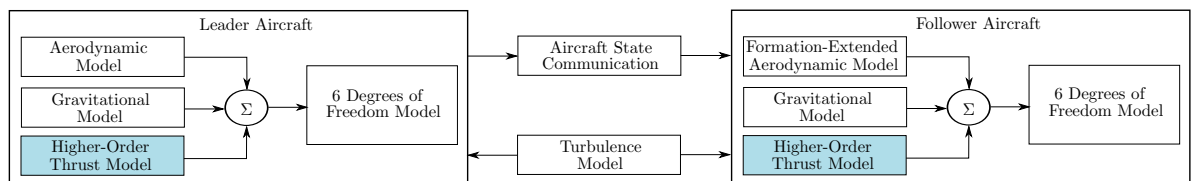


Figure 3.1: Mathematical model system overview

3.1 Conventional Axis Systems

Before applying Newton's laws to describe the mathematical model of the aircraft, an inertial axis system is defined, together with three orthogonal axes, commonly referred to as the body, stability and wind axis. The conventions described by Peddle [34] and Engelbrecht [35] will be followed. Figure 3.2 illustrates the axis representations that will be discussed in the following sections.

3.1 Conventional Axis Systems

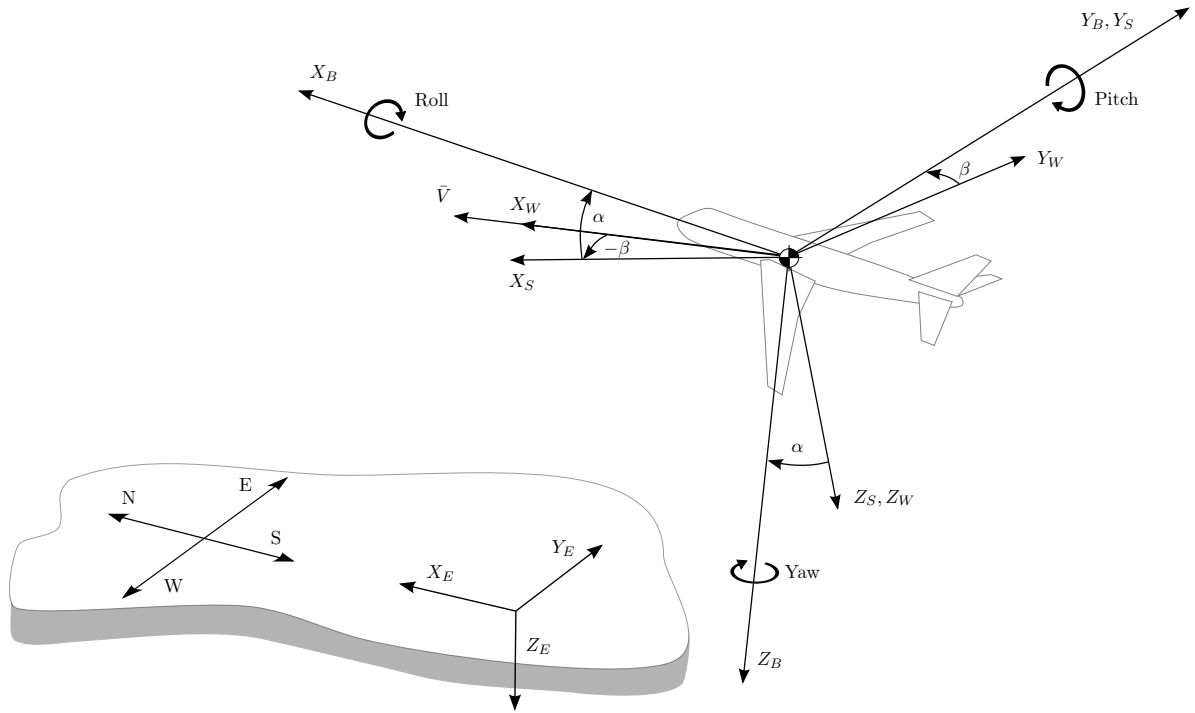


Figure 3.2: Body, wind, stability and inertial axis representation

3.1.1 Body Axis

The body axis system, X_B, Y_B, Z_B , is defined as a right-handed reference frame fixed at the aircraft's center of gravity. Figure 3.2 shows the alignment of the body axis with the aircraft. The X_B -axis is defined in the aircraft's X, Z -plane of symmetry and in the zero angle of attack line with the aircraft's forward as the positive X direction. Orthogonal to X_B is Z_B , defined as positive downward relative to fuselage. Finally, perpendicular to the plane of symmetry or the X_B, Z_B -plane is the Y_B axis, with starboard positive convention. For aircraft orientation, the right hand rule applies. Roll is defined about the X_B -axis, pitch about the Y_B -axis and yaw about the Z_B -axis.

3.1.2 Stability and Wind Axes

The stability axis is useful when defining the aerodynamic coefficients. Its advantage is that this rotation of the body axis reduces the aerodynamic model to its simplest possible form, and maximizes the visibility of the physical phenomena involved [36]. The stability axis, X_S, Y_S, Z_S , differs from the body axis in the sense that the X and Z -axes are rotated about the Y -axis through α , the angle of attack. This X_S -axis also lies in the X, Z plane of symmetry of the aircraft, and is rotated about Z_S away from the relative wind by β , the sideslip angle [37]. Thus the transformation from body axis to stability axis is only a rotation in α . This axis orientation is indicated in Figure 3.2.

3.2 Aircraft Model Sign Conventions

The wind axis system, X_W, Y_W, Z_W , differs from the stability axis in that it requires another rotation this time about the Z_S -axis into the relative wind by β , the sideslip angle. Thus the transformation from the body axis to the wind axis requires a rotation of α and β . This axis is termed the wind axis, since it points in the direction from which the oncoming freestream wind flows onto the aircraft.

3.1.3 Inertial Axis

The inertial axis system, X_E, Y_E, Z_E , describes the aircraft's position with regard to the world or physical space. This axis system is fixed to the Earth at some convenient point. For this project, the Earth will be considered flat and non-rotating. This assumption can be made, since the angular rotation of the Earth is considered negligible when compared to the angular rotations of the aircraft [34]. The inertial axis is right-handed, as indicated in Figure 3.2, with the positive Z_E -axis pointing down. Perpendicular to Z_E is X_E , which is orientated with positive North. Finally, the Y_E -axis is perpendicular to the X_E, Z_E -plane, with positive pointing East.

3.2 Aircraft Model Sign Conventions

As the aircraft model is constructed, the sign conventions between model parameters should be consistent. Figure 3.3 provides the most important model coordinate vectors and control surface sign conventions. The parameter descriptions are given in Table 3.1. For positive elevator and rudder deflections, negative pitching and yawing moments are induced respectively. However, for a positive aileron deflection, which increases downwash on the starboard wing, a negative rolling moment is induced on the aircraft [37].

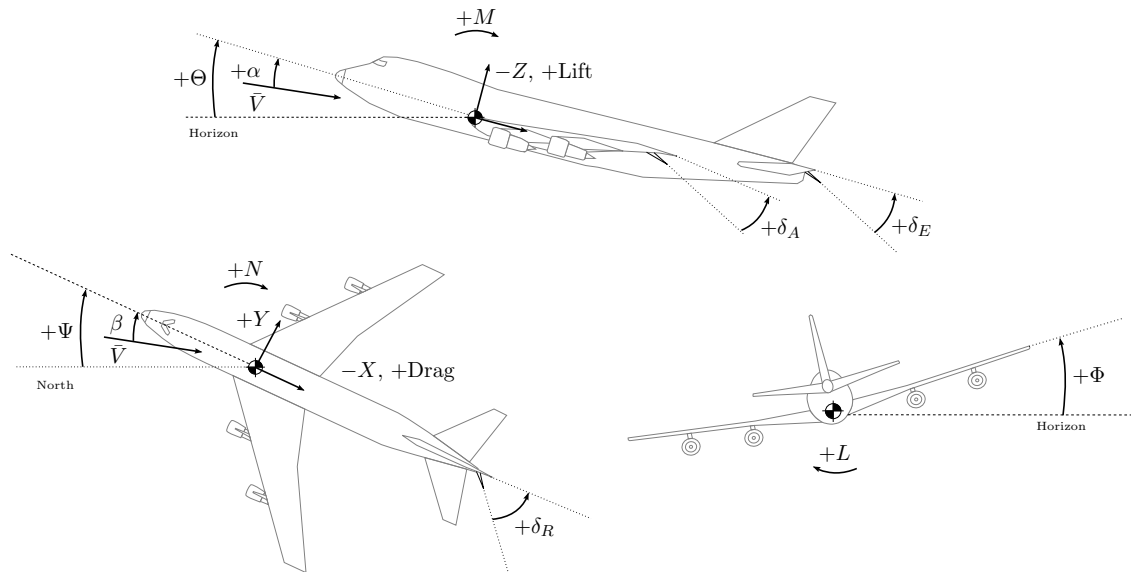


Figure 3.3: Sign conventions of the aircraft model

3.3 Six Degrees of Freedom Equations of Motion

Symbols	Definition
X, Y, Z	Axial, lateral and normal force vectors in the body axis system.
L, M, N	Rolling, pitching and yawing moments in the body axis system.
U, V, W	Axial, lateral and normal velocities in the body axis.
P, Q, R	Roll, pitch and yaw rates in the body axis.
N, E, D	Coordinates of the position vector in the inertial axis.
Φ, Θ, Ψ	The Euler 3-2-1 attitude parameters of the body axis system with respect to the inertial axis space.
\bar{V}	Velocity magnitude in the wind axis. $\bar{V} = \sqrt{U^2 + V^2 + W^2}$
α, β	Aircraft angle of attack and sideslip. $\alpha = \arctan\left(\frac{W}{U}\right)$ $\beta = \arcsin\left(\frac{V}{\bar{V}}\right)$

Table 3.1: Sign conventions and aircraft model parameters

3.3 Six Degrees of Freedom Equations of Motion

The six degrees of freedom refer to the aircraft's three translational degrees and three rotational degrees of freedom. In the modeling of aircraft for control system design purposes, an aircraft is often treated as a single rigid body, which implies that the position of each mass element on the aircraft remains fixed relative to the body axis system. The structural flexibility of the aircraft for control design purposes considered negligible to simplify the models. This section will focus on the kinetic and kinematic mechanics of aircraft motion with the relation as given in Figure 3.4.

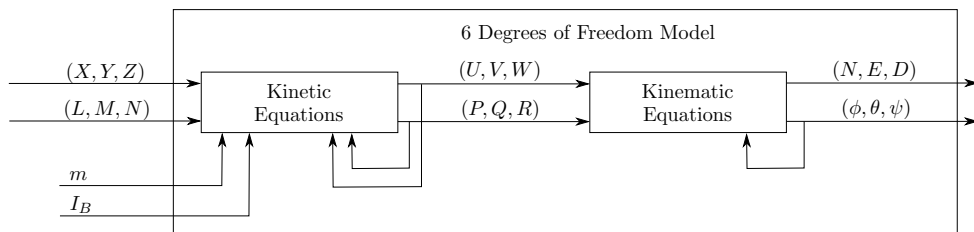


Figure 3.4: Six degrees of freedom model

3.3.1 Aircraft Kinetics

Aircraft kinetics refer to the relationships between the forces and moments acting on the aircraft and the kinematics states. The position, velocity and acceleration states can be described by Newton's laws of motion. Equations 3.1 are the aircraft's equations of motion with all vectors in the body axis [35].

3.3 Six Degrees of Freedom Equations of Motion

$$\begin{aligned}
 X &= m(\dot{U} - VR + WQ) & L &= \dot{P}I_{xx} + QR(I_{zz} - I_{yy}) \\
 Y &= m(\dot{V} + UR - WP) & M &= \dot{Q}I_{yy} + PR(I_{xx} - I_{zz}) \\
 Z &= m(\dot{W} - UQ + VP) & N &= \dot{R}I_{zz} + PQ(I_{yy} - I_{xx})
 \end{aligned} \tag{3.1}$$

For the above equations, two simplifying assumptions have been made [35]:

- The aircraft is symmetric about the X_B, Z_B -plane. As a result, the cross product of the moments of inertia, I_{xy} and I_{yz} , is zero.
- The cross product of inertia I_{xz} is negligibly small.
- The mass (m) and principle moments of inertia (I_{xx}, I_{yy}, I_{zz}) of the aircraft will be considered constant.

If the forces and moments acting on the aircraft are known for a specific instant in time, the linear velocity and angular rates can be propagated over time using Equations 3.1, as long as the aircraft's mass and moments of inertia are also known.

3.3.2 Aircraft Kinematics

Aircraft kinematics refer to the aircraft motion variables. These include the linear velocity, angular rate, attitude and position of the aircraft. In this thesis, Euler 3-2-1 attitude parameterization is used. Figure 3.3 indicates the aircraft attitude angles with regard to the inertial axis. The transformation from the aircraft angular rates coordinated in the body axis to the inertial axis is given by Equation 3.2 [35].

$$\begin{bmatrix} \dot{\Phi} \\ \dot{\Theta} \\ \dot{\Psi} \end{bmatrix} = \begin{bmatrix} 1 & \sin \Phi \tan \Theta & \cos \Phi \tan \Theta \\ 0 & \cos \Phi & -\sin \Phi \\ 0 & \sin \Phi \sec \Theta & \cos \Phi \sec \Theta \end{bmatrix} \begin{bmatrix} P \\ Q \\ R \end{bmatrix} \quad \text{with } |\Theta| \neq \frac{\pi}{2} \tag{3.2}$$

The linear velocity as given in the body axis can be converted to the inertial axis using the inverse of the directional cosine matrix (DCM). Equation 3.3 illustrates this relationship. Furthermore, natural integration takes place to convert the velocity and angular rate states to position and attitude system states.

$$\begin{aligned}
 \begin{bmatrix} \dot{N} \\ \dot{E} \\ \dot{D} \end{bmatrix} &= \begin{bmatrix} \cos \Psi \cos \Theta & \cos \Psi \sin \Phi \sin \Theta - \sin \Psi \cos \Phi & \cos \Psi \sin \Phi \cos \Theta - \sin \Psi \sin \Phi \\ \sin \Psi \cos \Theta & \sin \Psi \sin \Phi \sin \Theta - \cos \Psi \cos \Phi & \sin \Psi \sin \Phi \cos \Theta - \cos \Psi \sin \Phi \\ -\sin \Theta & \cos \Theta \sin \Phi & \cos \Theta \cos \Phi \end{bmatrix} \begin{bmatrix} U \\ V \\ W \end{bmatrix} \\
 &= [DCM]^{-1} \begin{bmatrix} U \\ V \\ W \end{bmatrix}
 \end{aligned} \tag{3.3}$$

3.4 Aircraft Forces and Moments

The current state forces and moments calculation is used to calculate the next state coordinate vectors. The dynamics modeled in Section 3.3 are not aircraft-specific, although the forces and moments acting on the aircraft are related to the type of aircraft. To calculate the forces and moments, the model parameters for a Boeing 747 model were used. The Boeing 747 aircraft was selected due to its popularity in commercial aviation, and because of the vast amount of modeling data available in the public domain. For this thesis, the Boeing 747 model parameters as given in Hanke et al. [37] and Hefelely [3] were used.

The forces and moments acting on the Boeing 747 can be categorized into aerodynamic, thrust and gravitational. Equations 3.4 are the expanded forms of the forces and moments states given in 3.1, with superscripts A , G and T denoting the aerodynamic, gravitational and thrust forces and moments respectively.

$$\begin{aligned}
 X &= X^A + X^T + X^G & L &= L^A + L^T + L^G \\
 Y &= Y^A + Y^T + Y^G & M &= M^A + M^T + M^G \\
 Z &= Z^A + Z^T + Z^G & N &= N^A + N^T + N^G
 \end{aligned} \tag{3.4}$$

In formation flight, the wake of the leader aircraft induces additional aerodynamic forces and moments on the follower aircraft. For this thesis, the wake model as derived by Bizinos et al. [13] was implemented. In his model, Bizinos gave the effects of the wake as additional aerodynamic coefficients. The wake aerodynamic coefficients are given as functions of lateral and vertical separations. Calculating the forces and moments acting on the follower aircraft, therefore introduces wake effects into the aerodynamic model of the follower aircraft.

In this section, a detailed description of the gravitational, thrust, aerodynamic and wake-induced forces and moments will be presented.

3.4.1 Gravitational Model

The effect of gravity on an aircraft is modeled as a force induced downwards in the inertial axis Z_E direction. It is assumed that the gravitational field across the simulation space is uniform and constant with an acceleration of 9.81 m/s^2 . From this assumption, it follows that the center of mass and the center of gravity coincide perfectly, resulting in zero moments acting on the aircraft due to gravity. If the gravitational field was considered spatially varying over the object, the center of mass and the center of gravity would be separated, and the aircraft would experience a moment about the center of mass due to gravity. This would require

a more complex gravitational model. With the uniform gravitational field assumption, the forces induced by gravity can be written as:

$$\begin{bmatrix} X^G \\ Y^G \\ Z^G \end{bmatrix} = \begin{bmatrix} -\sin \Theta \\ \cos \Theta \sin \Phi \\ \cos \Theta \cos \Phi \end{bmatrix} mg \quad \begin{bmatrix} L^G \\ M^G \\ N^G \end{bmatrix} = \mathbf{0}_{3 \times 1} \quad (3.5)$$

3.4.2 The Higher-Order Boeing 747 Thrust Model

The Boeing 747 aircraft is constructed with four engines, two mounted on the starboard and two on the port wings. The placement and orientation of the engines influence the forces and moments induced on the aircraft due to engine thrust. This enables the system to actuate differential thrust (δ_T) on the aircraft by increasing thrust on one side of the rigid body. Two model blocks are added to combine the four engines into a representative thrust model. The first calculates the thrust distribution, and the second the forces and moments. Figure 3.5 gives the block diagram for the thrust model.

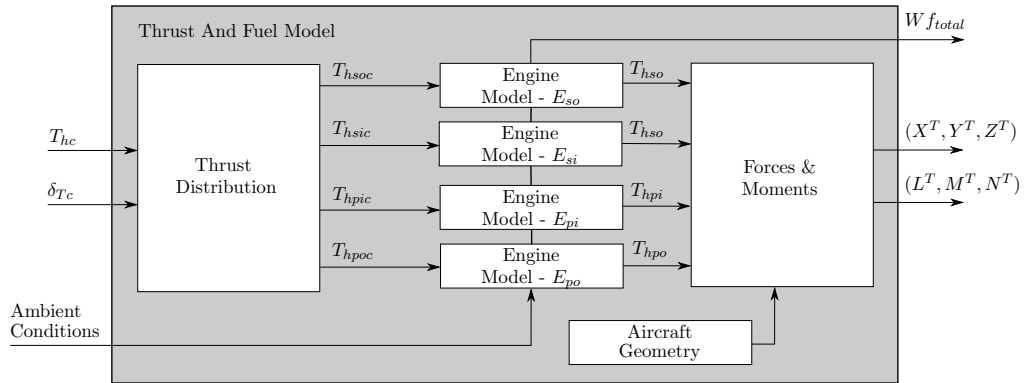


Figure 3.5: Higher-order thrust model diagram

In this section, the thrust distribution and forces and moments models will be defined as calculated from the Boeing 747 parameters given by Hanke et al. [37]. The engine actuator model, as derived in Chapter 2, is implemented to simulate the induced thrust. The total fuel flow rate (Wf_{total}) model is simply the sum of the fuel flows of the four engine models.

3.4.2.1 Thrust Distribution Model

The purpose of the thrust distribution model is to assign the thrust command (T_{hc}) to the four individual engines of the Boeing 747. A differential thrust command (δ_{Tc}) is included in the model, enabling thrust increments on the starboard side while decrementing the port side equally, or vice versa.

3.4 Aircraft Forces and Moments

This simple model takes the thrust command (T_{hc}), as received from the controller, and splits it evenly between the four engines. When a differential thrust (δ_{Tc}) is applied, the thrust balance is shifted. This introduces an extra control variable into the aircraft model. Equation 3.6 defines the engine thrust command as a function of T_{hc} and δ_{Tc} . The differential thrust δ_T is defined so that a positive command produces a positive yawing moment. The thrusts produced by the two starboard engines (T_{so}, T_{si}) are always equal, and the same applies to the port engines (T_{po}, T_{pi}). If a simplified controller is used, the differential thrust signal can simply be set to zero to deactivate this effect and balance the thrust.

$$\begin{aligned} T_{soc}, T_{sic} &= \frac{T_{hc} + \delta_{Tc}}{4} \\ T_{poc}, T_{pic} &= \frac{T_{hc} - \delta_{Tc}}{4} \end{aligned} \tag{3.6}$$

3.4.2.2 The Forces And Moments Produced by Engine Thrust

The dimensional engine placement and alignment data of the Boeing 747, as obtained from Hanke et al. [37], was used to calculate the forces and moments produced by engine thrust. A parameterized force and moment model was developed. Figure 3.6 shows a Boeing 747 with all the relevant dimensions indicated.

3.4 Aircraft Forces and Moments

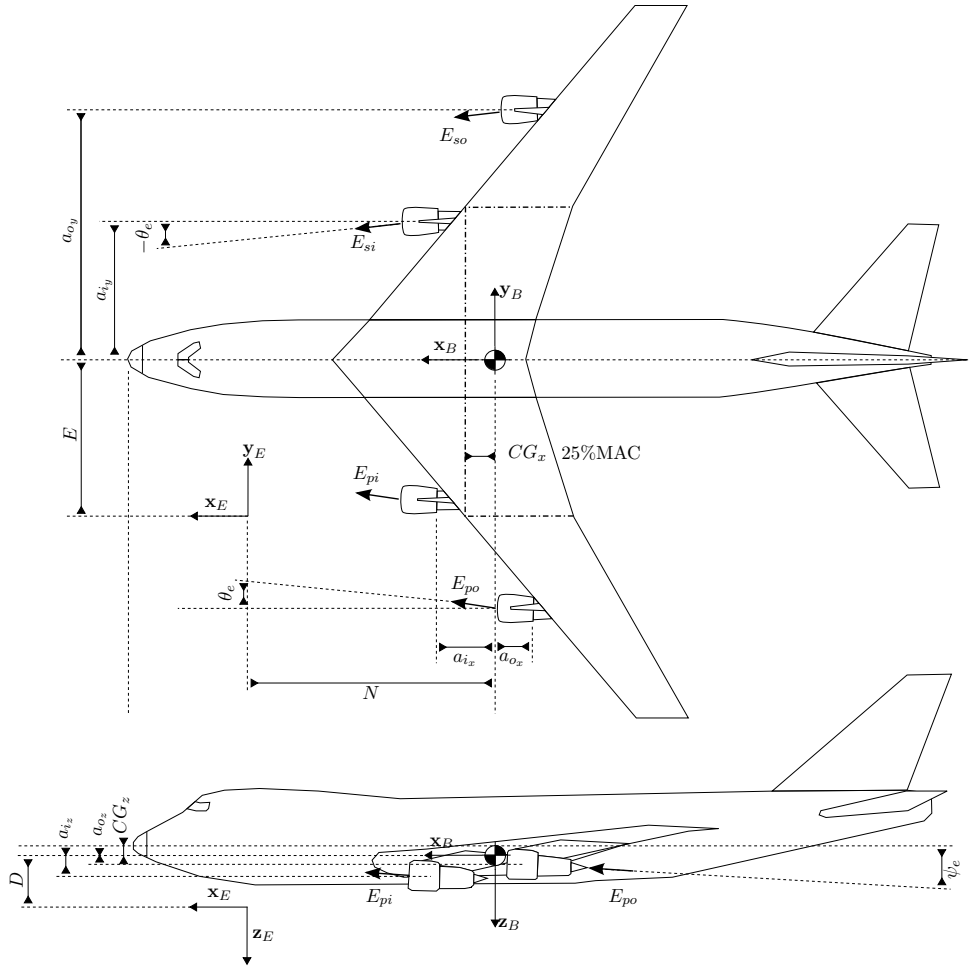


Figure 3.6: Engine placement and alignment variables of the Boeing 747 aircraft

For this project, the aircraft's center of gravity (CG) will be defined at 25% mean aerodynamic chord (MAC) and 0.84 m beneath the main floor of the aircraft. The forces and moments, as induced by the four engines, are given by Equation 3.7 and Equation 3.8 respectively. In these equations, it is clear that thrust (T_h) is a function of the longitudinal coordinate vectors and differential thrust (δ_T) a function of the lateral coordinate vectors.

$$\begin{aligned}
 X^T &= \cos \theta_e \cos \psi_e (T_h) \\
 Y^T &= \sin \theta_e (\delta_T) \\
 Z^T &= -\sin \psi_e (T_h)
 \end{aligned} \tag{3.7}$$

$$\begin{aligned}
 L^T &= \frac{\delta_T}{2} (\sin \theta_e (a_{iz} + a_{oz}) - \sin \theta_e (a_{iy} + a_{oy})) \\
 M^T &= \frac{T_h}{2} (\sin \psi_e (a_{ix} - a_{ox}) + \cos \theta_e \cos \psi_e (a_{iz} + a_{oz})) \\
 N^T &= -\frac{\delta_T}{2} (\sin \theta_e (a_{ix} - a_{ox}) + \cos \theta_e \cos \psi_e (a_{iy} + a_{oy}))
 \end{aligned} \tag{3.8}$$

3.4.2.3 Thrust Model Simulation

When simulating the aircraft thrust model, as shown in Figure 3.5, the actuating effect of the four engines is applied to the aircraft. Figure 3.7a shows the force vector as actuated by thrust command (T_{hc}), with no differential thrust (δ_{Tc}) applied. From this figure, it is concluded that if T_h is applied, a large thrust force results in the X_B -axis, and a light upward force in the Z_B -axis, due to the alignment of the engines. As for the moments, Figure 3.7b indicates a large pitching moment, as the engines are all mounted beneath the aircraft center of gravity. The rolling and yawing moments are zero, as the thrust output between the four engines is balanced.

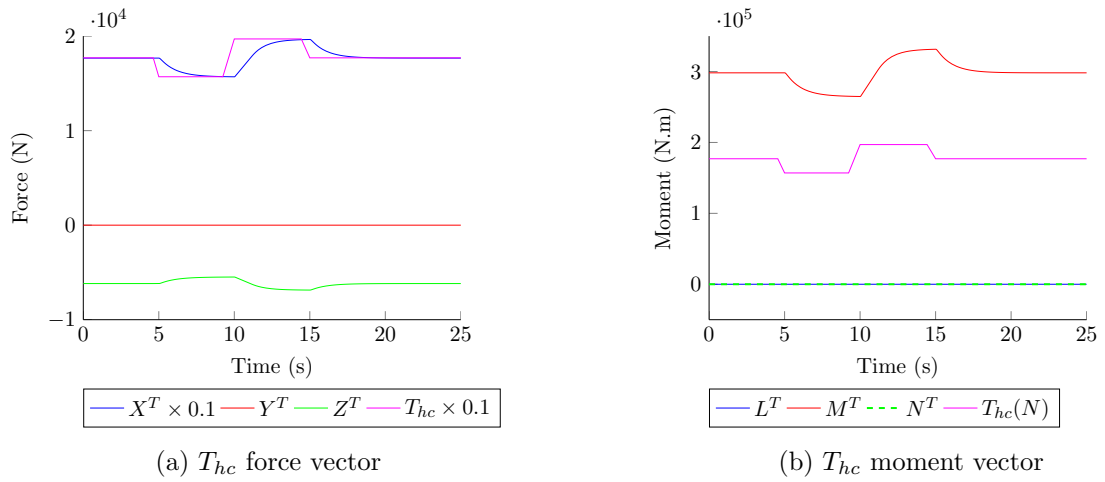


Figure 3.7: Thrust model output as actuated by T_h command with no δ_T applied

Figure 3.8a shows the force vector with differential thrust (δ_{Tc}) applied while maintaining a constant thrust (T_{hc}). It was observed that a slight side force in the Y_B -axis is actuated with δ_T , as the engines on the one side drive more thrust than the engines on the opposing side of the aircraft. As for the moments, Figure 3.8b demonstrates a large yawing moment due to the force applied on one moment arm being larger than that of the opposing. A slight rolling moment was also observed, with the longitudinal coordinate vectors remaining close to constant.

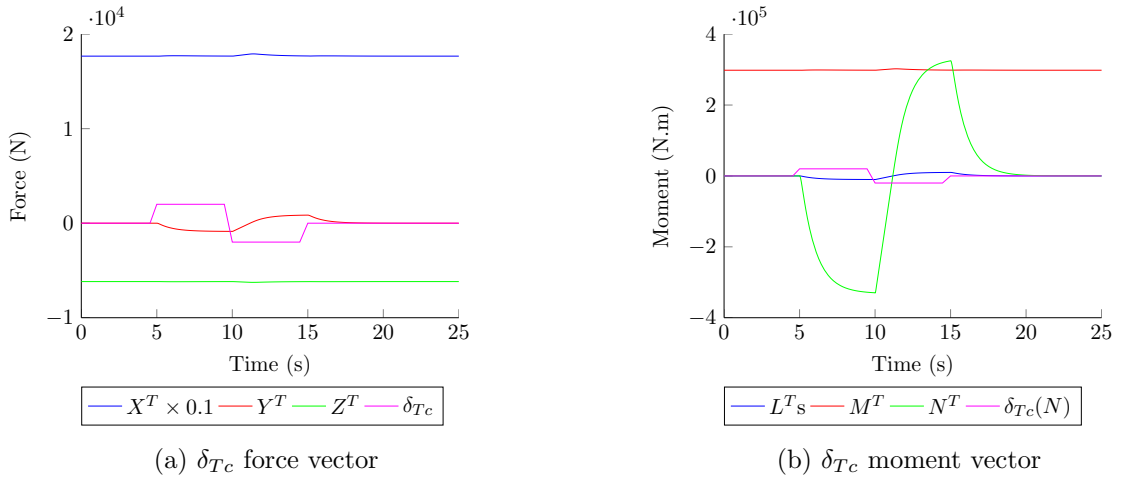


Figure 3.8: Thrust model output as actuated with constant T_{hc} and δ_{Tc} applied

3.5 Control Actuators

The control actuators govern the application of control surfaces in the model. The actuator models are imposed on the actuator input signals, as the actuator filters the signal before it is passed to the aerodynamic model. Actuator models were included for the elevator, rudder and aileron. To realistically model actuators, a high-order transfer function with other nonlinearities such as rate limiters, saturation levels and hysteresis, should be included. However, for the current model, lower-fidelity actuator models were implemented, which only model the rate limits and saturation levels. This decision can be justified by the large timescale separation between the actuators with very fast dynamics, and the very slow dynamics of a commercial aircraft. Table A.5 in Appendix A gives the actuator saturation levels and slew rates as taken from the Boeing 747 modeling data [37]. The first-order transfer function time constants are also presented to justify the timescale separation assumption.

3.6 Aerodynamic Model for Isolated Flight

In Hanke et al. [37], a full non-linear aerodynamic model is given in terms of normalized aerodynamic force and moment coefficients. Due to the complexity of this model, a simplified approach was followed which uses the linearized stability and control derivatives. The simulation of the aircraft model was conducted around a single flight condition and since the gradient change in the stability and control derivative values around this operating point was very small, a linear aerodynamic model was a good approximation. The subsonic flight condition, at 12 192 meters and Mach 0.8 was considered the linearization point for the aerodynamic model, and all simulations were started about this operating condition. Equation 3.9 gives the coefficient representation, where C_A is the aerodynamic coefficient effected by

3.6 Aerodynamic Model for Isolated Flight

the state or control variable B , and n is the optional normalizing coefficient associated with change in B [14].

$$C_{AB} \equiv n \frac{\partial C_A}{\partial B} \quad (3.9)$$

The aerodynamic coefficient model used in this thesis is given in stability axis, as this simplifies the presentation of the aerodynamic functions. The empirical coefficient data for the Boeing 747, as published by NASA and Heffely et al. [3], was used. Equation 3.10 gives the aerodynamic coefficient model for isolated flight.

$$\begin{aligned} C_{L_S} &= C_{L_{LP}} + C_{L_\alpha}(\alpha - \alpha_{LP}) + \frac{\bar{c}}{2\bar{V}_{LP}} C_{L_{\dot{\alpha}}}(\dot{\alpha} - \dot{\alpha}_{LP}) + C_{L_{\delta_E}}(\delta_E) + \frac{\bar{V} - \bar{V}_{LP}}{V_s} C_{L_M} \\ &\quad + \frac{\bar{c}}{2\bar{V}_{LP}} C_{L_q}(Q - Q_{LP}) \\ C_{D_S} &= C_{D_{LP}} + C_{D_\alpha}(\alpha - \alpha_{LP}) + \frac{\bar{V} - \bar{V}_{LP}}{V_s} C_{D_M} + C_{D_\beta} |\beta - \beta_{LP}| + \text{sign}(\beta) C_{D_{\delta_R}}(\delta_R) \\ C_{Y_S} &= C_{Y_\beta}(\beta - \beta_{LP}) + \frac{b}{2\bar{V}_{LP}} C_{Y_p}(P - P_{LP}) + \frac{b}{2\bar{V}_{LP}} C_{Y_r}(R - R_{LP}) + C_{Y_{\delta_A}}(\delta_A) + C_{Y_{\delta_R}}(\delta_R) \\ C_{l_S} &= C_{l_\beta}(\beta - \beta_{LP}) + \frac{b}{2\bar{V}_{LP}} C_{l_p}(P - P_{LP}) + \frac{b}{2\bar{V}_{LP}} C_{l_r}(R - R_{LP}) + C_{l_{\delta_A}}(\delta_A) + C_{l_{\delta_R}}(\delta_R) \\ C_{m_S} &= C_{m_{LP}} + C_{m_\alpha}(\alpha - \alpha_{LP}) + \frac{\bar{c}}{2\bar{V}_{LP}} C_{m_{\dot{\alpha}}}(\dot{\alpha} - \dot{\alpha}_{LP}) + \frac{\bar{V} - \bar{V}_{LP}}{V_s} C_{m_M} \\ &\quad + \frac{\bar{c}}{2\bar{V}_{LP}} C_{m_q}(Q - Q_{LP}) + C_{m_{\delta_E}}(\delta_E) + C_{m_{\delta_R}}(\delta_R) + C_{m_\beta}(\beta - \beta_{LP}) \\ C_{n_S} &= C_{n_\beta}(\beta - \beta_{LP}) + \frac{b}{2\bar{V}_{LP}} C_{n_p}(P - P_{LP}) + \frac{b}{2\bar{V}_{LP}} C_{n_r}(R - R_{LP}) + C_{n_{\delta_A}}(\delta_A) + C_{n_{\delta_R}}(\delta_R) \end{aligned} \quad (3.10)$$

In order to calculate the aerodynamic forces induced on the aircraft, the coefficients in Equation 3.10 need to be transformed from, stability to the body axis. Equation 3.11 shows that the lift (C_{L_S}) and drag (C_{D_S}) coefficients convert to coefficients in the X and Y body axis through a rotation in the angle of attack (α).

$$\begin{aligned} C_X &= -C_{D_S} \cos \alpha + C_{L_S} \sin \alpha & C_l &= C_{l_S} \\ C_Y &= C_{Y_S} & C_m &= C_{m_S} \\ C_Z &= -C_{L_S} \cos \alpha - C_{D_S} \sin \alpha & C_n &= C_{n_S} \end{aligned} \quad (3.11)$$

The dynamic pressure (q), wingspan (b), wing surface area (S) and the mean aerodynamic chord (\bar{c}) are the parameters required to scale the non-dimensional aerodynamic coefficient

3.7 Relative Formation Separation

to the Boeing 747 aircraft at the linearization point. Equation 3.12 gives this relationship.

$$\begin{aligned} X^A &= qSC_X & L^A &= qSbC_l \\ Y^A &= qSC_Y & M^A &= qS\bar{c}C_m \\ Z^A &= qSC_Z & N^A &= qSbC_n \end{aligned} \quad (3.12)$$

For which the dynamic pressure is a function of airspeed (\bar{V}) and air density (ρ), calculated by:

$$q = \frac{\rho}{2} \bar{V}^2 \quad (3.13)$$

From these equations, it is observed that the aerodynamic forces and moments are dependent on the ambient density of the air at the specific flight condition. The Standard Atmosphere model was used to determine a constant value for the atmospheric parameters under the assumption that the atmosphere is static and a function of altitude only [38]. Table A.2 in Appendix A gives the values for the Boeing 747 aerodynamic coefficients from Heffley et. al [3].

3.7 Relative Formation Separation

Formation flight in this thesis considers two aircraft in right echelon formation. The leader aircraft flies straight and level in a cruise scenario. In order to perform station keeping in formation, the spatial separation should be known. Figure 3.9 shows the formation separation defined as the distance between the centers of gravity of the two aircraft, where a represents the exact separation and a^* the effective separation in the specified direction.

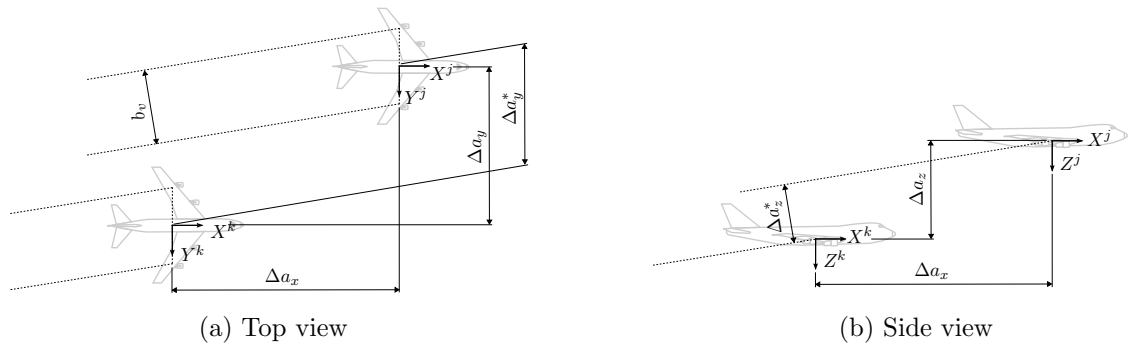


Figure 3.9: Formation flight separation and effective separation

The exact separation between the two aircraft can be calculated with Equation 3.14, where the geometric separation in the inertial axis is rotated by the heading angle of the leader (Ψ^j), with the leader's sideslip (β^j) taken out of the equation.

$$\begin{bmatrix} \xi \\ \eta \\ \zeta \end{bmatrix} = \frac{1}{b} \begin{bmatrix} a_x \\ a_y \\ a_z \end{bmatrix} = \frac{1}{b} \begin{bmatrix} \cos \Psi^* & \sin \Psi^* & 0 \\ -\sin \Psi^* & \cos \Psi^* & 0 \\ 0 & 0 & -1 \end{bmatrix} \begin{bmatrix} N^j - N^k \\ E^j - E^k \\ D^j - D^k \end{bmatrix} \quad \text{with } \Psi^* = \Psi^j + \beta^j \quad (3.14)$$

3.8 Formation Aerodynamic Interaction Model

The equation above gives the separation as it would be measured with no noise or signal propagation delays. This is the separation that will be used in control feedback for station keeping. However, the wake of an aircraft is not immune against gusts and turbulence and such disturbances must be taken into account in the mathematical wake model. If these factors are taken into account, it causes the wake to shift around as the aircraft moves. To account for this movement, the effective separation is calculated as to where the wake would be if it was skewed by atmospheric disturbances in the form of linear (v_a) and angular velocities (ω_a). Apart from the atmospheric disturbance, the atmospheric interaction between the follower and the leader is also delayed by the time-step (t^*) between the two aircraft. This effective separation is indicated with a (*) superscript, as seen in Equation 3.15 (derived by Bizinos et al. [13]).

$$\begin{aligned} \begin{bmatrix} \xi^* \\ \eta^* \\ \zeta^* \end{bmatrix} &= \begin{bmatrix} \xi \\ \sqrt{\xi^2 + \eta^2} \sin \left(\arctan \left(\frac{\eta}{\xi} \right) - \left(\frac{v_a \langle t+t^* \rangle}{V} \right) \right) \\ \sqrt{\xi^2 + \zeta^2} \sin \left(\arctan \left(\frac{\zeta}{\xi} \right) - \left(\frac{\omega_a \langle t+t^* \rangle}{V} \right) \right) \end{bmatrix} \\ &\approx \begin{bmatrix} \xi \\ \eta - \xi \left(\frac{v_a \langle t+t^* \rangle}{V} \right) \\ \zeta - \xi \left(\frac{\omega_a \langle t+t^* \rangle}{V} \right) \end{bmatrix} \quad \text{with } t^* = \frac{a_x}{V^k} \end{aligned} \quad (3.15)$$

In a real-world implementation, it is suggested that the relative position estimation between the leader and the follower be established by communicating the blended inertial navigation (INS) and global positioning system (GPS) measurements across an air-to-air telemetry link [12]. This would introduce a level of measurement noise and signal propagation delay into the system, which should also be accounted for, although it is expected that these disturbances should be small. For this thesis it was assumed that the geometric position of the leader is known to the follower exactly and without delay in all simulations. It is advised that future work reevaluate this assumption as the design of aircraft state communication systems is further developed.

3.8 Formation Aerodynamic Interaction Model

In other research, the effect of the leader aircraft's wake on the follower aircraft in formation has been modeled by lifting line theory, vortex lattice approaches and other methods [21, 39]. This study uses a single horseshoe vortex model, as derived by Bizinos et al. [13]. This method offers a simple yet close approximation of the two fully rolled-up wingtip vortices with reasonable correlation to experimental and vortex lattice results [21, 40]. In this model, two identical aircraft are considered in right echelon formation. The following surfaces are each modeled by a single horseshoe vortex: the leader aircraft main wing, the follower aircraft main wing, the follower aircraft tailfin and the follower tailplane. The horseshoe vortex has a

3.8 Formation Aerodynamic Interaction Model

specific circulation strength in the reduced-span bound vortex ($b_v = \frac{\pi}{4}b$) and two trailing vortices extending to infinity, as illustrated in Figure 1.4. Unfortunately, this model comes with limitations, as its numerical approach is known to overestimate the aerodynamic interactions, especially in the near-field wake [23]. The section presents the approximate aerodynamic interaction model as derived by Bizinos, and discusses some of its limitations and how these affected model development in this thesis.

3.8.1 Approximate Aerodynamic Interaction Model.

In the aerodynamic interaction model by Bizinos et al. [13], a Burnham-Hallock vortex circulation profile with $r_c = 0.03b$, $\mu = 0.03$ was implemented, where the vortex core radius (r_c) is defined as the radius where the vortex flow reaches the maximum tangential velocity. This circulation profile approximates viscous effects, and thus avoids singularity issues present in a Rankine vortex approximation. The aerodynamic loads acting on the follower aircraft's wing, tailfin and tailplane were approximated by first determining the downwash or sidewash at a particular position along the bound vortex. The wash or airflow causes a change in the angle of attack of the surface, and affects lift or side force via the Kutta-Joukowski theorem. Next, integration along the bound vortex span was performed, resulting in expressions for the incremental lift, drag, side force, rolling moment and yawing moment. Finally, these induced loads were converted to coefficients. These incremental coefficients, which are dimensionless parameters, were found to be proportional only to the lateral and vertical formation separation. In Equation 3.16, these in parameters are given, with σ influencing the lift, drag, side force and yawing moment and τ influencing the rolling and yawing moments.

$$\begin{aligned}
 \sigma_{jk} < \eta^*, \zeta^* > &= \ln \left| \frac{((\eta^* - \frac{\pi}{4})^2 + \zeta^{*2} + \mu^2)((\eta^* + \frac{\pi}{4})^2 + \zeta^{*2} + \mu^2)}{(\eta^{*2} + \zeta^{*2} + \mu^2)} \right| \\
 \sigma_{jkf} < \eta^*, \zeta^* > &= \ln \left| \frac{(\eta^* - \frac{\pi}{8})^2 + (\zeta^* + \zeta_v)^2 + \mu^2}{(\eta^* - \frac{\pi}{8})^2 + (\zeta^* + \zeta_v - \frac{\pi}{8}\zeta_f)^2 + \mu^2} \right| \cdots \\
 &\quad - \ln \left| \frac{(\eta^* + \frac{\pi}{8})^2 + (\zeta^* + \zeta_v)^2 + \mu^2}{(\eta^* + \frac{\pi}{8})^2 + (\zeta^* + \zeta_v - \frac{\pi}{8}\zeta_f)^2 + \mu^2} \right| \\
 \tau_{jk} < \eta^*, \zeta^* > &= -2\sqrt{\zeta^{*2} + \mu^2} \left[\tan^{-1} \left(\frac{\eta^* - \frac{\pi}{4}}{\sqrt{\zeta^{*2} + \mu^2}} \right) + \tan^{-1} \left(\frac{\eta^* + \frac{\pi}{4}}{\sqrt{\zeta^{*2} + \mu^2}} \right) \cdots \right. \\
 &\quad \left. - 2 \tan^{-1} \left(\frac{\eta^*}{\sqrt{\zeta^{*2} + \mu^2}} \right) \right] - \frac{\pi}{8} \ln \left| \frac{(\eta^* + \frac{\pi}{4})^2 + \zeta^{*2} + \mu^2}{(\eta^* - \frac{\pi}{4})^2 + \zeta^{*2} + \mu^2} \right| \cdots \\
 &\quad - \eta^* \ln \left| \frac{((\eta^* - \frac{\pi}{4})^2 + \zeta^{*2} + \mu^2)((\eta^* + \frac{\pi}{4})^2 + \zeta^{*2} + \mu^2)}{(\eta^{*2} + \zeta^{*2} + \mu^2)} \right| \\
 \sigma_{jkw} < \eta^*, \zeta^* > &= \ln \left| \frac{(\zeta^{*2} + (\eta^* - \frac{\pi}{8} - \frac{\pi}{8}\eta_h)^2 + \mu^2) (\zeta^{*2} + (\eta^* + \frac{\pi}{8} + \frac{\pi}{8}\eta_h)^2 + \mu^2)}{(\zeta^{*2} + (\eta^* - \frac{\pi}{8} + \frac{\pi}{8}\eta_h)^2 + \mu^2) (\zeta^{*2} + (\eta^* + \frac{\pi}{8} - \frac{\pi}{8}\eta_h)^2 + \mu^2)} \right| \quad (3.16)
 \end{aligned}$$

3.8 Formation Aerodynamic Interaction Model

With the influencing factors defined as functions of the lateral and vertical separation, the incremental formation aerodynamic coefficients could be calculated by scaling these influencing factors by the appropriate factors. Equation 3.17 shows the relationship between the influencing factors and the incremental formation aerodynamic coefficients.

$$\begin{aligned}
C_{D_f}^* < \eta^*, \zeta^* > &= \frac{2C_{L_S}^j C_{L_S}^k}{\pi^3 \mathcal{R}} \sigma_{jk} < \eta^*, \zeta^* > \\
C_{L_f}^* < \eta^*, \zeta^* > &= \frac{-c_{l_\alpha} C_{L_S}^j}{2\pi^2 \mathcal{R}} \sigma_{jk} < \eta^*, \zeta^* > \\
C_{Y_f}^* < \eta^*, \zeta^* > &= \frac{2S_f C_{L_S}^j}{\pi S \mathcal{R} \zeta_f} \sigma_{jkf} < \eta^*, \zeta^* > \\
C_{l_f}^* < \eta^*, \zeta^* > &= \frac{c_{l_\alpha} C_{L_S}^j}{2\pi^2 \mathcal{R}} \tau_{jk} < \eta^*, \zeta^* > \\
C_{m_f}^* < \eta^*, \zeta^* > &= C_{L_S}^k (h - h_0) + \bar{V}_T \frac{2a_1 C_{L_S}^j}{\pi^3 n_h \mathcal{R}} \left(1 - \frac{d\varepsilon}{d\alpha} \right) \sigma_{jkw} < \eta^*, \zeta^* > \\
C_{n_f}^* < \eta^*, \zeta^* > &= \frac{2C_{L_S}^j C_{L_S}^k}{\pi^3 \mathcal{R}} \tau_{jk} < \eta^*, \zeta^* > - \bar{V}_f \frac{2C_{L_S}^j}{\pi \mathcal{R} \zeta_f} \sigma_{jkf} < \eta^*, \zeta^* > \quad (3.17)
\end{aligned}$$

Calculating the incremental formation-induced aerodynamic effects over two wingspans of lateral and vertical separation produces the results shown in Figure 3.10. Notice that the clear optimum is where drag is at a minimum, and that lift is at a maximum around zero vertical separation.

3.8 Formation Aerodynamic Interaction Model

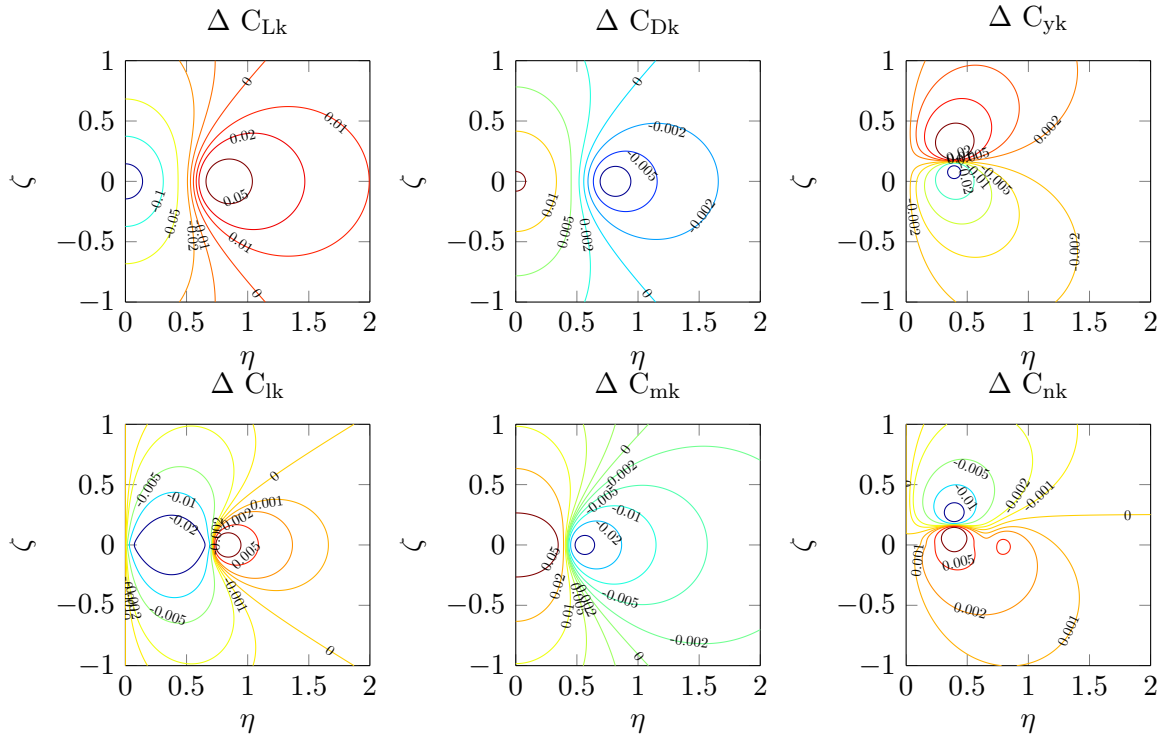


Figure 3.10: Wake-induced incremental aerodynamic coefficients ($\xi = -10, \eta = 0 : 2, \zeta = -1 : 1$)

Calculating the incremental formation-induced aerodynamic effects over a slice of two wingspans in lateral separation only provides more insight into the effects at the optimum location. A large rolling moment is also induced on the follower aircraft at the optimum location, where lift is maximized and drag is minimized ($\eta = 0.78, \zeta = 0$) as illustrated in Figure 3.11. These two figures correlate with the work by Bizinos et al. [13].

3.8 Formation Aerodynamic Interaction Model

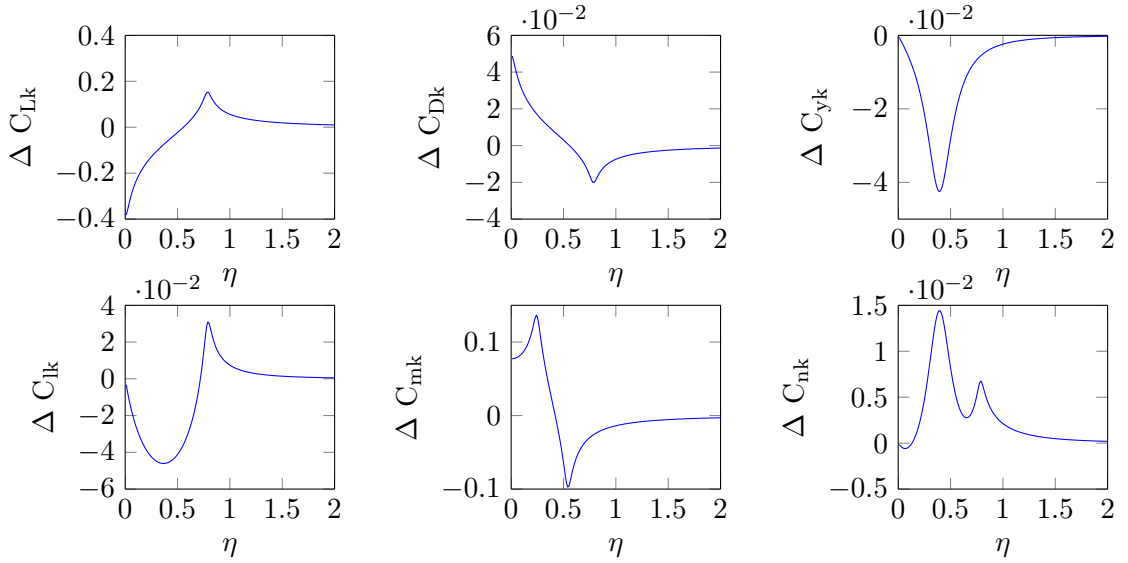


Figure 3.11: Wake-induced aerodynamic coefficients at zero vertical separation ($\xi = -10, \eta = 0 : 2, \zeta = 0$)

The incremental aerodynamic effects on the follower aircraft should be superimposed on the isolated flight aerodynamic model, as presented in Section 3.6. Equation 3.18 gives the calculation for the aerodynamic model of the follower aircraft, presented as the aerodynamic coefficient in the stability axis. These dimensionless aerodynamic coefficients should be converted to the body axis, as in Equation 3.11, and scaled to the aircraft size and dynamic pressure, as given in Equation 3.12, to complete the wake aerodynamic forces and moments calculation.

$$\begin{aligned}
 C_{D_S}^k &= C_{D_S} + C_{D_f}^* \langle \eta^*, \zeta^* \rangle & C_{l_S}^k &= C_{l_S} + C_{l_f}^* \langle \eta^*, \zeta^* \rangle \\
 C_{L_S}^k &= C_{L_S} + C_{L_f}^* \langle \eta^*, \zeta^* \rangle & C_{m_S}^k &= C_{m_S} + C_{m_f}^* \langle \eta^*, \zeta^* \rangle \\
 C_{Y_S}^k &= C_{Y_S} + C_{Y_f}^* \langle \eta^*, \zeta^* \rangle & C_{n_S}^k &= C_{n_S} + C_{n_f}^* \langle \eta^*, \zeta^* \rangle
 \end{aligned} \tag{3.18}$$

Table A.2 and A.3 in Appendix A give the values required to calculate the wake interactions of the Boeing 747 as given by Bizinos et al. [2].

3.8.2 Aerodynamic Interaction Model Limitations

The approximate aerodynamic interaction model, as presented in Section 3.8.1, made some core assumptions to simplify the mathematical integration in the induced drag calculation given by Equation 3.19. In this calculation, the circulation (Γ) and the downwash (ω) should be integrated over the entire aircraft wingspan (b).

$$D_i = \rho \int_{-b/2}^{b/2} \Gamma(y) \omega(y) dy \tag{3.19}$$

3.8 Formation Aerodynamic Interaction Model

In the interaction calculation of the approximate method derived by Bizinos et al. [2], a single horseshoe vortex is used to model the wake - a method previously used by Blake et al. [21] and others. In this model, a square circulation distribution profile is assumed over a reduced span ($b_v = \frac{\pi}{4}b$) to approximate an elliptical lift distribution or downwash distribution. As a result, a far greater average downwash is present near the wingtips, resulting in amplified wake aerodynamic interaction. To correct this, the integration of downwash must take place across the full wingspan of the trailing aircraft, with a representative downwash distribution. Taking a square downwash distribution over a reduced span to approximate elliptical lift does not capture the physics of the wake interaction in the inner wake region, i.e. closer than one wingspan in lateral separation ($\eta < 1$). This artificially increases the maximum achievable drag savings. Figure 3.12 shows a comparison by Bizinos, which compares the approximate method and the numerical integration method. It is observed that the predicted induced drag savings are almost double for the approximated method. Other coefficients, such as the rolling moment, also do not correlate well between the models for lateral separations closer than one wingspan. However, in this analysis, it is observed that the results are closely matched for lateral separations larger than one wingspan.

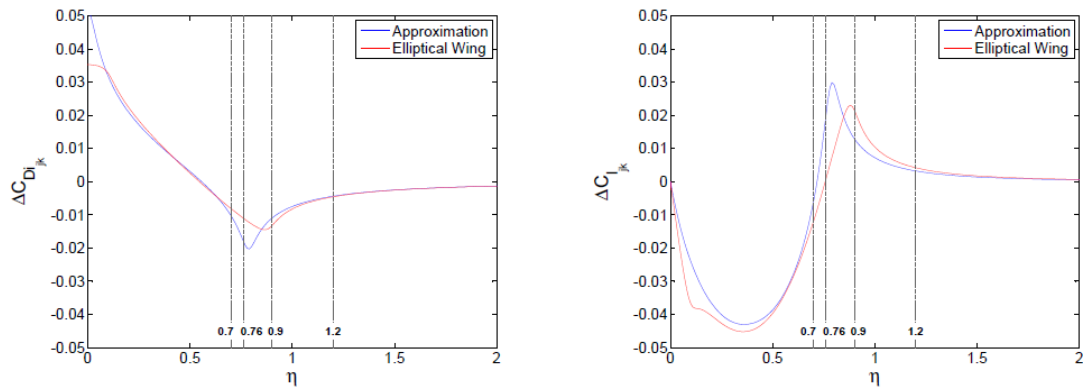


Figure 3.12: Induced drag and rolling moment incremental coefficient comparison between the approximate and numerical method over an elliptical wing for $\zeta = 0$ by Bizinos et al. [2]

Bizinos also went further, by comparing these two models to the results obtained in other studies. In Figure 3.13 by Bizinos, the approximate method and the numerical integration method are compared to wind tunnel and flight test data. In this figure, it is clear that even the numerical method overpredicts the aerodynamic interaction for the inner wake. However, both models correlate and hold well for the outer wake, lateral separations larger than one wingspan.

3.9 Atmospheric Turbulence Model

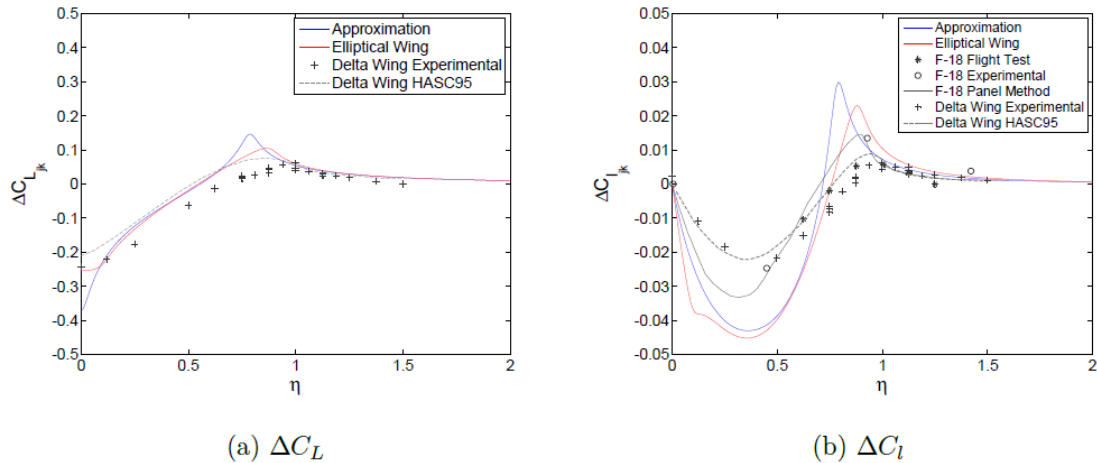


Figure 3.13: Lift and rolling moment incremental coefficient comparison between wind tunnel data, vortex lattice code, and the approximate and numerical integration methods $\zeta = 0$ by Bizinos et al. [2]

Although the numerical integration of downwash for an elliptical downwash distribution generates more accurate results compared to the approximated method when considering field test data, it still remains difficult to reproduce, as it introduces more complexities into the aerodynamic interaction model. Although this option could be explored further, it is outside the scope of this thesis. The implementation of such a model is not a simple task, and must be accompanied by an extensive model-validation process in a field with currently limited test data available. The development of such a model is also outside the field of the current researcher's expertise and it was decided not to attempt this process. The Bizinos aerodynamic interaction model was used, but the limitations in the inner wake will be acknowledged. For these reasons, the aerodynamic interaction model by Bizinos is only considered for formations larger than one wingspan in lateral separation, avoiding flight in the inner wake region. It should be noted that other researchers have also speculated that flying in the inner wake could introduce complicated unmodeled safety concerns, such as large moments on the wing structures and irregular engine flow.

3.9 Atmospheric Turbulence Model

An atmospheric turbulence model was included to increase the fidelity of the simulation. For this thesis, the von Kármán wind turbulence model was implemented, which represents stationary, homogeneous, isotropic, Gaussian turbulence [2]. This turbulence model treats the linear and angular velocity components of continuous gusts as specially varying stochastic processes, and specifies each component's power spectral density as proposed by the von Kármán spectral representation, defined in MIL-F-8785C [41] and Schaeffer et al. [42]. To

3.10 Concluding the Mathematical Modeling

simulate turbulence according to this model, band-limited white noise is passed through the following forming filters [41]:

$$\begin{aligned}
 H_u(s) &= \frac{\sigma_u \sqrt{\frac{2L_u}{\pi V}} (1 + 0.25 \frac{L_u}{V} s)}{1 + 1.357 \frac{L_u}{V} s + 0.1987 (\frac{L_u}{V})^2 s^2} \\
 H_v(s) &= \frac{\sigma_v \sqrt{\frac{L_v}{\pi V}} (1 + 2.7478 \frac{L_v}{V} s + 0.3398 (\frac{2L_v}{V})^2 s^2)}{1 + 2.9958 \frac{2L_v}{V} s + 1.9754 (\frac{2L_v}{V})^2 s^2 + 0.1539 (\frac{2L_v}{V})^3 s^3} \\
 H_w(s) &= \frac{\sigma_w \sqrt{2 \frac{L_w}{\pi V}} (1 + 2.7478 \frac{L_w}{V} s + 0.3398 (\frac{2L_w}{V})^2 s^2)}{1 + 2.9958 \frac{2L_w}{V} s + 1.9754 (\frac{2L_w}{V})^2 s^2 + 0.1539 (\frac{2L_w}{V})^3 s^3} \\
 H_p(s) &= \frac{\sigma_w \sqrt{\frac{0.8}{V}} (\frac{\pi}{4b})^{\frac{1}{6}}}{(2L_w)^{\frac{1}{3}} (1 + \frac{4b}{\pi V} s)} \\
 H_r(s) &= \frac{H_v(s)s}{\bar{V} (1 + \frac{3b}{\pi V} s)} \\
 H_q(s) &= \frac{H_w(s)s}{\bar{V} (1 + \frac{4b}{\pi V} s)} \tag{3.20}
 \end{aligned}$$

Where L_u , L_v and L_w represent the turbulence scale lengths and are equal and constant at 762 meters for altitudes higher than 610 meters [41]. The turbulence RMS intensities are given by σ_u , σ_v and σ_w , and are also equal for altitudes higher than 610 meters. The RMS magnitudes of the turbulence intensities are set to 4.7 m/s for severe turbulence, 1.3 m/s for moderate turbulence and 0.06 m/s for light turbulence at 12196 meters altitude [13, 41]. The noise power of the band-limited white noise is set equal to π . Passing the band-limited white noise through the given forming filters produces linear and angular velocity vectors, which are superimposed on the 6 DOF model aircraft velocity states.

For the formation flight model, the same turbulence is applied to both the leader and the follower aircraft. However, the turbulence on the follower is delayed by the longitudinal time separation between the leader and follower aircraft, assuming that the turbulence field remains constant in velocity for the duration of this separation time. The lateral and vertical formation separations are considered small compared to the turbulence length scale and can thus be ignored.

3.10 Concluding the Mathematical Modeling

This chapter gave an in-depth description of the mathematical models involved in the simulation of two aircraft in extended formation flight. All model conventions were presented as implemented in MATLAB and Simulink for flight simulation purposes. A six degrees of

3.10 Concluding the Mathematical Modeling

freedom model, which calculates the aircraft's kinetics and kinematics was discussed, with the forces and moments model as input. The forces and moments were calculated as the sum of the thrust, gravitational and aerodynamic model force and moment outputs, as discussed individually. An aerodynamics model for both isolated and formation flight was proposed, where the isolated aerodynamic model is used to calculate the aerodynamic forces and moments acting on the leader, and an aerodynamic interaction model was implemented on the follower to include the effects of the wake on the flight dynamics of the follower aircraft. The limitations of this wake model, proposed by Bizinos [13], were also investigated. It was concluded that the current wake model can only be applied for lateral separations larger than one wingspan. Finally, a von Kármán turbulence model was included to test the controller designs and formation flight performance when exposed to noisy turbulent conditions.

Thus far, the aircraft model has been defined and constructed with the model parameters as given in Appendix A for both isolated flight and formation interactions. In the chapters to follow, trim calculations and linear models will be derived from this non-linear system, after which the flight controls will be designed using linear control theory.

Chapter 4

Trim and Linear Dynamic Analysis

In Chapter 3, the full non-linear model of a two-aircraft formation was described. To perform straight and level flight in isolated as well as in formation scenarios, the steady-state trim has to be calculated for a specified trim condition. This involves solving the non-linear dynamic equations simultaneously to calculate all model states and inputs. Furthermore, a linear model must be derived at the calculated trim condition to perform design and stability analysis by applying linear systems theory.

In the sections to follow, the trim condition will be calculated for both the isolated aircraft and the formation flight model at the aerodynamic linearization point, as described in Section 3.6. Linear models will also be derived for both the isolated and formation flight models. These linear models will be used to aid in the design of the linear flight controllers to be implemented in the non-linear aircraft model.

4.1 Trim Analysis

The aerodynamic model linearized in Section 3.6 defines a straight and level flight trajectory at an altitude of 12 192 m and an airspeed of Mach 0.8 as the cruise flight linearization point. For this steady-state condition to hold constant, all the forces and moments acting on the aircraft should amount to zero as the aircraft remains in equilibrium. In isolated flight, this equilibrium can be obtained by solving only the longitudinal states, as the lateral forces and moments are all zero and remain so naturally. However, in formation flight a side force, rolling and yawing moment are introduced. Thus the equilibrium of the aircraft should be calculated for the full six degrees of freedom equations.

In this section, trim will be calculated for both isolated and formation flight by solving the system states for the six degrees of freedom.

4.1.1 Isolated Flight Trim Analysis

Isolated straight and level flight equilibrium can be defined by setting the lateral modes of motion to zero with zero lateral control command, due to the aircraft symmetry about the X, Z -plane. This reduces the problem to three degrees of freedom. Equation 4.1 gives the trim as calculated for longitudinal states in conventional isolated flight with three degrees of freedom.

$$\begin{aligned}
 0 &= X = X^A + X^T + X^G \\
 0 &= Z = Z^A + Z^T + Z^G \\
 0 &= M = M^A + M^T + M^G
 \end{aligned}$$

Select: $(\bar{V}, \Theta)_T$ Calculate: $(\alpha, \delta_E, T_h)_T$ With: $(\Phi, \beta, \delta_A, \delta_R, \delta_T)_T = 0$ (4.1)

Although zero sideslip (β) flight is the desired convention for cruise conditions, it is also possible to trim the aircraft at an unconventional sideslip while maintaining the equilibrium of straight and level flight. This mode of flight requires the balancing of both the lateral and longitudinal dynamics. To define this equilibrium, a trim calculation should be solved including six degrees of freedom. Equation 4.2 gives the six dynamic equations which can be solved simultaneously to calculate six system variables. Thus, aside from the airspeed state related to the trim condition, three states should be selected before calculating the six remaining states. Notice that Ψ, N, E and D are left out as they do not form part of the fundamental dynamic equations and are considered arbitrary.

Longitudinal States	Lateral States
$0 = X = X^A + X^T + X^G$	$0 = Y = Y^A + Y^T + Y^G$
$0 = Z = Z^A + Z^T + Z^G$	$0 = L = L^A + L^T + L^G$
$0 = M = M^A + M^T + M^G$	$0 = N = N^A + N^T + N^G$
Select: $(\bar{V}, \Theta)_T$ and 2 variables.	Calculate 6 variables: $(\alpha, \delta_E, T_h, \Phi, \beta, \delta_A, \delta_R, \delta_T)_T$

(4.2)

To resolve these simultaneous equations, MATLAB's Symbolic Math Toolbox was used. First, the aerodynamic forces and moments were defined as described in Equations 3.10, 3.11 and 3.12. The thrust forces and moments were also defined, as given by Equation 3.7 and 3.8 and the gravitational forces, as in Equation 3.5. At first, the trim calculation was performed in three degrees of freedom. Using symbolic variables for the unknown system states, the simultaneous equation solver calculated the three unknown variables given three balanced equations. The results are presented by Condition One in Table 4.1.

Condition	Selected	Calculated
$\bar{V}_T = 236$ m/s, One with 3° of Freedom	$\Theta_T = \alpha_T,$ $(\Phi, \beta, \delta_A, \delta_R, \delta_T)_T = 0$	$\alpha_T = 4.43^\circ,$ $\delta_{ET} = 0.47^\circ,$ $T_{hT} = 175.81kN$
$\bar{V}_T = 236$ m/s, Two with 6° of Freedom	$\Theta_T = \alpha_T,$ $\beta_T = 1^\circ, \delta_{TT} = 0$	$\alpha_T = 4.42^\circ, \delta_{ET} = 0.49^\circ,$ $\delta_{AT} = 19.4^\circ, \delta_{RT} = 1.58^\circ$ $\Phi_T = 1.07^\circ, T_{hT} = 180.1kN$
$\bar{V}_T = 236$ m/s, Three with 6° of Freedom	$\Theta_T = \alpha_T,$ $\delta_{AT} = 20^\circ, \delta_{TT} = 0$	$\alpha_T = 4.42^\circ, \delta_{ET} = 0.49^\circ,$ $\beta_T = 1.03^\circ, \delta_{RT} = 1.63^\circ,$ $\Phi_T = 1.1^\circ, T_{hT} = 180.2kN$
$\bar{V}_T = 236$ m/s, Four with 6° of Freedom	$\Theta_T = \alpha_T,$ $\delta_{AT} = 20^\circ, \delta_{RT} = 0^\circ$	$\alpha_T = 4.64^\circ, \delta_{ET} = 0.43^\circ,$ $\beta_T = 0.56^\circ, \delta_{TT} = 33kN,$ $\Phi_T = 0.79^\circ, T_{hT} = 177.1kN$

Table 4.1: Straight and level flight trim in isolated flight

For Condition Two, Three and Four in Table 4.1, the trim was calculated for the lateral and longitudinal states using the six balanced equations given by Equation 4.2. Condition Two presents more complex flight dynamics, as the aircraft is trimmed for a sideslip of one degree. When an aircraft is trimmed at a positive sideslip angle by applying some degree of rudder, the angle of attack and aspect ratio on the starboard wing increase. This induces a negative rolling moment on the aircraft and the ailerons are raised to counter this moment, as illustrated in Figure 4.1.

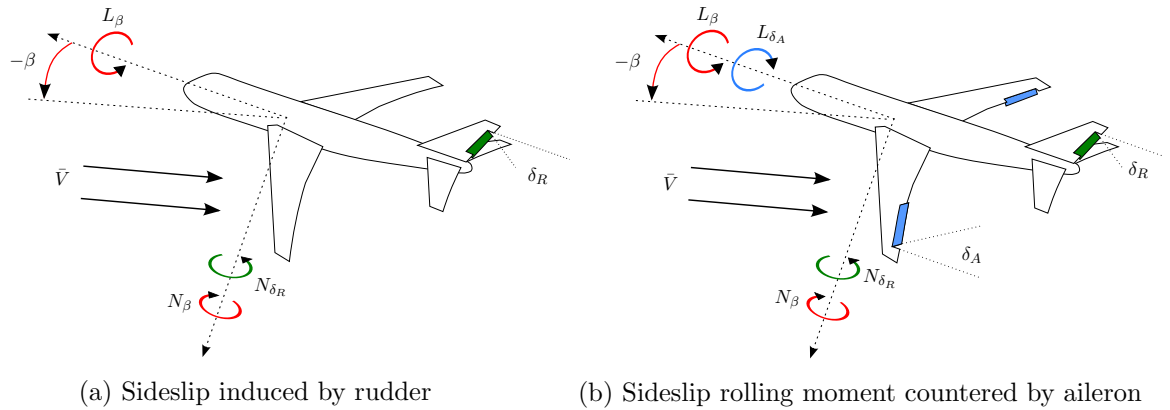


Figure 4.1: Sideslip trim equilibrium of moments achieved with ailerons countering the sideslip-induced rolling moment

Aside from the rolling moment, a side force is also induced as the fuselage turns into the wind. To maintain the required equilibrium for straight and level flight, the aircraft must increase the roll angle to bank into the side force and balance the forces acting on the aircraft, as illustrated in Figure 4.2.

4.2 Formation Flight Trim Analysis

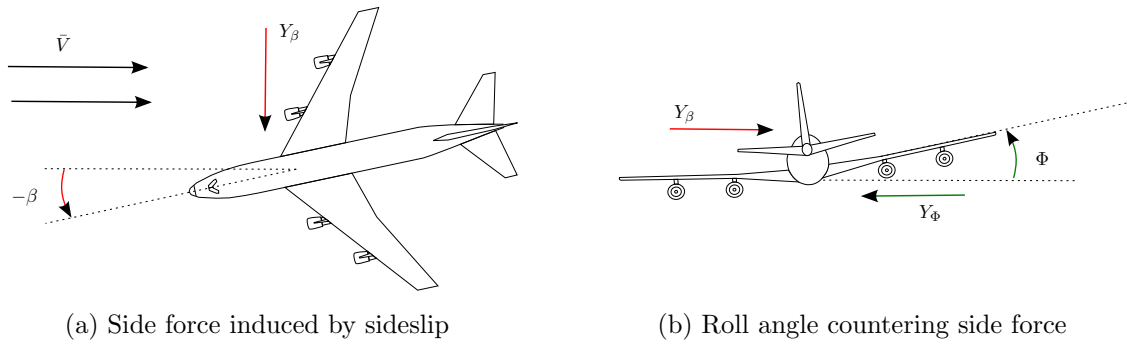


Figure 4.2: Sideslip trim equilibrium of forces achieved by roll angle countering the sideslip induced side force

In Condition Four the rudder is replaced by a level of differential thrust. A noteworthy observation is that in Condition Three 20° of aileron was applied, and this produced a rolling moment that required 1° of sideslip to counter. In Condition Four, only 0.54° of sideslip was required to counter the rolling moment induced by 20° of aileron. This reduction in sideslip was achieved by applying differential thrust instead of rudder. Thus the rolling moment in formation could be countered by introducing some sideslip, and the level of sideslip required could be reduced by applying differential thrust instead of rudder. This trim approach will be investigated in the next section.

4.2 Formation Flight Trim Analysis

To trim the follower in the wake of the leader aircraft, all forces and moments acting on the follower must be in equilibrium, as shown in Equation 4.2. In formation flight the follower trim is complicated by the wake forces and moments. These forces and moments can be written as functions of the lateral and vertical separation, as described by the wake coefficients illustrated in Figure 3.10. From this figure, it can be concluded that the wake is almost symmetrical about the X, Y -plane, and thus the follower trim analysis will be conducted over the lateral separation (η) with the vertical separation (ζ) constant at zero.

The trim in formation was calculated in six degrees of freedom with the same approach as described in Section 4.1.1. Figure 4.3 gives the trim results for the follower thrust (T_{hT}^k), aileron (δ_{AT}) and rudder (δ_{RT}). The isolated flight thrust is also indicated, as it is the same as the leader thrust (T_{hT}^k). Figure 4.3a confirms the expected model limitations and overpredictions as discussed in Section 3.8.2. The inner wake shows suspiciously high thrust reductions of almost 80% at the optimum, which is significantly more than what is presented in the literature [21, 30, 40]. This amplified result was expected due to the simplification assumptions made in the wake model. Due to the unrealistic strength of the wake model, the

4.2 Formation Flight Trim Analysis

inner region closer than one wingspan in lateral separation ($\eta < 1$), as indicated by the gray area, will be avoided in flight. However, at $\eta = 1$, a reduction in thrust of 30% is predicted by the trim calculation. This significant saving is considered realistic, as the outer wake model ($\eta > 1$) correlates well with other models (this is illustrated by Figures 3.12 and 3.13 and discussed in Section 3.8.2). Figure 4.3b shows that at this separation ($\eta = 1, \zeta = 0$) the rolling moment experienced by the follower becomes problematic, as 20° aileron is required to counter the wake-induced rolling moment. This high aileron trim is not acceptable, since it pushes the ailerons close to saturation. To overcome this problem, other trim configurations were investigated.

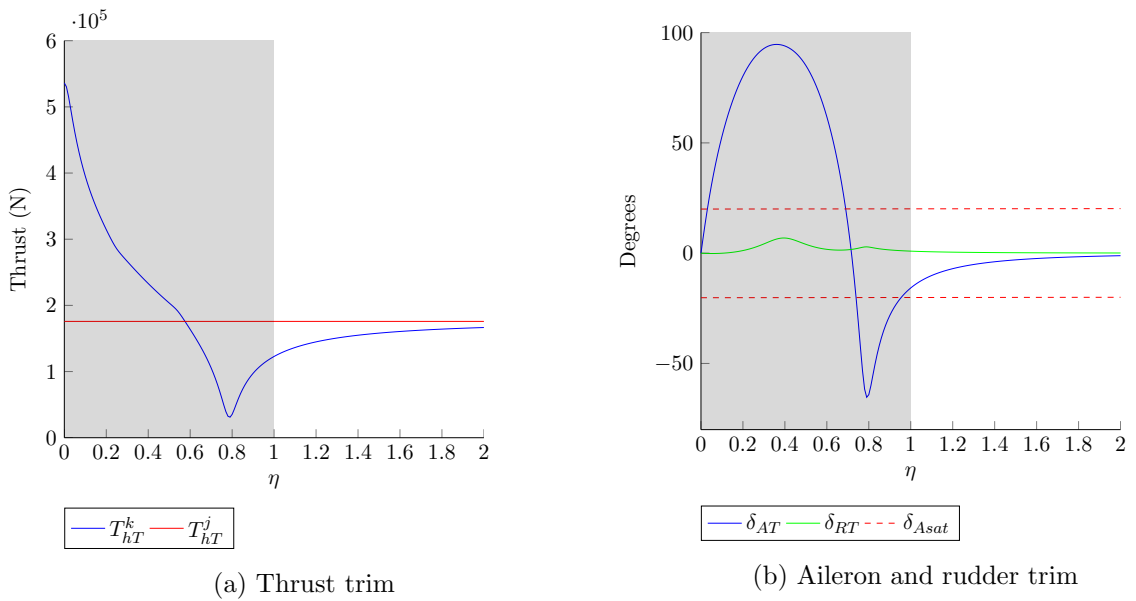


Figure 4.3: Calculated follower trim for $\zeta = 0$ and $\beta_T, \delta_{TT} = 0$.

In Section 4.1.1 it was stated that by introducing some degree of sideslip in the trim calculation, a large rolling moment could be induced on the aircraft. If this phenomenon is applied in formation, as proposed by Jordan Adams, the rolling moment produced by sideslip could be used to counter the rolling moment induced on the follower in formation. As a result, lower aileron demand would be required. Figure 4.4 shows how the aileron trim could be set to zero, while using rudder and sideslip to counter the large rolling moment experienced in the wake. In this configuration, a roll angle is also present, as the follower banks to counter the side force produced by the combination of wake- and sideslip-induced forces as presented in Figure 4.4b. The result of using sideslip instead of aileron to counter the wake roll is ideal, since most of the aileron control authority is available to counter other disturbances. However, sideslip should be minimized, as this unconventional mode of flight can bring about other unmodeled complexities such as high cabin noise and undesired structural tensions. Thus a proposed controller should be able to limit the level of sideslip induced. The thrust

4.2 Formation Flight Trim Analysis

savings for this trim configuration closely correspond to the thrust savings in Figure 4.3a.

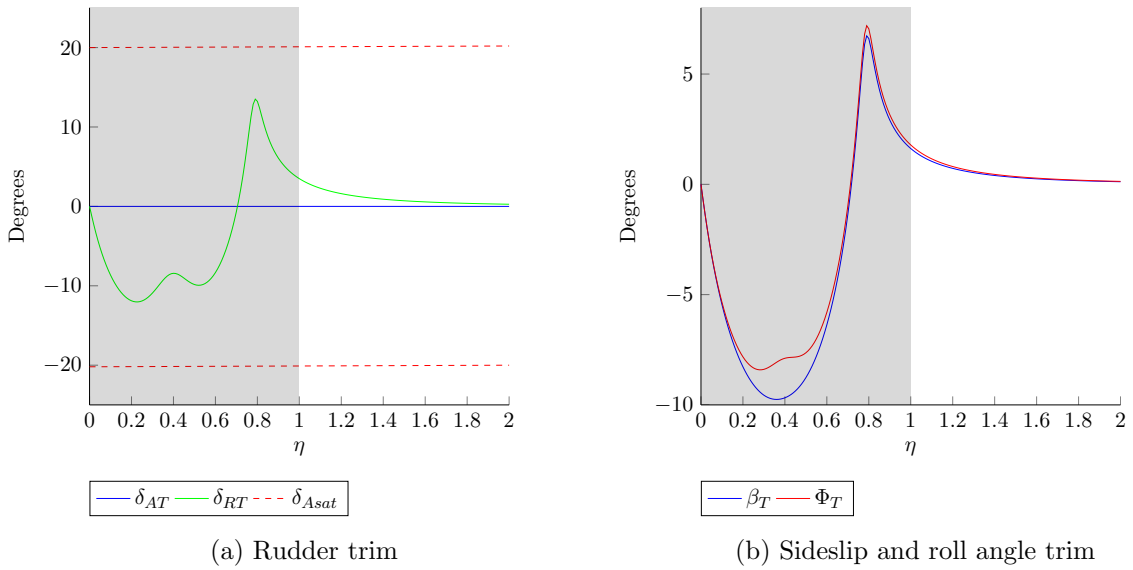


Figure 4.4: Calculated follower trim for $\zeta = 0$ and $\delta_{AT}, \delta_{TT} = 0$

Since the rudder and differential thrust can produce a large yawing moment on the aircraft, both are capable of generating sideslip. Setting both the aileron and rudder to zero while applying differential thrust produces a new trim configuration, as presented by Figure 4.5. In this configuration, all the control authority of the rudder is absorbed in differential thrust. Figure 4.5b shows that the differential thrust required for trim can push the engines outside their operating range. Thus it is advised to design the controllers to limit the amount of differential thrust applied. Another interesting observation when comparing Figure 4.5c to Figure 4.4b is that a smaller angle of sideslip is required to counter the wake rolling moment when using differential thrust instead of rudder to induce sideslip. This is a result of the additional forces and moments introduced by applying differential thrust, as demonstrated in Figures 3.8a and 3.8b.

4.3 Aircraft Model Linearization

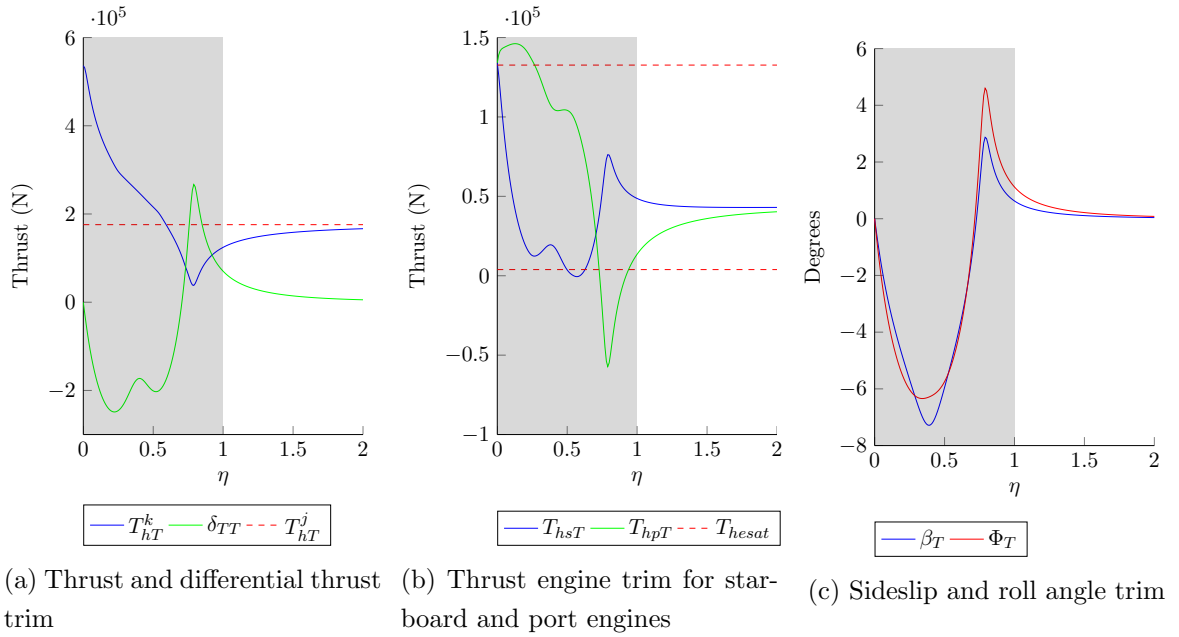


Figure 4.5: Calculated follower trim for $\zeta = 0$ and $\delta_{AT}, \delta_{RT} = 0$

This trim analysis revealed how the follower aircraft would apply its control authority at steady state over a range of lateral separations. The advantages of different trim configurations were also considered. Through the use of sideslip, the level of aileron required could be absorbed in rudder, and the level of rudder required could in turn be absorbed in differential thrust. The use of differential thrust also decreased the level of sideslip required to counter the wake-induced rolling moment. In the next section, a linear model will be derived for the Boeing 747 in isolated and formation flight for wings-level trim.

4.3 Aircraft Model Linearization

A leader and follower linear aircraft model was derived to better analyze the aircraft dynamics, and to apply linear control design theories to the aircraft model. Through linear models the stability and performance of closed-loop systems can be determined. The leader aircraft can be described as always in isolated flight, even during formation simulations, since the formation coupling has very little effect on the leader. Thus an isolated flight linear model was derived for the leader. The follower aircraft model includes the aerodynamic interactions of the leader's wake, and the follower linear model is derived at a specific defined trim separation. In this section, linearization theory will be reviewed, and an isolated linear aircraft model as well as a follower linear aircraft model in the wake will be presented.

4.3.1 Linearizing About Trim

In order to determine state space models for the aircraft, the velocity states must be known. Equation 4.3 gives the velocity states for the aircraft motion dynamics. These states form a coupled set of differential equations describing the primary motions of a fixed-wing aircraft, such as the Boeing 747. The states Ψ, N, E and D are left out, as they are not coupled back into the dynamics and thus are considered arbitrary. Equation 4.3 can be derived by rewriting Equation 3.1.

$$\begin{aligned}
 \dot{U} &= \frac{X}{m} + VR - WQ & \dot{P} &= \frac{L}{I_{xx}} - QR \frac{I_{zz} - I_{yy}}{I_{xx}} \\
 \dot{V} &= \frac{Y}{m} - UR + WP & \dot{Q} &= \frac{M}{I_{yy}} - PR \frac{I_{xx} - I_{zz}}{I_{yy}} \\
 \dot{W} &= \frac{Z}{m} + UQ - VP & \dot{R} &= \frac{N}{I_{zz}} - PQ \frac{I_{yy} - I_{xx}}{I_{zz}} \\
 \dot{\Phi} &= P + Q \sin \Phi \tan \Theta + R \cos \Phi \tan \Theta \\
 \dot{\Theta} &= Q \cos \Phi - R \sin \Phi
 \end{aligned} \tag{4.3}$$

The aircraft dynamics can be written more concisely in the non-linear state space form:

$$\begin{aligned}
 \dot{\mathbf{x}} &= \mathbf{f}(\mathbf{x}, \mathbf{u}) \quad \text{where} & \mathbf{x} &= [U \ V \ W \ P \ Q \ R \ \Phi \ \Theta]^T \\
 & & \mathbf{u} &= [\delta_E \ T_h \ \delta_A \ \delta_R \ \delta_T]^T
 \end{aligned} \tag{4.4}$$

In the above Equation, \mathbf{f} is a vector function representing the respective dynamic equations. Each state and control input can be written as the sum of the trim value and a perturbation about trim.

$$\begin{aligned}
 \mathbf{x} &= \mathbf{x}_T + \Delta \mathbf{x} \quad \text{where} & \Delta \mathbf{x} &= [u \ v \ w \ p \ q \ r \ \phi \ \theta]^T \\
 \mathbf{u} &= \mathbf{u}_T + \Delta \mathbf{u} & \Delta \mathbf{u} &= [\delta_e \ \Delta T_h \ \delta_a \ \delta_r \ \delta_t]^T
 \end{aligned} \tag{4.5}$$

Combining Equations 4.4 and 4.5 and writing the vector function \mathbf{f} 's Taylor series expansion about the trim condition yields:

$$\dot{\mathbf{x}} = \dot{\mathbf{x}}_T + \Delta \dot{\mathbf{x}} = \mathbf{f}(\mathbf{x}_T + \Delta \mathbf{x}, \mathbf{u}_T + \Delta \mathbf{u}) = \mathbf{f}(\mathbf{x}_T, \mathbf{u}_T) + \left. \frac{\partial \mathbf{f}}{\partial \mathbf{x}} \right|_T \Delta \mathbf{x} + \left. \frac{\partial \mathbf{f}}{\partial \mathbf{u}} \right|_T \Delta \mathbf{u} + \text{h.o.t.} \tag{4.6}$$

In linearization theory, it is common to assume that the higher-order terms generated by the Taylor series expansion can be ignored for small deviations about trim. As $\mathbf{f}(\mathbf{x}_T, \mathbf{u}_T)$, since all the forces and moments at trim equal zero, the velocity state influenced by the trim condition will also be zero ($\mathbf{f}(\mathbf{x}_T, \mathbf{u}_T) = 0$). Thus Equation 4.6 can be written as:

$$\Delta \dot{\mathbf{x}} \approx \mathbf{A} \Delta \mathbf{x} + \mathbf{B} \Delta \mathbf{u} \quad \text{where} \quad \mathbf{A} = \left. \frac{\partial \mathbf{f}}{\partial \mathbf{x}} \right|_T, \mathbf{B} = \left. \frac{\partial \mathbf{f}}{\partial \mathbf{u}} \right|_T \tag{4.7}$$

The state space approach described above will be used in the following sections to determine the longitudinal and lateral aircraft state space models for both isolated and follower formation flight models.

4.3.2 Isolated Flight Linear Aircraft Model

The eight system states and five control inputs given in Equation 4.5 can be divided into the longitudinal and lateral system variables. Due to this symmetry about the X, Z -plane, the coupling between the longitudinal and lateral states is approximated to zero in the linear state space representation.

$$\Delta \dot{\mathbf{x}} = \mathbf{A} \Delta \mathbf{x} + \mathbf{B} \Delta \mathbf{u} = \begin{bmatrix} \Delta \dot{\mathbf{x}}_{long} \\ \Delta \dot{\mathbf{x}}_{lat} \end{bmatrix} = \begin{bmatrix} \mathbf{A}_{long} & \mathbf{0} \\ \mathbf{0} & \mathbf{A}_{lat} \end{bmatrix} \begin{bmatrix} \Delta \mathbf{x}_{long} \\ \Delta \mathbf{x}_{lat} \end{bmatrix} + \begin{bmatrix} \mathbf{B}_{long} & \mathbf{0} \\ \mathbf{0} & \mathbf{B}_{lat} \end{bmatrix} \begin{bmatrix} \Delta \mathbf{u}_{long} \\ \Delta \mathbf{u}_{lat} \end{bmatrix}$$

$$\begin{aligned} \text{with } \Delta \mathbf{x}_{long} &= [u \quad w \quad q \quad \theta]^T, & \Delta \mathbf{u}_{long} &= [\delta_e \quad \Delta T_h]^T \\ \text{with } \Delta \mathbf{x}_{lat} &= [v \quad p \quad r \quad \phi]^T, & \Delta \mathbf{u}_{lat} &= [\delta_a \quad \delta_r \quad \delta_t]^T \end{aligned} \quad (4.8)$$

In Equation 4.8, the states are presented in orthogonal vector format (u, v, w) . However, it is often more meaningful to present the aircraft velocity in terms of polar coordinates (\bar{v}, α, β) . The following assumptions can be made for straight and level flight at small angles of attack and sideslip:

$$\begin{aligned} U &= \bar{V} \cos \alpha \cos \beta \approx \bar{V} & \text{thus } \dot{U} &= \dot{\bar{V}} \\ V &= \bar{V} \sin \beta \approx \bar{V}_T \beta & \text{thus } \dot{V} &= \bar{V}_T \dot{\beta} \\ W &= \bar{V} \sin \alpha \cos \beta \approx \bar{V}_T \alpha & \text{thus } \dot{W} &= \bar{V}_T \dot{\alpha} \end{aligned} \quad (4.9)$$

Substituting these approximations into Equation 4.8 gives the longitudinal linear state space model as:

$$\begin{aligned} \Delta \dot{\mathbf{x}}_{long} &= \mathbf{A}_{long} \Delta \mathbf{x}_{long} + \mathbf{B}_{long} \Delta \mathbf{u}_{long} & (4.10) \\ \begin{bmatrix} \dot{\bar{v}} \\ \dot{\alpha} \\ \dot{q} \\ \dot{\theta} \end{bmatrix} &= \begin{bmatrix} \frac{\partial \dot{\bar{V}}}{\partial \bar{V}} & \frac{\partial \dot{\bar{V}}}{\partial \alpha} & \frac{\partial \dot{\bar{V}}}{\partial Q} & \frac{\partial \dot{\bar{V}}}{\partial \theta} \\ \frac{\partial \dot{\alpha}}{\partial \bar{V}} & \frac{\partial \dot{\alpha}}{\partial \alpha} & \frac{\partial \dot{\alpha}}{\partial Q} & \frac{\partial \dot{\alpha}}{\partial \theta} \\ \frac{\partial \dot{Q}}{\partial \bar{V}} & \frac{\partial \dot{Q}}{\partial \alpha} & \frac{\partial \dot{Q}}{\partial Q} & \frac{\partial \dot{Q}}{\partial \theta} \\ \frac{\partial \dot{\theta}}{\partial \bar{V}} & \frac{\partial \dot{\theta}}{\partial \alpha} & \frac{\partial \dot{\theta}}{\partial Q} & \frac{\partial \dot{\theta}}{\partial \theta} \end{bmatrix} \begin{bmatrix} \bar{v} \\ \alpha \\ q \\ \theta \end{bmatrix} + \begin{bmatrix} \frac{\partial \dot{\bar{V}}}{\partial \delta_E} & \frac{\partial \dot{\bar{V}}}{\partial T_h} \\ \frac{\partial \dot{\alpha}}{\partial \delta_E} & \frac{\partial \dot{\alpha}}{\partial T_h} \\ \frac{\partial \dot{Q}}{\partial \delta_E} & \frac{\partial \dot{Q}}{\partial T_h} \\ \frac{\partial \dot{\theta}}{\partial \delta_E} & \frac{\partial \dot{\theta}}{\partial T_h} \end{bmatrix} \begin{bmatrix} \delta_e \\ \Delta T_h \end{bmatrix} \end{aligned}$$

The lateral linear state space model can also be written as:

$$\begin{aligned} \Delta \dot{\mathbf{x}}_{lat} &= \mathbf{A}_{lat} \Delta \mathbf{x}_{lat} + \mathbf{B}_{lat} \Delta \mathbf{u}_{lat} & (4.11) \\ \begin{bmatrix} \dot{\beta} \\ \dot{p} \\ \dot{r} \\ \dot{\phi} \end{bmatrix} &= \begin{bmatrix} \frac{\partial \dot{\beta}}{\partial \beta} & \frac{\partial \dot{\beta}}{\partial P} & \frac{\partial \dot{\beta}}{\partial R} & \frac{\partial \dot{\beta}}{\partial \phi} \\ \frac{\partial \dot{P}}{\partial \beta} & \frac{\partial \dot{P}}{\partial P} & \frac{\partial \dot{P}}{\partial R} & \frac{\partial \dot{P}}{\partial \phi} \\ \frac{\partial \dot{R}}{\partial \beta} & \frac{\partial \dot{R}}{\partial P} & \frac{\partial \dot{R}}{\partial R} & \frac{\partial \dot{R}}{\partial \phi} \\ \frac{\partial \dot{\phi}}{\partial \beta} & \frac{\partial \dot{\phi}}{\partial P} & \frac{\partial \dot{\phi}}{\partial R} & \frac{\partial \dot{\phi}}{\partial \phi} \end{bmatrix} \begin{bmatrix} \beta \\ p \\ r \\ \phi \end{bmatrix} + \begin{bmatrix} \frac{\partial \dot{\beta}}{\partial \delta_A} & \frac{\partial \dot{\beta}}{\partial \delta_R} & \frac{\partial \dot{\beta}}{\partial \delta_T} \\ \frac{\partial \dot{P}}{\partial \delta_A} & \frac{\partial \dot{P}}{\partial \delta_R} & \frac{\partial \dot{P}}{\partial \delta_T} \\ \frac{\partial \dot{R}}{\partial \delta_A} & \frac{\partial \dot{R}}{\partial \delta_R} & \frac{\partial \dot{R}}{\partial \delta_T} \\ \frac{\partial \dot{\phi}}{\partial \delta_A} & \frac{\partial \dot{\phi}}{\partial \delta_R} & \frac{\partial \dot{\phi}}{\partial \delta_T} \end{bmatrix} \begin{bmatrix} \delta_a \\ \delta_r \\ \delta_t \end{bmatrix} \end{aligned}$$

4.3 Aircraft Model Linearization

Calculating these partial derivatives can be a time consuming task. By using MATLAB's Symbolic Math Toolbox a function was implemented to calculate a defined trim condition. Figure 4.6 gives the lateral and longitudinal poles for the decoupled linear \mathbf{A}_{long} and \mathbf{A}_{lat} matrices, as calculated for Trim Condition One, wings-level cruise flight in Table 4.1. These poles corresponded well to others in the literature, such as those given by Heffley et al. [3] for the Boeing 747 aircraft. In this trim calculation, the engine model was excluded, only connecting the thrust distribution model to the thrust forces and moments model in the differential equations, as in Section 3.4.2.2. Thus the delayed dynamics of the engine are ignored in this linear representation.

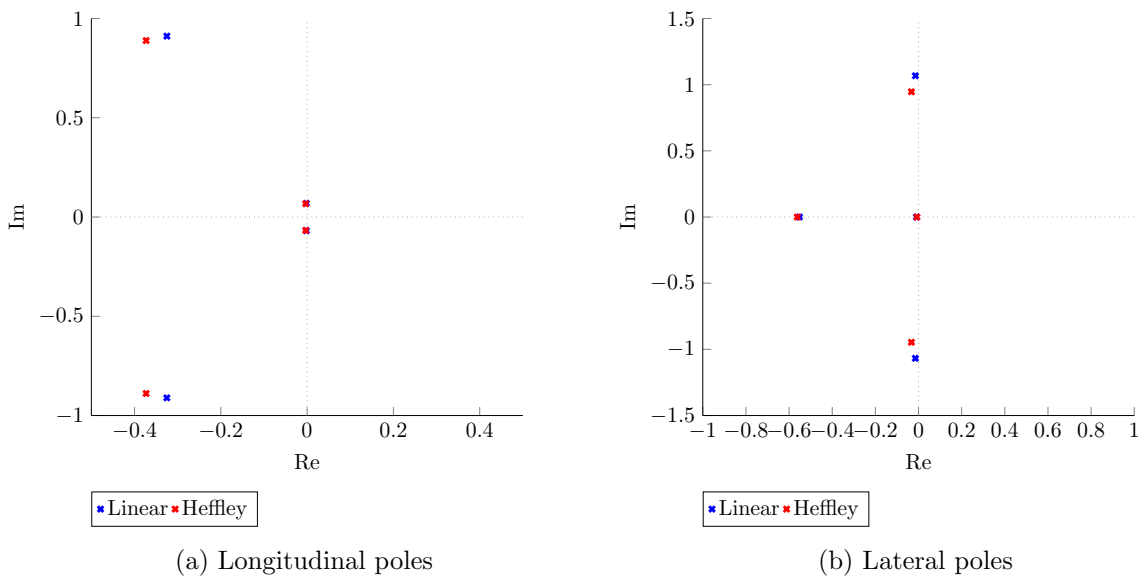


Figure 4.6: Boeing 747 aircraft poles as calculated and compared to Heffley data [3]

The calculated aircraft poles correspond to the five classic modes of fixed-wing aircraft motion, although the dynamics are very slow for a large aircraft such as the Boeing 747 [35, 38, 43]. The higher-frequency pole pair in the longitudinal dynamics is referred to as the short period mode. This mode describes the aircraft's tendency to realign itself with the velocity vector when disturbed in the longitudinal X, Z -plane. The low-frequency pole pair in Figure 4.6a represents the phugoid mode. This mode is a kinematic mode of motion and describes the aircraft's exchange between kinetic and potential energy observed when the aircraft is disturbed from trimmed flight longitudinally.

As for the lateral modes of motion, the higher-frequency real pole in Figure 4.6b is categorized as roll mode. This mode describes the roll rate dynamics of the aircraft. As the aircraft experiences a rolling moment, the roll rate will grow by the integral of the moment disturbance. The second lateral mode of motion is known as the Dutch roll mode. This mode is represented by the complex pole pair, and is often poorly naturally damped. This mode

4.3 Aircraft Model Linearization

describes the aircraft's tendency to realign with the velocity vector when disturbed laterally. The final mode of motion is the spiral mode. On some aircraft, this mode may be slightly unstable. The kinematic spiral mode describes the aircraft's natural ability to restore to wings-level flight or to diverge from it when laterally disturbed. In the case of the Boeing 747, the spiral mode is known to be stable.

To confirm that the linear state space systems correspond to the non-linear simulation model for the Boeing 747 in isolated flight as implemented in MATLAB Simulink, both systems are simulated and a small step command is applied to all the inputs individually. Figure 4.7 shows that the longitudinal linear system corresponds accurately to the non-linear simulation. The case is the same for the lateral system, shown in Figure 4.8.

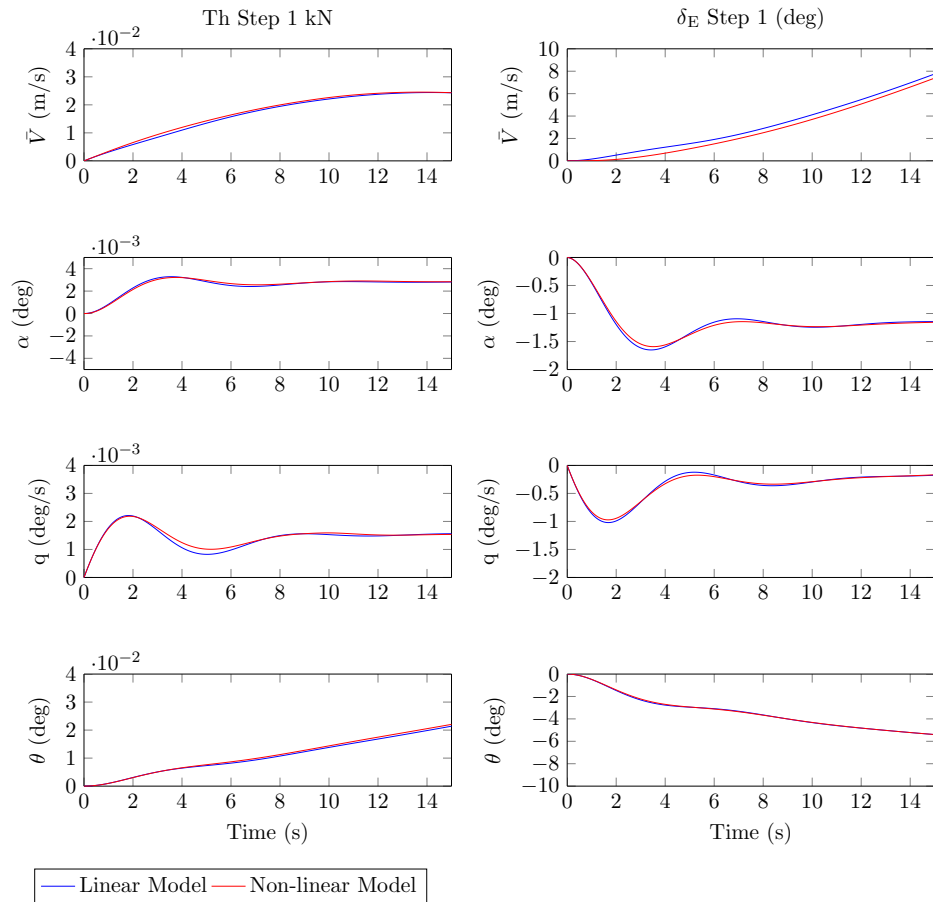


Figure 4.7: Linear versus non-linear system response for small control input step in the longitudinal system

In these simulations, the linear and non-linear systems match suspiciously well. This would not be the case in a real-world system, where all the aerodynamic coefficients are not known exactly. However, when the linear system is derived from all the mathematical

4.3 Aircraft Model Linearization

equations used to model the aircraft for simulation purposes, this exact matching can be explained. The small angle assumptions, ignored higher-order Taylor series expansion terms and other approximation assumptions are thus valid, and their combined contribution results in the small differences between the decoupled linear state space models and the full non-linear simulation model. The lateral and longitudinal state space models can now be used together with linear controller design theories to develop conventional aircraft controllers for the Boeing 747 simulation model.

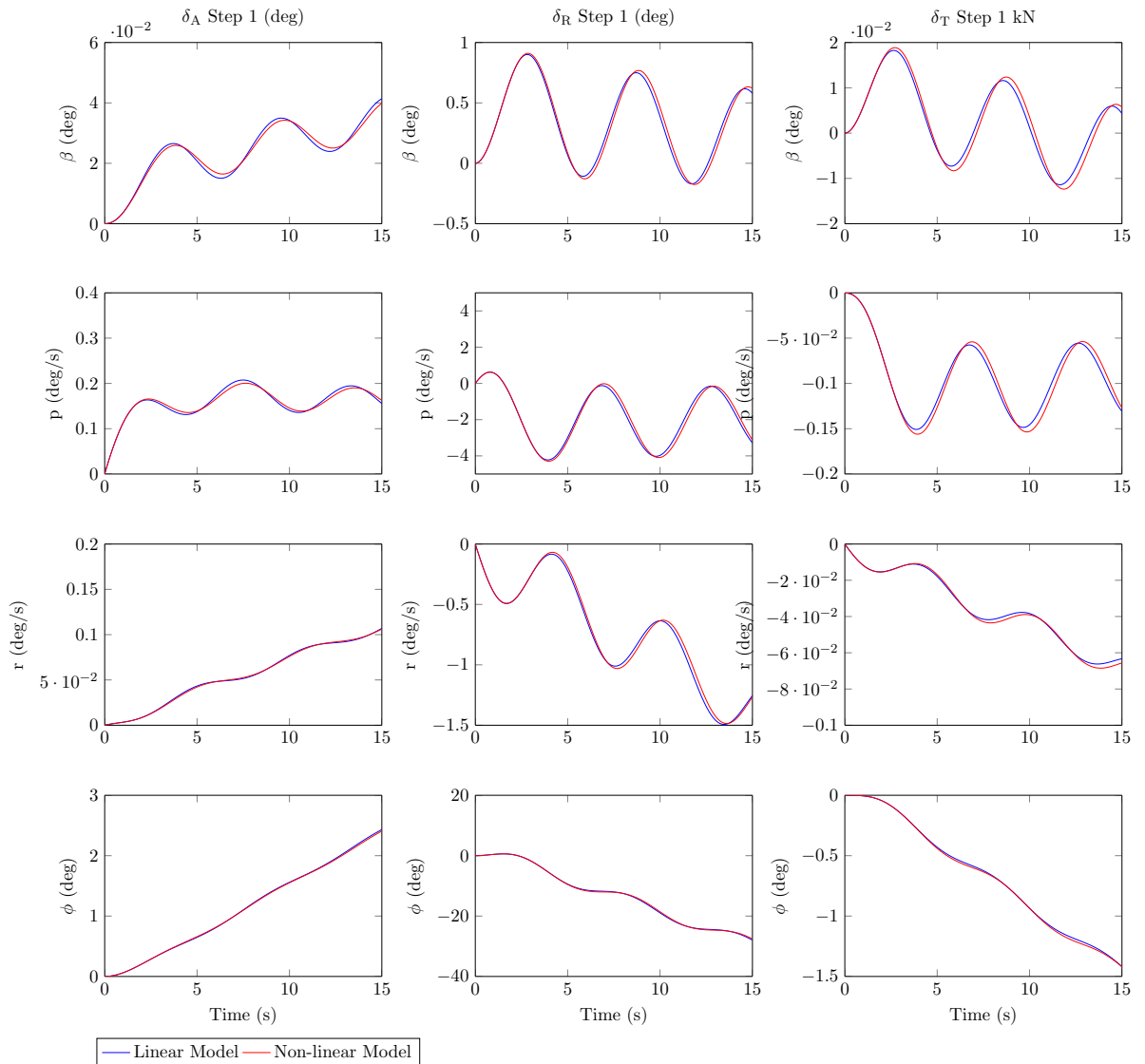


Figure 4.8: Linear versus nonlinear system response for small control input step in the lateral system

4.3.3 Linear Follower Aircraft in Formation

Formation flight introduces additional dynamics to the follower aircraft. In order to analyze the dynamics of formation flight through linear theory, these formation interaction dynamics

4.3 Aircraft Model Linearization

must be included in the linear model of the follower aircraft. In Section 3.8 it was observed that the lateral and vertical separations directly influence the forces and moments induced on the follower aircraft. For this reason, these two separation states should be included in the follower aircraft linear model. Equation 4.12 gives the vertical separation velocity ($\dot{\zeta}$) and lateral separation acceleration ($\ddot{\eta}$) state calculations that were used to linearize the follower model at a specified trim separation as derived by [14].

$$\begin{aligned}\dot{\zeta} &= -\frac{\bar{V}}{b} \sin(\theta - \alpha) \\ \ddot{\eta} &= \frac{\bar{V}}{b} \dot{\Psi} = \frac{\bar{V}}{b} (R \sec(\theta) \cos(\phi) + Q \sec(\theta) \sin(\phi))\end{aligned}\quad (4.12)$$

Expanding the longitudinal system to include the vertical separation velocity information gives Equation 4.13.

$$\begin{aligned}\Delta \dot{\mathbf{x}}_{long}^k &= \mathbf{A}_{long}^k \Delta \mathbf{x}_{long}^k + \mathbf{B}_{long}^k \Delta \mathbf{u}_{long}^k \\ \begin{bmatrix} \dot{v} \\ \dot{\alpha} \\ \dot{q} \\ \dot{\theta} \\ \dot{\zeta} \end{bmatrix} &= \begin{bmatrix} & & & & \frac{\partial \dot{V}}{\partial \zeta} \\ & \mathbf{A}_{long} & & & \frac{\partial \dot{\alpha}}{\partial \zeta} \\ & & & & \frac{\partial \dot{Q}}{\partial \zeta} \\ & & & & \frac{\partial \dot{\theta}}{\partial \zeta} \\ \frac{\partial \dot{\zeta}}{\partial V} & \frac{\partial \dot{\zeta}}{\partial \alpha} & \frac{\partial \dot{\zeta}}{\partial Q} & \frac{\partial \dot{\zeta}}{\partial \theta} & \frac{\partial \dot{\zeta}}{\partial \zeta} \end{bmatrix} \begin{bmatrix} v \\ \alpha \\ q \\ \theta \\ \zeta \end{bmatrix} + \begin{bmatrix} \frac{\partial \dot{V}}{\partial \delta_E} & \frac{\partial \dot{V}}{\partial T_h} \\ \frac{\partial \dot{\alpha}}{\partial \delta_E} & \frac{\partial \dot{\alpha}}{\partial T_h} \\ \frac{\partial \dot{Q}}{\partial \delta_E} & \frac{\partial \dot{Q}}{\partial T_h} \\ \frac{\partial \dot{\theta}}{\partial \delta_E} & \frac{\partial \dot{\theta}}{\partial T_h} \\ 0 & 0 \end{bmatrix} \begin{bmatrix} \delta_e \\ T_h \end{bmatrix}\end{aligned}\quad (4.13)$$

Expanding the lateral system to include the lateral separation acceleration and velocity information gives Equation 4.14.

$$\begin{aligned}\Delta \dot{\mathbf{x}}_{lat}^k &= \mathbf{A}_{lat}^k \Delta \mathbf{x}_{lat}^k + \mathbf{B}_{lat}^k \Delta \mathbf{u}_{lat}^k \\ \begin{bmatrix} \dot{\beta} \\ \dot{p} \\ \dot{r} \\ \dot{\phi} \\ \dot{\eta} \\ \dot{\eta} \end{bmatrix} &= \begin{bmatrix} & & & & \frac{\partial \dot{\beta}}{\partial \zeta} & \frac{\partial \dot{\beta}}{\partial \zeta} \\ & \mathbf{A}_{lat} & & & \frac{\partial \dot{p}}{\partial \zeta} & \frac{\partial \dot{p}}{\partial \zeta} \\ & & & & \frac{\partial \dot{r}}{\partial \zeta} & \frac{\partial \dot{r}}{\partial \zeta} \\ & & & & \frac{\partial \dot{\phi}}{\partial \zeta} & \frac{\partial \dot{\phi}}{\partial \zeta} \\ \frac{\partial \dot{\zeta}}{\partial \beta} & \frac{\partial \dot{\zeta}}{\partial P} & \frac{\partial \dot{\zeta}}{\partial R} & \frac{\partial \dot{\zeta}}{\partial \phi} & \frac{\partial \dot{\zeta}}{\partial \zeta} & \frac{\partial \dot{\zeta}}{\partial \zeta} \\ 0 & 0 & 0 & 0 & 1 & 0 \end{bmatrix} \begin{bmatrix} \beta \\ p \\ r \\ \phi \\ \eta \\ \eta \end{bmatrix} + \begin{bmatrix} \frac{\partial \dot{\beta}}{\partial \delta_A} & \frac{\partial \dot{\beta}}{\partial \delta_R} & \frac{\partial \dot{\beta}}{\partial \delta_T} \\ \frac{\partial \dot{p}}{\partial \delta_A} & \frac{\partial \dot{p}}{\partial \delta_R} & \frac{\partial \dot{p}}{\partial \delta_T} \\ \frac{\partial \dot{r}}{\partial \delta_A} & \frac{\partial \dot{r}}{\partial \delta_R} & \frac{\partial \dot{r}}{\partial \delta_T} \\ \frac{\partial \dot{\phi}}{\partial \delta_A} & \frac{\partial \dot{\phi}}{\partial \delta_R} & \frac{\partial \dot{\phi}}{\partial \delta_T} \\ 0 & 0 & 0 \\ 0 & 0 & 0 \end{bmatrix} \begin{bmatrix} \delta_a \\ \delta_r \\ \delta_t \end{bmatrix}\end{aligned}\quad (4.14)$$

The highly non-linear wake can be characterized by defining several trim conditions and linearizing the follower aircraft about these trim conditions. It was observed from Figures 3.10 and 3.11 that the most fuel-efficient static separation (minimum drag and maximum lift) is at $\eta = 0.78$ and $\zeta = 0$. However, as discussed in Section 3.8.2, the most economical location

4.3 Aircraft Model Linearization

for the current wake model is defined at $\eta = 1$ and $\zeta = 0$, due to inner wake model limitations.

For the first follower linear analysis, the trim condition is selected for separations from $\eta = 1.4$ to $\eta = 1$ in lateral, with vertical constant at $\zeta = 0$. Figure 4.9 gives the linearized follower aircraft's pole movement in the wake with the follower at these trim separations. Pole movement with regard to variation in lateral separation, moving from blue to red as the follower moves from $\eta = 1.4$ to $\eta = 1$, is presented. From this analysis, it can be derived, that in formation, the lateral spiral mode breaks into three poles, expanding from its isolated location into three opposing directions as the aircraft becomes unstable, moving deeper into the wake. The rolling moment of the wake turns the aircraft into a bank, and it spirals out of the wake. This is termed the wake-roll mode, as the effect is caused by the wake inducing a rolling moment on the follower. This outward spiral moves the aircraft to isolation, and the three poles move back to the original location of the isolated aircraft's spiral mode. The Dutch roll mode poles also become unstable as the follower moves deep into the wake. While the longitudinal poles remain almost constant and stable for changes in lateral separation.

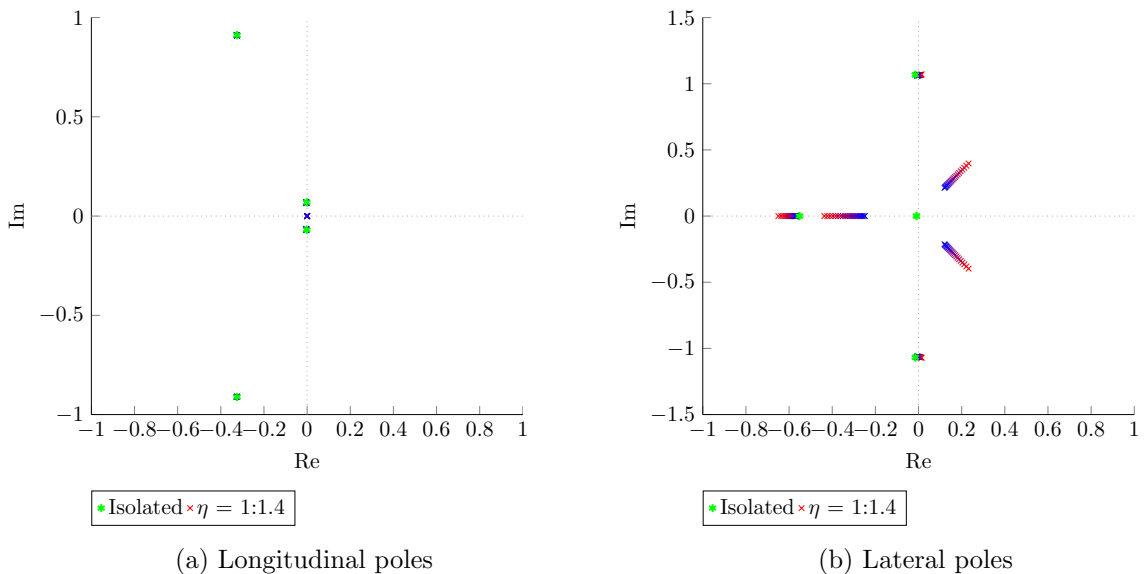


Figure 4.9: Pole movement over lateral separation with the follower at $\zeta = 0$ and $\eta = 1$ to 1.4, where red represents $\eta = 1$ and blue represents $\eta = 1.4$

The same analysis was conducted for trim conditions, which change in vertical separation while keeping the lateral separation constant. For this analysis, the follower's vertical separation is considered from $\zeta = -0.2$ to 0.2, with a constant lateral separation at $\eta = 1$. In these graphs, the poles move from red to orange to blue as the aircraft moves from $\zeta = -0.2$ to 0.2. In Figure 4.10b the wake-roll mode is observed again in the lateral poles as the follower moves over the region with maximum rolling moment at $\zeta = 0$. The longitudinal poles also become unstable as the aircraft moves vertically and crosses the optimum location.

4.3 Aircraft Model Linearization

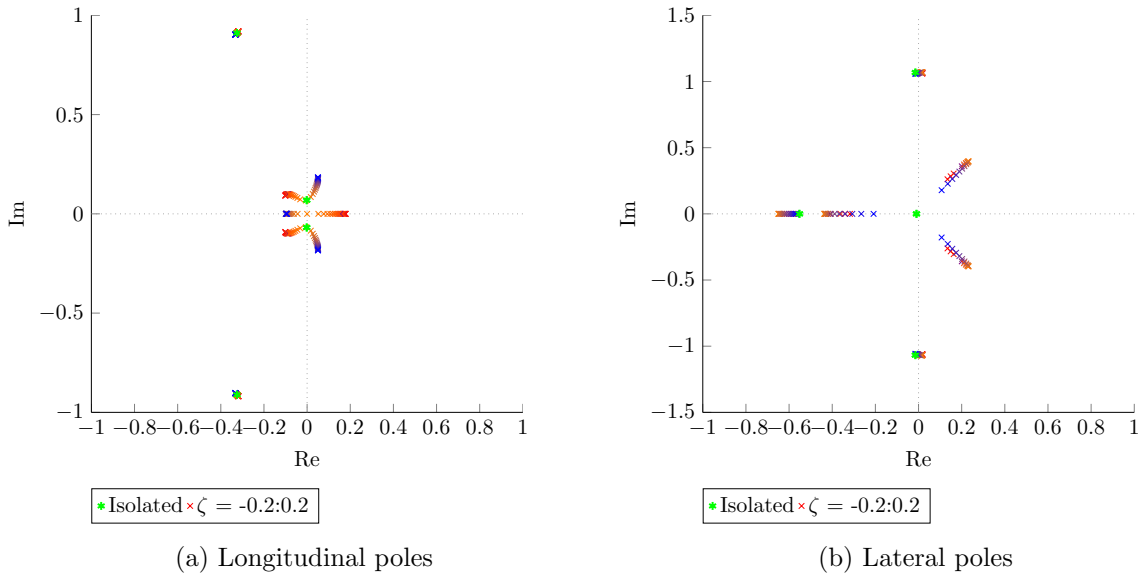


Figure 4.10: Pole movement over vertical separation with the follower at $\eta = 1$ and $\zeta = -0.2$ to 0.2 , where red represents $\zeta = -0.2$ and blue represents $\zeta = 0.2$

In order to validate the linear model presented in this section, a linear and non-linear model comparison was simulated. The results given in Figure 4.11 and 4.12 show that the linear and non-linear model closely matched in system states for a small step control input. Notice that the linear model starts to diverge significantly from the non-linear model after approximately 10 seconds. This is expected due to the highly non-linear nature of the wake, since the model diverges from the trim separation.

4.3 Aircraft Model Linearization

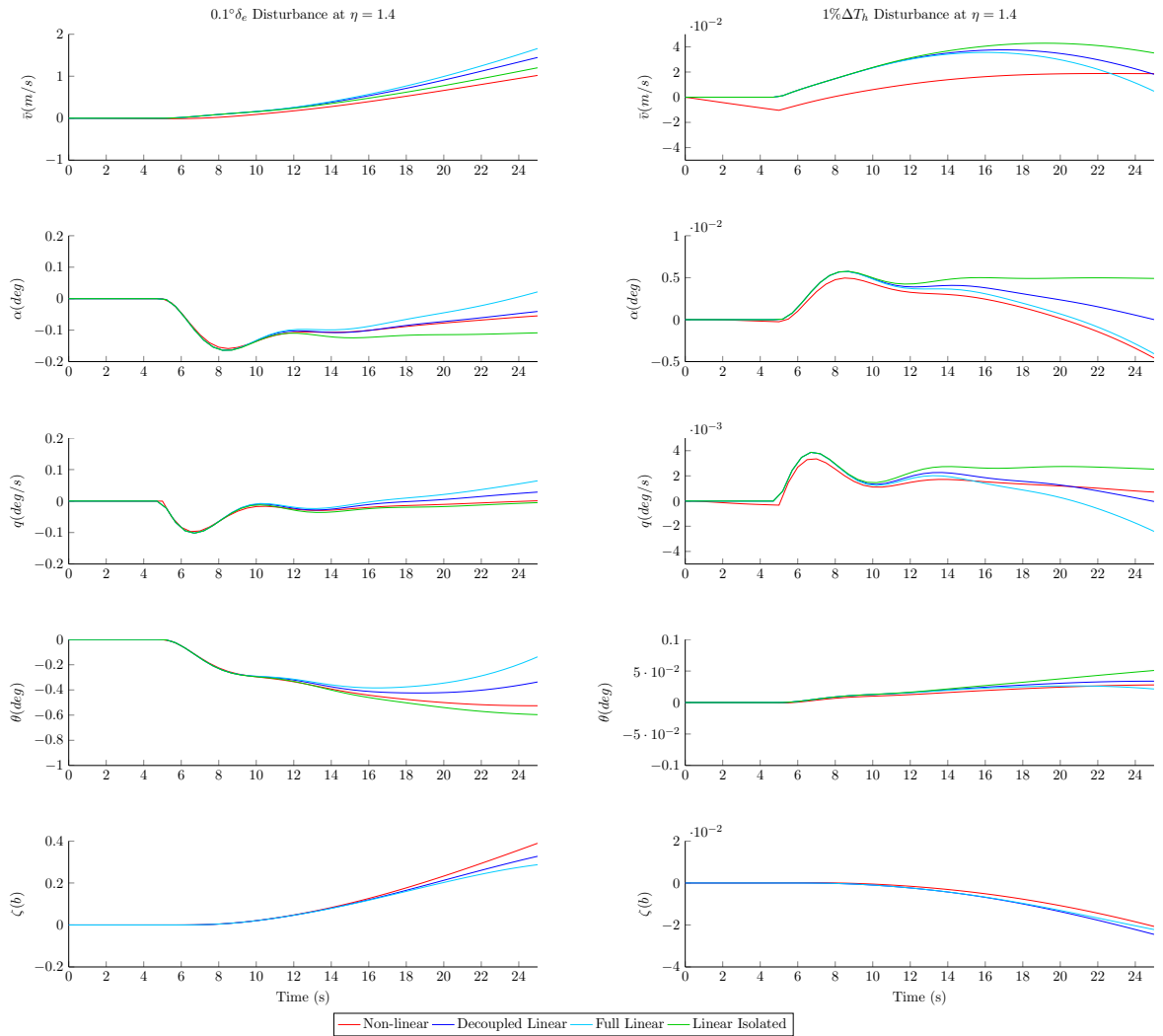


Figure 4.11: Longitudinal linear vs. non-linear model states for small step input

In order to investigate the coupling between the lateral and longitudinal dynamics in the wake, a full state linear model with $\mathbf{A}_{11 \times 11}$ was derived, which assumed that the coupling between the lateral and longitudinal states is not zero. The simulated results are presented in Figure 4.11 and 4.12 by the light blue line. From these figures, it can be concluded that the decoupling assumption of the lateral and longitudinal linear model holds valid for the follower in the wake, as the difference between the full order model and decoupled models is minimal for the first few seconds of the simulation. These derived linear models can thus be used in conjunction with linear theory to design and analyze the control stability of the follower aircraft in the wake.

4.4 Trim and Linearization Conclusion

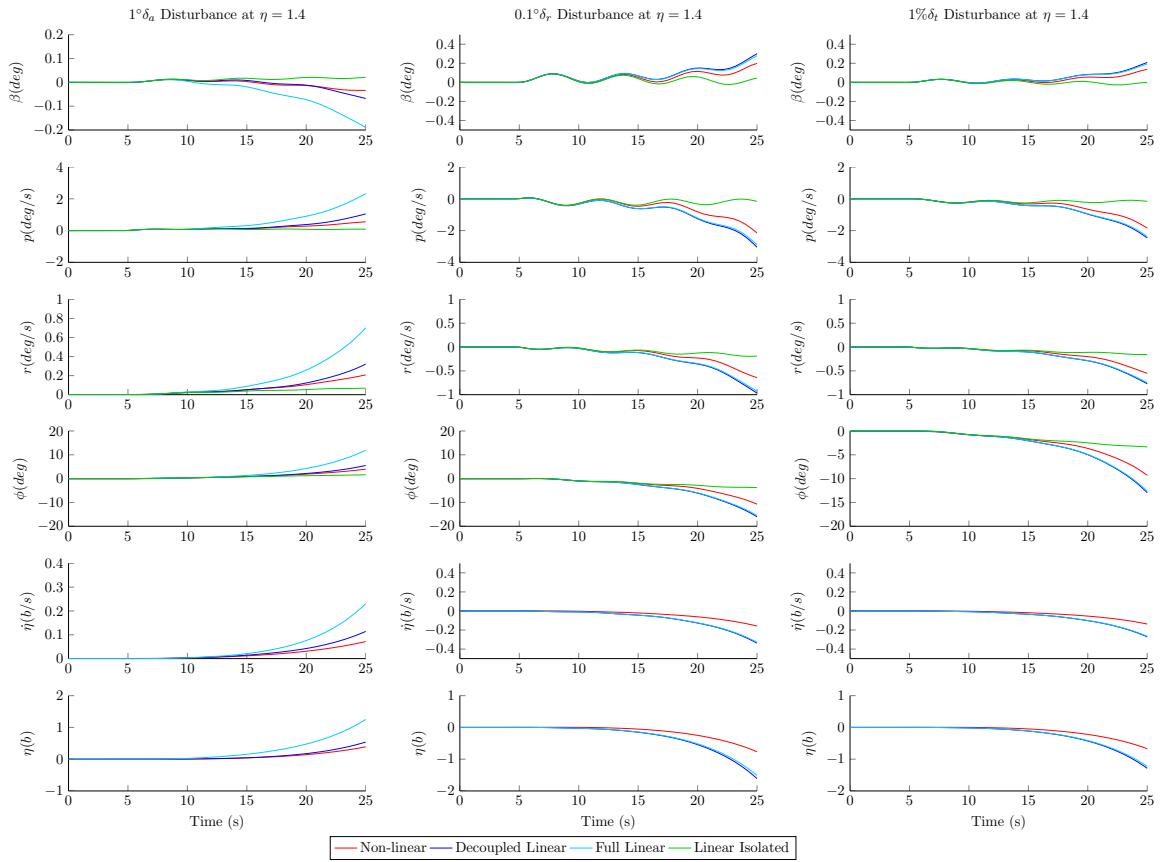


Figure 4.12: Lateral linear vs. non-linear model states for small step input

4.4 Trim and Linearization Conclusion

In this chapter, the trim conditions were calculated for the Boeing 747 in isolated flight. This trim was then used to derive a linear model for the aircraft, which was shown to be an accurate representation of the non-linear simulation model discussed in Chapter 3. A trim analysis was also conducted for the follower aircraft in the wake, and different trim configurations were explored. It was found that by inducing sideslip, the rolling moment of the wake could be countered, which can be applied to reduce aileron demand on the follower in the wake. The use of differential thrust in steady-state was investigated and proved to hold advantages for trim flight, as aileron and rudder demand could be reduced while also decreasing the degree of sideslip required when trimming in the wake for high levels of differential thrust. Finally, linear models were derived for the follower and these represented the non-linear simulation model with sufficient accuracy, useful for linear control design and analysis. With trim defined for both the leader and follower aircraft and the representative linear models in place, the flight controller designs followed.

Chapter 5

Conventional Flight Aircraft Controllers

A classic aircraft control approach was followed to control both aircraft in right echelon formation. With the longitudinal and lateral dynamics decoupled, as discussed in Chapter 4, the design process for the longitudinal and lateral flight controllers could also be separated. The elevator and thrust could be applied by the longitudinal controllers to fly the aircraft at the reference altitude and airspeed, thus controlling the aircraft in both the vertical and longitudinal directions. The lateral controller utilizes aileron and rudder control surfaces to maintain the desired cross-track separation or flight path in the lateral direction. For the inner-loop control, fly-by-wire techniques were followed to represent the conventional pilot control inputs to some extent. The outer-loop controllers represent conventional autopilot systems such as airspeed, altitude and cross-track control systems.

In the following chapter, the control design and isolated flight implementation for the decoupled longitudinal and lateral systems will be presented. This serves as the first step towards formation flight control, as these controllers were utilized on the leader and follower aircraft.

5.1 Longitudinal Control

In Section 4.1.1, the trim condition was defined and calculated, followed by the linearization of the Boeing 747 model in Section 4.3.2. The linear longitudinal model presented in Equation 4.11 could now be used to develop controllers in the X, Z -plane, as the dynamics in the axial and vertical direction are closely coupled. The longitudinal model was used to design the altitude and airspeed controllers. This section gives an in-depth look at the design process, controller specification and closed-loop response for and leading up to altitude and

airspeed control.

Figure 5.1 presents the four control stages through which the aircraft model is tuned to produce the desired dynamic response for altitude and airspeed commands. The first inner-loop controller is the pitch rate damper and normal acceleration control in combination, referred to as the DQ control law. This controller is representative of a pilot's forward or backward control stick command. The pitch rate damper is used to move the short-period poles to increase system damping. Together with this, the normal acceleration control is included to form the DQ control law. These principles of these controllers were derived in collaboration with Evert Trollip.

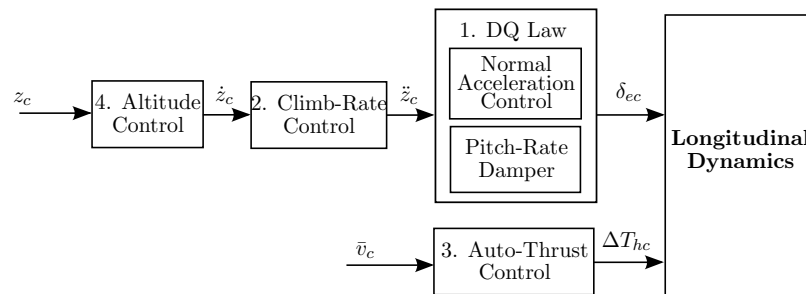


Figure 5.1: Aircraft longitudinal control diagram for isolated flight

The second longitudinal controller shown in Figure 5.1 governs climb rate control by commanding normal acceleration to the DQ controller. The third controller, auto-thrust control, is responsible for maintaining a specified airspeed by utilizing engine thrust. In the design procedure, the climb rate control is followed by the auto-thrust controller. This design choice was made because the climb rate and auto-thrust are closely coupled in the model dynamics. This coupling exists since the aircraft speed is proportional to the rate of altitude increase or decrease, and thus effective performance tracking in the climb rate can only be achieved once the auto-thrust control is in place. Finally, the altitude control regulates the climb rate to guide the aircraft to the desired altitude level. In the following subsection the design, controller specifications and closed-loop results for these controllers will be discussed.

5.1.1 DQ Control: Pitch Rate Damper and Normal Acceleration Control

The DQ control law performs the tasks of pitch rate damping and normal acceleration control. This inner-loop control directly commands the elevator and thrust control input. The elevator deflects airflow around the aircraft tailplane and can thus increase or decrease the aerodynamics pressure on the tail of the aircraft, effectively rotating the aircraft about the center of pressure in the X, Z -plane. A down-force action on the tail, induced by the elevators, can increase the aircraft's angle of attack, resulting in a lift gain and aircraft climb. On

5.1 Longitudinal Control

the contrary, if the elevator increases lift on the tail, the aircraft nose is pushed down and the angle of attack decreases, causing a loss in overall lift and a loss of altitude. As for the thrust, the force vector dominantly acts in the axial direction and is best used to increase or decrease the aircraft airspeed.

In this section, the linear longitudinal model of the Boeing 747 will be used, which utilizes both elevator and thrust control authority. The DQ controller design, specification and closed-loop simulation results will follow as designed for the aircraft in isolated flight.

5.1.1.1 DQ Control: Design

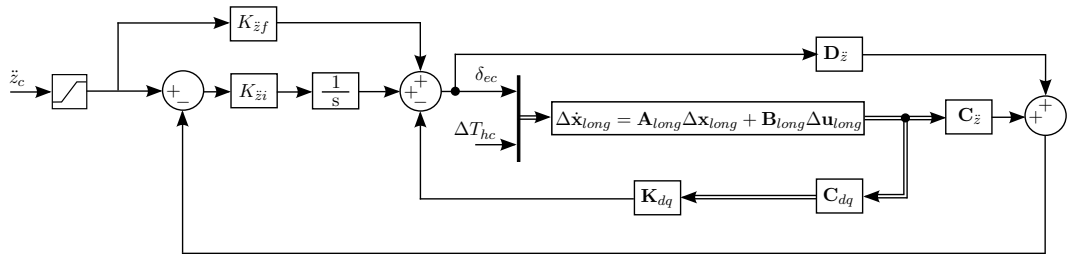


Figure 5.2: DQ law: pitch rate damper and normal acceleration control diagram

For the DQ control law design, given by Figure 5.2, a pole placement design method was used. In the longitudinal dynamics, the initial response is dominated by the higher-frequency poles or short-period mode, as discussed in Section 4.3.2. For the pitch rate damper design, a reduced-order approach was followed, where the phugoid poles were omitted to simplify pole placement design. Thus, the state feedback DQ output matrix (\mathbf{C}_{dq}) extracts only the angle of attack (α) and pitch rate (q), as shown in Equation 5.1.

The normal acceleration output matrix ($\mathbf{C}_{\ddot{z}}$) was determined by linearizing the aircraft model about the normal acceleration state for the calculated trim condition. The partial derivative terms were calculated using MATLAB's Symbolic Math Toolbox. It was also determined that feed-forward does exist between elevator input and normal acceleration output. Some feed-forward from thrust input to normal acceleration output was also detected, but was found to be negligibly small. The elevator to normal acceleration feed-forward term ($D_{\ddot{z}}$) was included in the normal acceleration output. The control input (\ddot{z}_c) was saturated to protect against normal accelerations exceeding normal flight levels.

For the diagram in Figure 5.2, the additional linear state space model matrices were

defined:

$$\mathbf{C}_{dq} = \begin{bmatrix} 0 & 0 & 0 & 0 \\ 0 & 1 & 0 & 0 \\ 0 & 0 & 1 & 0 \\ 0 & 0 & 0 & 0 \end{bmatrix} \quad \mathbf{C}_{\ddot{z}} = \begin{bmatrix} \frac{\partial \ddot{z}}{\partial \bar{V}} & \frac{\partial \ddot{z}}{\partial \alpha} & \frac{\partial \ddot{z}}{\partial Q} & \frac{\partial \ddot{z}}{\partial \Theta} \end{bmatrix} \quad \mathbf{K}_{dq} = [0 \quad K_\alpha \quad K_q \quad 0]$$

$$\mathbf{B}_{long:\delta_E} = \begin{bmatrix} \frac{\partial \bar{V}}{\partial \delta_E} & \frac{\partial \alpha}{\partial \delta_E} & \frac{\partial Q}{\partial \delta_E} & \frac{\partial \Theta}{\partial \delta_E} \end{bmatrix}^T \quad D_{\ddot{z}} = \begin{bmatrix} \frac{\partial \ddot{z}}{\partial \delta_E} \end{bmatrix} \quad (5.1)$$

Furthermore, the system was augmented with an integral error state to ensure zero steady-state error tracking of the normal acceleration. This augments the longitudinal state space system with a normal acceleration error state. For the pole placement design, this normal acceleration error state (x_{dqi}) pole was placed close to the origin, with the integral error state defined as:

$$\dot{x}_{dqi} = \ddot{z}_c - (\mathbf{C}_{\ddot{z}} \Delta \mathbf{x}_{long} + D_{\ddot{z}} \delta_e) \quad (5.2)$$

However, adding the integral error state produces unwanted integral dynamics, such as an increased system settling time. To reduce the dominance of these dynamics, pole-zero cancellation was used. The feed-forward gain ($K_{\ddot{z}f}$) was introduced and calculated to place a zero close to the error state integrator pole (p_i). This speeds up the system response, as it reduces the effect of the integrator pole. Through block diagram algebra it was determined that the feed-forward gain should be the ratio between the integral state feedback gain and the selected integral error state pole:

$$K_{\ddot{z}f} = \frac{K_{\ddot{z}i}}{p_i} \quad (5.3)$$

With the integral error state augmented to the state space system model, the open-loop system could be represented by:

$$\begin{bmatrix} \Delta \dot{\mathbf{x}}_{long} \\ \dot{x}_{dqi} \end{bmatrix} = \begin{bmatrix} \mathbf{A}_{long} & \mathbf{0}_{4 \times 1} \\ -\mathbf{C}_{\ddot{z}} & 0 \end{bmatrix} \begin{bmatrix} \Delta \mathbf{x}_{long} \\ x_{dqi} \end{bmatrix} + \begin{bmatrix} \mathbf{B}_{long:\delta_E} \\ -D_{\ddot{z}} \end{bmatrix} \delta_e$$

$$\ddot{z} = \mathbf{C}_{\ddot{z}} \begin{bmatrix} \Delta \mathbf{x}_{long} \\ x_{dqi} \end{bmatrix} \quad (5.4)$$

As this controller only commands the elevator as control input, the DQ control law was defined as:

$$\delta_{ec} = - [\mathbf{K}_{dq} \quad K_{\ddot{z}i}] \begin{bmatrix} \Delta \mathbf{x}_{long} \\ x_{dqi} \end{bmatrix} + K_{\ddot{z}f} \ddot{z}_c \quad (5.5)$$

5.1.1.2 DQ Control: Specifications and Closed-Loop Response

The Boeing 747 model, as described in Section 4.1.1, has a natural short-period mode with a low damping ratio of 0.34. This low damping in the short-period creates an oscillatory response in the initial longitudinal dynamics, as seen in Figure 4.7. The purpose of the

DQ controller is to increase the damping of the short-period mode and to follow a reference normal acceleration command input. For the DQ control design, as given in Section 5.1.1.1 MATLAB's `place.m` function was used to determine the feedback gains. To simplify the pole placement selection, the longitudinal system was reduced to only angle of attack and pitch rate feedback, which are the dominant states in the short-period mode. By reducing the system, only a single pole pair and the integrator pole had to be selected.

Since current short-period mode poles give a natural frequency of 0.96 rad/s and a damping ratio of 0.34, it was decided to keep the natural frequency close to 1 rad/s and increase the damping to 0.9. This selection is in the range for the short-period mode as specified in MIN-STD-1797A [43] for the dynamic requirements of Category A aircraft. This standard specifies short-period damping between 0.35 and 1.3, and a natural frequency between 0.28 and 3.6. Furthermore, the normal acceleration integrator pole was placed close to the origin at -0.125, but not too close to the phugoid mode. Table 5.1 summarizes the DQ control law design with the design-specific choices in bold.

Longitudinal System	Mode	Poles	ω_n	ζ
Open-Loop	Short-Period	$-0.325 \pm 0.911i$	0.967	0.336
DQ Design Closed-Loop	Short-Period	$-0.899 \pm 0.442i$	1.00	0.9
DQ Integrator Placement		-0.125		

Table 5.1: Longitudinal system DQ controller design specification

Figure 5.3 shows the difference in pole locations between the open-loop longitudinal poles for the Boeing 747 and the closed-loop DQ system poles. Note the extra pole added in the closed-loop system due to the augmentation of the normal acceleration integral control.

5.1 Longitudinal Control

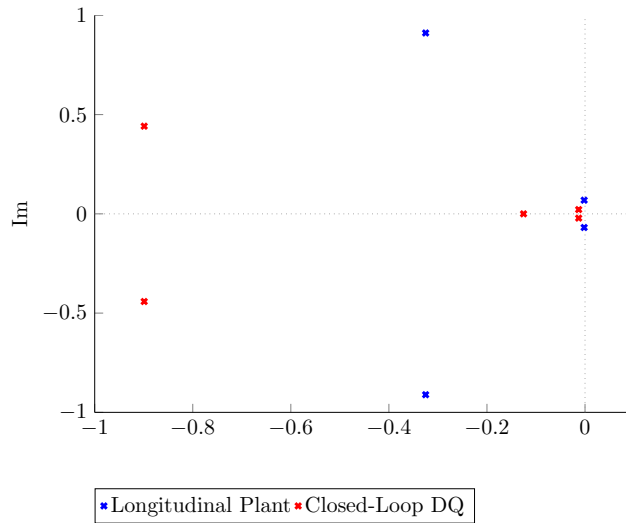
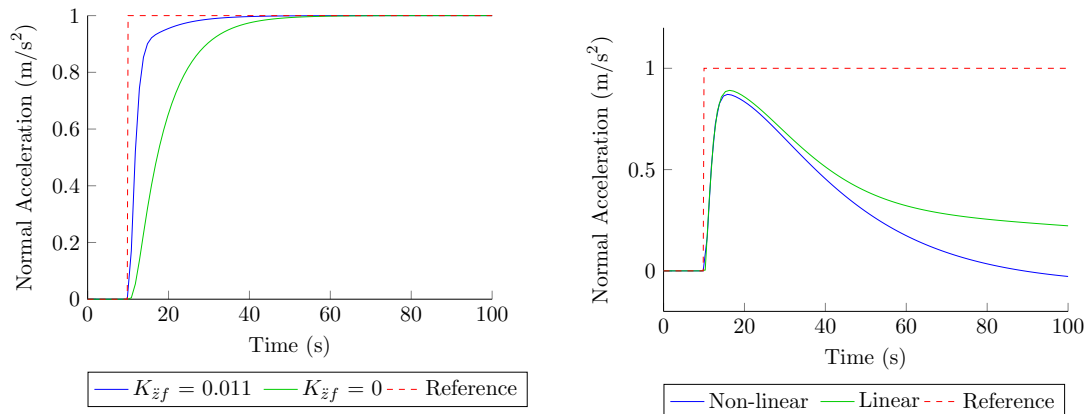


Figure 5.3: Longitudinal dynamics plant and closed-loop DQ controller poles

The simulation for the DQ controller produced the desired response, with the feed-forward action speeding up the normal acceleration response, while the integrator introduced zero steady-state tracking. Figure 5.4a gives the DQ controller's reduced-order normal acceleration response, with the feed-forward gain (K_{zf}) either omitted or included to demonstrate its effect. Reduced-order here means that the airspeed (\bar{v}) and pitch angle (θ) states have been omitted from this linear model simulation, as mentioned in the control design, where \mathbf{C}_{dq} feeds back only the angle of attack (α) and pitch rate (q) states. Figure 5.4a shows the system response without the phugoid mode influencing the lower-frequency response.



(a) Reduced-order feed-forward vs. non-feed-forward

(b) Longitudinal linear vs. non-linear

Figure 5.4: DQ controller normal acceleration unit step response

The phugoid mode effects the system response of the longitudinal linear model, which includes all four longitudinal states and the integrator error state. As a result, the normal acceleration does not follow the commanded unit step reference in steady state for both the

linear and non-linear simulation. Figure 5.4b shows the normal acceleration response for the linear longitudinal and non-linear aircraft simulation.

Figure 5.5 shows the DQ controller damping the short-period oscillations, and the aircraft reducing its angle of attack to produce a normal acceleration towards the ground. Thus, the DQ controller has been effective in applying a fast response normal acceleration, and damping the short-period mode oscillations.

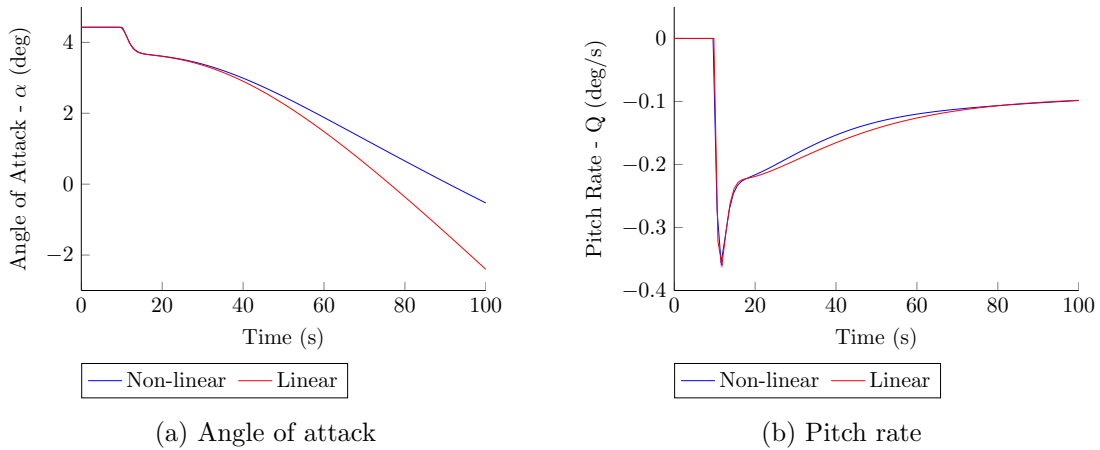


Figure 5.5: DQ controller longitudinal linear vs. non-linear aircraft for unit step normal acceleration command

Since the DQ controller commands the elevator control surface, this control input is primarily responsible for regulating normal accelerations on the aircraft. Figure 5.6 shows the elevator actuator response for the same unit step command in normal acceleration. Notice how the elevator keeps increasing as the controller tries to maintain this large constant acceleration on the aircraft.

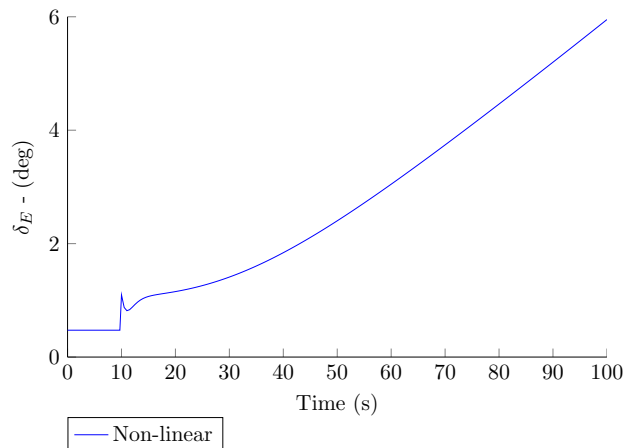


Figure 5.6: DQ controller elevator actuator response for unit step normal acceleration command.

The normal acceleration controller suffers to maintain a constant normal acceleration without airspeed regulation in place. In the sections to follow climb rate and airspeed control will be designed and implemented to support the normal acceleration control towards altitude regulation.

5.1.2 Climb Rate Control

With a normal acceleration controller in place, as given by the DQ controller in Section 5.1.1, climb rate control can be achieved by commanding a normal acceleration. Climb rate refers to the rate at which the aircraft gains or reduces altitude. This can be achieved by regulating normal acceleration, which in turn regulates angle of attack by deflecting the elevator. However, due to the close coupling between climb rate and airspeed, both controllers are active when testing the model simulation response. In the design approach, the two controllers are designed and tested separately.

5.1.2.1 Climb Rate Control: Design

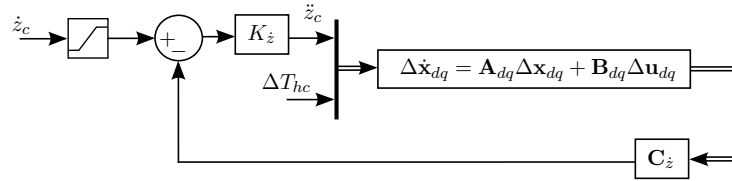


Figure 5.7: Climb Rate control diagram

In this design simple, proportional control was used to achieve a given climb rate, where root locus methods were applied to determine the feedback gain ($K_{\dot{z}}$). Figure 5.7 gives the design diagram for the climb rate controller. The climb rate is approximated with small angle assumptions calculated by:

$$\dot{z} = \bar{V} \sin(\Theta - \alpha) \approx \bar{V}(\Theta - \alpha) \quad (5.6)$$

The the inner-loop state space matrices in Figure 5.7 are defined as:

$$\begin{aligned} \Delta \mathbf{x}_{dq} &= \begin{bmatrix} \Delta \mathbf{x}_{long} \\ x_{dq_i} \end{bmatrix} & \Delta \mathbf{u}_{dq} &= \begin{bmatrix} \ddot{z}_c \\ \Delta T_{hc} \end{bmatrix} \\ \mathbf{A}_{dq} &= \begin{bmatrix} \mathbf{A}_{long} & \mathbf{0}_{4 \times 1} \\ -\mathbf{C}_{\dot{z}} & 0 \end{bmatrix} - \begin{bmatrix} \mathbf{B}_{long:\delta_E} \\ -D_{\dot{z}} \end{bmatrix} \begin{bmatrix} \mathbf{K}_{dq} & K_{\dot{z}i} \end{bmatrix} & \mathbf{B}_{dq} &= \begin{bmatrix} \mathbf{B}_{long:\delta_E} K_{\dot{z}f} & \mathbf{B}_{long:T_h} \\ -D_{\dot{z}} + 1 & 0 \end{bmatrix} \\ \mathbf{C}_{\dot{z}} &= [0 \quad \bar{V} \quad 0 \quad -\bar{V} \quad 0] \end{aligned} \quad (5.7)$$

With the climb rate system matrices defined, the climb rate controller state space model can be given by:

$$\begin{aligned} \Delta \dot{\mathbf{x}}_{dq} &= \mathbf{A}_{dq} \Delta \mathbf{x}_{dq} + \mathbf{B}_{dq:\delta_E} \delta_{ec} \\ \dot{z} &= \mathbf{C}_{\dot{z}} \Delta \mathbf{x}_{dq} \end{aligned} \quad (5.8)$$

The DQ control law was defined as:

$$\ddot{z}_c = K_z(\dot{z}_c - C_z \Delta \mathbf{x}_{dq}) = K_z(\dot{z}_c - \dot{z}) \quad (5.9)$$

5.1.2.2 Climb Rate Control: Specifications and Closed-Loop Response

The climb rate control consists of a simple proportional (P) feedback controller. The control gain (K_z) was determined using MATLAB's root locus tool and adjusted to provide a second-order response with a damping ratio of 1.22. This high damping limited the overshoot to less than 5%. The gain was selected to produce the fastest possible response time while limiting the overshoot as much as possible. A 5% settling time of about 15 seconds was achieved. Figure 5.8a give the closed-loop DQ system poles as the open-loop to the climb rate controller in blue, and the closed-loop climb rate controller poles in red. Note the stable, over-damped nature of the closed-loop poles.

Simulating the climb rate controller on both the linear and non-linear simulation yields a similar dynamic responses for both systems. Figure 5.8b gives the climb rate response for a unit step command in climb rate. Thus effective climb rate control was achieved with zero steady state tracking as the aircraft follows the exact normal acceleration required due to the integrator in the inner-loop DQ control. However to maintain the zero error steady-state tracking, airspeed control support was required due to the strong coupling between the vertical and longitudinal dynamics. For this reason, the airspeed controller, as presented in the next section was active for this simulation.

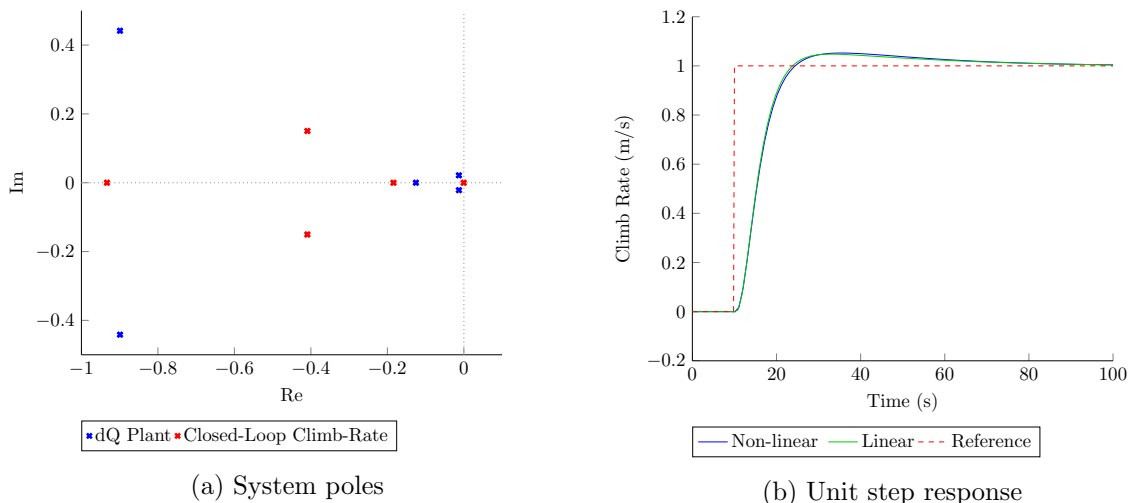


Figure 5.8: Climb rate proportional (P) controller: a) system open-loop and closed-loop poles and b) unit step response for climb rate

To regulate the climb rate to a reference command, elevator and thrust control actuation is required. Although the climb rate controller only regulates the DQ or acceleration controller,

the airspeed controller was active for this simulation to assist the climb rate controller to regulate the system dynamics. Figure 5.9a gives the elevator actuator response for a unit step in climb rate, and Figure 5.9b shows the supporting thrust response to help regulate the airspeed required to maintain the drop in altitude. The next section presents the auto-thrust or airspeed controller in detail.

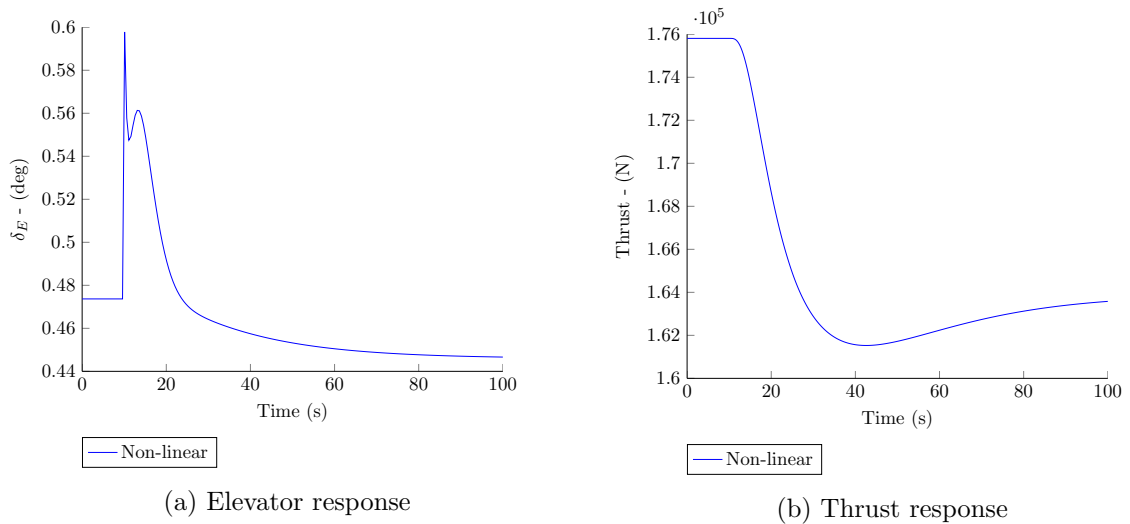


Figure 5.9: Climb rate proportional (P) controller: a) elevator actuator response and b) thrust response for a unit step response in climb rate

5.1.3 Auto-Thrust Control

To control aircraft airspeed, a thrust command is regulated to provide the level of forward force required to achieve a given trim airspeed. As the airspeed couples strongly with the vertical dynamics, the climb rate and airspeed control are both active when testing the design response.

Figure 5.10a illustrates the forces present when controlling airspeed by thrust. As thrust is applied, the dominant force acts in the positive X direction and the aircraft is accelerated forward, resulting in an increase in airspeed until a new equilibrium is reached. This is because the parasitic drag increases with an increase in airspeed. When some thrust is relieved, less force acts on the aircraft in the X direction, and the airspeed reduces and settles at a lower speed. This lower speed will be the equilibrium point where the forward reduced thrust force cancels the total drag force and no acceleration takes place, thus the aircraft settles at a lower trim speed. However, the relationship between drag and airspeed is non-linear. Figure 5.10b demonstrates how the induced drag decreases with an increase in airspeed. This occurs because more speed equals a lower angle of attack required to induce the same lift, resulting

5.1 Longitudinal Control

in the lowered induced drag. On the other hand, the parasitic drag increases as the airspeed increases, and thus the complex relationship between the total drag and airspeed exists.

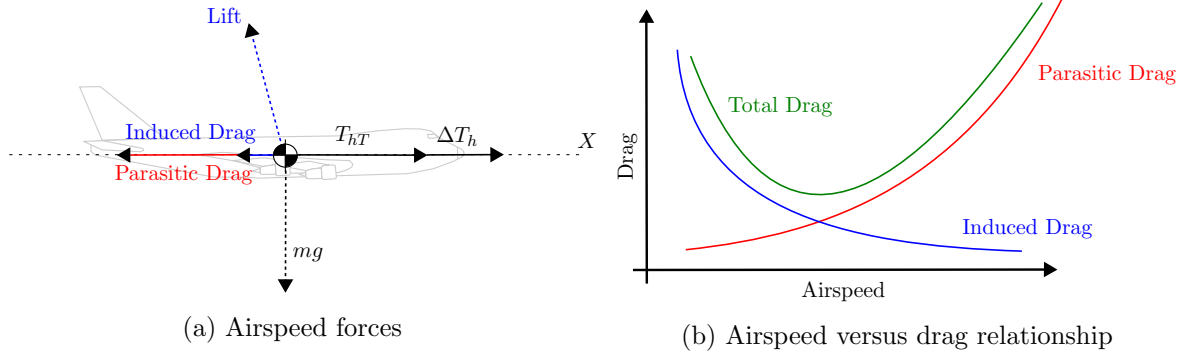


Figure 5.10: Airspeed control concept

In this section, an auto-thrust controller will be proposed which regulates thrust command to follow a reference airspeed. The auto-thrust design, specifications and simulation follow.

5.1.3.1 Auto-Thrust Control: Design

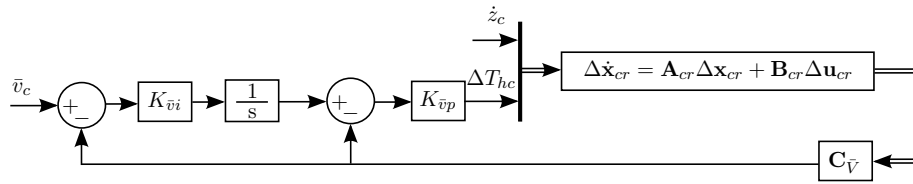


Figure 5.11: Aircraft auto-thrust control diagram

The auto-thrust controller, as proposed in Figure 5.11, consists of an airspeed state feedback to a proportional integral controller applying engine thrust. Note that the proportional and integral control schema are applied in series. This proved effective in the root locus design process that was followed. By first closing the proportional loop, the climb rate closed-loop pole near the origin is shifted away before the integral pole is introduced to the design process. If the proportional gain loop is omitted, two real poles are placed very close to the origin. This causes the root locus to branch out into two complex poles, which can be hard to damp, resulting in very low gains and a slow airspeed response.

The plant matrices for the auto-thrust controller diagram in Figure 5.11 are defined as:

$$\begin{aligned}
 \Delta \mathbf{x}_{cr} &= \begin{bmatrix} \Delta \mathbf{x}_{long} \\ x_{dq} \end{bmatrix} & \Delta \mathbf{u}_{cr} &= \begin{bmatrix} \ddot{z}_c \\ \Delta T_{hc} \end{bmatrix} \\
 \mathbf{A}_{cr} &= \mathbf{A}_{dq} - \mathbf{B}_{dq} \delta_E K_{\dot{z}} \mathbf{C}_{\dot{z}} & \mathbf{B}_{cr} &= \begin{bmatrix} \mathbf{B}_{long} \delta_E K_{\dot{z}f} & \mathbf{B}_{long} T_h \\ -D_{\dot{z}} K_{\dot{z}f} + 1 & 0 \end{bmatrix} \\
 \mathbf{C}_{\bar{v}} &= [1 \ 0 \ 0 \ 0 \ 0] & &
 \end{aligned} \tag{5.10}$$

The plant state space model for the auto-thrust proportional controller is defined as:

$$\begin{aligned}\Delta\dot{\mathbf{x}}_{cr} &= \mathbf{A}_{cr}\Delta\mathbf{x}_{cr} + \mathbf{B}_{cr:T_h}\Delta T_{hc} \\ y_{\bar{v}} &= \mathbf{C}_{\bar{V}}\Delta\mathbf{x}_{cr}\end{aligned}\quad (5.11)$$

Where the closed-loop system matrices for the proportional airspeed control is given by:

$$\begin{aligned}\mathbf{A}_{crp} &= \mathbf{A}_{cr} - \mathbf{B}_{cr:T_h}K_{\bar{v}p}\Delta T_{hc} \\ \mathbf{B}_{crp} &= \mathbf{B}_{cr}\end{aligned}\quad (5.12)$$

In order to design the integral controller, the following integral state is defined:

$$x_{vi} = \bar{v}_c - \bar{v}\quad (5.13)$$

Finally, the state space system used to calculate the airspeed integral control root locus is augmented with the airspeed integral state to give:

$$\begin{aligned}\begin{bmatrix} \Delta\dot{\mathbf{x}}_{cr} \\ \dot{x}_{vi} \end{bmatrix} &= \begin{bmatrix} \mathbf{A}_{crp} & \mathbf{0}_{5\times 1} \\ -\mathbf{C}_{\bar{V}} & 0 \end{bmatrix} \begin{bmatrix} \Delta\mathbf{x}_{cr} \\ x_{vi} \end{bmatrix} + \begin{bmatrix} \mathbf{B}_{crp:T_h} \\ 0 \end{bmatrix} \Delta T_{hc} \\ \bar{v} &= [\mathbf{C}_{\bar{V}} \quad 0] \begin{bmatrix} \Delta\mathbf{x}_{cr} \\ x_{vi} \end{bmatrix}\end{aligned}\quad (5.14)$$

Thus, the control law for the auto-thrust control is defined as:

$$\Delta T_{hc} = K_{\bar{v}p} (K_{\bar{v}i} (\bar{v}_c - \bar{v}) - \bar{v})\quad (5.15)$$

5.1.3.2 Auto-Thrust Control: Specifications and Closed-Loop Response

MATLAB's root locus tool was used for the auto-thrust root locus design. The proportional gain ($K_{\bar{v}p}$) was first calculated by drawing the root locus for the transfer function from thrust input to airspeed output. The state space representation for this transfer function is given by Equation 5.11. This state space model gives the poles of the climb rate closed-loop system. The auto-thrust proportional controller forms the plant model for the integral controller, as given by Equation 5.12. The auto-thrust controller closed-loop system poles, with the proportional and integral control applied, are given by Figure 5.12a. This controller was designed to have a 5% settling time of less than 100 seconds with as little overshoot as possible, while aiming for an over-damped response and zero steady-state error tracking.

5.1 Longitudinal Control

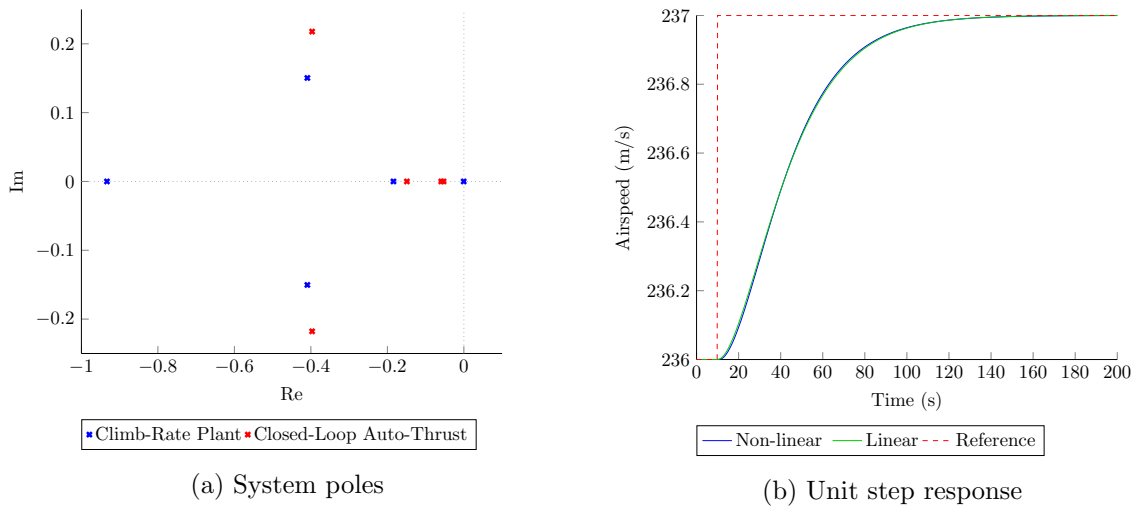


Figure 5.12: Auto-thrust proportional integral controller: a) climb rate plant to auto-thrust controller closed-loop system poles and b) response for unit step input

Figure 5.12b shows airspeed tracking for a unit step command in airspeed. Zero error steady-state tracking and a satisfying response time were achieved in both the linear and non-linear simulations. Thus, through the auto-thrust controller, effective airspeed tracking with a 5% settling time of approximately 90 seconds was achieved.

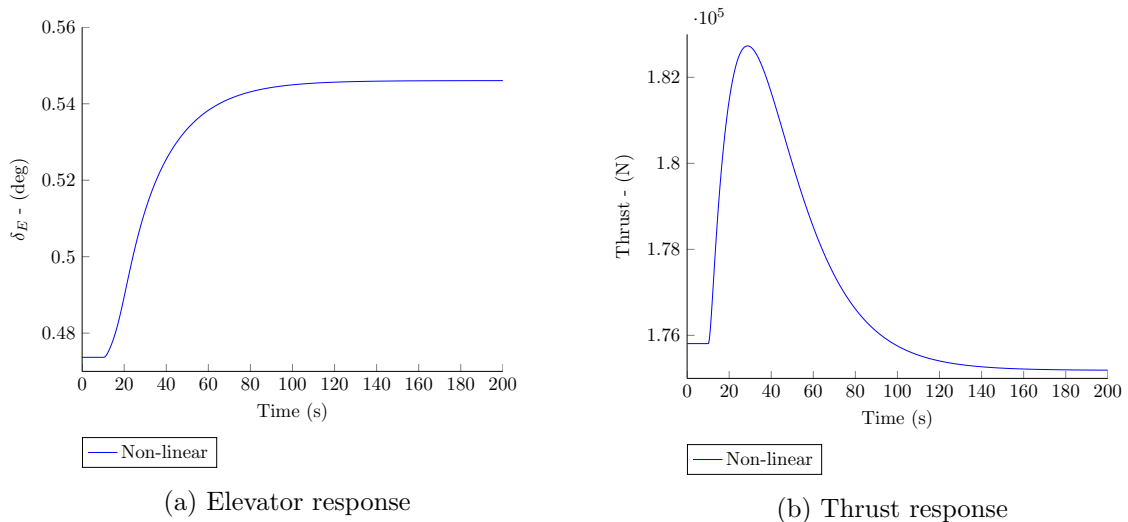


Figure 5.13: Auto-thrust proportional integral (PI) controller: a) elevator actuator response and b) thrust response for a unit step response in airspeed

To increase the airspeed, a thrust force was applied as seen in Figure 5.13b. The higher airspeed directly results in higher lift on the main wing, and a larger up force is required on the tailplane to push the nose of the aircraft down as the pitch angle pivots about the aircraft’s CG. To produce this higher tailplane force the elevator is regulated by the climb rate controller to follow the zero climb rate reference command. Figure 5.13a gives the elevator

actuator response for a unit step airspeed input. The auto-thrust control forms the inner-loop for the altitude control, which will be discussed in the next section.

5.1.4 Altitude Control

The altitude controller forms the final stage of the longitudinal consecutive loop closure scheme. This controller holds the aircraft at a specified altitude, which is particularly useful for cruise flight as it drastically reduces pilot workload. The altitude controller regulates the climb rate to move the aircraft up or down, effectively maintaining altitude even in turn maneuvers. During a turn or bank, the lift vector turns out of the longitudinal plane and the lift vector opposing the gravity force reduces. This results in a loss of altitude. To counter this effect, the inner-loop control will apply elevator to increase the angle of attack, and as a result will increase the lift vector to such an extent that the portion of the lift vector in the negative Z_E direction will counter the gravitational force acting on the aircraft.

This section will cover the design, specifications and implementation of the conventional altitude control.

5.1.4.1 Altitude Control: Design

At first only a proportional (P) controller was designed for altitude control. However, it was later augmented by a proportional integral derivative controller (PID) to improve disturbance rejection. These disturbances were caused by coupling between the longitudinal and lateral states, or in a higher-fidelity application could be the result of measurement noise or sensor bias. This is discussed in more detail in Section 5.1.4.2.

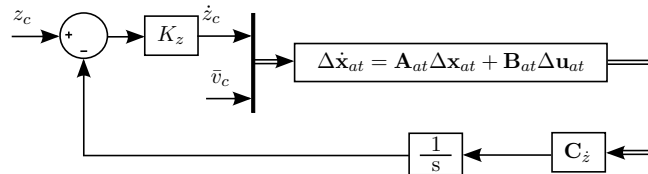


Figure 5.14: Aircraft altitude proportional (P) control diagram

In Figure 5.14, the proportional (P) altitude controller is presented. Climb rate integration is required to extract the altitude from the linear model for feedback. In the non-linear model, however, the altitude can be measured directly, as natural integration is present between climb rate and altitude in the model dynamics. For Diagram 5.14, the system matrices are defined

as:

$$\begin{aligned} \Delta \mathbf{x}_{at} &= \begin{bmatrix} \Delta \mathbf{x}_{cr} \\ x_{vi} \end{bmatrix} & \Delta \mathbf{u}_{at} &= \begin{bmatrix} \dot{z}_c \\ \bar{v}_c \end{bmatrix} \\ \mathbf{A}_{at} &= \begin{bmatrix} \mathbf{A}_{crp} & \mathbf{0}_{5 \times 1} \\ -\mathbf{C}_{\bar{V}} & 0 \end{bmatrix} & \mathbf{B}_{at} &= \begin{bmatrix} \mathbf{B}_{crp:\delta_E} & \mathbf{B}_{crp:T_h} \\ 0 & 0 \end{bmatrix} \\ & & \mathbf{C}_z &= [0 \quad \bar{V} \quad 0 \quad -\bar{V} \quad 0 \quad 0] \end{aligned} \quad (5.16)$$

The altitude plant state space model is augmented with the natural integrator state as given by:

$$\begin{aligned} \begin{bmatrix} \Delta \dot{\mathbf{x}}_{at} \\ \dot{x}_z \end{bmatrix} &= \begin{bmatrix} \mathbf{A}_{at} & \mathbf{0}_{6 \times 1} \\ -\mathbf{C}_z & 0 \end{bmatrix} \begin{bmatrix} \Delta \mathbf{x}_{at} \\ x_z \end{bmatrix} + \begin{bmatrix} \mathbf{B}_{at:\delta_E} \\ 0 \end{bmatrix} \delta_{ec} \\ z &= \mathbf{C}_z \begin{bmatrix} \Delta \mathbf{x}_{at} \\ x_z \end{bmatrix} \quad \text{where} \quad \mathbf{C}_z = [0 \quad 0 \quad 0 \quad 0 \quad 0 \quad 0 \quad 0 \quad 1] \end{aligned} \quad (5.17)$$

The closed-loop system matrices for Figure 5.14 are given by:

$$\begin{aligned} \mathbf{A}_{atp} &= \mathbf{A}_{at} - \mathbf{B}_{at:\delta_E} K_z \delta_{ec} \\ \mathbf{B}_{atp} &= \mathbf{B}_{at} \end{aligned} \quad (5.18)$$

Next, the closed-loop system given by Equation 5.18 was augmented with a PID controller. Theoretically, it might seem unnecessary to first close the P control loop and then augment the system with a PID control. One might ask, why not simplify and only use PID? Although the system could be condensed to only a PID controller, in doing this, the design process would not be accurately represented. In designing this consecutive loop closure system, first closing the P control loop before adding integrator poles in the root locus proved to ease the design. In the P control, the system poles could be shifted away from the origin and thus away from the integrator pole that is placed at the origin. A larger range of gains can therefore be applied before the two real poles meet and break out into a complex pair. In short, the P control loop closure shifts the poles to make space for the PID control integrator pole in the root locus design.

Figure 5.15 gives the altitude PID controller design. The gain placement in the PID scheme is unconventional, although this order corresponds to the one used and calculated with MATLAB's root locus PID design tool.

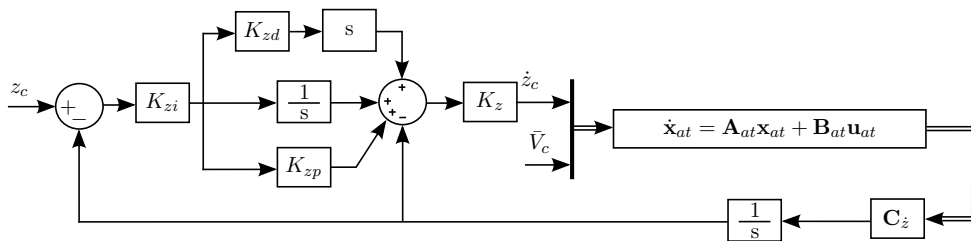


Figure 5.15: Aircraft altitude proportional integral derivative (PID) control diagram

The system matrices for Figure 5.15 are given by Equation 5.16. The plant system matrices for the PID controller are given by the closed-loop system of the altitude P controller in Equation 5.18. For the PID controller, the state space model is augmented with the control integrator error state.

$$\begin{aligned} \begin{bmatrix} \Delta \dot{\mathbf{x}}_{at} \\ \dot{x}_z \\ \dot{x}_{zi} \end{bmatrix} &= \begin{bmatrix} \mathbf{A}_{atp} & \mathbf{0}_{7 \times 1} \\ -\mathbf{C}_z & 0 \end{bmatrix} \begin{bmatrix} \Delta \mathbf{x}_{at} \\ x_z \\ x_{zi} \end{bmatrix} + \begin{bmatrix} \mathbf{B}_{at:\delta_E} \\ 0 \\ 0 \end{bmatrix} \delta_{ec} \\ z &= [\mathbf{C}_z \quad 0] \begin{bmatrix} \Delta \mathbf{x}_{at} \\ x_z \\ x_{zi} \end{bmatrix} \end{aligned} \quad (5.19)$$

The state space system in Equation 5.19 is SISO, which is why a root locus design was used. To complete the PID control design, a complex zero pair was placed and the system gains could be selected using MATLAB's root locus tool. Thus, the altitude control law was defined as:

$$\dot{z}_c = K_z (K_{zi} (z_c - (K_{zp}x_z + x_{zi} + K_{zd}\dot{x}_z)) - x_z) \quad (5.20)$$

5.1.4.2 Altitude Control: Specifications and Closed-Loop Response

The P altitude control was designed to give the fastest settling time, while limiting overshoot as much as possible. An altitude settling time of approximately 30 seconds was achieved, with less than 5% overshoot. Figure 5.16 gives the altitude P control closed-loop system poles, with the auto-thrust closed-loop poles as the system plant.

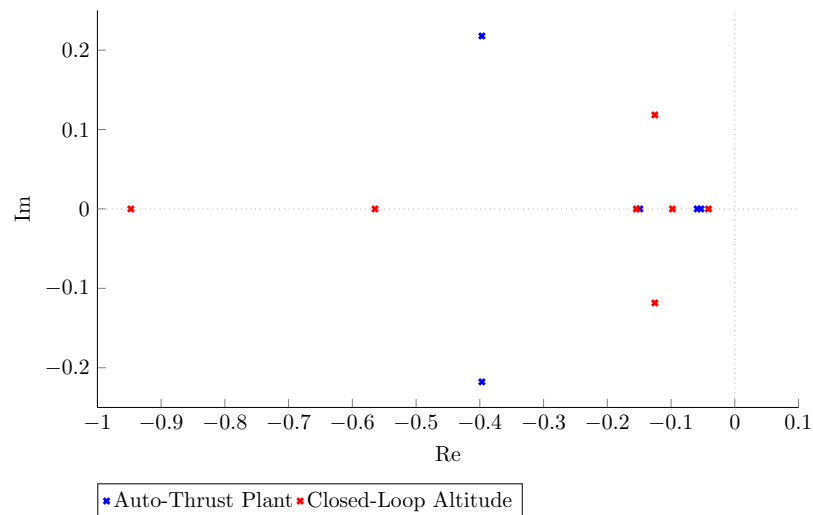


Figure 5.16: Auto-thrust plant to altitude proportional (P) controller closed-loop system poles

Figure 5.17a gives a one meter descent for an altitude P controller step response. The specifications of a 30 second settling time and less than 5% overshoot were achieved. The

5.1 Longitudinal Control

linear state space system results matched the results of the non-linear altitude controller in simulation. On further investigation, it was found that the strong coupling between the lateral and longitudinal dynamics, specifically between aircraft roll and altitude response, introduced notable disturbances to the altitude steady-state tracking. This is expected, as the lift vector in the vertical Z_E direction decreases as the aircraft rolls or banks, resulting in a loss of altitude. Figure 5.17b shows the altitude response as a roll command is induced in the non-linear simulation. This disturbance is not present in the linear simulation, since the lateral and longitudinal systems are assumed to be fully decoupled. Initially, there is a loss of altitude; however, the integrator in the DQ law cancels the acceleration and the aircraft settles at a constant error altitude. Because of this coupling between the lateral and longitudinal systems, it was decided to include an integral controller in the altitude loop, as precise altitude tracking is required for accurate formation station keeping.

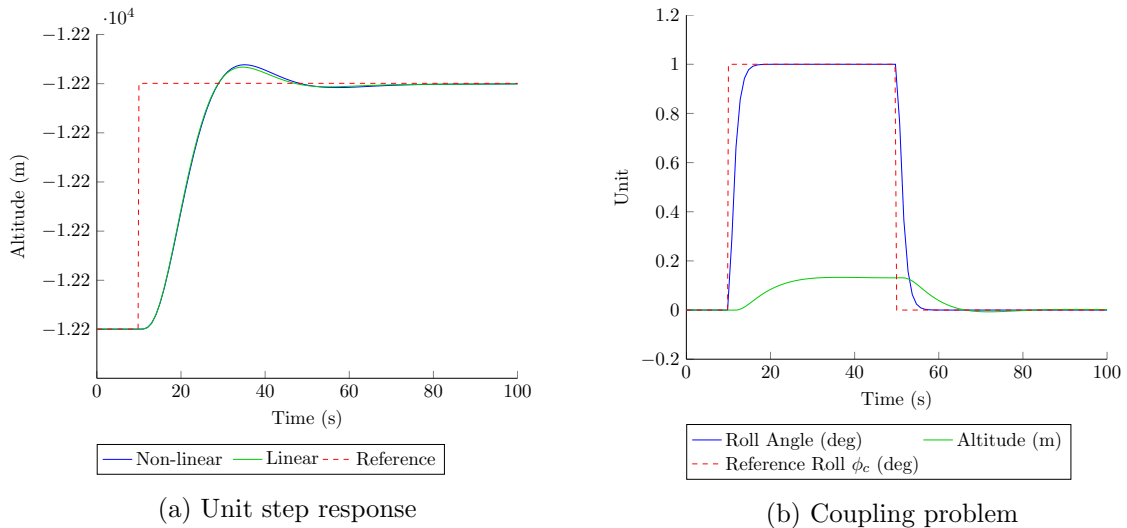


Figure 5.17: Altitude proportional (P) controller response for: a) unit step input and b) coupling between lateral states and altitude control

To regulate the coupling disturbance rejection, the altitude P controller, was augmented with a PID controller as seen in Figure 5.15. The PID control introduces a new pole into the system with the implementation of the integral error state (x_{zi}), as given by Equation 5.19. The altitude PID closed-loop system poles are given by Figure 5.18a, with the altitude P control as the system plant. The root locus design for the PID control are given by Figure 5.18b. The two zeros of the PID control are strategically placed close to, but in front of the complex pole pair, and in line with the pole pair breakaway point. This constrains the breakaway pole pair, while pushing the complex pole pair away from the origin in a way that further increases system damping.

5.1 Longitudinal Control

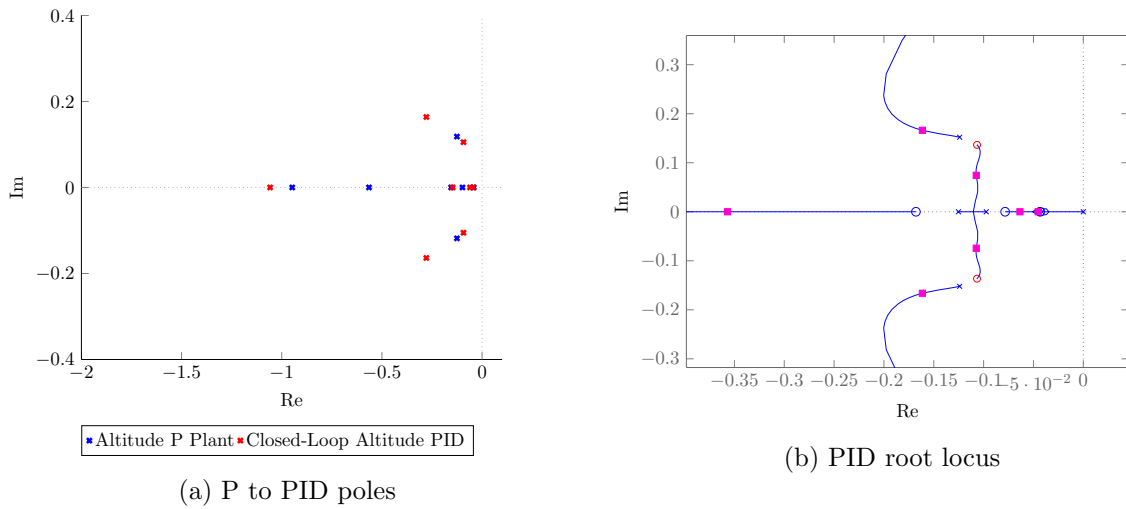


Figure 5.18: a) Altitude proportional (P) controller plant poles to proportional integral derivative (PID) control system closed-loop poles b) PID control root locus design

The zeros introduced by the PID control increased system damping from about 0.7 to 0.8. Figure 5.19a shows the altitude step response with the PID controller included and excluded. Although the settling time is roughly the same, it is the decrease in overshoot and better steady-state error rejection which make the PID control favorable. Figure 5.19b shows how the altitude response is corrected by the integral in the altitude loop. This figure shows that the coupling problem presented in Figure 5.17b has been fixed, and zero error altitude tracking can be achieved.

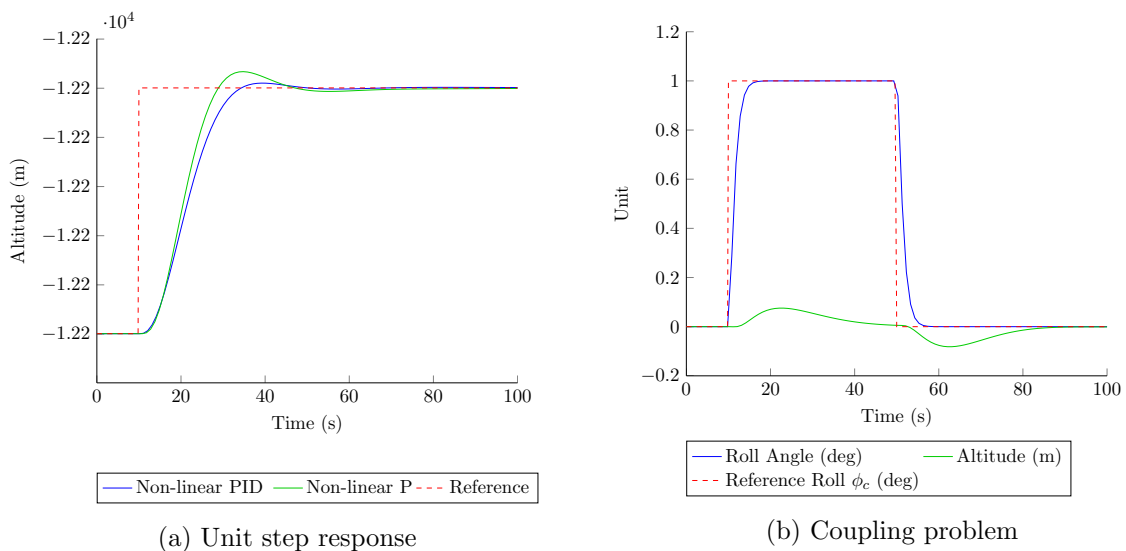


Figure 5.19: a) Altitude P and PID controller response for unit step input and b) coupling between lateral states and altitude state with PID control

To effectively achieve altitude control, a climb rate is regulated which commands the normal acceleration controller to apply the required level of elevator to produce the altitude

step. Figure 5.20a gives the elevator response for a unit step in altitude with the PID altitude controller active. The sharp increase of the elevator increases the angle of attack on the tailplane momentarily and a up-force is induced on the rear of the aircraft, pivoting the aircraft about the CG and pointing the nose down. This result in a lowered angle of attack on the main wing and the altitude is decreases as te elevator regulates to correct the angle of attack, effectively controlling the altitude. In support of the altitude controller, the auto-thrust controller is also active to regulate the airspeed as the vertical and longitudinal dynamics is closely coupled. Figure 5.20 gives the thrust response for a unit step command in altitude. The thrust force is reduced as the aircraft descends, gaining airspeed due to the exchange between potential and kinetic energy. The maintain the constant airspeed command, the thrust force is reduced until the aircraft settles at the new airspeed, after which the thrust returns to the same level to maintain the required lift.

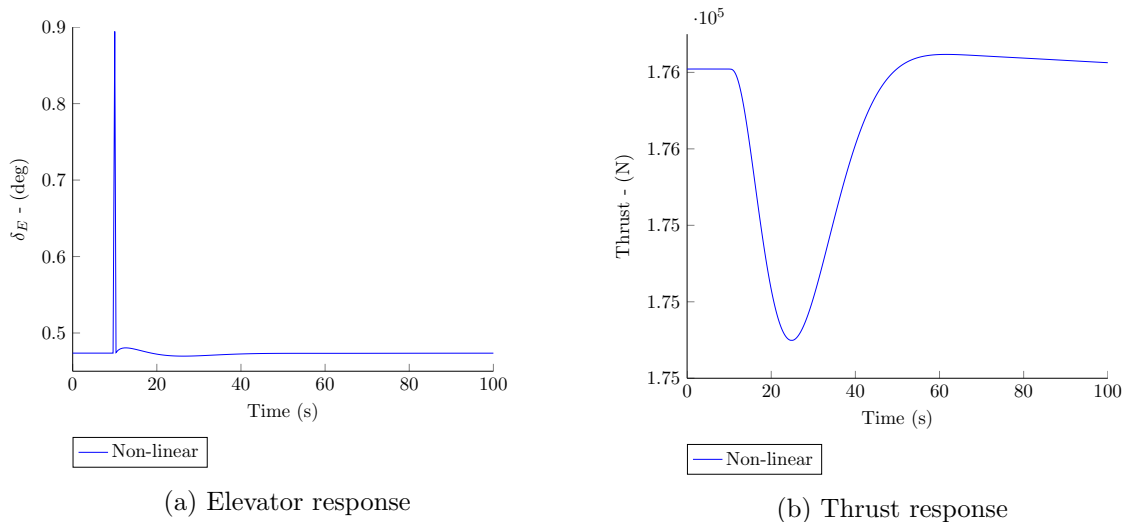


Figure 5.20: Auto-thrust proportional integral (PI) controller: a) elevator actuator response and b) thrust response for a unit step response in airspeed

5.1.5 Concluding the Longitudinal Control

For the Boeing 747 aircraft, the longitudinal and lateral dynamics have been separated by assuming that the coupling between these systems is minimal. In this section, conventional airspeed and altitude control was proposed as the first step towards controlling the longitudinal dynamics for both the leader and the follower aircraft in formation flight. For the airspeed, a settling time of less than 100 seconds was achieved. The altitude controller required the use of PID control to increase the disturbance rejection of coupling effects. A settling time of less than 30 seconds was achieved for the altitude controller, with the system damping slightly higher than that of an optimally damped system. With the conventional

longitudinal control design complete, the lateral control was designed and implemented, as presented in the section to follow.

5.2 Lateral Control

The lateral control for isolated flight is responsible for wings-level and heading control. A consecutive loop closure control strategy was followed to build up to cross-track separation control. In conventional flight, it is critical to control sideslip during a bank to prevent the aircraft from slipping or skidding in a turn. A roll angle and sideslip controller was designed as the inner-loop control, defined as the DPDR control law. For this control, fly-by-wire architecture is proposed, where the inner-loop control artificially supports the pilot to easily perform integrator control. To some degree, the roll angle command represents controlled side-stick inputs. When applying a roll angle, the aircraft is forced into a bank by deflecting ailerons and applying rudder to correct turn coordination. The sideslip command represents controlled pedal input, as it primarily applies rudder, forcing the aircraft into a sideslip and deflecting ailerons to counter induced rolling moment. The outer-loop, cross-track controller feeds back flight path separation to correct the aircraft's turn and consequently make it follow a given flightpath. Accompanied by the cross-track control, aircraft guidance control is normally included. However, for the simulation of two aircraft in formation, only the DPDR law and cross-track control are essential.

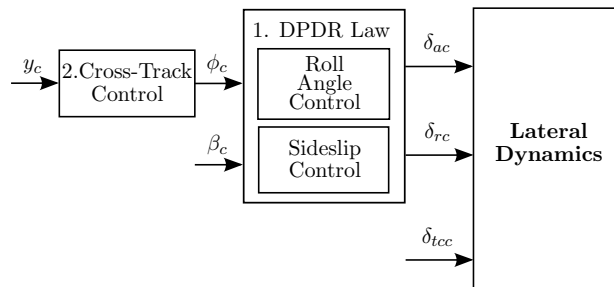


Figure 5.21: Integrator windup protection for controller integrators

Figure 5.21 illustrates how the lateral control system connects with the aircraft lateral dynamics. In the following subsections, the DPDR and cross-track control design, specifications and simulation results will be discussed. This lateral control scheme will be included on both the leader and the follower aircraft in the chapters to follow.

5.2.1 DPDR Controller

The DPDR controller is designed represent the inner-loop control of the lateral dynamics. Its main function is to control roll and sideslip angles in the X, Y -plane. In this control process, the lightly damped Dutch roll mode, as described in Section 4.3.2, is artificially damped to

stop the elliptical motion of the tail when disturbed by applying rudder. However, the lateral motion of the aircraft is strongly coupled between roll and sideslip. In Section 4.1.1, this interaction was briefly discussed. As a positive sideslip is induced, the angle of attack and aspect ratio of the starboard wing are increased. This increases the lift on the starboard side of the aircraft, and as a result introduces a rolling moment. Furthermore, when a roll or bank angle is introduced by applying aileron, the aircraft has a natural tendency to slip, and the rudder must be applied to push the aircraft into the bank by reducing sideslip. If too much sideslip is induced in the bank, the aircraft will skid and experience a side force, resulting in additional loss of airspeed. Thus, to balance these forces when turning the aircraft, turn coordination should be corrected.

In this section, the DPDR controller design, specifications and implementation are discussed. The reference inputs for this control are roll and sideslip commands, with aileron and rudder actuation controlled.

5.2.1.1 DPDR Controller: Design

For this design, full state feedback was chosen, and the gains were calculated using the linear quadratic regulator (LQR) algorithm in MATLAB. Figure 5.22 gives the control scheme for the DPDR control. In this inner-loop controller, the differential thrust (δ_{tc}) remains unused. Roll angle control is achieved by passing the command through mixing gains, which generates the right amount of aileron and rudder to perform a near-perfect coordinated turn. When a sideslip command is applied, some degree of roll angle response is included in the mix to maintain the natural feel of the aircraft. This is also achieved by inducing some rudder and aileron deflection.

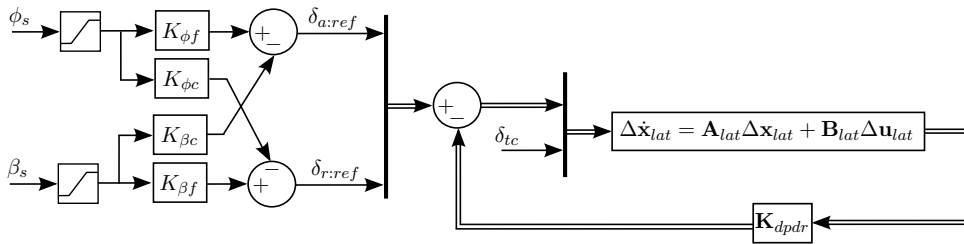


Figure 5.22: Lateral DPDR control diagram

The state space plant model in Figure 5.22 is defined by Equation 4.11. The full state feedback control law is given by:

$$\Delta \mathbf{u}_{\delta_a \delta_r} = \begin{bmatrix} \delta_{ac} \\ \delta_{rc} \end{bmatrix} = \begin{bmatrix} \delta_{a:ref} \\ \delta_{r:ref} \end{bmatrix} - \mathbf{K}_{dpdr} \Delta \mathbf{x}_{lat} \quad (5.21)$$

The optimal control gain (\mathbf{K}_{dpdr}) was calculated with an LQR optimization algorithm that minimizes the cost function:

$$J = \int_0^{\infty} (\Delta \mathbf{x}_{lat}^T \mathbf{Q} \Delta \mathbf{x}_{lat} + \Delta \mathbf{u}_{\delta_a \delta_r}^T \mathbf{R} \Delta \mathbf{u}_{\delta_a \delta_r}) dt \quad (5.22)$$

Where the initial state weighting matrix \mathbf{Q} and input weighting matrix \mathbf{R} are defined using Bryson's rule:

$$\begin{aligned} \mathbf{Q} &= \text{diag} \left[\frac{1}{\max(\beta)^2} \quad \frac{1}{\max(P)^2} \quad \frac{1}{\max(R)^2} \quad \frac{1}{\max(\Phi)^2} \right] \\ \mathbf{R} &= \text{diag} \left[\frac{1}{\max(\delta_A)^2} \quad \frac{1}{\max(\delta_R)^2} \right] \end{aligned} \quad (5.23)$$

The diagonal matrices in Equation 5.23 were slightly adjusted by decreasing the weight of matrix \mathbf{Q} relative to matrix \mathbf{R} until the control specifications were met.

With the input mixing gains augmented to the full state feedback controller, the control law is redefined as:

$$\Delta \mathbf{u}_{\delta_a \delta_r} = \begin{bmatrix} K_{\phi f} & -K_{\phi s} \\ -K_{\beta s} & K_{\beta f} \end{bmatrix} \begin{bmatrix} \phi_c \\ \beta_c \end{bmatrix} - \mathbf{K}_{dpdr} \Delta \mathbf{x}_{lat} \quad (5.24)$$

5.2.1.2 DPDR Controller: Specifications and Closed-Loop Response

For the DPDR controller, the design was tuned to achieve the fastest possible settling time with no overshoot to ensure highly responsive inner-loop control. This produced faster lateral dynamics in the outer control loops. After a few design iterations, the LQR weighting matrices were defined as:

$$\begin{aligned} \mathbf{Q} &= \text{diag} \left[\frac{1}{(\pi/180)^2} \quad \frac{1}{(\pi/180)^2} \quad \frac{1}{(\pi/180)^2} \quad \frac{1}{(\pi/180)^2} \right] \\ \mathbf{R} &= \text{diag} \left[\frac{1}{(10\pi/180)^2} \quad \frac{1}{(10\pi/180)^2} \right] \end{aligned} \quad (5.25)$$

With the weighting matrices in Equation 5.25, the LQR full state feedback gain (\mathbf{K}_{dpdr}) was calculated using MATLAB's `LQR.m` function. The input mixing in-line control gains ($\mathbf{K}_{\phi f}$, $\mathbf{K}_{\beta f}$) were tuned to achieve one degree of roll or sideslip for one degree of input command. The input mixing cross-coupling gains ($\mathbf{K}_{\phi s}$, $\mathbf{K}_{\beta s}$) were selected to correct turn coordination for a roll command and give five degrees of roll for one degree of sideslip.

5.2 Lateral Control

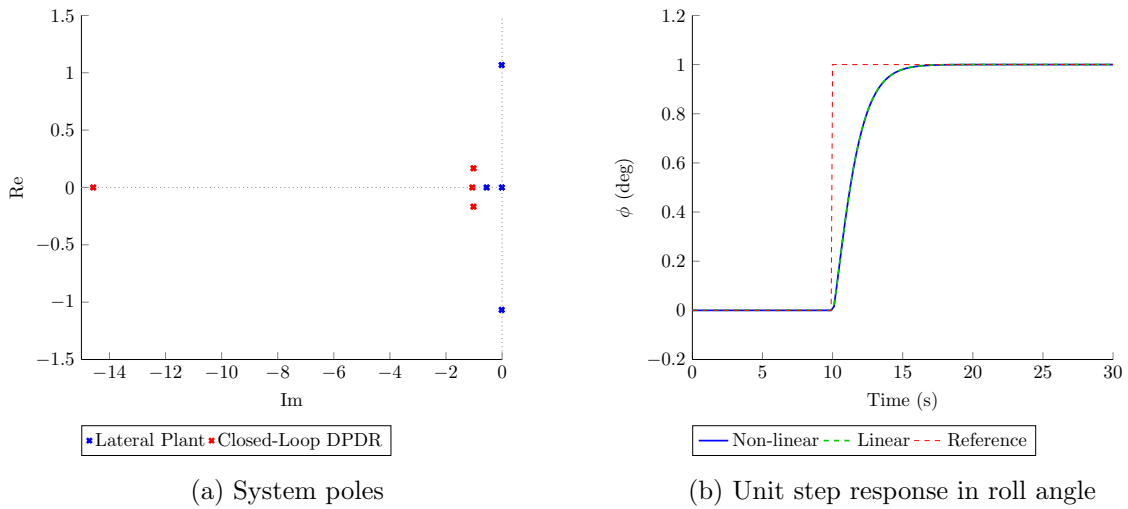


Figure 5.23: a) Lateral aircraft plant to DPDR controller closed-loop system poles and b) roll response for one degree step in roll command

Figure 5.23a gives the aircraft lateral dynamics plant poles and the DPDR closed-loop system poles. This figure shows that the DPDR controller increased the Dutch roll mode damping from 0.015 to 1.4. A settling time of 4 seconds was achieved for a unit step in roll angle command, as shown in Figure 5.23b.

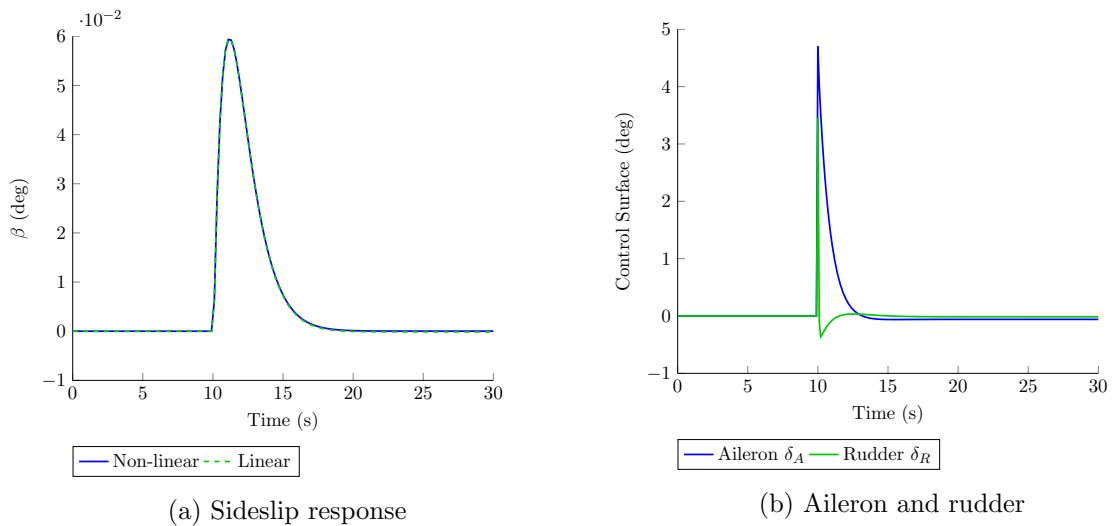


Figure 5.24: a) DPDR controller sideslip response and b) control aileron and rudder demand for one degree step in roll command

Figure 5.24a shows the sideslip angle response for a unit step input in roll command. The peak sideslip was less than 0.06 degrees, with almost zero sideslip at steady state, thus almost perfect turn coordination was achieved. The aileron and rudder demand is given by Figure 5.24b. For a step in roll command, the ailerons are deflected to produce a short rolling moment, and the rudder is applied to effectively damp the unwanted dynamic modes, tilting

the aircraft into a constant roll angle before resting the control surfaces back to zero as the maneuver is completed.

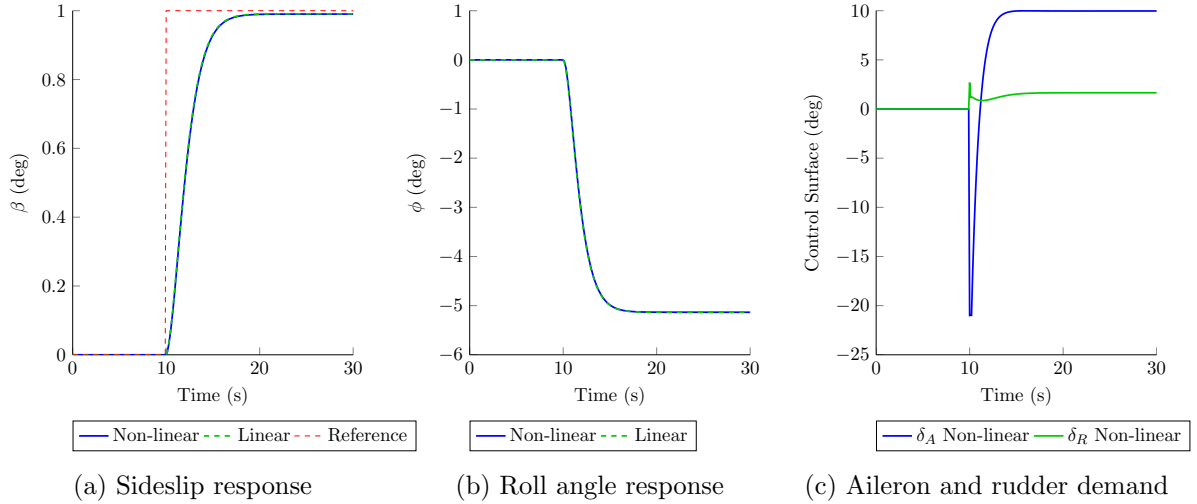


Figure 5.25: DPDR controller: a) sideslip response, b) roll angle response and c) aileron and rudder response for one degree step in sideslip command

For a one degree or unit step command in sideslip, a natural response was achieved. This means that for a positive change in sideslip, a negative change in aircraft roll angle occurs. This effect results because the aspect ratio and angle of attack increase on the starboard wing during positive sideslip, which in return tilts the starboard wing up. This pushes the aircraft into a bank, where equilibrium is regained. Figure 5.25b shows the response for a unit step in sideslip. A settling time of six seconds was achieved with an over-damped system. Figure 5.25b shows that a negative five degrees in roll was required to regain equilibrium following the one degree step in sideslip. For this maneuver, a high level of aileron is required to counter the constant rolling moment due to sideslip. A constant level of rudder is also required to keep the aircraft from naturally returning to zero sideslip as the tailfin pushes into the wind. The control surface demand for a unit step in sideslip command is shown in Figure 5.25c.

The DPDR controller demonstrated effective roll and sideslip control for the inner-loop system. The roll command with near-perfect turn coordination will be used in the following control loop to correct cross-track error. In the following subsection, the cross-track controller will be discussed.

5.2.2 Cross-Track Controller

The cross-track controller is responsible for regulating the separation between the aircraft and a lateral reference flight track, which in the case of formation flight, is the lateral separation between the leader and the follower aircraft. The cross-track control is in a sense the

same as a conventional heading controller, as it commands a roll angle to turn the aircraft to a desired flight path. However, whereas the heading control guides the aircraft to fly at a command heading angle (ψ), the cross-track control flies the aircraft to follow a specific track. In order to perform way-point tracking, an additional guidance controller is augmented to the lateral control. For this study, aircraft way-point guidance is not of particular concern, as the simulation of formation flight at cruise conditions will be conducted at a constant heading.

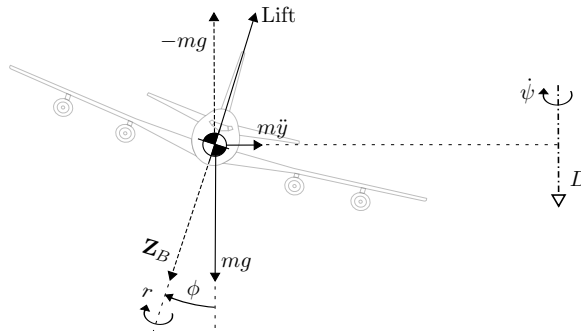


Figure 5.26: Aircraft cross-track control diagram

To get an aircraft to follow a specific track separation, a better understanding of the forces and moments induced during a bank turn is useful. Figure 5.26 gives the basic forces at work as a constant roll angle is applied. As the lift force turns out of the X, Z -plane, a side force is induced on the aircraft ($m\ddot{y}$), resulting in a lateral velocity. Since the aircraft velocity vector is now in the axial and lateral direction, a change heading angular rate ($\dot{\psi}$) exists. Thus, if the roll angle can be controlled, the lateral acceleration can be controlled.

5.2.2.1 Cross-Track Controller: Design

The cross-track controller commands the DPDR controller's roll angle input to control the lateral acceleration exerted on the aircraft. During a turn, the lift vector is responsible for countering the weight of the aircraft and for providing the centripetal acceleration required for the turn. The ideal lateral acceleration with no external disturbance can be written as:

$$\ddot{y} = \bar{V}\dot{\psi} = g \tan \phi \approx g\phi \quad (5.26)$$

The natural integration from cross-track acceleration to cross-track velocity and again to cross-track separation makes the system type 2, meaning it should be able to follow a step and ramp signal with zero steady-state error tracking. Roll angle command saturation is also included to keep the cross-track velocity control from commanding large roll angles, which can result in an uncontrolled loss in altitude as the lift vector turns out of the longitudinal or X, Z -plane.

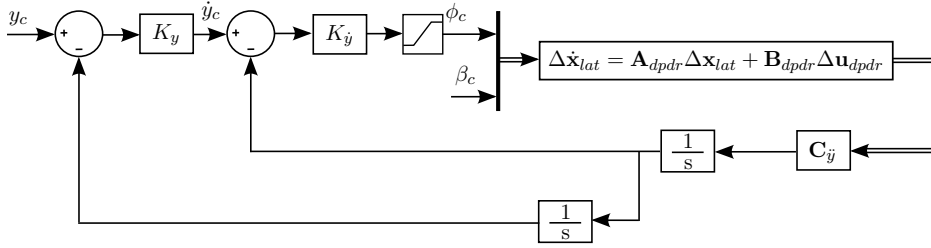


Figure 5.27: Aircraft cross-track control diagram

The system plant matrices for the cross-track velocity loop are defined as:

$$\begin{aligned} \Delta \mathbf{u}_{dpdr} &= \begin{bmatrix} \phi_c \\ \beta_c \end{bmatrix} \\ \mathbf{A}_{dpdr} &= \mathbf{A}_{lat} - \mathbf{B}_{lat} \mathbf{K}_{dpdr} & \mathbf{B}_{dpdr} &= \mathbf{B}_{lat} \begin{bmatrix} K_{\phi_f} & -K_{\phi_s} \\ -K_{\beta_s} & K_{\beta_f} \end{bmatrix} \\ \mathbf{C}_{ij} &= [0 \quad 0 \quad 0 \quad g] \end{aligned} \quad (5.27)$$

Augmenting the state space model with the cross-track velocity state gives:

$$\begin{aligned} \begin{bmatrix} \Delta \dot{\mathbf{x}}_{lat} \\ \dot{x}_{\dot{y}} \end{bmatrix} &= \begin{bmatrix} \mathbf{A}_{dpdr} & \mathbf{0}_{4 \times 1} \\ -\mathbf{C}_{ij} & 0 \end{bmatrix} \begin{bmatrix} \Delta \mathbf{x}_{lat} \\ x_{\dot{y}} \end{bmatrix} + \begin{bmatrix} \mathbf{B}_{dpdr:\phi_c} \\ 0 \end{bmatrix} \phi_c \\ \dot{y} &= [\mathbf{0}_{1 \times 4} \quad 1] \begin{bmatrix} \Delta \mathbf{x}_{lat} \\ x_{\dot{y}} \end{bmatrix} \end{aligned} \quad (5.28)$$

A root locus design method was used to determine the cross-track velocity gain ($K_{\dot{y}}$) for the SISO system given in Equation 5.28. This cross-track velocity control formed the inner loop for the cross-track separation controller of which the system matrices were defined as:

$$\begin{aligned} \Delta \mathbf{u}_{\dot{y}} &= [\dot{y}_c] \\ \mathbf{A}_{\dot{y}} &= \begin{bmatrix} \mathbf{A}_{dpdr} & \mathbf{0}_{4 \times 1} \\ -\mathbf{C}_{ij} & 0 \end{bmatrix} - \begin{bmatrix} \mathbf{B}_{dpdr:\phi_c} \\ 0 \end{bmatrix} [0 \quad 0 \quad 0 \quad 0 \quad K_{\dot{y}}] & \mathbf{B}_{\dot{y}} &= \begin{bmatrix} \mathbf{B}_{dpdr:\phi_c} \\ 0 \end{bmatrix} \\ \mathbf{C}_{\dot{y}} &= [0 \quad 0 \quad 0 \quad 0 \quad 1] \end{aligned} \quad (5.29)$$

To perform cross-track separation control, the state space model is augmented with the cross-track separation state:

$$\begin{aligned} \begin{bmatrix} \Delta \dot{\mathbf{x}}_{lat} \\ \dot{x}_{\dot{y}} \\ \dot{x}_y \end{bmatrix} &= \begin{bmatrix} \mathbf{A}_{\dot{y}} & \mathbf{0}_{5 \times 1} \\ -\mathbf{C}_{ij} & 0 \end{bmatrix} \begin{bmatrix} \Delta \mathbf{x}_{lat} \\ x_{\dot{y}} \\ x_y \end{bmatrix} + \begin{bmatrix} \mathbf{B}_{dpdr:\phi_c} \\ 0 \\ 0 \end{bmatrix} \phi_c \\ y &= [\mathbf{0}_{1 \times 5} \quad 1] \begin{bmatrix} \Delta \mathbf{x}_{lat} \\ x_{\dot{y}} \\ x_y \end{bmatrix} \end{aligned} \quad (5.30)$$

Again, root locus design was used to determine the cross-track separation gain (K_y) for the SISO system given in Equation 5.30. With the cross-track controller defined, the cross-track separation control law can be written as:

$$\Delta \mathbf{u}_{dpdr:\phi_c} = \phi_c = K_{\dot{y}}(\dot{y}_c - \dot{y}) = K_{\dot{y}}(K_y(y_c - y) - \dot{y}) \quad (5.31)$$

In the linear model control design, the cross-track separation is determined by integrating the cross-track velocity. However, since this is a natural integrator in the system dynamics, the cross-track separation can be fed back by measurement into the non-linear model. In the non-linear simulation, the cross-track separation and velocity are defined as:

$$\begin{aligned} y &= -\sin \Psi_{track}(N - N_{src}) + \cos \Psi_{track}(E - E_{src}) \\ \dot{y} &= \bar{V} \sin(\Psi - \Psi_{track}) \end{aligned} \quad (5.32)$$

In Equation 5.32, Ψ_{track} is the heading angle between North and the flight path direction, and N_{src} , E_{src} are the coordinates of a point on the flight path. On the follower aircraft these variables were replaced by those of the leader aircraft's position and attitude states in order to perform cross-track control in formation. This will be discussed in more detail in Chapter 6.

5.2.2.2 Cross-Track Controller: Specifications and Closed-Loop Response

The cross-track control was designed using two consecutive loop closures superimposed on the DPDR controller, as discussed in Section 5.2.2.1. The gains for this controller were determined using a root locus design approach with the help of MATLAB's root locus tool.

The cross-track velocity gain ($K_{\dot{y}}$) was first determined. A settling time of 10 seconds was achieved with no overshoot or steady-state error, as the cross-track velocity is a type 1 over-damped system. Figure 5.28a shows the DPDR controller closed-loop poles, used as the plant for the cross-track velocity control design, and the closed-loop cross-track velocity poles. Figure 5.28b gives the cross-track velocity response given a unit step input for both the linear and non-linear simulations.

5.2 Lateral Control

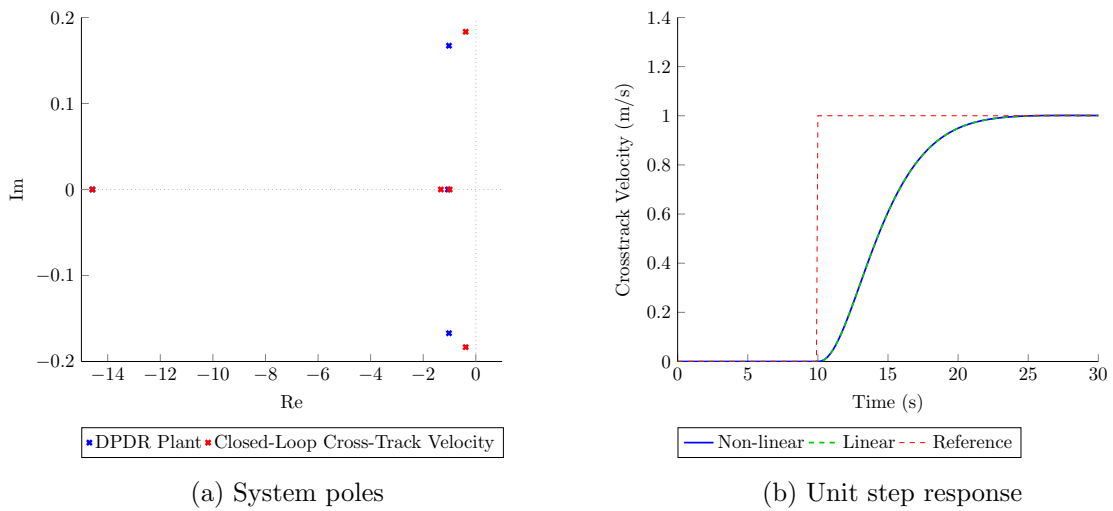


Figure 5.28: a) DPDR plant to cross-track velocity closed loop system poles and b) cross-track velocity unit step response

For the cross-track separation control, a second feedback loop was closed. The cross-track velocity forms the inner loop or plant of the cross-track separation controller. The cross-track separation gain was determined by root locus design. A settling time of 30 seconds was achieved with no overshoot and zero steady-state tracking, since the cross-track separation is a type 2 over-damped system. The closed-loop system poles are given by Figure 5.29a, with the cross-track velocity loop forming the system plant. A unit step response in cross-track separation is given by Figure 5.29b for both the linear and non-linear simulation.

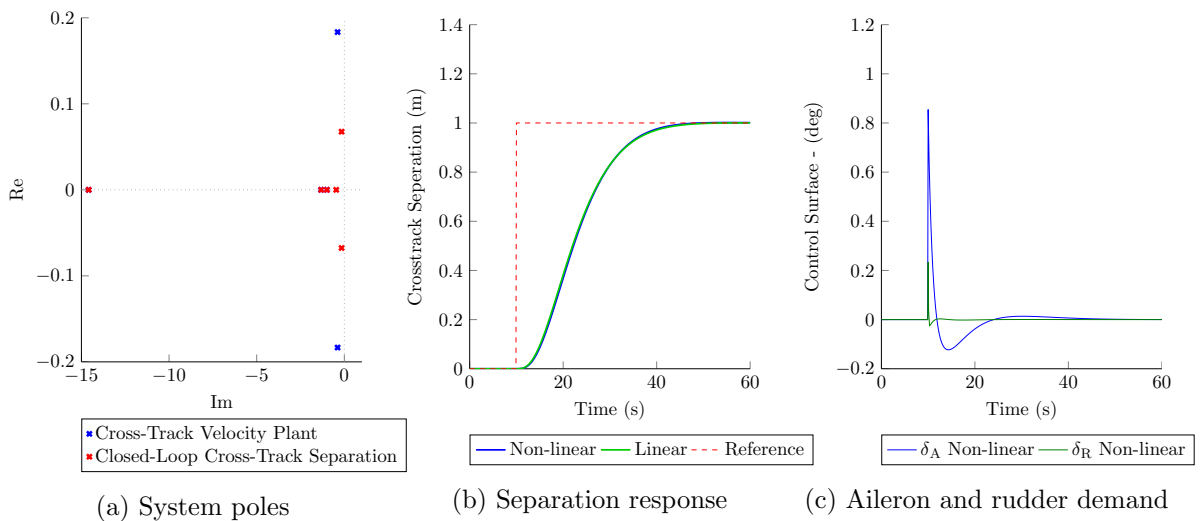


Figure 5.29: a) Cross-track velocity plant to cross-track separation proportional controller closed loop system poles, b) cross-track separation response c) aileron and rudder response for cross-track unit step command

Figure 5.29c gives the aileron and rudder control surface demand for a unit step command

in cross-track. In this maneuver the ailerons bank the aircraft to perform in and out of the turn to change cross-track separation while the rudder corrects turn coordination.

5.2.3 Concluding the Lateral Control

With lateral and longitudinal aircraft dynamics decoupled, a separate control system could be proposed for the lateral controller. A consecutive loop closing strategy was followed to achieve cross-track control on the Boeing 747 linear and non-linear simulation models. Roll angle and sideslip control were achieved by LQR design and formed the DPDR control law. The roll angle response was further tuned to perform near-perfect turn coordination. Two consecutive proportional control loops were closed in order to perform cross-track separation control by regulating the DPDR roll angle command. Effective cross-track control was achieved with a 5% settling time of less than 25 seconds, no overshoot and zero error steady-state tracking.

With effective cross-track control in place, the aircraft could now track a given separation distance from a flight track. This would be useful, as the follower aircraft tracks the leader aircraft at a given lateral separation, which will be demonstrated in the chapters to follow.

5.3 Control Anti-Windup

Adding integral control to a system introduces the possibility of integral windup. This occurs when a part of the system saturates, causing the integral state to grow for an extended time. During integral windup, the integral state grows far beyond the sum of the error signals and thus introduces an additional error into the system as the controlled state approaches the command value. This usually occurs for command signals which are large enough to saturate system controls. In effect, the system cannot reach the command value in the relative settling time due to lack of control authority or safety limitations. Many anti-windup control strategies have been developed on the working principle of stopping the control integration when inner-loop saturations occurs.

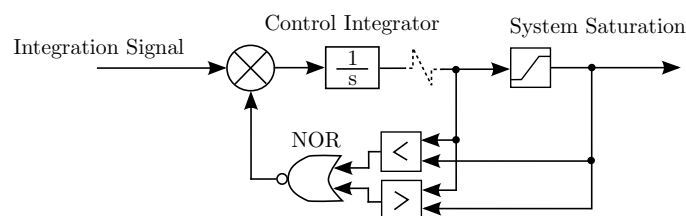


Figure 5.30: Integrator windup protection for controller integrators

Figure 5.30 gives the anti-windup logic protection scheme implemented on all control integrators for the flight simulations. In this scheme, the anti-windup logic tests for saturations

5.4 Conventional Control Under Turbulent Conditions

in the control loop or sub-/inner loops and turns off the integration when the system is in saturation. This is achieved by multiplying the integrator signal by zero, effectively disabling integration while saturation occurs. The integral control is re-enabled when the system comes out of saturation by multiplying the integration signal by one.

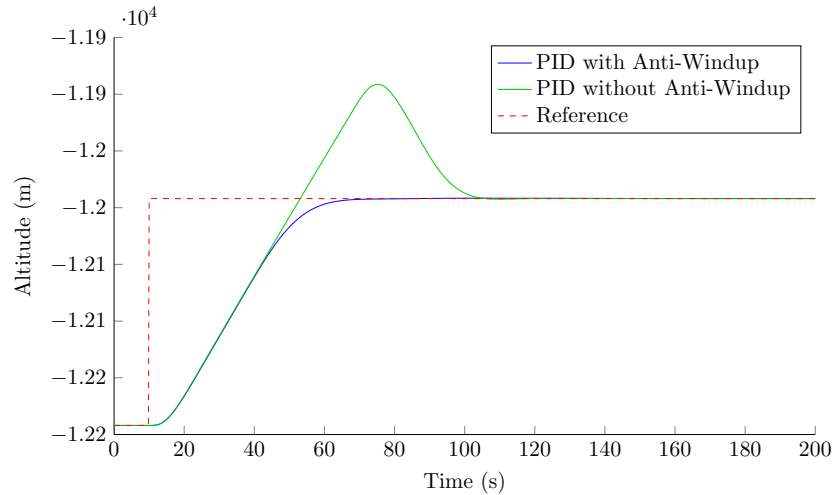


Figure 5.31: Altitude anti-windup in PID controller

A typical example of integral windup is given in Figure 5.31, where a large altitude step was given to the aircraft. Integral windup causes the controller to overshoot the target altitude until the integral state reduces and brings the aircraft to the desired value. With anti-windup, active control integration is stopped as climb rate saturation occurs. When deactivated, the integral state remains constant until the target altitude is approached, and the integrator is reactivated as the climb rate comes out of saturation. Figure 5.31 shows that the anti-windup control logic was successful in protecting the aircraft from altitude integrator windup overshoot. The same principle holds for the other control integrators in the system design.

5.4 Conventional Control Under Turbulent Conditions

In this chapter, the design and simulation of conventional flight controls for an aircraft in isolated flight were presented. To analyze the performance of these controls, a simulation under turbulent conditions was conducted to represent a more realistic environment. With the von Kármán turbulence model active, as presented in Section 3.9, the altitude, auto-thrust and cross-track controller were analyzed under light, moderate and severe turbulence. Although the test for severe turbulence is presented here, it should be noted that the controller gains were not designed to operate under this rare case of turbulence. For the controller design, the gains were set as high as possible to induce fast and responsive aircraft dynamics. This strategy drives the control actuators very hard to achieve these fast reaction times, pushing

5.5 Concluding the Conventional Flight Controls

System State	Light	Moderate	Severe
Altitude (b)	0.003	0.073	0.239
Airspeed (b/s)	0.001	0.022	0.092
Cross-track (b)	0.005	0.101	0.462
Aileron (deg)	0.380	8.622	17.1024
Rudder (deg)	0.023	1.675	18.925
Elevator (deg)	0.017	0.405	1.363
Thrust (kN)	1.540	31.991	83.326

Table 5.2: The standard deviation of conventional controllers under turbulent conditions normalized to aircraft wingspan

the actuators to saturation under high levels of turbulence. Thus it is advisable to design a gain schedule for medium and severe turbulence to reduce the load on the actuators in these extreme conditions. However, for this study, only a high gain set was designed, since the fast dynamics will be preferred in the formation-hold and extremum seeking controllers to follow, and formation flight under highly turbulent conditions should be avoided.

Table 5.2 gives the standard deviation for the altitude, airspeed and cross-track controlled states normalized to aircraft wingspan, as well as control actuators in light, moderate and severe turbulence over 15 minutes of simulation. The simulation result samples are presented in Appendix B.1. In light turbulence, the controllers perform exceptionally well, since all three control parameters produce a standard deviation of less than 0.5% when normalized to aircraft wingspan. In moderate turbulence, the controller performance is still acceptable, since the standard deviation of the control parameters are kept within 10% when normalized to wingspan. However, severe turbulence drives the control actuators to their limits, and a standard deviation of about 46% of wingspan was observed on the control parameters. A standard deviation of 90% on ailerons' actuators when normalized to the saturation level of the ailerons confirms that the control gains are too high to fly in the extreme condition of severe turbulence. Thus, for this study, these control gains are sufficient, as they give good performance in light and moderate conditions. Formation flight controllers will thus be proposed for these two conditions based on the conventional controllers presented in this chapter.

5.5 Concluding the Conventional Flight Controls

In right echelon formation flight during cruise, the leader aircraft flies straight and level at a selected trim condition. A follower aircraft is initialized to approach the leader aircraft and perform constant station keeping in the wake of the leader. Conventional flight controls can

5.5 Concluding the Conventional Flight Controls

be seen as a first step towards formation flight station keeping, as both aircraft maintain a constant airspeed, altitude and cross-track. The Boeing 747 aircraft presented in Chapter 3, and linearized in Chapter 4, represented the raw aircraft model with control surface deflections as control inputs. This unconditioned model was augmented with flight controls so as to achieve constant airspeed, altitude and cross-track control on both the leader and the follower aircraft. These control systems were divided, together with the decoupled aircraft dynamics, into longitudinal and lateral control systems. Since the conventional controllers will form the foundation of the formation flight controllers, the control gains were tuned as stiff as possible to ensure precision formation control to better optimize thrust efficiency.

The longitudinal control system regulates elevator actuation to achieve normal acceleration and pitch rate damping through the defined DQ control law in Section 5.1.1. A consecutive loop closure strategy was used to superimpose climb rate and altitude control on the DQ system. An altitude settling time of 30 seconds was achieved, as presented in 5.1.4. Airspeed control was also designed and implemented successfully by regulating thrust command, as presented in Section 5.1.3. An airspeed settling time of 100 seconds was achieved.

The lateral control system was designed and tested with the longitudinal control successfully implemented and active. This was required since minor coupling between the lateral and longitudinal non-linear systems exist, especially when roll angles are applied. The lateral inner-loop control consisted of the DPDR control law to govern roll angle and sideslip, as presented in Section 5.2.1. The roll angle command performs near-perfect turn coordination during bank-to-turn maneuvers. This roll angle command was utilized by the cross-track controller to fly the aircraft a given separation from a flight track. A cross-track settling time of less than 30 seconds was achieved, as described in Section 5.2.2.

Finally, the altitude, airspeed and cross-track controllers were evaluated under turbulent conditions. In light turbulence all controllers performed well, with standard deviations on control parameters of less than 1%. In moderate turbulence the control performance was still acceptable, with standard deviations on control parameters under 10%, when normalized to wingspan. However, in severe turbulence the controllers struggled to regulate the control parameters and it was advised to release the stiffness of the control gains for high turbulent levels. For the study of formation flight evaluation under light and moderate turbulence is sufficient since it is advised to disengage formation flight under high turbulent levels. Thus the presented conventional control gains showed good performance under conditions suitable for formation flight, and extra gains was not redesigned for flight in severe turbulence.

5.5 Concluding the Conventional Flight Controls

With altitude, airspeed and cross-track control implemented on the Boeing 747 aircraft model for isolated flight, a formation flight interaction controller could be designed. The first objective in formation flight control was to perform constant station keeping for the follower in the wake during cruise flight. In the following chapter, a formation-hold autopilot will be presented.

Chapter 6

Formation-Hold Control

The first control objective for successful formation flight is to maintain a constant spatial separation between the aircraft. To achieve this, formation-hold control architecture was developed to regulate the separation for all three axes, namely the longitudinal (ξ), lateral (η) and vertical (ζ) separation [13, 14]. These separations are normalized to the aircraft's wingspan (b) and calculated as described in Section 3.7.

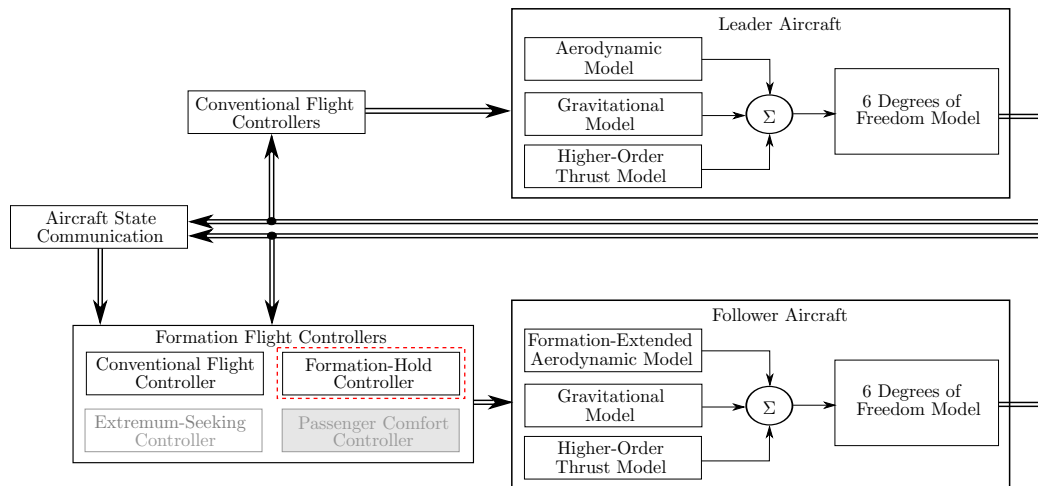


Figure 6.1: Formation flight systems overview

Figure 6.1 shows the systems involved in the simulation and control design of formation flight. The leader and follower aircraft models were defined in Chapter 3, and conventional controls were included on each aircraft as discussed in Chapter 5. This chapter will introduce formation-hold control to regulate the separation between the leader and the follower aircraft. An inner-loop complementary filter system was also developed for the lateral systems to prevent control surface saturation due to the large rolling moment in the wake. In the chapter to follow, extremum seeking will be discussed. The consideration of passenger comfort in formation flight for commercial aircraft also requires control design adjustments, but such an

6.1 Formation-Hold by Conventional Control Augmentation

endeavor falls outside the scope of this project.

6.1 Formation-Hold by Conventional Control Augmentation

In Chapter 5, a set of conventional isolated flight controllers was designed to regulate aircraft altitude, airspeed and cross-track separation to a given reference command. These controllers form the core of the formation-hold control system. By simple augmentation and remapping of the outer loop, follower station keeping becomes possible. By reusing the same controllers presented in Chapter 5, a formation control system was developed which meets performance objectives for both isolated and formation flight.

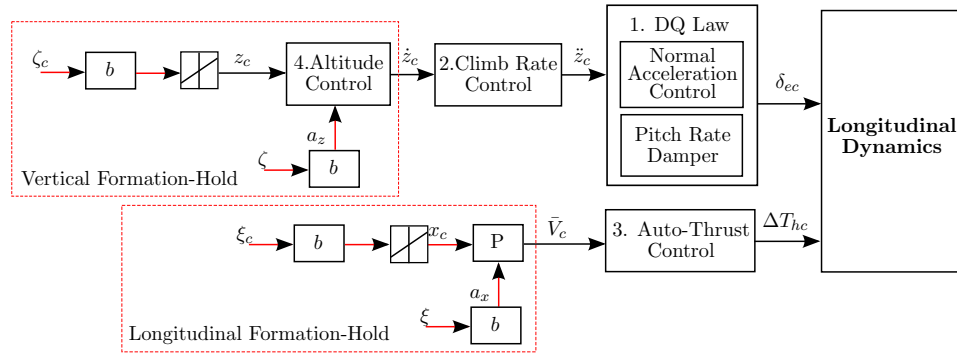


Figure 6.2: Formation-hold longitudinal control augmentation on follower aircraft

Figure 6.2 gives the formation-hold augmentation of the longitudinal flight controls. Vertical formation-hold was achieved by adjusting the feedback in the altitude control to regulate the vertical (ζ) separation. Longitudinal formation-hold was achieved by augmenting the airspeed control input with a proportional controller, which uses the longitudinal separation for feedback, enabling longitudinal (ξ) separation control.

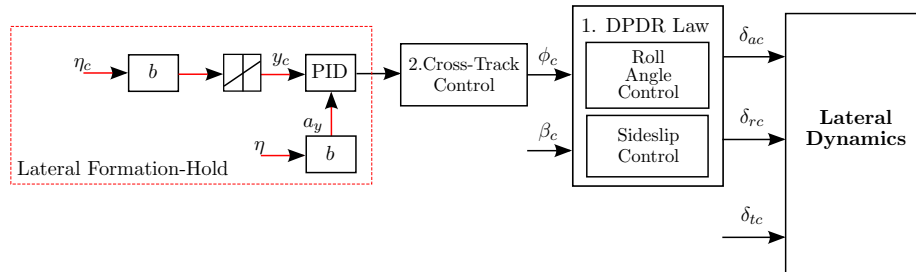


Figure 6.3: Formation-hold lateral control augmentation on follower aircraft

Lateral formation-hold was achieved by augmenting the cross-track control with a proportional integral derivative (PID) controller. Figure 6.3 illustrates the changes made to the

6.1 Formation-Hold by Conventional Control Augmentation

lateral control architecture to enable lateral (η) separation regulation.

In the following sections, formation-hold control will be discussed in more detail for each axis.

6.1.1 Longitudinal Formation-Hold

The purpose of longitudinal formation-hold control is to regulate the airspeed of the follower aircraft to produce a consistent longitudinal (ξ) formation separation. When both aircraft fly at the same trim airspeed, the longitudinal separation remains constant. If the follower aircraft reduces speed, the longitudinal separation will increase by the integral of the airspeed difference. As the follower increases speed, the longitudinal separation decreases by the integral of the airspeed difference. This section will discuss the design, specifications and simulation response for the longitudinal formation-hold controller.

6.1.1.1 Longitudinal Formation-Hold: Control Design

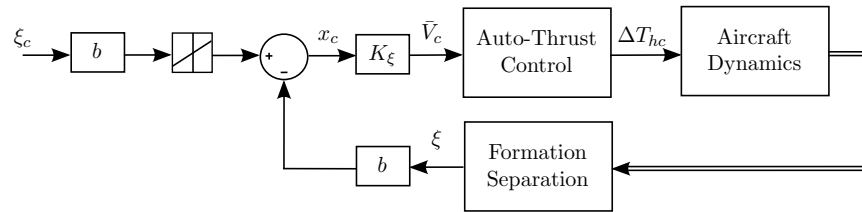


Figure 6.4: Longitudinal formation-hold control design

The longitudinal formation-hold control was developed by augmenting the auto-thrust controller with proportional control to regulate the airspeed command. Figure 6.4 gives the control scheme which utilizes longitudinal separation feedback (ξ). The proportional gain (K_ξ) was determined using the Ziegler-Nichols tuning method as a first guess. This heuristic method was selected because it gives a simplistic approach to find the gain for a complex model. In this empirical method of tuning, the critical gain ($K_{\xi cr}$) is first determined by adjusting the gain until the critical value is obtained, as illustrated by Figure 6.5, where the critical gain is defined as the proportional feedback gain for which the closed-loop system becomes marginally stable.

6.1 Formation-Hold by Conventional Control Augmentation

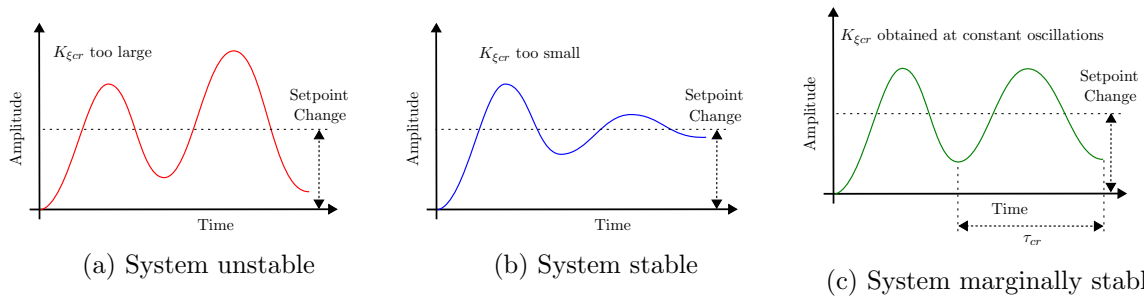


Figure 6.5: Experimentally determining the critical parameter for Ziegler-Nichols controller tuning

Equation 6.1 gives the Zeigler-Nichols relation between the critical gain and the proportional controller gain, as well as the selected gain used for the longitudinal formation-hold control. The Zeigler-Nichols gain was decreased until an acceptable level of overshoot was achieved, yielding the selected gain (K_ξ).

$$\begin{aligned} \text{Zeigler-Nichols P gain:} \quad K_\xi &= 0.5K_{\xi_{cr}} \\ \text{Selected gain:} \quad K_\xi &= 0.125K_{\xi_{cr}} \end{aligned} \quad (6.1)$$

The rate limiter in Figure 6.4 regulates the speed at which the follower aircraft can approach the leader. This rate limiter is placed outside the loop to preserve the fast system dynamics, thus only regulating the speed at which the longitudinal separation command is applied.

6.1.1.2 Longitudinal Formation-Hold: Specifications and Response

The longitudinal separation parameter has low sensitivity in this formation flight model, since the longitudinal wake propagation is assumed to be constant between 10 and 40 wingspans [13, 39]. A slow longitudinal response is preferred to reduce dynamic throttling on the engines, which can lead to irregular engine use and excessive fuel consumption. Thus, in order to optimize fuel consumption, overshooting the longitudinal separation should be avoided.

Figure 6.6 shows the longitudinal separation response for the different gain values. With the Zeigler-Nichols tuning method, the critical gain ($K_{\xi_{cr}}$) was obtained for which the closed-loop system becomes marginally stable. For the longitudinal formation-hold proportional controller, a 120 seconds setting time was achieved with less than 5% overshoot for a proportional control gain (K_ξ) of 0.125 the critical gain ($K_{\xi_{cr}}$).

6.1 Formation-Hold by Conventional Control Augmentation

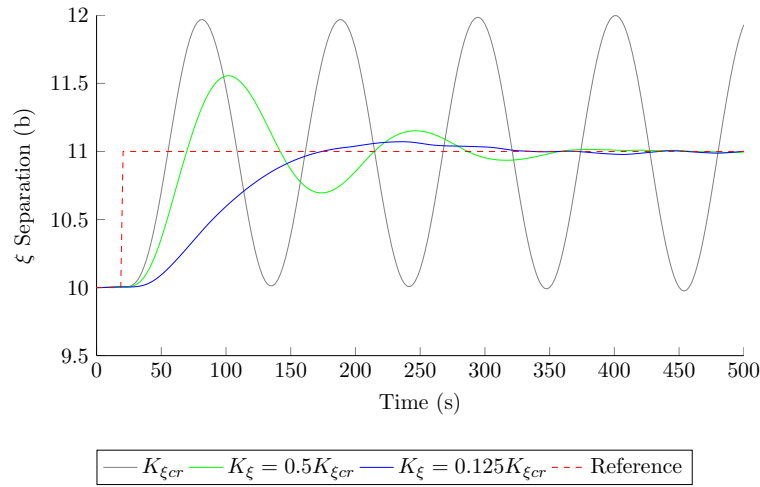


Figure 6.6: Longitudinal formation-hold proportional controller response for a unit step command in longitudinal separation for various gains where $\eta = 1$ and $\zeta = 0$

In the longitudinal formation-hold controller, the proportional controller was effective in regulating the longitudinal separation between the leader and the follower aircraft. Zeigler-Nichols proportional control tuning served as a simple first estimate to find the control gain for this complex system.

6.1.2 Vertical Formation-Hold

The vertical formation-hold control regulates the follower aircraft's altitude with respect to the leader aircraft. The vertical separation parameter (ζ) is defined as the altitude difference between the leader and the follower aircraft, normalized by the aircraft wingspan as given by Section 3.7. Since altitude control was designed and implemented in Section 5.1.4 on both the leader and the follower aircraft, only a slight remapping of the follower control feedback was required to achieve vertical formation-hold.

This section will discuss the design, specifications and response for the vertical formation-hold control augmentation.

6.1.2.1 Vertical Formation-Hold: Control Design

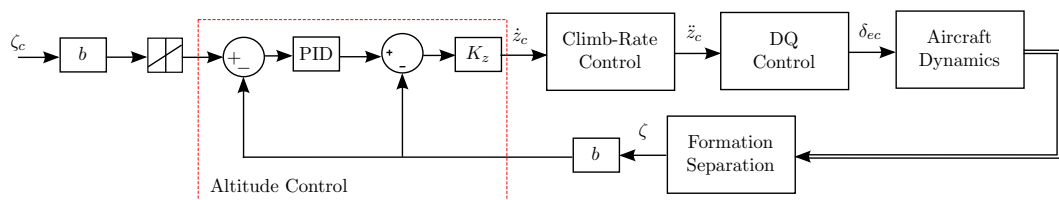


Figure 6.7: Formation-hold vertical control design

6.1 Formation-Hold by Conventional Control Augmentation

The primary difference between the altitude controller for isolated flight and the vertical formation-hold control for the follower aircraft is the feedback source. The altitude control feeds back altitude perturbation about trim, whereas the vertical formation-hold feeds back the vertical separation state (ζ), as seen in Figure 6.7. This state is normalized to aircraft wingspan (b) and must be converted back to meters in order to retain the control gains as used in altitude control. This gives the vertical formation-hold control the same zero error tracking, quick response time and effective disturbance rejection as the altitude controller. The vertical separation command signal is scaled and regulated by a rate limiter outside of the control feedback loop. This rate limiter commands the speed at which one aircraft approaches the other, while not affecting the fast inner-loop dynamics of the altitude control. This command rate limitation also decreases vertical separation overshoot for large step commands.

6.1.2.2 Vertical Formation-Hold: Specifications and Response

The altitude control was designed and tested to provide zero error tracking and a settling time of less than 30 seconds. With the PID in the altitude control, good disturbance rejection was also achieved. Since the altitude control and the vertical formation-hold control use the same control gains, a similar response was expected, but with the effect of wake non-linearities included in the follower dynamics.

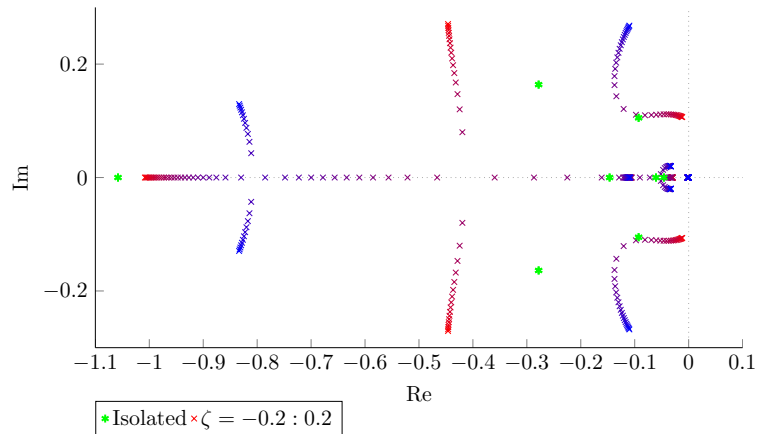


Figure 6.8: Vertical formation-hold controller pole movement for ζ between -0.2 and 0.2, from red to blue, with $\eta = 1$ and $\xi = 10$

Figure 6.8 gives the vertical formation-hold controller pole movement over the optimum region in the wake. This figure shows that the altitude control design stabilizes the follower aircraft in the wake. From this pole plot it is observed that the system damping reduces as the aircraft moves above or below the optimum vertical separation of $\zeta = 0$. However, approaching the optimum from above yields a higher system damping. This is an effect of the vortex circulation velocity vector hitting the wing surface at an angle instead of the perpendicular wash at zero ζ .

6.1 Formation-Hold by Conventional Control Augmentation

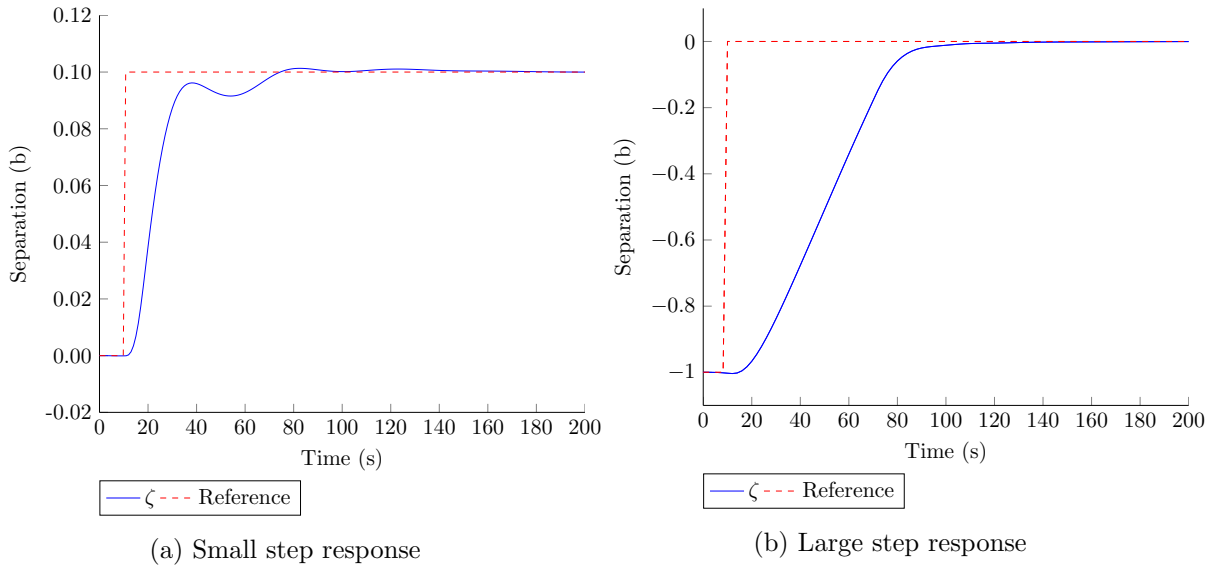


Figure 6.9: Vertical formation-hold controller for $\eta = 1$ and $\xi = 10$: a) small step response for vertical separation from $\zeta = 0$ to $\zeta = 0.1$ and b) large step response for vertical separation from $\zeta = -1$ to $\zeta = 0$

Figure 6.9 gives the control responses for both a small and a large step in vertical separation. For the small step response in a), the fast response time of the altitude controller can be observed in the vertical formation-hold control. However, the oscillatory settling response is a result of light damping of the wake dynamics above zero ζ , which can be observed in Figure 6.8. The response for a large step input in b) is mostly governed by the vertical separation command rate limiter, which is set to 1 m/s.

By remapping the altitude controller, effective vertical separation control was achieved, as illustrated in Figure 6.9. This results in a vertical formation-hold controller with fast dynamics, zero steady-state tracking and good disturbance rejection, similar to the altitude control.

6.1.3 Lateral Formation-Hold

The lateral formation-hold control is responsible for regulating the follower aircraft's lateral separation (η) with regard to the leader. The lateral separation is defined as the distance between the leader and the follower aircraft's center of gravity in the Y -direction, as described in Section 3.7. The conventional lateral control proposed in Section 5.2 forms the core of the lateral formation-hold control, since it can provide cross-track distance regulation.

In this section, the lateral formation-hold design, specifications and response are presented.

6.1 Formation-Hold by Conventional Control Augmentation

6.1.3.1 Lateral Formation-Hold: Design

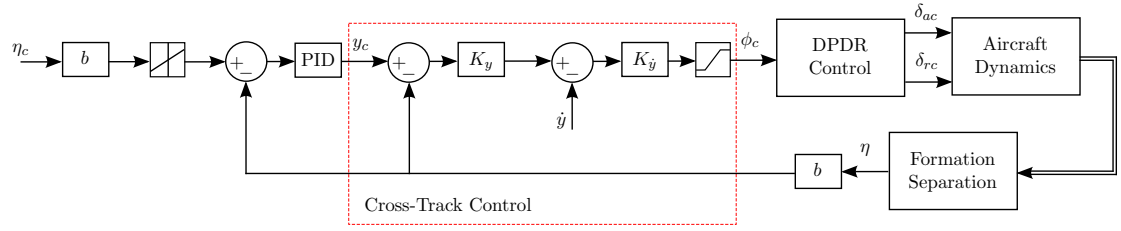


Figure 6.10: Formation-hold lateral control design.

The cross-track controller, as presented in Section 5.2.2, proposed a proportional controller to regulate the cross-track separation with regard to a flight track. By remapping the feedback from the flight track, as presented in Equation 5.32, to lateral formation separation (η), the control effectively becomes a lateral formation-hold controller. However, for the aircraft in isolated flight, the ideal lateral acceleration was calculated with Equation 5.26, which assumes that the aerodynamic force in the Y -direction is zero. In formation flight, this is no longer a valid approximation, as the leader's wake introduces additional aerodynamic forces on the follower (illustrated in Figure 3.10). For the lateral acceleration of the follower aircraft, the aerodynamic force in the Y -direction ($Y_k^A < \eta^*, \zeta^* >$) produces a constant additional acceleration. Thus Equation 5.26 for the follower aircraft should be written as:

$$\ddot{y} = \frac{Y_k^A < \eta^*, \zeta^* >}{m} + \bar{V}\dot{\psi} = \frac{Y_k^A < \eta^*, \zeta^* >}{m} + g \tan \phi \approx \frac{Y_k^A < \eta^*, \zeta^* >}{m} + g\phi \quad (6.2)$$

Changing the cross-track control design to incorporate this wake-induced lateral force requires the practice of non-linear control theory. In order to approach this design with linear theory, this wake-induced lateral force was treated as a disturbance. Thus, for the lateral formation-hold control, the same design was used as for the cross-track controller by ignoring the wake-induced disturbance in the design process. To cancel the disturbance caused by the wake on the follower, a PID controller was augmented to the cross-track P controller. This was done to achieve zero error steady-state tracking, improving the disturbance rejection of the lateral formation-hold control, since the fuel savings are very sensitive to the lateral separation parameter.

6.1 Formation-Hold by Conventional Control Augmentation

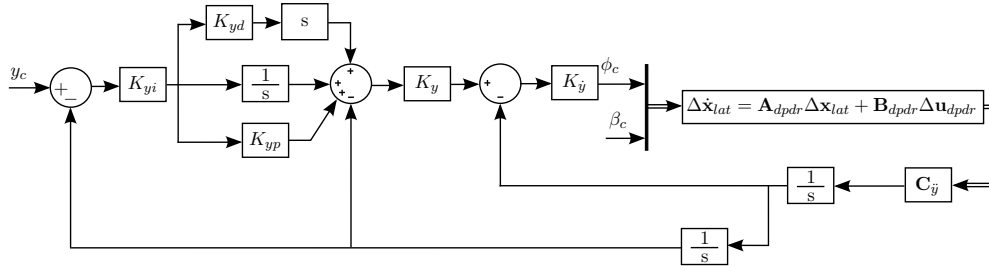


Figure 6.11: Lateral formation-hold control by expanding the cross-track with a PID controller

For the lateral formation-hold control design, the isolated flight cross-track controller was extended with a PID controller, as seen in Figure 6.11. Equation 5.30 gives the open-loop state space model where the cross-track closed-loop P controller isolated flight system matrices can be defined as:

$$\begin{aligned}
 \Delta \mathbf{u}_y &= [y_c] \\
 \mathbf{A}_y &= \begin{bmatrix} \mathbf{A}_{\dot{y}} & \mathbf{0}_{5 \times 1} \\ -\mathbf{C}_{\dot{y}} & 0 \end{bmatrix} - \begin{bmatrix} \mathbf{B}_{dpr:\phi_c} \\ 0 \\ 0 \end{bmatrix} [0 \ 0 \ 0 \ 0 \ 0 \ K_y] & \mathbf{B}_y &= \begin{bmatrix} \mathbf{B}_{dpr:\phi_c} \\ 0 \\ 0 \end{bmatrix} \\
 \mathbf{C}_y &= [0 \ 0 \ 0 \ 0 \ 1 \ 0]
 \end{aligned} \tag{6.3}$$

The cross-track PID control state space model is obtained by augmenting the cross-track P control closed-loop state space model with the PID control integrator state:

$$\begin{aligned}
 \begin{bmatrix} \Delta \dot{\mathbf{x}}_{lat} \\ \dot{x}_{\dot{y}} \\ \dot{x}_y \\ \dot{x}_{yi} \end{bmatrix} &= \begin{bmatrix} \mathbf{A}_y & \mathbf{0}_{6 \times 1} \\ -\mathbf{C}_y & 0 \end{bmatrix} \begin{bmatrix} \Delta \mathbf{x}_{lat} \\ x_{\dot{y}} \\ x_y \\ x_{yi} \end{bmatrix} + \begin{bmatrix} \mathbf{B}_{dpr:\phi_c} \\ 0 \\ 0 \\ 0 \end{bmatrix} \phi_c \\
 y &= [\mathbf{0}_{1 \times 5} \ 1 \ 0] \begin{bmatrix} \Delta \mathbf{x}_{lat} \\ x_{\dot{y}} \\ x_y \\ x_{yi} \end{bmatrix}
 \end{aligned} \tag{6.4}$$

For the SISO state space system in Equation 6.4, a root locus design method was used to place a complex zero pair to increase system damping. This design was completed with MATLAB's root locus design tool.

6.1.3.2 Lateral Formation-Hold: Specifications and Response

For effective lateral formation-hold control, the cross-track P control in Section 5.2.2 was extended to include PID control in the outer loop, as described in Section 6.1.3.1. In the root locus design as given by Figure 6.12a the PID complex zero pair was placed in the region

6.1 Formation-Hold by Conventional Control Augmentation

of the complex pole pair in the cross-track P control closed-loop model. This moved the breakaway point of the root locus branch further away from the origin, thereby increasing the system damping to 0.9. In an isolated flight simulation of the non-linear aircraft model, the PID cross-track response achieved a settling time of about 30 seconds, as presented in Figure 6.12b.

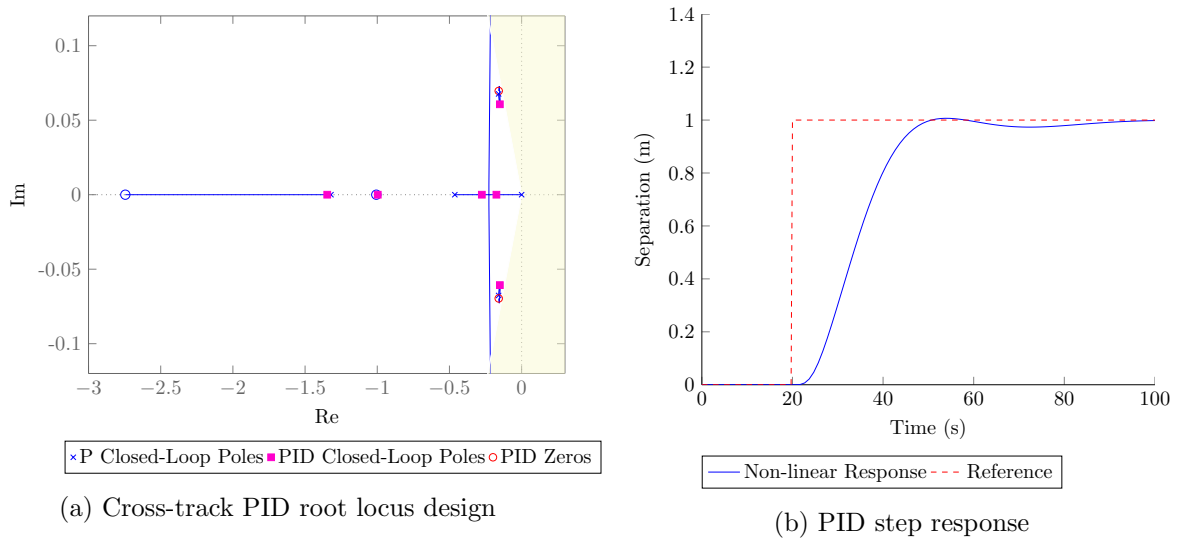


Figure 6.12: PID control: a) root locus design and b) step response in isolated flight

With the design and testing completed for isolated flight, the PID cross-track control was implemented to perform lateral formation-hold control on the follower aircraft. However, as the follower enters the wake of the leader, the system dynamics change and the system damping decreases to 0.3 at the optimum location in the wake ($\eta = 1, \zeta = 0$). Figure 6.13 gives the lateral formation-hold control pole movement as the follower aircraft approaches the optimum. The higher-frequency complex pole pair's damping ratio is reduced as the follower moves deeper into the wake laterally.

6.1 Formation-Hold by Conventional Control Augmentation

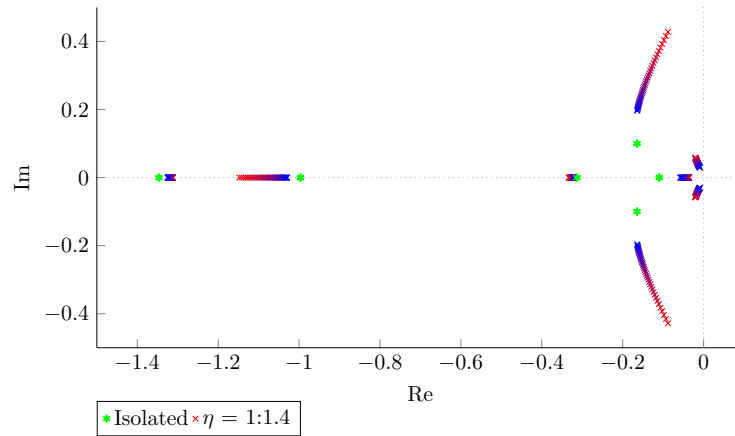


Figure 6.13: Lateral formation-hold controller pole movement for η from 1 to 1.4, moving from red to blue with $\zeta = 0$ and $\xi = 10$

Figure 6.14a shows the lateral formation-hold controller response for a small step in lateral separation deep in the wake. This figure demonstrates the importance of adding the PID controller to the outer loop, as the P controller does not follow the lateral separation command with zero steady-state tracking. For a large step command as seen in Figure 6.14b, the PID controller effectively brings the follower aircraft from the outer wake to the optimum location. The approaching speed is controlled by regulating the separation command signal with a rate limiter outside the control loop. An approaching speed of 1 m/s was selected. Thus the lateral formation-hold controller can effectively regulate the lateral separation between the leader and the follower aircraft even in non-linear wake conditions.

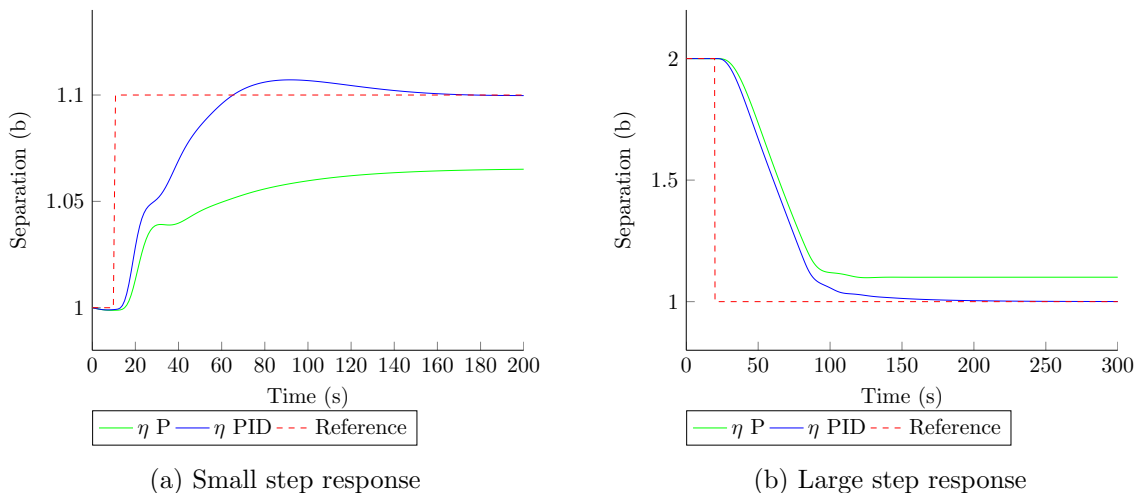


Figure 6.14: Lateral formation-hold controller for $\zeta = 0$ and $\xi = 10$: a) small step response for lateral separation from $\eta = 1$ to $\eta = 1.1$ and b) large step response for vertical separation from $\eta = 2$ to $\eta = 1$

6.1 Formation-Hold by Conventional Control Augmentation

6.1.4 Formation-Hold Control Authority Problem

Thus far in Section 6.1, the formation-hold controller has been discussed and demonstrated. It was observed that the longitudinal, vertical and lateral formation-hold controls all meet the requirement for effective station keeping in the wake. However, the impact of these maneuvers on all aircraft states and control actuators must be considered.

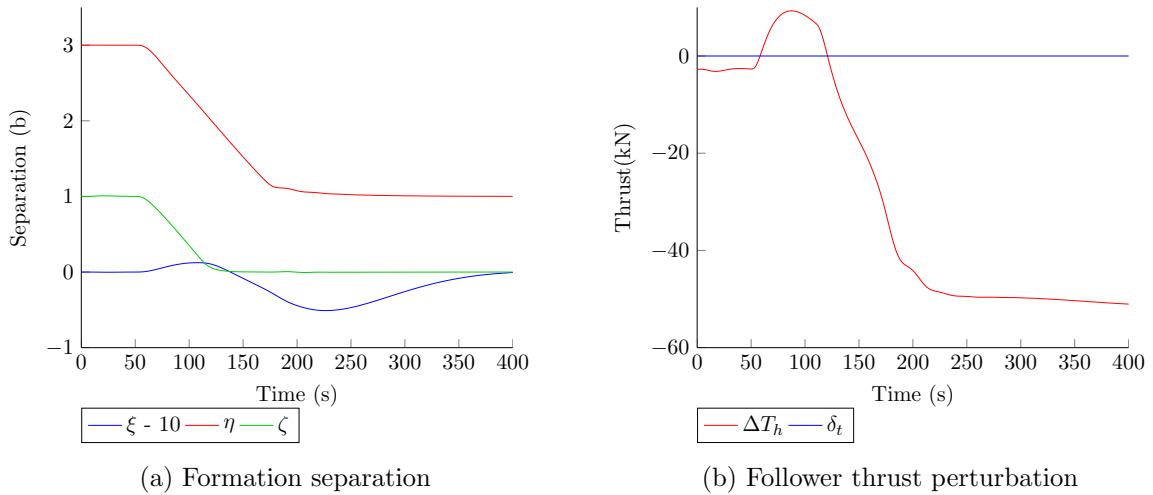


Figure 6.15: Formation-hold control response when flying from the outer wake to the optimum separation ($\eta = 1, \zeta = 0$) for: a) formation separation parameters and b) thrust and differential thrust control perturbation

To investigate the effect of formation-hold control on the follower states and actuators, a separation command was given to the follower to move from the outer wake ($\eta = 3, \zeta = 1$) to the optimal separation ($\eta = 1, \zeta = 0$). Figure 6.15a shows that the follower aircraft could effectively perform this complicated simultaneous maneuver. Figure 6.15b gives the thrust reduction as the follower moves into the wake. Since isolated flight trim thrust is calculated at 176 kN, a total thrust reduction of 51 kN was achieved, thereby producing a 29% decrease in thrust setting on the follower aircraft at the optimal formation separation. This steady-state thrust setting corresponds to the formation trim calculation presented in Figure 4.3a.

6.1 Formation-Hold by Conventional Control Augmentation

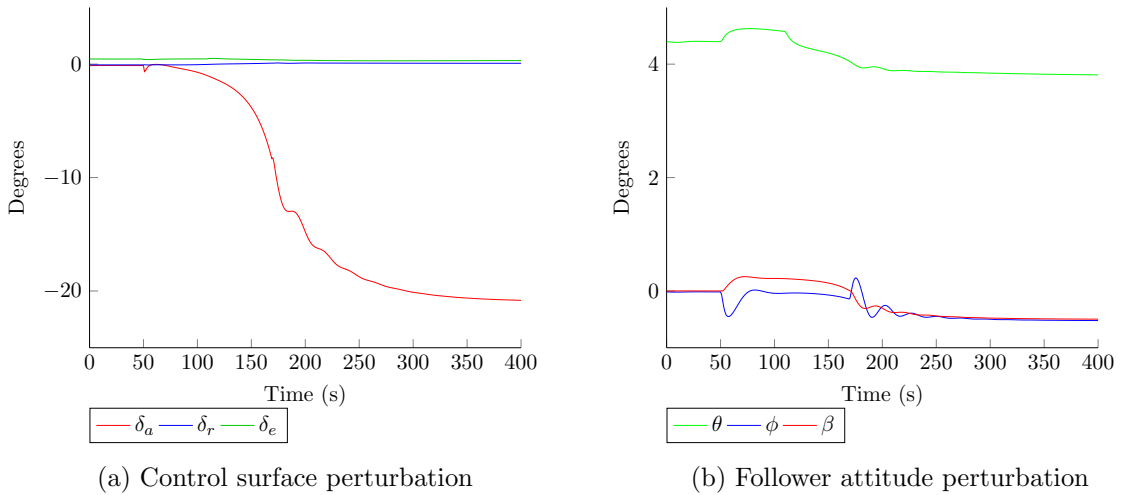


Figure 6.16: Formation-hold control response when flying from the outer wake to the optimum separation ($\eta = 1, \zeta = 0$) for: a) control surface deflection and b) follower aircraft attitude

The large thrust saving caused by the upwash of the leader's wingtip vortex acting on the follower is very favorable. However, the vortex also induces other unwanted forces and moments. The most predominant of these effects are the rolling moment and secondarily the side force induced by the wake. As the follower moves closer to the core of the vortex, the rolling moments increase and additional control authority is required to counter this effect. Figure 6.16a shows how the control surfaces deflect to maintain equilibrium as the follower performs the formation maneuver presented in Figure 6.15a. This figure shows that about 20 degrees of aileron is required to counter the wake's rolling moment, clearly operating the ailerons close their saturation level of 21 degrees. This restricts aileron usage from performing proper disturbance rejection. A secondary practical disadvantage of pushing the ailerons to operate near their limits in steady state is that prolonged use at these deflection levels could increase the occurrence of aileron malfunction, since the design point for the aileron is about zero degrees. From Figure 6.16a, it is also observed that the rudder application is minimal.

The final set of noteworthy parameters is the aircraft attitude angles, which include the pitch, roll and sideslip angles as presented by Figure 6.16b. When the follower performs the formation maneuver given by Figure 6.15a, the steady-state attitude angles changes slightly. The observed reduction in pitch angle is a result of a lowered angle of attack due to reduction in induced drag in the wake. The roll and sideslip angles also reached an equilibrium at about -0.5 degrees from the optimum separation. This roll and sideslip counter the wake-induced side force as the follower banks against the wake.

The primary problem when flying deep in the wake was identified as the large rolling moment induced by the vortex, since it requires extremely high aileron deflection at steady state

[14]. Thus, in order not to saturate the ailerons, a different control strategy was proposed. The following section will present a possible solution to overcome high aileron demand in formation flight.

6.2 Complementary Filter Control

In formation flight, the follower aircraft is continuously exposed to all forces and moments induced by the leader's wake. Although the wake can produce a large reduction in induced drag, it also exposes the follower to a large rolling moment. To counter this rolling moment, the follower has to apply a high-level control deflection, to such an extent that the ailerons saturate as discussed in Section 6.1.4. To address this problem, the other control surfaces were utilized by implementing a complementary filter control authority distribution system as proposed by Prof. Thomas Jones.

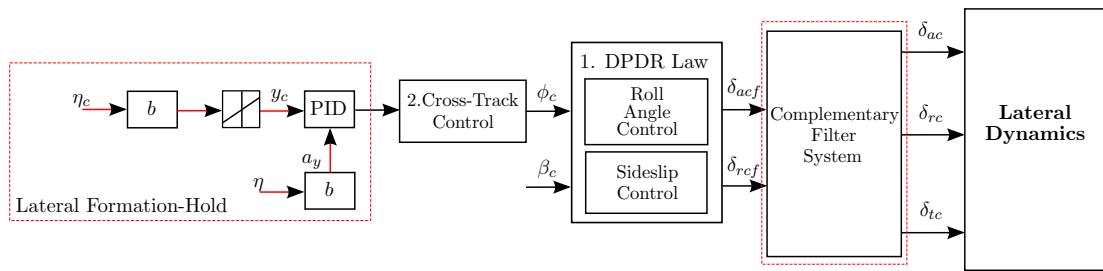


Figure 6.17: Formation-hold lateral control with complementary filter system

Figure 6.17 shows how the complementary filter system links to the lateral formation-hold controller. This system receives control commands from the aircraft inner loop, namely the DPDR controller, which was designed to actuate the ailerons and rudder. These control signals are restructured to mix the control authority in order to utilize all aircraft actuators.

This section will discuss the design and response of the complementary filter system as implemented to reduce aileron demand in formation.

6.2.1 Sideslip Formation-Hold Control

Under the current control design, the follower ailerons saturate deep in the wake while the other lateral control surfaces are left underutilized. This can be changed by applying rudder to produce a sideslip, which results in a rolling moment. This action could potentially relieve some of the aileron demand, as illustrated by Figure 6.18 and demonstrated by the trim calculations presented in Section 4.2.

6.2 Complementary Filter Control

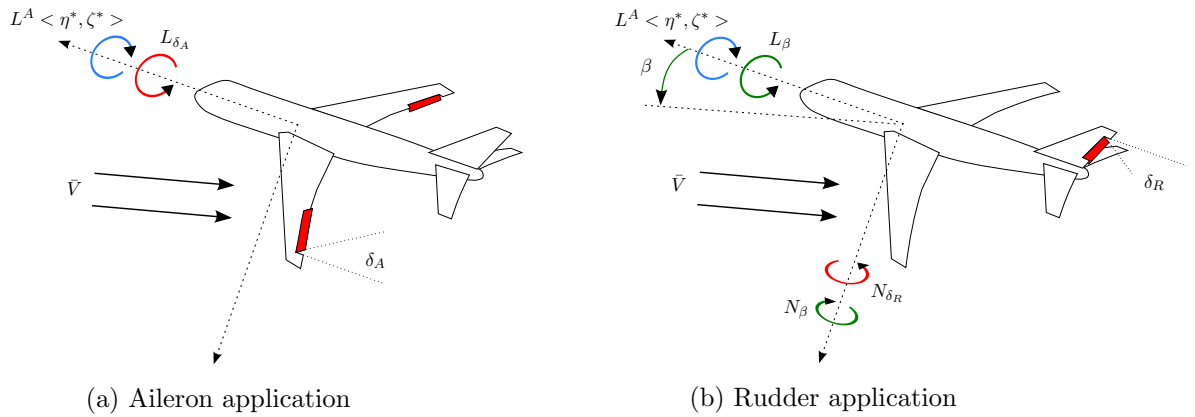


Figure 6.18: Counteracting the wake-induced rolling moment by applying: a) ailerons or b) rudder through the complementary filter system

This section will present and demonstrate a complementary filter system design to relieve aileron demand by inducing sideslip through rudder application.

6.2.1.1 Sideslip Formation-Hold Control: Design

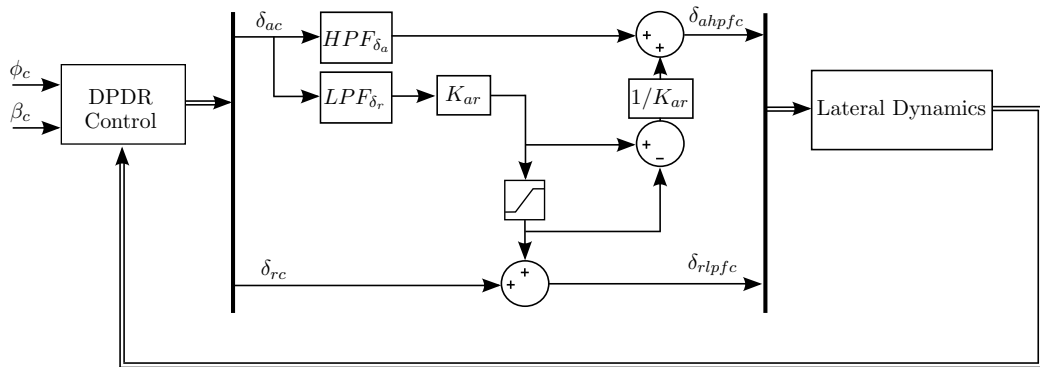


Figure 6.19: Complementary filter system to mix aileron authority to rudder

The sideslip complementary filter system was designed to take the aileron signal from the inner-loop DPDR controller and redistribute some authority to the rudder. Figure 6.19 gives the design scheme to the sideslip complementary filter system. In this case, complementary filter refers to a high-pass filter (HPF) and low-pass filter (LPF) pair, calculated so that the sum of the HPF and LPF signal equals the input signal. In this design, the DPDR aileron signal (δ_{ac}) is passed through the HPF_{δ_a} , sending the high frequency control information to the aileron actuators (δ_{ahpfc}). Parallel to this, the complementary pair’s low-frequency information is filtered out and passed to the rudder, effectively redistributing the aileron steady-state information to the rudder. The HPF_{δ_a} and LPF_{δ_r} filters’ cut-off frequency time constants were selected at twice the lateral formation-hold response time.

6.2 Complementary Filter Control

The gain (K_{ar}) is defined as the gearing ratio between aileron, rudder and sideslip, as given by:

$$K_{ar} = \delta_a : (\beta, \delta_r) = \frac{\left(\frac{C_{n\delta_r}}{C_{n\beta}} C_{l\beta} + C_{l\delta_r} \right)}{C_{l\delta_a}} \quad (6.5)$$

The feed through saturation is included to limit the level of sideslip induced by the complementary filter. The saturated information is fed back to the aileron actuator command.

6.2.1.2 Sideslip Formation-Hold Control: Specifications and Response

The gearing ratio (K_{ar}) was calculated with Equation 6.5 to be 13.5, but was found not to be insensitive in simulation as the control loop adjusts to find a new equilibrium. The complementary filter system HPF_{δ_a} and LPF_{δ_r} pair was designed as two first-order filters with the same cut-off frequency of 0.016 Hz (60 seconds time constant), about twice the settling time of the lateral formation-hold controller. Figure 6.20 gives the magnitude and phase plots for the HPF_{δ_a} and LPF_{δ_r} design.

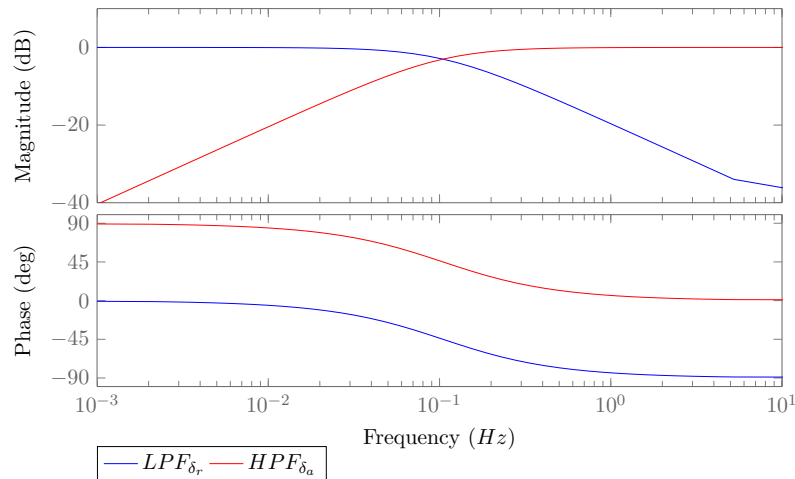


Figure 6.20: Aileron to rudder complementary filter design

With the complementary filter system of Figure 6.19 in action, the same formation maneuver was performed as presented in Section 6.1.4. From Figure 6.21a, the formation separation response with the sideslip complementary filter system active closely matched the formation separation, as presented in Figure 6.15, where the ailerons were primarily applied to counter the wake-induced rolling moment. However, by countering the rolling moment via sideslip, the steady-state thrust reduction dropped to only 42 kN at the optimum separation ($\eta = 1, \zeta = 0$). Thus, a 23 % thrust saving was achieved compared to the 28% in the high aileron application of Section 6.1.4.

6.2 Complementary Filter Control

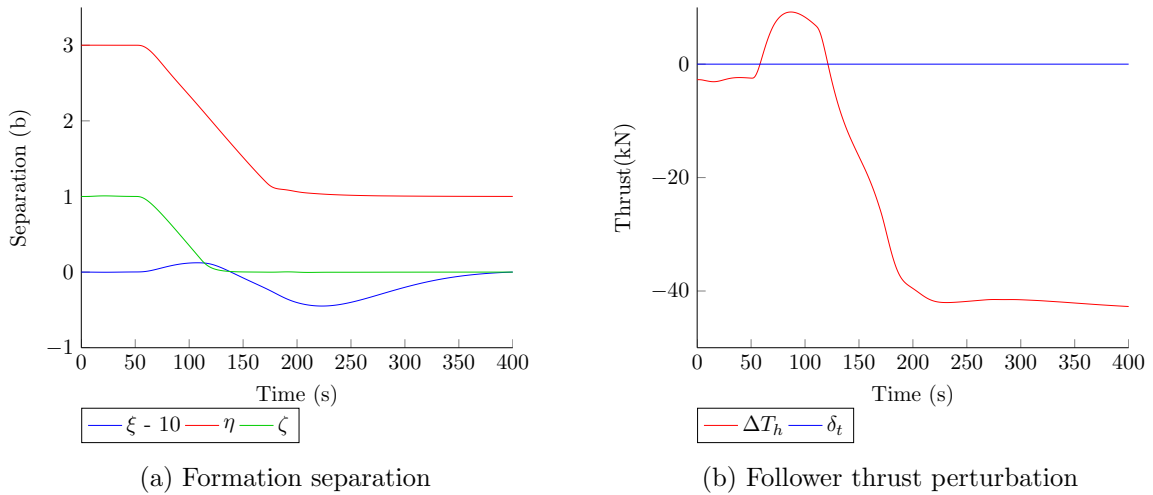


Figure 6.21: Formation-hold control with sideslip complementary filter active. Response for flying from the outer wake to the optimum separation ($\eta = 1, \zeta = 0$) for: a) formation separation and b) follower thrust perturbation

By comparing Figure 6.16a to 6.22a, the significant advantage of using the complementary filter control authority distribution technique in formation flight is demonstrated. This system reduces the aileron demand at the optimum location from 20° to almost zero degrees aileron in steady state. The use of rudder control to counter roll requires the application of sideslip to induce the rolling moment on the follower in the wake. The Boeing 747 has a sideslip-to-aileron rolling moment ratio of 20.2 ($C_{l\beta}/C_{l\delta_A}$). Thus, by applying one degree of sideslip, about 20° of aileron was removed. Figure 6.22b shows the sideslip and roll angles for this simulation. The roll angle also increases to oppose the side force induced by the sideslip as the aircraft banks into the sideslip. This turns the aircraft's lift vector to oppose the sideslip-induced side force ($C_{Y\beta}$). For this simulation, the complementary filter feed through saturation was set to limit the sideslip to 1.5° . The system hits saturation at about 270 seconds, where the LPF_{δ_r} information is fed back to the aileron. The sideslip is limited to create a safety margin, as too much sideslip may introduce unwanted or dangerous effects such as unbalanced wing load distribution or excessive cabin noise. Thus, the level of allowable sideslip and its effects in cruise flight should be further explored.

6.2 Complementary Filter Control

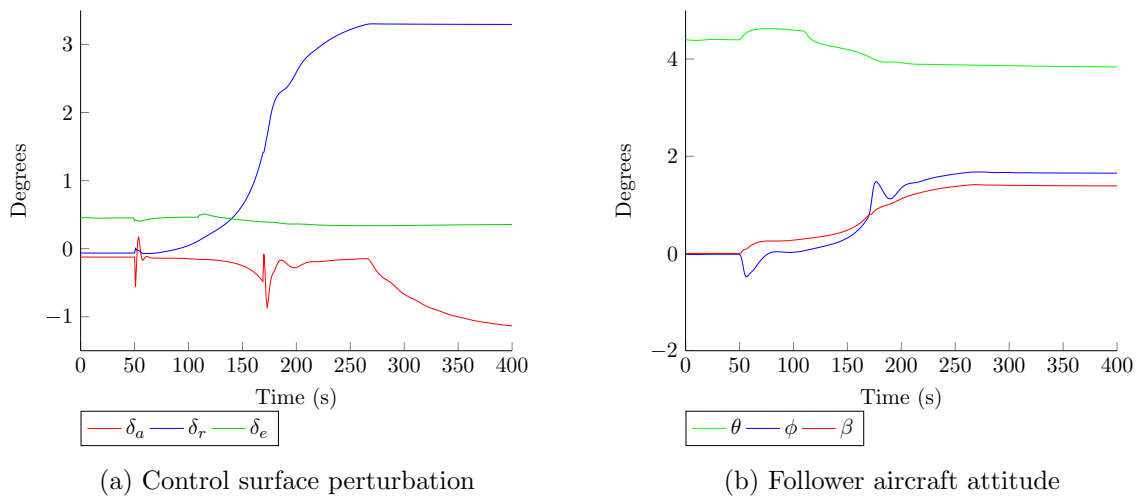


Figure 6.22: Formation-hold control with sideslip complementary filter active. Response for flying from the outer wake to the optimum separation ($\eta = 1, \zeta = 0$) for: a) control surface deflection and b) follower aircraft attitude

These simulation results show how the control authority can be selectively distributed between the control actuators, as long as the control actuation influences the same system states directly or indirectly. In the next section another approach will be considered to relieve steady-state aileron demand.

6.2.2 Sideslip and Differential Thrust Formation-Hold Control

Differential thrust, as defined in Section 3.4.2, offers an additional control input. Applying differential thrust primarily induces a yawing moment on the aircraft, as illustrated by Figure 3.8. This yawing action is capable of pushing the aircraft into a sideslip, resulting in a rolling moment ideal for controlling in the wake. This produces a similar effect as that produced by rudder application. Figure 6.23 shows this principle where differential thrust is applied, instead of rudder is applied to induce sideslip.

6.2 Complementary Filter Control

$(LPF_{\delta_r}, HPF_{\delta_t})$ to divide the rudder control authority to the differential thrust. The cut-off frequency for this set of filters is selected at double that of the aileron-to-rudder set, or four times the lateral formation-hold bandwidth. Thus the high frequencies pass through HPF_{δ_a} to the aileron, maintaining normal flight response in the short band. The aileron command mid-band frequencies pass through LPF_{δ_r} and HPF_{δ_r} to actuate the rudder and therefore the rudder acts between the short band application of aileron and the steady-state application of differential thrust. Note that this control signal is superimposed on the conventional rudder, wide-band control signal. Finally, the differential thrust receives the steady state and lower band frequencies through the LPF_{δ_t} filter, ideal for driving the engines to avoid excessive dynamic commands.

The rudder signal lower-band frequencies passing to the differential thrust command are scaled by the yawing moment gearing ratio (K_{rt}) between the rudder and differential thrust. This ratio was determined by calculating trim with a degree of sideslip for two cases: by setting the differential thrust to zero and applying rudder, and by setting rudder to zero and applying differential thrust. The gearing ratio is defined as the level of differential thrust divided by the level of rudder required to hold the same degree of sideslip trim. Saturation protection is included to prevent immoderate application of differential thrust, which can lead to abnormal engine use far off the recommended design point condition. The saturated information is calculated, scaled and fed back to rudder command.

6.2.2.2 Sideslip and Differential Thrust Formation-Hold Control: Specifications and Response

In the extended complementary filter design, the higher-frequency complementary filter pair $(HPF_{\delta_a}, LPH_{\delta_r})$ and the aileron-to-rudder gearing ratio (K_{ar}) remain unchanged as presented in Section 6.2.1.2. For the rudder-to-differential thrust complementary filter pair, a cut-off frequency of $0.0083Hz$ was selected as half that of the aileron-to-rudder filter pair or four times the lateral formation-hold settling time. Figure 6.25 gives the magnitude and phase plots for the rudder to differential thrust complementary filter pair. First-order filters were designed in which the sum of the LPF and HPF output signals equals the filter pair input signal.

6.2 Complementary Filter Control

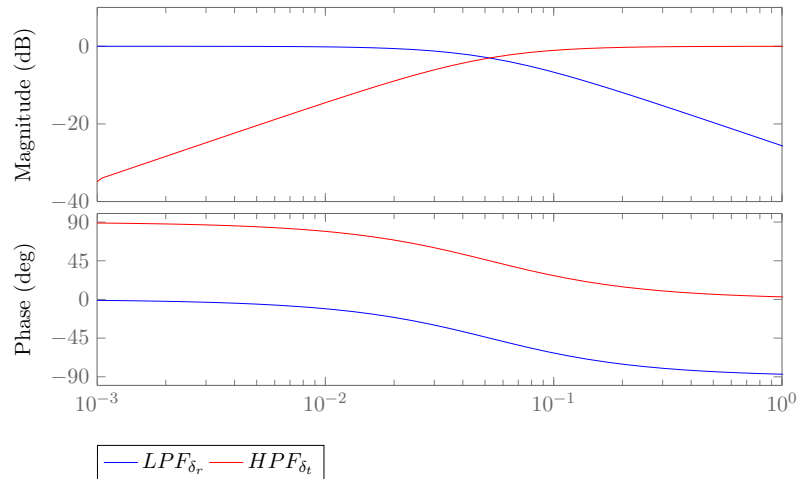


Figure 6.25: Rudder-to-differential thrust complementary filter design

The rudder-to-differential thrust gearing ratio (K_{rt}) was calculated by using Trim Condition Three and Four in Table 4.1. For both trim conditions, the aircraft was set up for isolated level flight at about 1° of sideslip. The first trim condition was calculated with zero differential thrust selected, and the second trim condition was calculated with zero rudder selected. The gearing ratio was then calculated by dividing the differential thrust trim of Condition Four by the rudder trim of Condition Three and gives 1.16×10^6 . The reciprocal of this gearing ratio was used to convert the saturated information back to rudder command. The differential thrust saturation level was selected at 25% of balanced thrust.

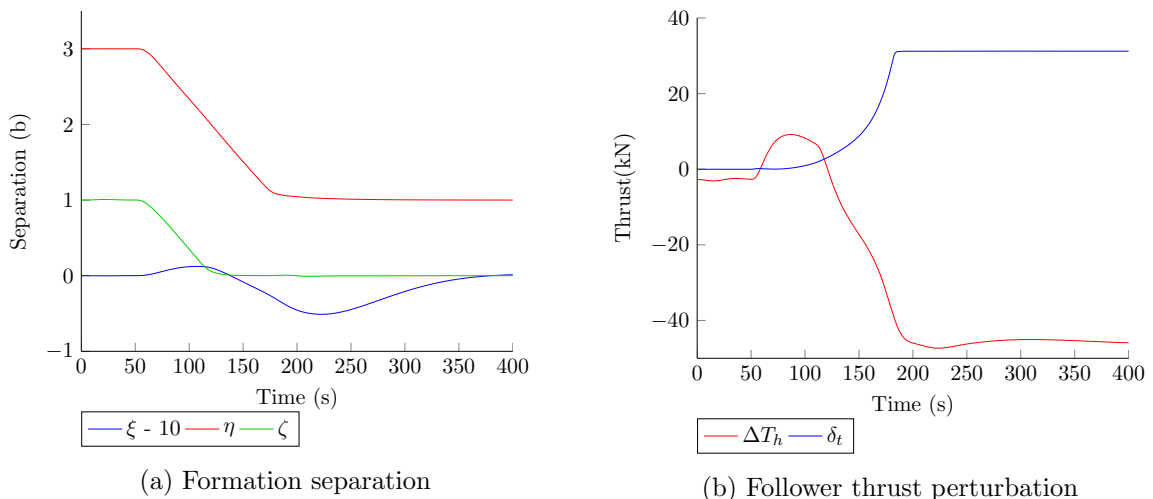


Figure 6.26: Formation-hold control with sideslip and differential thrust complementary filter active. Response for flying from the outer wake to the optimum separation ($\eta = 1, \zeta = 0$) for: a) formation separation and b) follower thrust perturbation

The same formation maneuver as presented in Section 6.1.4 was performed to test extended complementary filter control authority application. Figure 6.27a shows that the same

6.2 Complementary Filter Control

control ability was achieved with the extended complementary filter active, as the response is identical to Figure 6.15a, where no complementary filter was active. The total thrust saving slightly decreases when sideslip and differential thrust are utilized, from a 28% reduction with no complementary filter active to 26% with the extended complementary filter system applied. The result presented in Figure 6.27b also proves that the use of the extended complementary filter with differential thrust (26% thrust savings) is more efficient than the rudder-only complementary filter application (23% thrust savings).

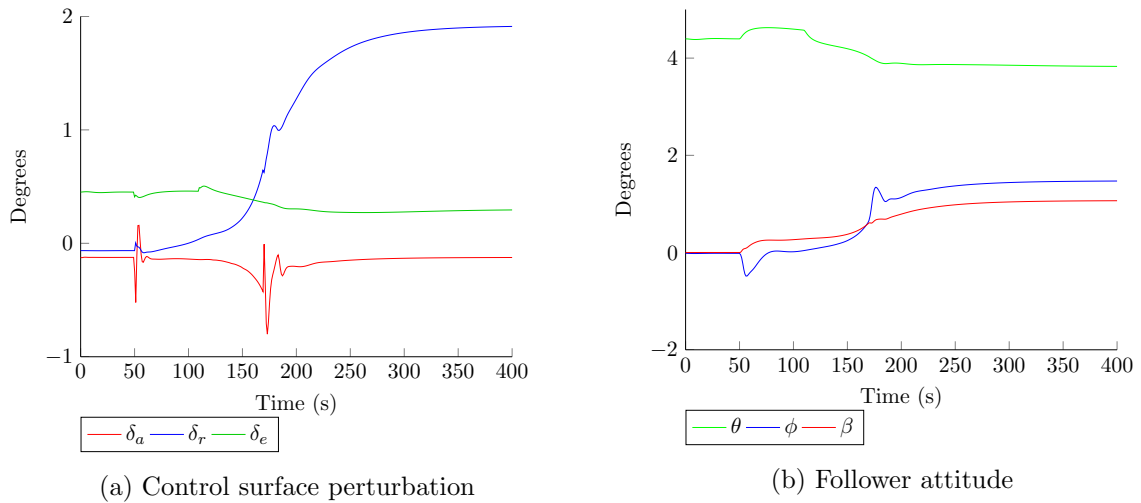


Figure 6.27: Formation-hold control with sideslip and differential thrust complementary filter active. Response for flying from the outer wake to the optimum separation ($\eta = 1, \zeta = 0$) for: a) control surface deflection and b) follower aircraft attitude

For the extended complementary filter system, the differential thrust was limited to 25% that of trim thrust, or 31 kN, as given in Figure 6.26b. As a result, the yawing force created by the additional differential thrust successfully relieved the rudder and aileron application in steady state. When comparing Figure 6.27a to Figure 6.22a, it is observed that the sideslip does not saturate, which means that no steady-state control authority is fed back to the aileron and the steady-state remains about zero. A lower level of rudder application is also observed when flying at the optimum location. Furthermore, due to the force and moment vectors of the differential thrust, a lower level of sideslip is required to counter the wake's rolling moment, as presented in Figure 6.27b.

By applying differential thrust through the extended complementary filter system, the aileron demand to control in the wake was effectively reduced to almost zero. When comparing the rudder complementary filter system and the differential thrust complementary filter system, this extended system has the advantage of requiring less sideslip to counter the roll induced by the wake. Thus, the follower aircraft could be controlled in the wake with a

6.3 Formation-Hold Control Under Turbulent Conditions

minimum level of control surface deflection and sideslip applied.

6.3 Formation-Hold Control Under Turbulent Conditions

In this chapter, a control scheme was proposed to regulate the follower aircraft's spacial separation with respect to the leader, referred to in this work as formation-hold control. In this section, this formation-hold controller is evaluated with von Kármán atmospheric turbulence, as defined in Section 3.9. In Section 5.4, the conventional controllers were evaluated under light, moderate and severe turbulence. It was concluded that the conventional controller struggled to control the aircraft under the rare case of severe turbulence, as the high wind velocities pushed the control surfaces to saturation due to high control gains, selected for fast aircraft dynamics in formation flight. For this reason, and due to the danger of high downwash forces in the inner-wake, formation flight under severe turbulence was not considered viable. These conditions will saturate control surfaces in the wake, which can force the aircraft into a dangerous, uncontrolled scenario. It is thus advisable to disengage from formation when high levels of turbulence are encountered, and to design a gain schedule for higher turbulence levels to relieve control actuators in these extreme conditions.

Test Condition		System State Standard Deviation							
η	ζ	$\eta(b)$	$\zeta(b)$	$\xi(b)$	$\delta_A(\text{deg})$	$\delta_R(\text{deg})$	$\delta_E(\text{deg})$	$T_h(\text{kN})$	$\delta_T(\text{kN})$
Light Turbulence									
1	0	0.002	0.005	0.008	0.413	0.316	0.017	1.628	0.070
1	0.25	0.005	0.006	0.006	0.493	0.341	0.018	1.638	0.447
1	-0.25	0.004	0.004	0.005	0.488	0.332	0.017	1.641	0.074
1.25	0	0.002	0.005	0.005	0.464	0.326	0.017	1.620	0.110
1.5	0	0.002	0.005	0.003	0.478	0.328	0.017	1.617	0.072
2	0	0.002	0.005	0.002	0.480	0.330	0.017	1.620	0.050
Moderate Turbulence									
1	0	0.072	0.126	0.075	10.095	6.924	0.402	34.407	1.009
1	0.25	0.077	0.129	0.087	11.030	7.393	0.434	23.348	5.745
1	-0.25	0.099	0.103	0.074	11.045	7.342	0.408	34.339	1.365
1.25	0	0.050	0.125	0.068	10.293	7.328	0.403	34.660	2.748
1.5	0	0.054	0.123	0.061	10.478	7.350	0.403	34.597	1.414
2	0	0.054	0.122	0.057	10.561	7.350	0.403	34.446	1.000

Table 6.1: The standard deviation over 15 minutes for the formation-hold controllers under turbulent conditions with rudder and differential thrust filter active and $\xi = 10$

Table 6.1 gives the standard deviations for the formation-hold separation parameters and control actuators for a 15 minute simulation in the wake. The follower aircraft was

6.3 Formation-Hold Control Under Turbulent Conditions

initialized at various critical locations in the wake with both the rudder and differential thrust complementary filter systems active. The follower aircraft showed a standard deviation of less than 1% movement, normalized to aircraft wingspan, in light turbulence, thus showing excellent formation tracking ability in the most common cruise flight scenario. In moderate turbulence, the vertical formation-hold controller maintained a 12% standard deviation, which is worse than the lateral and longitudinal formation-hold at about 7%. These standard deviations in the wake were slightly higher than those for the conventional controllers in isolated flight, as presented in Section 5.4. A surprising observation was that the various test conditions showed similar levels of standard deviation for the various selected critical locations in the wake, with only slight (2%) increase in lateral and vertical parameters between the outer wake and the optimum location at $\eta = 1$ and $\zeta = 0$. Thus, the controller performance is not drastically compromised by flight in the outer wake. However, it was found that if the level of turbulence is increased to such an extent that it pushes the follower closer than 0.9 wingspans in lateral separation, the control surfaces saturate and the aircraft loses controllability. This confirms that formation flight should be disengaged or separations increased immediately as moderate to high levels of turbulence are encountered, and that the control gains should be adjusted for medium to high turbulence levels.

Test Condition		System State Standard Deviation							
η	ζ	$\eta(b)$	$\zeta(b)$	$\xi(b)$	$\delta_A(\text{deg})$	$\delta_R(\text{deg})$	$\delta_E(\text{deg})$	$T_h(\text{kN})$	$\delta_T(\text{kN})$
No Complementary Filters Active in Moderate Turbulence									
1.25	0	0.057	0.124	0.061	8.242	5.85	0.390	35.330	-
2	0	0.055	0.121	0.055	8.579	5.823	0.390	34.488	-
Rudder Complementary Filter Active in Moderate Turbulence									
1.25	0	0.054	0.124	0.060	10.144	7.223	0.400	34.746	-
2	0	0.054	0.121	0.058	10.521	7.368	0.403	34.680	-
Rudder and Differential Thrust Complementary Filters Active in Moderate Turbulence									
1.25	0	0.050	0.125	0.068	10.293	7.328	0.403	34.660	2.748
2	0	0.054	0.122	0.057	10.561	7.350	0.403	34.446	1.000

Table 6.2: The standard deviation for the various formation-hold controllers under turbulent conditions with $\eta = 10$, evaluating the application of the complementary filter system

To evaluate the performance of complementary filter formation-hold controller augmentation, moderate turbulence simulations were conducted to test the three controller configurations. These configurations included the formation-hold controller with no complementary filters, with a rudder complementary filter pair and both a rudder and differential thrust complementary filter pair, with sample results displayed in Appendix B.2. The control actuator standard deviation for the no complementary filter controller was slightly lower than with

6.3 Formation-Hold Control Under Turbulent Conditions

the controllers with complementary filters included. However, for the no filter controller the aileron mean was -3.75 degrees and the aileron actuator saturated 4% of the time whereas the rudder complementary filter controller relieved the ailerons to a mean of 0.01 degrees and a level of saturation less than 1% for flight at $\eta = 1.25$ and $\zeta = 0$ under moderate turbulence. The aileron mean value drastically increased as the follower approached the optimum separation ($\eta = 1, \zeta = 0$) for the formation-hold controller with no complementary filter active, even pushing the aircraft to instability as the ailerons saturate.

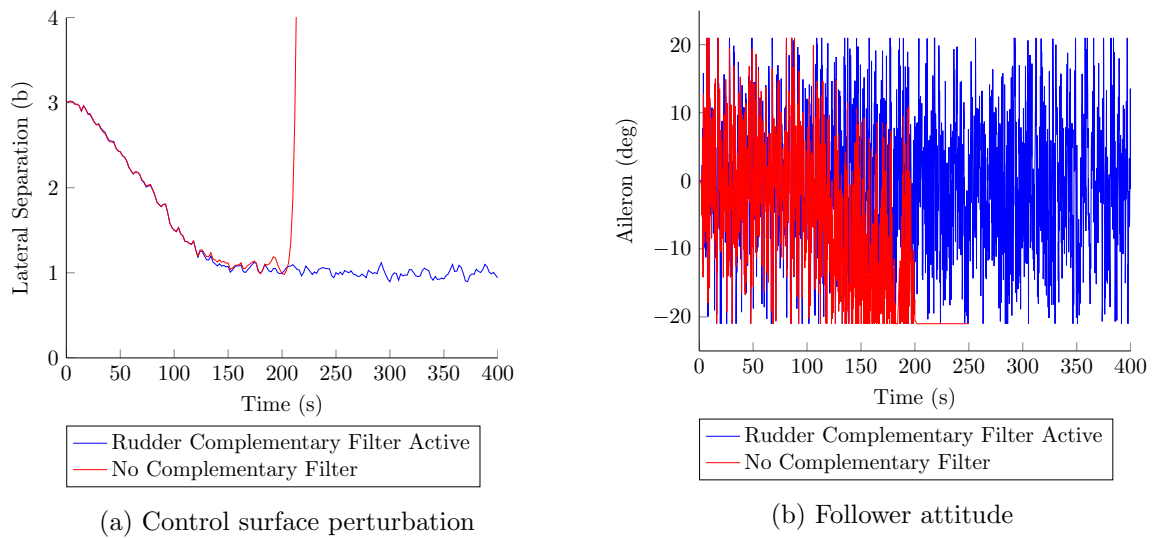


Figure 6.28: Formation-hold control with rudder complementary filter system and without the complementary filter system under moderate turbulence fly at the optimum separation

The follower aircraft could not be controlled for simulations at $\eta = 1$ and $\zeta = 0$ whereas the formation-hold controller had no complementary filter system active under moderate turbulence. For the same simulations with a complementary filter system active, the follower maintained controllability, as shown in Figure 6.28a. No great advantage was observed for simulations where the differential thrust complementary filter was included, and the results looked fairly similar under turbulence. In these simulations the differential thrust was limited to 10% of total thrust and thus induced only minor effects. A conservative 10% was selected to ensure that the aircraft engines remained within the design point limits. Figure 6.28a also illustrates the danger of flying in close formations in highly turbulent conditions. It is advised to further investigate control robustness and flight safety as more representative wake models become available.

These observations showed that the formation-hold control performance was not compromised over various formation separations. An analysis of the use of complementary filters to prevent aileron saturation found that such an augmentation made the formation-hold controller more robust, especially under medium to high turbulence conditions. This enabled

6.4 Formation Flight Efficiency Analysis

the follower to fly deeper in the wake, where more thrust savings can be obtained. Finally, through these simulations it was found that using the differential thrust in the complementary filter were limited to 10% held no real advantage for the system.

6.4 Formation Flight Efficiency Analysis

The formation flight interaction model implemented in this study, as derived by Bizinos et al. [13], was found to overestimate the forces and moments induced by the wake aerodynamic interactions, as discussed in Section 3.8.2. This over-prediction was confirmed by calculating the thrust trim in the wake. A maximum thrust savings of almost 80% was calculated for the optimum separation at $\eta = 0.78$ and $\zeta = 0$, as discussed in Section 4.2. It was decided to only fly in the follower aircraft in the outer wake where the wake model showed reasonable correlation to wind tunnel measurement data, as per Figure 3.13. At the optimum in the outer wake, $\eta = 1$ and $\zeta = 0$, thrust savings of about 30% were calculated by the trim analysis. With the formation-hold control implemented to fly the follower at $\eta = 1$ and $\zeta = 0$, this calculated savings prediction could now be evaluated. This full non-linear model also included an engine fuel flow model as discussed in Section 2.3.3, and derived by Sanders et al. [6].

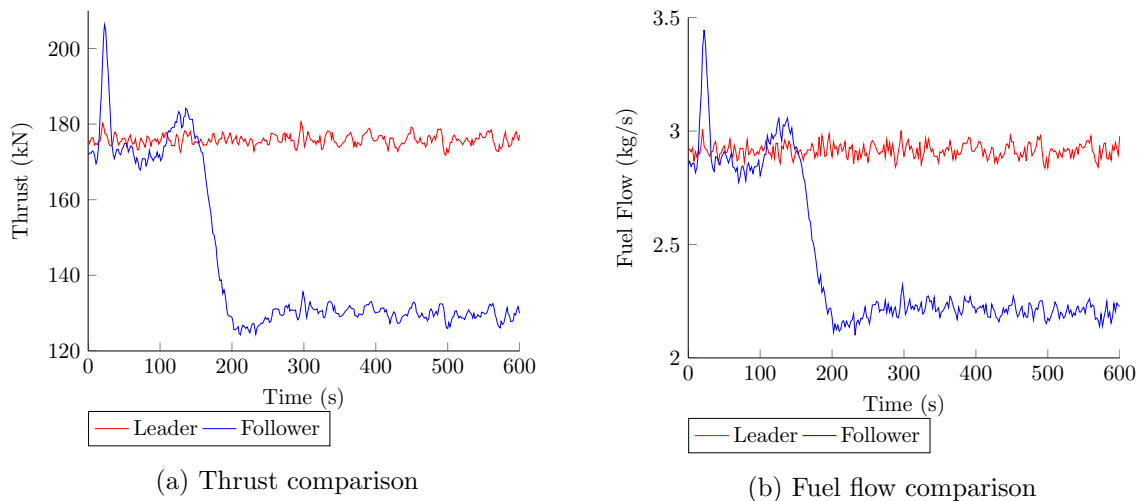


Figure 6.29: Formation flight a) thrust and b) fuel response at $\eta = 1$ and $\zeta = 0$ in light turbulence

Figure 6.29a shows a thrust comparison between the leader and follower aircraft as the formation-hold controller guides the follower to $\eta = 1$ and $\zeta = 0$ in light turbulence. The leader aircraft applied a mean thrust of 175.8 kN and the follower reduced its mean thrust to 130 kN, which gives a thrust reduction of 26% in light turbulence. Figure 6.29b shows the combined total fuel flow for the four engines for the leader and follower aircraft. The leader aircraft maintained a mean fuel flow of 2.91 kg/s and the follower a mean fuel flow of 2.21

6.5 Concluding Formation-Hold Control

kg/s at $\eta = 1$ and $\zeta = 0$. This 24% reduction in fuel usage signifies the economic potential of formation flight.

This fuel flow and thrust savings estimation accuracy are primarily related to the accuracy of the aerodynamic interaction and fuel flow models. Thus, these results should not be considered a definite but rather a first estimate or attempt to relate formation flight wake interactions directly to fuel savings.

6.5 Concluding Formation-Hold Control

In the first part of this chapter, three controllers were proposed to regulate formation separation by utilizing the conventional flight controls proposed in Chapter 5. Remapping and augmenting the conventional flight controls proved effective in stabilizing and regulating vertical, lateral and longitudinal formation-hold control, up to one wingspan in lateral separation.

Flying close to the optimum separation exposed the follower aircraft to the extremely large rolling moment induced by the wake. This rolling moment was countered by applying dangerously high levels of aileron to counter the rolling moment, pushing the ailerons close to saturation. To prevent aileron saturation, a complementary filter system was proposed.

The complementary filter system was designed to counter the wake roll by inducing sideslip on the follower aircraft. The design filtered the low frequencies of the aileron actuator signal out to the rudder, which induced a sideslip in steady-state, countering the wake rolling moment and relieving the ailerons to around zero at steady-state. The same principle was effectively applied to utilize the differential thrust instead of the rudder only in steady-state to induce sideslip. The filter system included conservative saturation limits to prevent the rudder and differential thrust from pushing the follower into large sideslip angles and operating the engines far from their normal operating design point.

The station keeping of the formation-hold controller under light turbulent conditions was exceptional with a standard deviation of less than 1% for all three separation control parameters. However in moderate turbulence this increased to around 10% which is still acceptable, yet approaches the actuator limit for the current control gains. The turbulence results showed that the complementary filter system significantly improved the formation-hold controller robustness, enabling the follower to fly stably deeper in the wake to obtain an additional lift benefit.

6.5 Concluding Formation-Hold Control

The formation-hold controllers, together with the complementary filter system proposed in this chapter, could effectively perform formation station keeping deep in the wake and follow separation commands with zero steady-state error tracking. The aileron saturation problems deep in the wake was observed, and a complementary filter augmentation was proposed to solve this problem. Thus, the complementary filter formation-hold controller is the first to overcome the large rolling moments induced by the wake on the follower aircraft, with low aileron demand.

Chapter 7

Extremum Seeking in Formation

In Chapter 6, a formation-hold autopilot was presented which effectively controls the follower aircraft to regulate formation separation. This robust formation-hold controller enables the follower aircraft to reduce power demand by flying in the upwash of the leader's wake. This more efficient flight condition is the research drive for the commercial application of formation flight. Through analysis of the wake interaction, as presented in Sections 3.8 and 4.3.3, an optimum formation separation that yields a maximum reduction in power demand is observed. The challenge is to design a controller which can guide the follower aircraft to fly at the most efficient separation. Thus, to maintain this optimum separation, a dedicated extremum-seeking autopilot is proposed for the follower aircraft.

In this chapter, a literature review focused on extremum-seeking control in formation flight is summarized, followed by a proposed controller for optimal fuel consumption in formation flight. In Figure 6.1, an overview of the simulation model components is provided, which shows where extremum-seeking control fits into the model. This chapter addresses the final research objective: the design, implementation and evaluation of a formation flight extremum-seeking controller to minimize power demand.

7.1 Literature Review

A broad-scope literature review on formation flight control for minimum power demand was presented in Section 1.4.4. In this review, the following conclusions were made: Open-loop, model-based approaches are limited by the uncertainty of aerodynamic interference modeling, which is further complicated by the sensitivity of power demand reduction with regard to formation separation [5]. Thus a closed-loop approach should be applied, which optimizes a measurable state. The current available aircraft states are preferred, since additional wake-sensing technologies can be expensive and require further development [25]. One such sensor-based solution made use of wing-distributed pressure sensors for wake-sensing [25].

This proved effective in simulation when combined with an optimization algorithm. Although this can be considered a viable option, the concept was not explored further. This was because the wake interaction model used in the current study, developed by Bizinos [13] and described in Section 3.8, gives the wake influence on the follower as a function of aerodynamic coefficients, while an airflow velocity model is required to simulate the measurements of the sensor array. Fuel flow or engine thrust is not used as an optimization objective, since the bandwidths of these states are very low. Other studies maximized follower aileron demand as a performance objective [20]. This approach is also not ideal, since it applies a high level of aileron for extended use as the follower flies near the optimum at cruise conditions. Angle of attack was further proposed to give an accurate representation of reduction in induced drag, but this measurement is complicated by the unconventional airflow of formation flight. Binetti and others proposed to use follower pitch angle as the optimization objective, since it is an easily measurable state, and related to the angle of attack, see the drag in Figure 3.3 [5].

To minimize pitch angle, various optimization algorithms can be utilized. One such optimization scheme, as implemented by Binetti, can locate the extrema with very limited knowledge of the aircraft and wake model. This adaptive-feedback, extremum-seeking control scheme, derived from extremum-seeking work by Krstić [4, 5], applies plant input perturbations to sense the gradient of the optimization objective. A controller then steers the plant states towards the maximum or minimum.

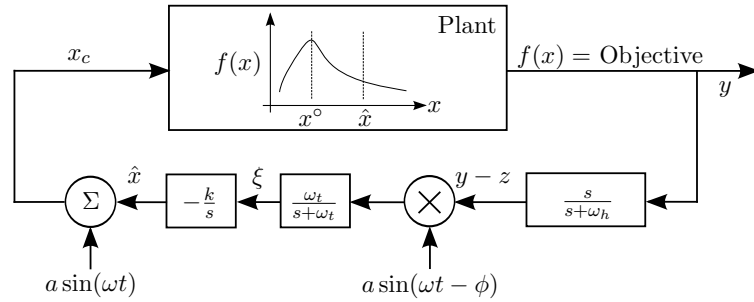


Figure 7.1: Extremum-seeking control scheme as proposed by Krstić [4]

This control scheme, as presented in Figure 7.1, is a simple method to seek extrema of static non-linear maps $f(x)$. The basic operation involves the induction of a 'slow' periodic perturbation signal $a \sin(\omega t)$, which is superimposed on the plant input x_c , to give the current best estimate $f(\hat{x}_c)$ of the extrema $f(x^\circ)$ as produced by the input setpoint \hat{x}_c . If the perturbation is 'slow', then the plant appears as a static map and its dynamics do not interfere with the extremum-seeking scheme. If \hat{x} is on either side of x° , the perturbation $a \sin(\omega t)$ will create a periodic response in y which is either in phase ($\hat{x} < x^\circ$) or out of phase ($\hat{x} > x^\circ$) with $a \sin(\omega t)$. This results in a positive or negative control reference signal ξ to converge the system towards the extremum x° . The high-pass filter, $\frac{s}{s+\omega_h}$, eliminates the

'DC component' in y , resulting in an approximately zero mean sinusoidal response in $(y - z)$ at a frequency of ω . The modulation of the two sinusoids will produce a 'DC component' and a higher-frequency component, as show by the following trigonometric relation:

$$(y - z)a \sin(\omega t - \phi) \approx \frac{(a^2)f'(\hat{x})}{2}(1 - \cos(2\omega t)) \quad (7.1)$$

Where ϕ represents the phase lag between $a \sin(\omega t)$ and $(y - z)$. The constant amplitude or 'DC component' in Equation 7.1 is extracted by the low-pass filter, $\frac{\omega_t}{s + \omega_t}$, and gives the control reference signal ξ , which is also referred to as the approximate sensitivity $(a^2/2)f'(\hat{x})$ or the gradient. The integrator result $\hat{x} = (k/s)\xi$ is driven by the new gradient update law $\dot{\hat{x}} = k(a^2/2)f'(\hat{x})$, tuning \hat{x} to the next best estimate. The feedback scheme as presented by Krstić and Wang [4] has proven stability under the following three assumptions [4]:

1. The plant gradient map is continues for the specified range of plant input command possibilities.
2. The plant is robust and thus converges for the entire range of input command possibilities.
3. The optimization objective has a maximum or minimum for a specific input command.

The extremum-seeking feedback system operates within three timescale ranges. The plant and stabilization controller acts in the fastest timescale range, the periodic perturbation signal acts in the medium range, and the filters in the extremum-seeking scheme act in the slowest timescale range.

Binetti implemented a formation simulation model of two Lockheed C-5s: a wake model and formation-hold autopilot to serve as the inner-loop dynamics or plant model for the extremum-seeking design procedure. The formation flight work of Binetti [5] based on the extremum-seeking theories of K. Ariyur and Krstić [44], extends the single input optimization problem (as given by Figure 7.1) to a multiple input approach with vertical and lateral formation separation as inputs. Figure 7.2 gives the formation flight extremum-seeking control scheme proposed by Binetti.

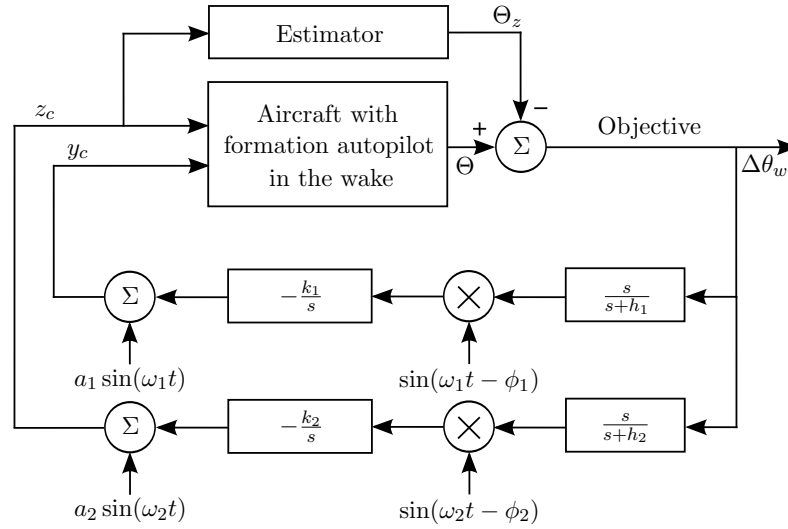


Figure 7.2: Formation flight extremum seeking as proposed by Binetti [5]

The summarized design algorithm proposed by Binetti is as follows [5]:

1. Develop a pitch angle estimator to calculate the change in pitch angle due to upwash, $\Delta\theta_w$, by subtracting Θ_z from Θ . The estimated pitch angle Θ_z describes the pitch angle response due to aircraft movement as induced by the perturbation signal in isolated flight, and Θ is the follower's measured pitch angle in formation.
2. Select ω_1 and ω_2 large, not at equal frequencies in the noise and ensure separation of timescales - about twice the frequency of the dominant poles in the plant model.
3. Set the perturbation amplitudes a_1 and a_2 to actuate a small steady-state error in Θ .
4. Design the low-pass filter to extract the frequency response induced in the optimization objective by the perturbation signal.
5. Determine the phase differences ϕ_1 and ϕ_2 between the perturbation signal and the low-pass filtered signal to perform near-perfect modulation.
6. Design the integrator gain small-limit overshoot.

Binetti successfully demonstrated the use of this extremum-seeking scheme to locate the optimum separation for minimum power demand in formation flight. When considering the current simulation setup and models as presented in previous chapters, selecting the follower pitch angle as an optimization objective and applying the input perturbation through the adaptive feedback scheme seemed feasible as a possible solution for this simulation. The work in this chapter focus on the development, implementation and testing of an extremum-seeking control scheme similar to that proposed by Binetti [5].

7.2 Optimization Objective and Assumption Evaluation

For the extremum-seeking controller an approach will be followed that is based on the adaptive, non-linear feedback control scheme proposed by Binetti [5] and as derived from the extremum-seeking theories of Krstić [4, 44]. However, to apply these theories an optimization objective must be selected, and the system must fit the three assumptions listed in Section 7.1.

Figure 7.3a gives the follower trim pitch angle in the wake (Θ_T) with relation to the lateral and vertical formation separation. When comparing Figure 7.3a to Figure 3.10, it is observed that the pitch angle provides a single, easily measurable optimization objective, which minimizes as the induced drag minimizes and lift maximizes in the wake. Thus, the minimum pitch angle location corresponds to the most efficient position in the wake, at 0.78 lateral and zero vertical separation. However, due to the inaccuracies of the inner-wake aerodynamic interaction model discussed in Section 3.8.2, the follower aircraft's extremum-seeking controller will be designed to only give commands larger than one wingspan in lateral separation ($\eta > 1$).

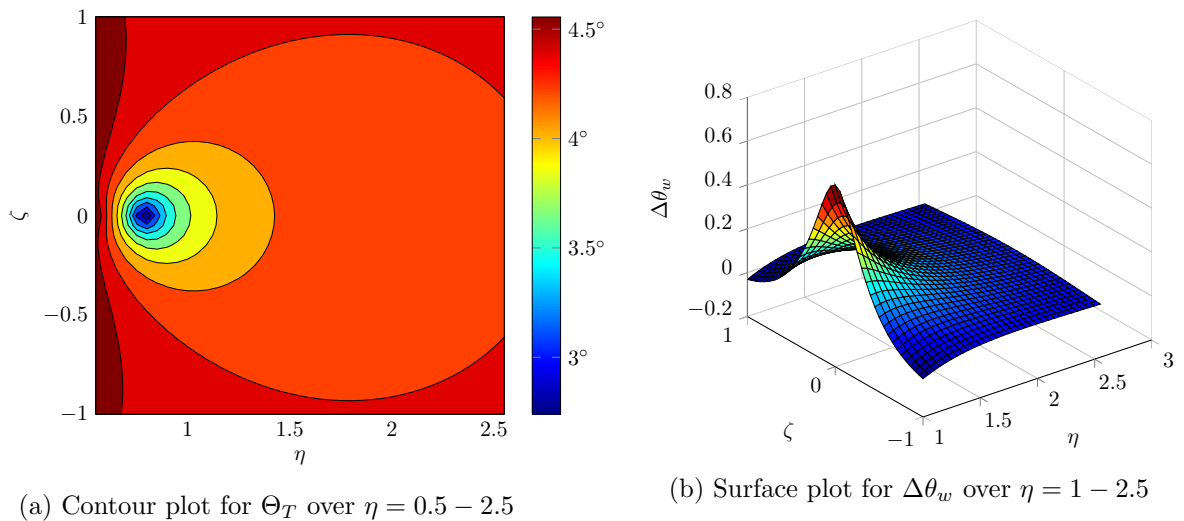


Figure 7.3: a) Follower trim pitch angle in the wake and b) wake-induced change in follower pitch angle trim

The wake-induced change in the follower pitch angle ($\Delta\theta_w$) is selected as the extremum-seeking optimization objective. The optimization objective works best as a static function of the control inputs. Figure 7.3b gives this steady-state objective function with relation to lateral and vertical inputs. This wake-altered pitch angle parameter or optimization objective is defined as:

$$\Delta\theta_w = \Theta - \Theta_z \quad (7.2)$$

7.2 Optimization Objective and Assumption Evaluation

Where Θ is the follower aircraft's measured pitch angle, and Θ_z is an estimation of the aircraft's pitch angle as if the follower was flying in isolated flight - thus a constant of about 4.43 degrees at steady state. The estimator will be discussed in Section 7.3.1.2. Θ_z is subtracted from Θ to give $\Delta\theta_w$, the optimization objective. In this step, as much as possible pitch angle variation of follower aircraft's movement is removed from the optimization objective to extract only the steady-state pitch angle. These removed pitch angle variations are created by movements such as altitude increases induced by the perturbation signal. The aim is to create a static steady-state gradient map of the wake influence on the pitch angle. For a slow perturbation signal, the aircraft movement results in small changes in the pitch angle, and thus it is assumed that the gradient map remains static. Figure 7.4 is the gradient map for wake influence on pitch angle with respect to lateral and vertical separation. For this formation scenario, the leader aircraft flies steady at a normal cruise condition, and thus the gradient map created by the leader's wake remains static, except under turbulent conditions in which the leader will move about a mean. Although this slightly varies the gradient map and affects the performance of the extremum-seeking controller, extremum-seeking should be functional, as the mean of the gradient map will remain static.

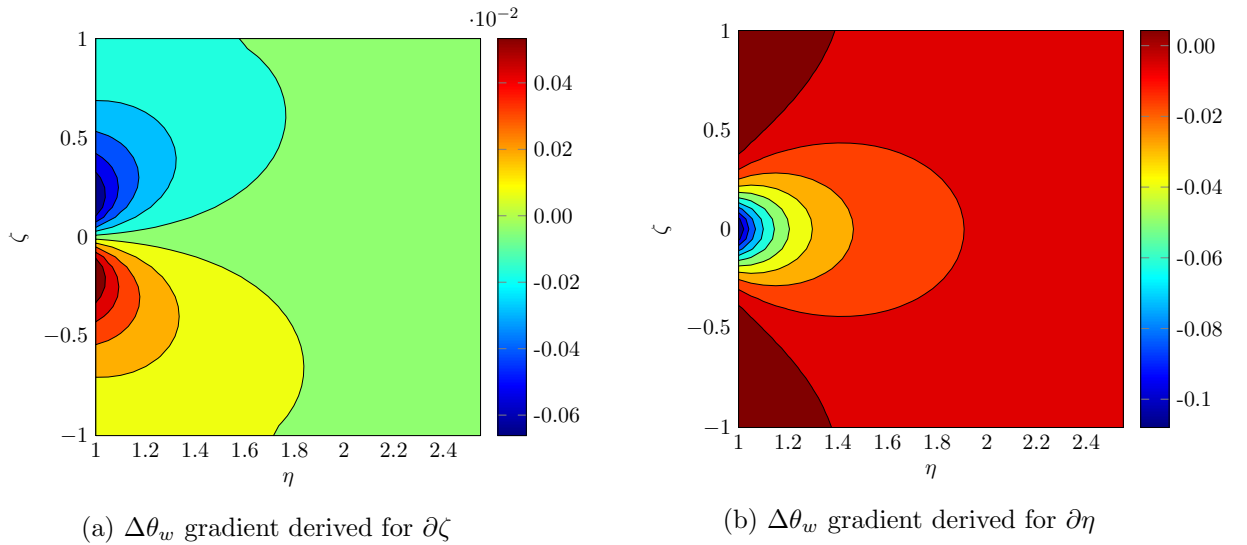


Figure 7.4: Gradient maps for the follower pitch angle in the wake

The first and third assumptions for the extremum-seeking controller, as listed in Section 7.1, can therefore be satisfied, since the optimization objective in Figure 7.3b is smooth and has a definite maximum. The second assumption also holds, since the formation-hold autopilot from Chapter 6 stabilizes the pitch angle for all separation input commands ($\eta > 1$ and all ζ).

7.3 Extremum-Seeking Controller

In this section, an extremum-seeking control scheme is proposed that is similar to the design of Binetti [5], which was based on the extremum-seeking principles developed by Krstić [4]. The follower aircraft's lateral and vertical formation-hold autopilot, with the follower aircraft's dynamics in the wake, served as the inner-loop or plant model for this controller. The follower's pitch angle was selected as the performance objective to be minimized by the extremum-seeking feedback scheme, reducing the induced drag in order to attain a more efficient flight condition.

The extremum-seeking controller operates on a perturbation or dither signal principle. This perturbation signal is applied to the plant inputs to move the aircraft around a mean separation in circular motions. This enables the controller to 'feel' the gradient of the wake as an integrals controller moves the follower towards the new, more efficient, mean separation, until the optimum is reached.

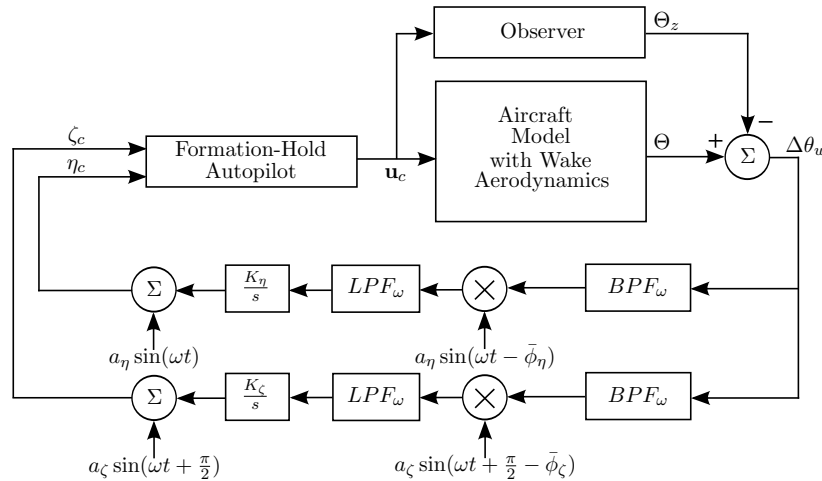


Figure 7.5: Proposed extremum-seeking control scheme for optimal fuel consumption in formation flight

Looking at this optimization process in more detail, Figure 7.5 gives the extremum-seeking control diagram. The perturbation signals, $a_\eta \sin(\omega t)$ and $a_\zeta \sin(\omega t + \frac{\pi}{2})$, are superimposed on the current best separation estimates, and applied to the extremum-seeking controller inputs η_c and ζ_c . The vertical separation dither is shifted 90 degrees out of phase with the lateral command to fly the follower aircraft in small, slow circular motions. The amplitudes, a_η and a_ζ , are adjusted to realize the small perturbation movement on aircraft. For this motion, the influence of the wake gradient on the follower's pitch angle, $\Delta\theta_w$, is extracted and used as feedback for the extremum-seeking optimization. The signal is further filtered by BPF_ω to pass only the information in the frequency range of the perturbation signal. This helps

7.3 Extremum-Seeking Controller

to structure the pass-through signal as purely sinusoidal in the ω frequency range, which is ideal for near-perfect signal modulation. To perform this modulation, a phase correction of $\bar{\phi}_\eta$ or $\bar{\phi}_\zeta$ must be applied, where the phase is determined by the mean of the plant phase lag between perturbation input and band-pass filter output. The post-modulation signal consists of a 'DC component' and a higher-frequency component, as shown by the trigonometric identity in Equation 7.1. The 'DC component' is extracted through a final filter LPF_ω , and integrated to produce the next best estimate of the optimal separation. Again, the perturbation signals are superimposed on the best separation estimate, and the process is repeated to converge the best estimate to the optimal separation.

7.3.1 Extremum-Seeking Design Procedure

The extremum-seeking controller is realized on the follower aircraft by including three supportive systems: a logic controller, a pitch angle observer, and phase synchronization on both the vertical and lateral loops. The architecture for the lateral extremum-seeking loop is given in Figure 7.6.

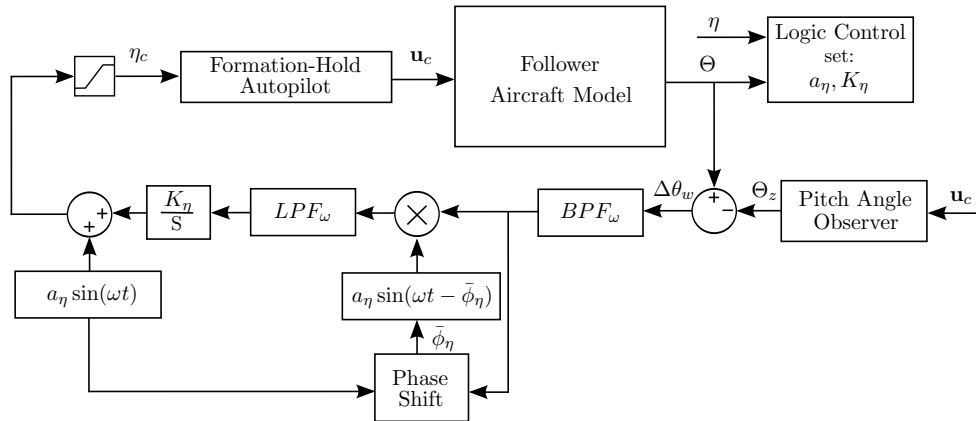


Figure 7.6: Lateral extremum-seeking control loop architecture

The vertical extremum seeking loop architecture is almost exactly similar to the lateral, except for the 90° phase shift in the perturbation signal as shown in Figure 7.7.

7.3 Extremum-Seeking Controller

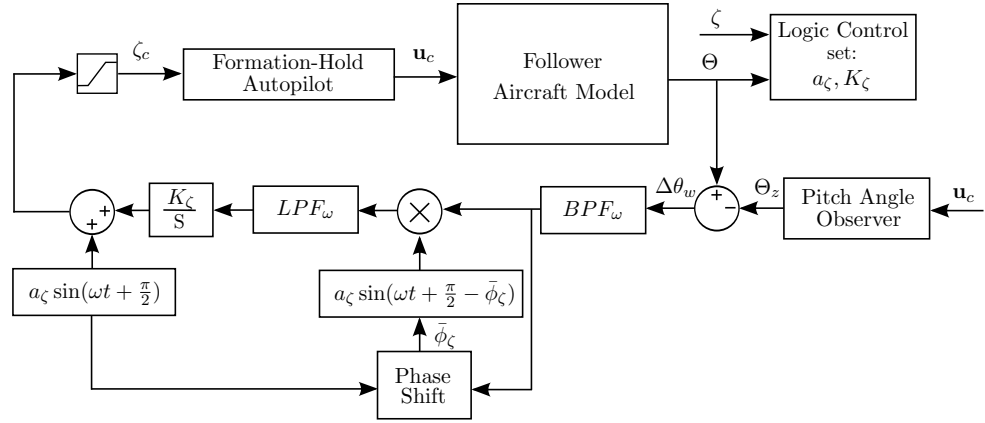


Figure 7.7: Lateral extremum-seeking control loop architecture

The following design procedure was followed to set up the lateral and vertical extremum-seeking control loops:

1. Set the integrator gains K_η and K_ζ to zero.
2. Select a perturbation frequency ω sufficiently slow not to saturate control actuators.
3. Design BPF_ω with ω as the center frequency, and LPF_ω with ω as the cut-off frequency.
4. Adjust the perturbation amplitude in a_η and a_ζ to produce the same oscillation amplitude for both axes in the range of 1% to 3% of wingspan.
5. Initialize the follower about 30% of wingspan from the optimum, and increase K_η and K_ζ until the extremum seeking converges to the optimum with a satisfactory settling time and limited overshoot.
6. Set the logic controller to activate and deactivate the extremum seeking at the defined boundaries.

The next three subsections will discuss the design and setup for the extremum-seeking supporting systems.

7.3.1.1 Phase Synchronization

Phase synchronization plays an important role in the extremum-seeking autopilot, as it sets up the modulation to calculate the gradient law update. The phase shift can be calculated through an in-depth model analysis of the isolated aircraft and all autopilots. However, this would only produce a single phase shift for the current model setup. Instead, 'online' phase synchronization is proposed. The following equation is used to calculate the mean phase difference between the perturbation signal and the band-pass filter output:

$$\bar{\phi} = \frac{\sum \cos^{-1} \left(\frac{\mathbf{Q}_\omega \cdot \mathbf{Q}_\theta}{\|\mathbf{Q}_\omega\| \|\mathbf{Q}_\theta\|} \right)}{N} \quad (7.3)$$

Where $\bar{\phi}$ is the calculated mean phase difference between the two signals, \mathbf{Q}_ω is a perturbation signal recording of more than two periods of ω , and \mathbf{Q}_θ is a BPF_ω output signal recording of the same length. It is proposed that the mean is taken over two or more periods, where N is the number of samples. When the extremum-seeking controller is activated the integrator gains, K_η and K_ζ , remain zero for two periods, after which the phase difference is calculated with Equation 7.3. With effective phase synchronization set up for modulation, the K_η and K_ζ gains are increased, and the extremum seeking takes place. The same calculated $\bar{\phi}$ mean is then used for the duration of the flight.

7.3.1.2 Pitch Angle Observer

The pitch angle observer removes pitch angle variation due to aircraft movement from the extremum feedback signal, passing only the mid-band gradient information acquired by the perturbations in the wake. This means that the observer has to estimate the follower's pitch angle response as if it was flying in isolation, Θ_z . If this estimation is inaccurate, $\Delta\theta_w$ will pass inaccurate gradient information to the integrator, and the extremum-seeking performance will be compromised. To simplify the design of the simulation extremum seeking controller, the full-order coupled isolated aircraft state space model will be used as an open-loop observer. The input is taken from the inner-loop control signals as it is passed to the aircraft actuators. The state space model is derived, as described in Chapter 4. However, in a real world flight scenario an accurate state space model can be difficult to obtain. Thus in future work, a more robust pitch angle observer should be developed.

7.3.1.3 Logic Control

The logic control is responsible for activating and deactivating the extremum seeking by adjusting control gains when necessary. To effectively automate the extremum-seeking procedure, the wake behind the leader was divided into five regions. Figure 7.8 shows how the wake was partitioned. A set of logic conditions was implemented to govern the formation control. The region boundaries were set conditional on measurable states, where the gray, blue and green boundaries are defined by formation separation parameters, and the yellow and red boundaries are defined by follower's mean pitch angle.

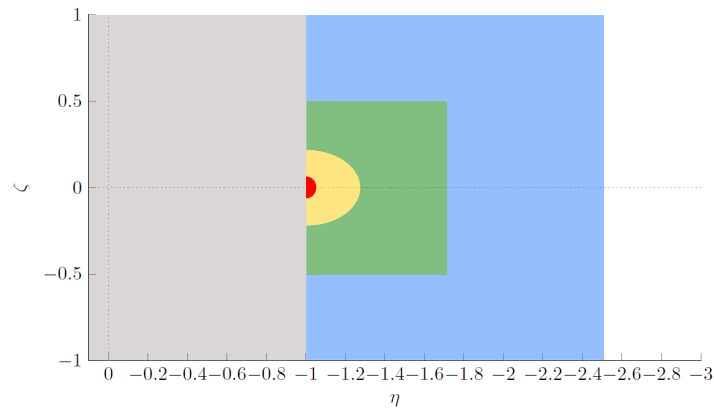


Figure 7.8: Wake map logic partitions

The gray region is considered a no-fly zone. In the blue region, the formation-hold autopilot is active and the green region enables the extremum-seeking. The yellow region adjust the extremum-seeking control gains to operate around the gradients near the optimum. Finally, the red is the defined optimum margin, where the extremum-seeking control is disabled and formation-hold is enabled to maintain the optimal flight condition.

The boundary setpoints for the current design were defined through performance observations during simulations. These boundaries should be recalculated for optimum performance, maximum ride comfort or other requirements as more wake data becomes available.

The control logic can best be explained by means of a flight scenario: As the leader and follower aircraft fly in far proximity, communication is enabled to start formation engagement. The follower pilot flies the aircraft to a medium proximity, and enables the formation flight autopilot by selecting an objective: efficiency, comfort etc. The system adjusts accordingly and the formation-hold autopilot activates, moving the follower aircraft through the blue region as the leader continues in straight and level cruise. When the follower enters the separation-defined green region, the extremum-seeking control is activated. The extremum-seeking controller now seeks the optimum in this region as it 'feels' around the wake gradient. When the mean pitch angle decreases by a predetermined level, the controller senses it has entered the yellow region and is approaching the optimum. As the final optimization margin is achieved, the follower deactivates the extremum-seeking control. This stops the perturbation signal, and the follower remains in formation-hold close to the optimum. If the logic control detects that the mean pitch angle falls outside of the optimization margin, the extremum seeking is reactivated and the process is repeated until the follower pilot selects to disengage from formation. The gray region can be seen as a safety margin. In the inner-wake the downwash of the leader causes large and dangerous forces and moments. Thus it is advised

7.3 Extremum-Seeking Controller

to include a safety margin which keeps the follower a safe distance away from the downwash of the leader.

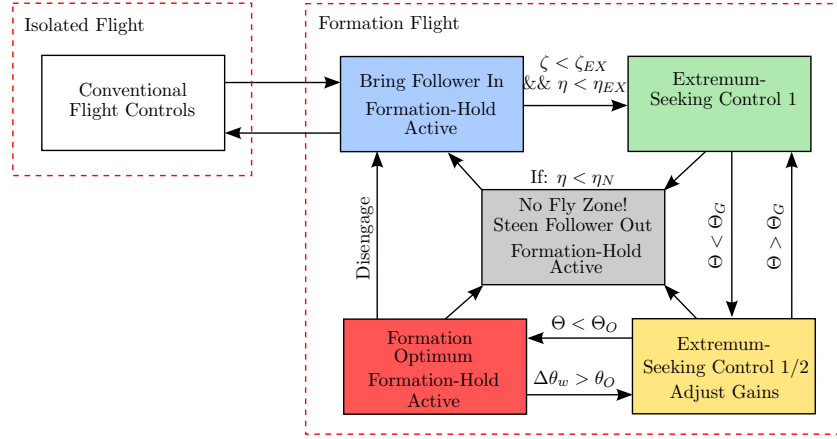


Figure 7.9: Formation flight state machine

The logic controller can be visualized in the form of a state machine based on the scenario described above. Figure 7.9 gives the state machine which supports the extremum-seeking controller, where η_{EX} and ζ_{EX} are the formation separation boundaries at which the extremum-seeking controller becomes activated. These boundaries should be determined to outline the optimum separation or wingtip vortex for all possibilities. The gain change boundary Θ_G should be determined based on the gradient of the wake in order to control effective convergence of the extremum-seeking controller. The gain change boundary is also designed as a 'soft' boundary, where the mean of Θ should meet the condition for a full period of ω . The optimization boundary Θ_O is the margin at which the extremum seeking is deactivated, since the follower is successfully placed at an acceptable degree of optimization, and the perturbation signals can be deactivated at this more efficient cruise condition. This optimization boundary is also designed as a 'soft' boundary because the mean of Θ should meet the boundary condition for a full period of ω before deactivating the extremum-seeking control (or reactivating when the follower strays from the optimum separation condition). Finally, η_N represents the safety margin to protect the follower from flying closer than a pre-determined lateral separation. This keeps the follower aircraft out of the downwash region, and also in this simulation case, out of the inaccurate wake model zone.

7.3.2 Extremum-Seeking Control Specification

To determine the extremum-seeking controller parameters, the design procedure as stated Section 7.3.1 was followed. The tuning process was started by initializing the follower aircraft out of the wake with K_η and K_ζ equal to zero. The first objective was to select a

7.3 Extremum-Seeking Controller

perturbation frequency ω , as fast as possible, yet this signal should not saturate the actuators when sufficiently large perturbations are applied. A perturbation signal period of 30 seconds was selected, which is in the range of settling time for both the altitude and cross-track controllers. The same ω , 90 degrees out of phase, was used for both the lateral and vertical extremum-seeking control to scan the wake in circular motions.

Next, the band-pass and low-pass filters were designed. For both filters a third-order Butterworth filter was selected and the magnitude and phase plots are given in Figure 7.10. The low-pass filter LPF_ω cut-off frequency was set to ω . The band-pass filter BPF_ω cut-off frequencies were set to 0.5ω and 2ω , with the center frequency equal to ω .

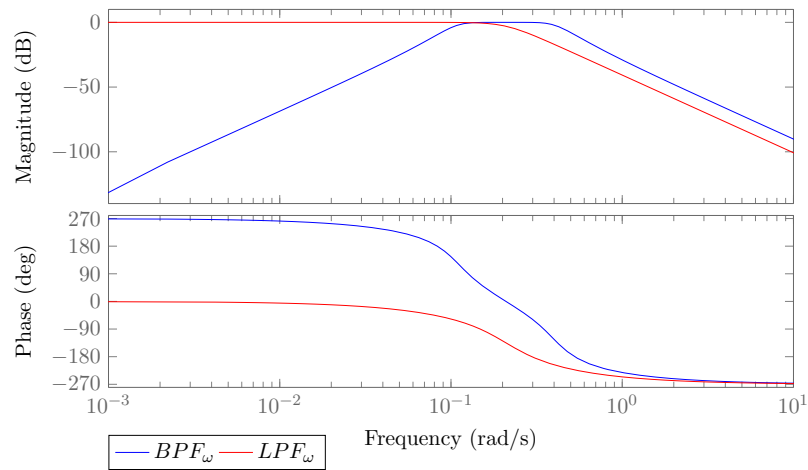


Figure 7.10: Extremum-seeking controller band-pass and low-pass filter design

The perturbation amplitudes a_η and a_ζ were increased to generate a separation response amplitude of about 3% of wingspan for this perturbation frequency. The integrator controller gains K_η and K_ζ were then tuned to achieve sufficient convergence speed with limited overshoot. A gain and perturbation amplitude schedule was implemented to create rough and finer seeking as the aircraft moves from the green to the yellow zone in Figure 7.8. The amplitude and gain values in the yellow zone were set to half those of the green zone. This effectively decreased the convergence time, as the gains could be high to roughly locate the optimum and low to slowly zone in on the peak without overshooting the optimum. Table 7.1 gives the selected logic control boundary values as discussed in Section 7.3.1.3.

7.4 Extremum-Seeking: Simulation Results

Zone Description	Boundary Condition	Zone Color
Safety margin. No-fly zone.	$\eta < 1$	Gray
Formation-hold active. Approach wake.	$1 < \eta < 2.5$ and $-1 < \zeta < 1$	Blue
Extremum-seeking active.	$1 < \eta < 1.5$ and $-0.5 < \zeta < 0.5$	Green
Extremum-seeking gain and amplitude change.	$3.9^\circ < \Theta < 4.1^\circ$	Yellow
Optimum margin. Formation-hold active.	$\Theta > 3.9^\circ$	Red

Table 7.1: Extremum-seeking logic control boundary values

In this section, the extremum-seeking controller was defined and the tuning process was described. The controller gain and amplitude values are included in Appendix A. In the current design example, the controller was tuned for a ω with a 30 second period; however, the process was repeated for 20 seconds to evaluate performance. For faster frequencies, higher amplitude loss and phase lag occur, resulting in high input perturbation amplitude and integrator gains, up to the point where the actuators saturate and turning up the input perturbation amplitude does not increase the realized perturbation amplitude. In the following section, the extremum seeking simulation results will be presented.

7.4 Extremum-Seeking: Simulation Results

With the extremum-seeking controller implemented, as presented in Section 7.3.1 and 7.3.2 the optimum separation $\eta = -1, \zeta = 0$, was successfully located by the follower aircraft with very limited prior knowledge this optimum. Figure 7.11 shows the follower's flight path with regard to lateral and vertical separation. In this simulation, the perturbation period was set to 30 seconds with a 2% of wingspan amplitude. For this simulation, the follower approaches the wake from above. In Appendix B, a simulation is presented where the follower approaches the wake from below for both 30 and 20 second perturbation periods ω .

7.4 Extremum-Seeking: Simulation Results

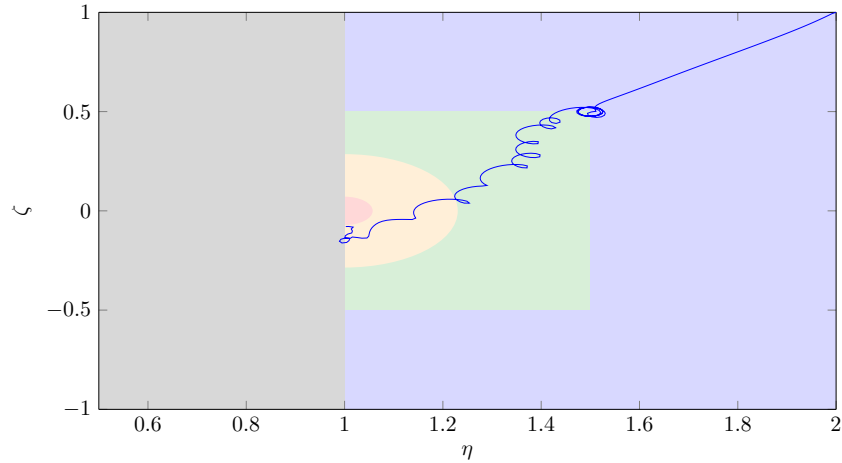


Figure 7.11: Extremum-seeking control flight path with regard to lateral and vertical separation, with a perturbation frequency period of 30 seconds and an amplitude of about $0.02b$

The formation separation parameters are presented in Figure 7.12a. In this simulation, the follower was brought in from the outer wake with the formation-hold autopilot through the blue zone. As the aircraft approaches the green zone, the extremum-seeking controller was activated with zero integral control gains K_η and K_ζ . The aircraft was moved in circular motions for two periods to detect the phase lag. Once the mean phases $\bar{\phi}_\eta$ and $\bar{\phi}_\zeta$ were detected and synchronized at about 270 seconds, the state machine turned on the integral gains and the follower started to converge to the optimum. The convergence time for this simulation was about 230 seconds over 50% of wingspan.

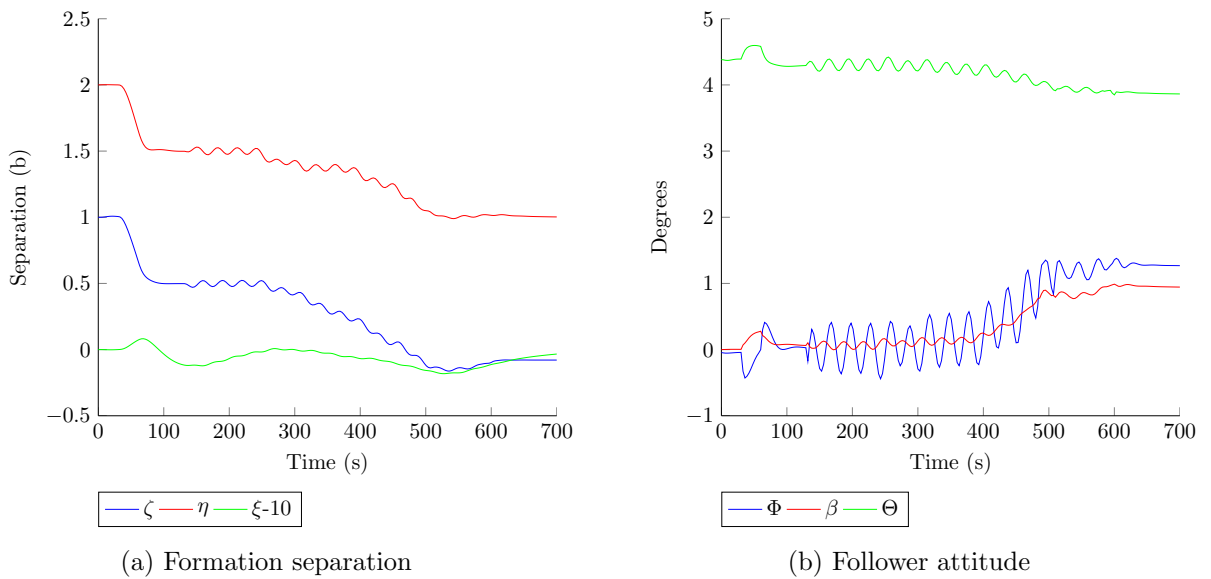


Figure 7.12: Extremum-seeking controller response for formation separation and attitude, with a perturbation frequency of 30 seconds and an amplitude of about $0.02b$

The aircraft attitude is presented in Figure 7.12b. The perturbing formation separation

7.4 Extremum-Seeking: Simulation Results

commands caused slight bank angle oscillation of about 0.5 degrees in amplitude. Due to the slow and subtle nature of these oscillations, it is likely that they would go unnoticed to most passengers, although a passenger comfort analysis is recommended. Very subtle pitch angle oscillations were also observed as the aircraft moves about the upwash gradient towards a more efficient flight condition. Here the aircraft again stabilizes at 500 seconds, when the state machine senses that the optimum margin of 3.9 degrees or 12% decrease in pitch angle was achieved. This optimum margin will have to be calculated through further analysis on a more accurate wake which includes wake-wandering data and aircraft load variation. Only as more data becomes available can the optimum margin be analytically designed. It is most likely that this optimum margin will be a function of trim pitch angle, aircraft load and other flight parameters, but this remains open for future analysis.

In Figure 7.12b, the follower sideslip angle is presented. About one degree of sideslip was induced by the complementary filter controller to counter the rolling moment in the wake and reduce the aileron load. Thus, the complementary filter controller design proved effective, even during the oscillatory motions of the extremum-seeking perturbations.

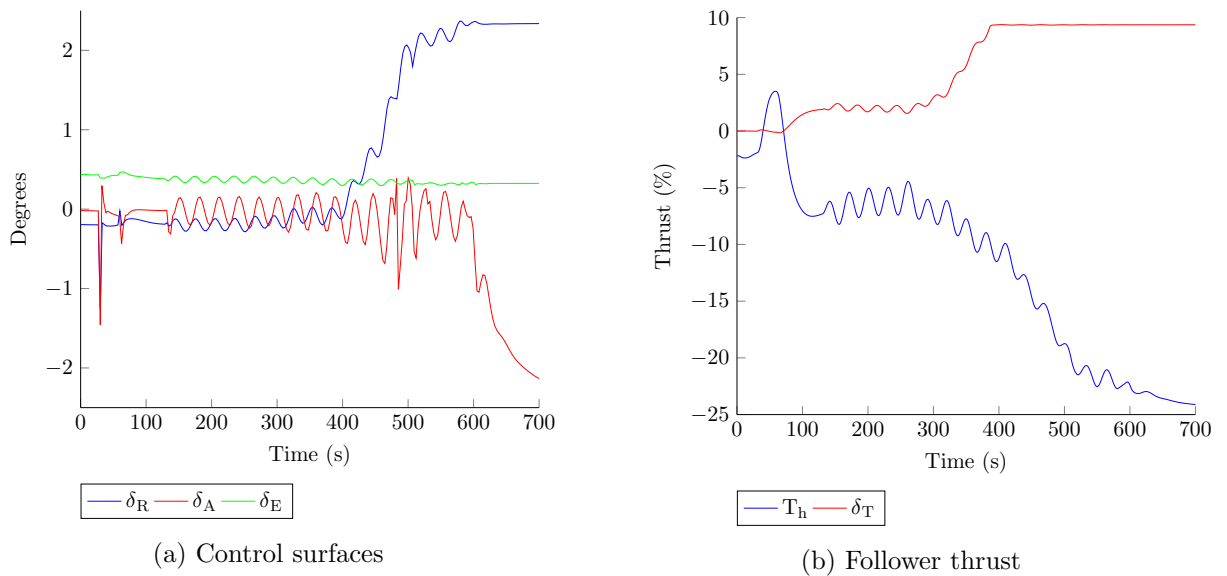


Figure 7.13: Extremum-seeking controller follower inputs for the control surfaces and thrust, with a perturbation frequency of 30 seconds and an amplitude of about $0.02b$

Next, the control surface deflections are presented in Figure 7.13a. Note that the maximum aileron and rudder demand is just above two degrees, which means that the aileron saturation problem was effectively solved by the complementary filter augmentation. The perturbation movements of the extremum-seeking controller do drive the control surfaces for extended periods, but as seen in Figure 7.13a, the control surface movement is very small

7.4 Extremum-Seeking: Simulation Results

in amplitude - mostly less than 0.5 degrees. If the perturbation frequency is increased, the control surface workload increases, as the actuators have to work harder to produce the same amplitude of aircraft movement. Appendix B shows a simulation where the extremum-seeking controller was designed for a perturbation period of 20 seconds. In this simulation, a maximum movement of 1.5% of aircraft wingspan could be achieved as the control surfaces are driven to their limits, where saturation and amplitude loss occur. Although a higher perturbation frequency is able to induce faster convergence to the optimum, it comes with the trade-off of higher actuator demands and increased levels of structural load which should be analyzed in future work. Thus, although a wide range of frequencies can be used for extremum seeking, there is likely to be a frequency which will not excite structural modes and induce large stresses on the aircraft structure. As more wake, ride comfort, structural load and test data becomes available, an analytical decision can be made regarding the most adequate and effective perturbation frequencies.

To relieve some rudder, differential thrust was limited to a modest 10%, as shown in Figure 7.13b. Although the simulation can handle the use of high differential thrust, it was not advised to do so, since the differential thrust can push the engines on the one side to its maximum and leave the others to idle or even stall. A conservative limit is placed on the differential thrust to ensure that the engines remain in their operating maps, thereby also more representative results.

The thrust reduction through the extremum seeking-controller is presented in Figure 7.13b. The trim thrust for isolated flight is 176 kN, as discussed Section 4.1.1. The extremum-seeking controller successfully maneuvered the follower aircraft to save 43 kN or about 25% of thrust. Some dynamic thrusting was induced by perturbation movements, but since the perturbation signal is only applied for a few minutes during flight, no further optimization was attempted.

7.5 Extremum Seeking Under Turbulent Conditions

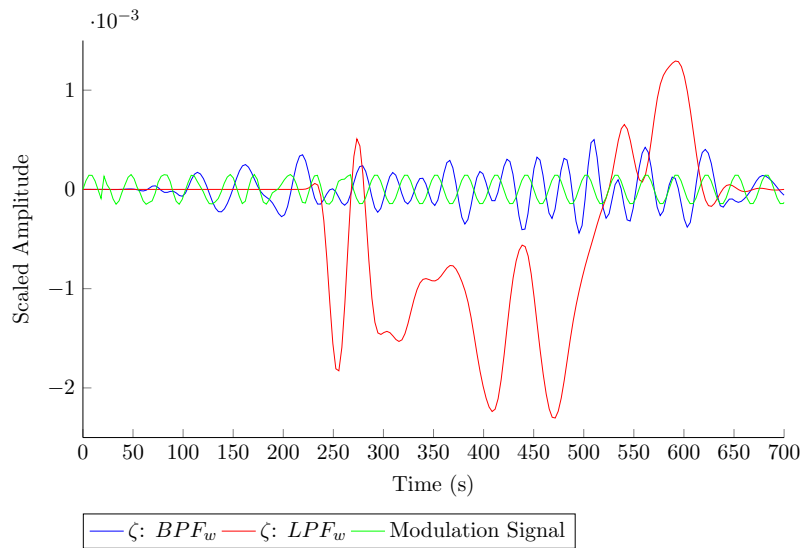


Figure 7.14: Extremum-seeking control band-pass and low-pass filter output for vertical optimization, with a perturbation frequency period of 30 seconds and an amplitude of about $0.02b$

To better understand the working of the extremum-seeking controller, the filter output data is also provided. Figure 7.14 shows the feedback signal at different stages of the extremum-seeking controller for the vertical optimization. The band-pass filter output represents a sinusoidal signal which, after multiplied by the phase-corrected modulation signal and passed through the low-pass filter, gives a constant offset that is integrated to produce the optimum estimate. The mean phase corrections $\bar{\phi}_\eta$ and $\bar{\phi}_\zeta$ were calculated at about 270 seconds after two perturbation periods were completed. The average phase offsets over the two periods were determined using Equation 7.3. After these two initialization periods, the phase was kept constant. In this simulation, the integrator gain was set slightly too high to induce some overshoot, demonstrating that the controller does converge to the optimum.

7.5 Extremum Seeking Under Turbulent Conditions

In the previous chapter, the formation-hold autopilot was evaluated under light and moderate turbulence conditions, as discussed in Section 6.3. The von Kármán atmospheric turbulence, as proposed in Section 3.9, superimposes the effect of a frozen turbulence field on the leader and the follower aircraft, with the time delay between the leader and follower proportional to the longitudinal separations between them. In this chapter, the formation-hold controller was extended with an extremum-seeking control scheme. To implement such a controller in practice, it must be robust against some level of turbulence. In this study, all turbulence analysis has been conducted under light, moderate and severe turbulence, as specified by the MIL-F-8785C [41] standard. It was found that the rare case of severe turbulence is too

7.5 Extremum Seeking Under Turbulent Conditions

intense for formation flight, and it is advised to disengage formation flight under these extreme conditions. Thus, this study only evaluates formation flight under light and moderate turbulence. In this section, the extremum-seeking controller performance will be evaluated under light turbulence. Moderate turbulence was attempted, but was unsuccessful, and this will be discussed further.

In light turbulence, the station keeping performance of the formation-hold controller was exceptional, restricting the standard deviation of the three separation parameters to less than 1% of wingspan in separation displacement, as discussed in Section 6.3. With the extremum-seeking controller commanding the formation-hold controller in the inner loop, the optimum location could successfully be located in light turbulence. Figure 7.15 shows the separation and attitude response as the follower aircraft seeks and locates the optimum in the wake with a perturbation period of 30 seconds. The follower attitude angles, given by Figure 7.15b, showed light process noise as expected.

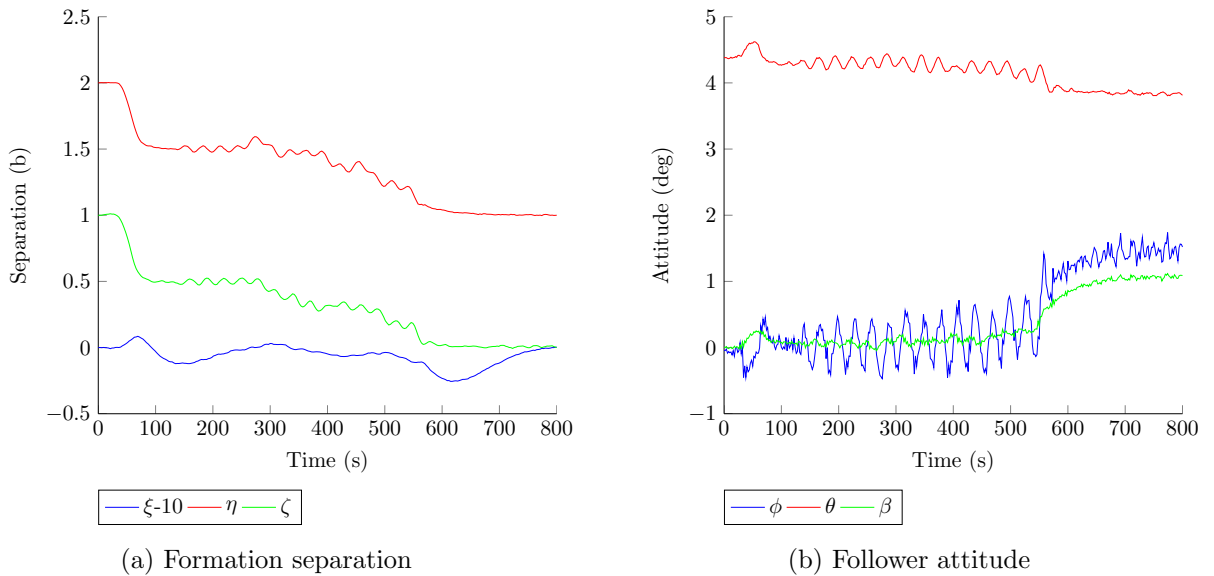


Figure 7.15: Extremum-seeking controller performance under light turbulence with a perturbation period of 30 seconds and an amplitude of about $0.02b$

The follower actuator and thrust responses are given by Figure 7.16. Even under light turbulence, thrust savings of about 25% were achieved near the optimum separation of $\eta = 1$ and $\zeta = 0$. These figures show that the extremum-seeking controller regulates similar performance in light turbulence as it did in the ideal design case simulation in Figures 7.12 and 7.13, where no turbulence was included. This proves that the extremum-seeking controller can absorb and function under normal levels of atmospheric disturbances.

7.5 Extremum Seeking Under Turbulent Conditions

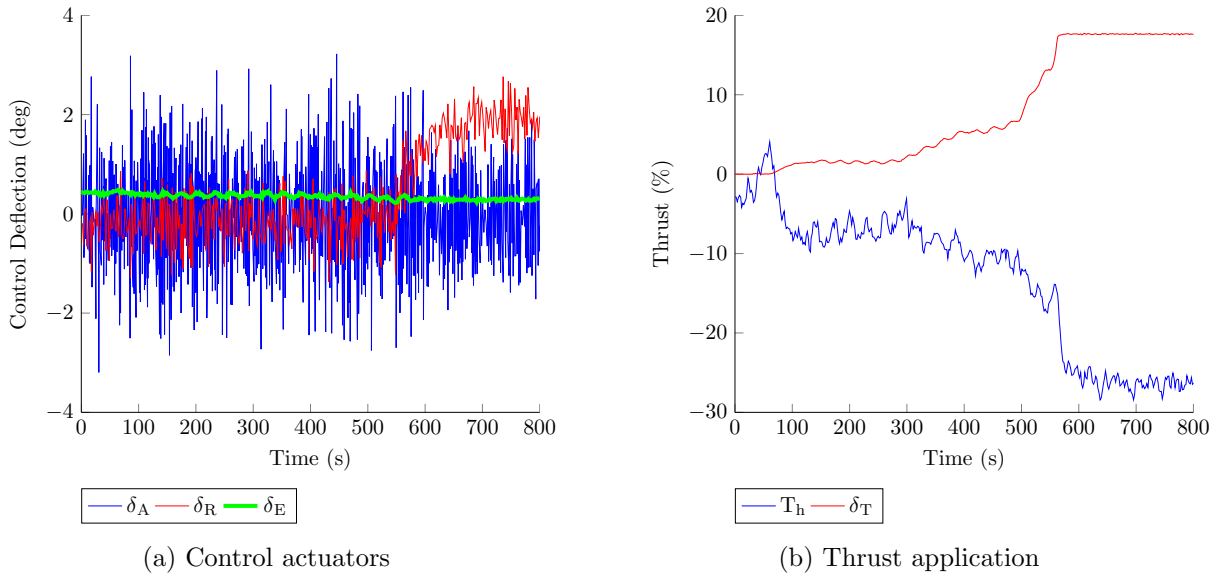


Figure 7.16: Extremum seeking controller performance under light turbulence with a perturbation period of 30 seconds and an amplitude of about $0.02b$

To further demonstrate, extremum-seeking controller's optimum tracking capability, the optimum location was artificially shifted within the 50% green boundary, where the optimum is assumed to be located. In this region, the extremum-seeking perturbation remains active, as discussed in the control logic in Section 7.3.1.3. Figure 7.17a shows the separation response for a simulation where the optimum is vertically shifted by a $0.2b$ step input at 700 seconds. For this simulation, the measured separation remained accurate, and only the wake was shifted with regard to the follower aircraft. The follower relocated to the new optimum successfully, where more than 25% thrust savings were reestablished, demonstrating successful extremum seeking. The full simulation results are given in Appendix B.3.

7.5 Extremum Seeking Under Turbulent Conditions

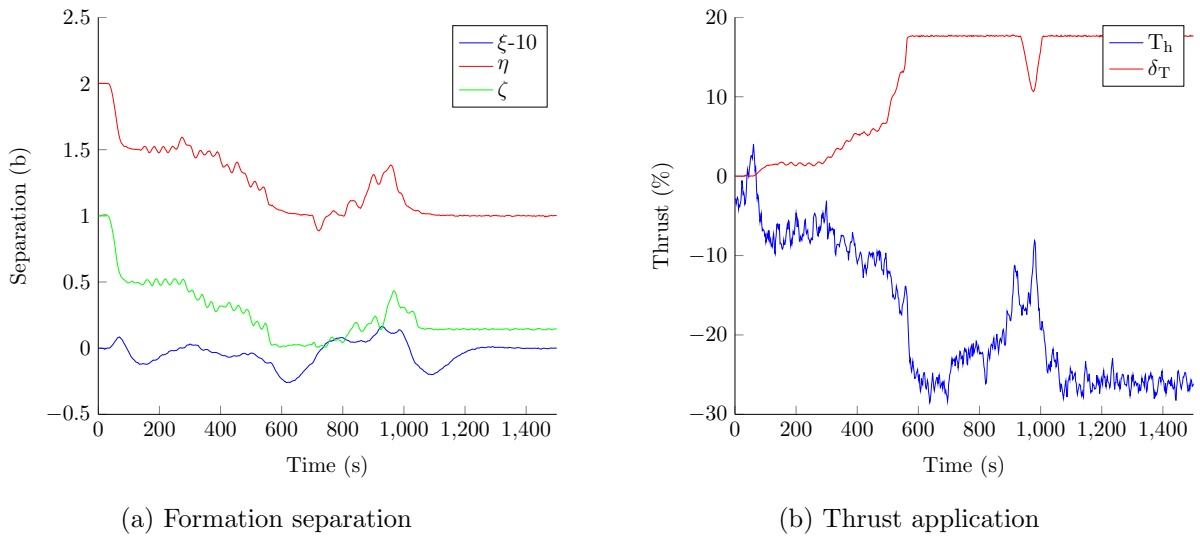


Figure 7.17: Extremum seeking controller performance under light turbulence where the optimum location shifted at 700 seconds from $\eta = 1, \zeta = 0$ to $\eta = 1, \zeta = 0.2$

Under moderate turbulence the standard deviation on the vertical and lateral separation parameters escalated to more than 5% for the formation-hold controller as presented in Section 6.3. Since the extremum-seeking controller commands the formation-hold controller, the same formation separation variance was observed in the extremum seeking response when the perturbation signal and control integrator was deactivated. The extremum-seeking controller can only function if the perturbation signal frequency can be detected in the optimization parameter. Thus, if the noise floor rises too high, which is the case in moderate turbulence, the perturbation signal disappear in process noise and extremum filter scheme can not read the gradient information from the optimization parameter. Since the perturbation signal only moves the follower aircraft about $0.02b$ in the lateral and vertical separation, the moderate turbulence noise induces and distorts this controlled parameter by amplitudes larger than $0.05b$. To operate extremum seeking under high levels of turbulence it is required to increase the perturbation signal amplitude to overpower the noise movement, so that change in the optimization parameter is primarily controlled by the perturbation input. This increases the load on the aircraft control actuators, possibly pushing them to their physical limitations, making extremum seeking in moderate to high turbulent conditions extremely difficult. A more practical proposal for high levels of turbulence, is to increase formation separation and move the follower to a safe location in the outer wake, as the turbulence calms down, optimum-seeking control resume.

This section successfully demonstrated that the extremum seeking controller could locate and maintain the optimum formation separation under light turbulent conditions, however

medium turbulence was problematic. Even as the optimum location shifted, the extremum-seeking controller could relocate the new optimum, simulating the situation of vortex wandering in the wake.

7.6 Extremum Seeking Conclusion

This chapter presented an extremum-seeking controller which minimizes power demand in formation flight of two commercial aircraft. An extremum-seeking controller proposed for this work was derived from Binetti [5], whose work was based on Krstić [4]. This system introduced a small perturbation signal on the lateral and vertical separation, in order to seek the gradient of the wake. The follower pitch angle was selected as the optimization objective to minimize. The pitch angle was fed back, filtered to extract only the gradient information, and passed to an integral controller to determine the next best estimate for the optimal separation.

This extremum-seeking scheme was augmented with three supportive systems to simplify the design procedure, and make the control system more robust. A phase synchronization module was included to detect the phase lag between the input perturbation and the realized pitch angle in order to perform near-perfect modulation. A simple pitch angle observer was implemented to calculate the change in pitch angle due to aircraft movement as if the follower was flying in isolation. This estimate was subtracted from the measured pitch angle to best estimate the change induced on the pitch angle by the wake gradient. The third system, a logic controller, was included to support and switch between the extremum-seeking controller and the formation-hold autopilot, based on a set of logic rules to minimize the time for which the extremum seeking perturbation is active.

The extremum-seeking controller was designed and tested in simulation. The controller could effectively guide the follower aircraft to the optimal separation, even under light turbulent conditions, with limited prior knowledge of the optimal location. The extremum-seeking controller could also relocate the optimum as the vortex shifted in the wake. Thus, effective extremum seeking was achieved through a control design which required very limited information about the system dynamics and the optimization objective. A more accurate wake model which include vortex movement or wandering could be beneficial for future work as the performance of the extremum-seeking controller could then be optimized within realistic boundaries.

Chapter 8

Concluding Optimal Formation Flight Control

8.1 Conclusion

This research focused on the commercial application of extended formation flight to maximize fuel efficiency. Formation flight takes advantage of the aerodynamic interaction between the leader and follower aircraft to lower the induced drag on the follower. At large longitudinal separations, between 10 and 40 wingspans, the aircraft's wingtip vortices produce a constant spool of airflow, creating the opportunity for the follower to be positioned in the wake so that the airflow produces an upwash on the follower. Flying the follower aircraft in this upwash region induces non-linear force and moment vectors on the follower, proportional to the formation separation. This non-linear forces and moments results in complex flight dynamics, superimposed on the follower. Advanced control techniques are required to stabilize the follower, regulate separation and optimize objectives such as minimizing fuel consumption.

The primary objective of this research was to develop a flight controller that minimizes follower thrust in right echelon formation of two commercial aircraft. To support this objective two Boeing 747 aircraft models was implemented in simulation as described in Chapter 3. For the leader aircraft an aerodynamic forces and moment model, linearized about cruise flight at Mach 0.8 and 12.19 km in altitude, was implemented together with uniform gravitational model and a more representative thrust model. This thrust model was derived from Boeing data [37] and a high fidelity General Electric CF6-80 engine model as developed by Sanders et al. [6] and discussed in Chapter 2. This thrust model simulated four second-order engines models with non-linearities to represent a higher fidelity thrust and differential thrust response. Finally, to simulate the follower aircraft in the wake, a aerodynamic forces and moment interaction model, based on a single horseshoe vortex model theory as derived

by Bizinos et al. [13], was superimposed on the conventional Boeing 747, linearized aerodynamic model. Besides the inclusion of this aerodynamic interaction model, the follower was a duplication of the Boeing 747 leader. With the mathematical models implemented and linearized, as discussed in Chapter 4, the flight controllers for these models could be developed.

To provide a basis for the formation flight controls, conventional linear altitude, airspeed and cross-track controllers, were designed and implemented on the leader aircraft in isolated flight, as presented in Chapter 5. 5% settling times of about 30 seconds were achieved for the altitude and cross-track control and about 100 seconds for the airspeed control. These slow dynamics are expected for a larger aircraft, such as the Boeing 747. The conventional controllers were evaluated in light, moderate and severe turbulence. It was found that the chosen control gains were satisfactory since low standard deviations on the control parameters was observed in light and moderate turbulence, with acceptable standard deviations on control actuators. Under severe turbulence the control gains were found to be too stiff as control actuators were saturated. This problem was not addressed since the controllers were designed for use in formation flight and flying in formation under severe turbulence is not advised. Thus, under severe turbulence the control gains should be adjusted and formation separation increased to ensure a safe flight condition.

The formation-hold controller was designed to utilize the conventional altitude, airspeed and cross-track control architecture, as presented in Chapter 6. By simply remapping and augmenting the conventional controllers, effective formation-hold control was created for the lateral, vertical and longitudinal formation separation parameters. Flying deep in the wake proved to be challenging as the large rolling moment easily saturated the follower aileron actuators. This large rolling moment experienced in the wake, is a well known challenge posed by formation flight due to the wake's non-uniform load distribution on the follower aircraft's wings. To reduce the load on the follower's ailerons, the inner-loop lateral controllers were augmented with a complimentary filter system. This filter system distributed the low-frequency information of the aileron control command to the rudder and/or differential thrust actuators to induce a sideslip on the follower. Flying at a sideslip increased the angle of attack on one side of the aircraft, which in return induced a counter rolling moment on the aircraft. With the introduction of a small sideslip angle, up to 1.5 degrees, a new equilibrium could be obtained with almost no aileron application. The high-frequency response of the ailerons was maintained, as the complimentary filters passed the upper half of the spectrum to the ailerons as usual. This complimentary filter system was the first to effectively prevent aileron saturation at separations close to the wingtip vortex, thus enabling the follower to fly deeper in the wake where larger thrust savings can be obtained. The formation-hold controller showed similar turbulence rejection capabilities when compared to the conventional flight controls for

8.2 Limitations and Recommendation for Future Work

the Boeing in isolated flight. It was also found that the complimentary filter system improved the controller robustness, as aileron actuators were less prone to saturation deep in the wake.

With effective formation-hold control in place, the final phase of this study was implemented as presented in Chapter 7. For this an extremum-seeking controller was designed and implemented on the non-linear follower aircraft in the wake. The optimization control scheme was derived from an formation flight extremum-seeking controller as proposed in the work of Binetti et al. [5], and derived from the extremum-seeking control theories of Krstić [4]. In this control scheme a small perturbation signal is applied to the lateral and vertical formation-hold separation commands. These perturbation signals move the follower in circular motions in the wake. The follower's pitch angle was selected as optimization objective, as it is assumed to be proportional to the aircraft's induced drag, yet more easily measured than the aircraft's angle of attack. This optimization objective is then filtered and modulated by the perturbation signal to extract the wake gradient information. This gradient information is passed through an integral controller to produce the next best estimate for the lateral and vertical separation. The extremum-seeking controller was supported by control logic to produce effective optimization even under light turbulent conditions. However, under moderate turbulent conditions the noise floor in the pitch angle was higher than the gradient information induced by the perturbation signal, and thus the extremum-seeking controller could not locate the optimum as the gradient information became too distorted.

For the proposed model, an effective extremum-seeking controller was designed and demonstrated. The controller automatically steered the follower aircraft towards the optimum formation separation by minimizing the follower's pitch angle. At the optimum separation of $\eta = 1$ and $\zeta = 0$, thrust reductions in the range of 26% were observed, resulting in an average fuel saving of 0.7 kg/s, improving fuel consumption on the follower by 24% in cruise flight. These predictions further emphasize the economic potential of formation flight applications for commercial use.

8.2 Limitations and Recommendation for Future Work

In this thesis a first attempt at optimal flight control for minimum thrust demand in extended formation flight is presented. During the process of compiling this thesis with reasonable fidelity, some simplifications had to be made to scale down the complexity of this project. A brief discussion on these simplifications and future design recommendations follows:

For the mathematical models:

- The aileron, rudder and elevator actuator models only included rate limits and saturation levels. Higher fidelity actuator models are required to improve the accuracy of the

8.2 Limitations and Recommendation for Future Work

simulation results, especially for analysis in turbulent conditions where the actuators are exposed to higher frequency inputs.

- For the engine model, the thrust output represents that of a high fidelity engine model thrust output which calculates the engine mass flow parameters that estimate the engine thrust output. However, no combustion model is included, and thus the fuel flow was only model as a fuel flow set-point with saturation and rate limits. For a more accurate fuel consumption estimation, a higher fidelity combustion model should be included.
- The aerodynamic interaction model, as developed by Bizinos [13], significantly simplified the complexity of the aerodynamic interaction between the leader and follower aircraft. These assumptions, such as uniform wing load distribution produced highly amplified results near the wingtip-vortices. For this reason, flight in the inner-wake could not be analyzed in this work as formation flight was limited to only include lateral separations greater than one wingspan. The development of a more representative wake model is the highest priority recommendation which may lead to more accurate simulation analysis for future work on formation flight control design.

For the formation flight controllers:

- The conventional controllers, which forms the foundation of the formation controllers, was designed with stiff control gains to ensure responsive dynamics for the follower in the wake. This induced high loads on the control actuators, which leads to saturation under high levels of turbulence. For a more holistic autopilot design, these control gains should be gain-scheduled on the severity of turbulence experienced to prevent actuator saturation.
- The complimentary filter cut-off frequencies were selected to be approximately twice that of the formation-hold controller response times to ensure time scale separation. However, further analysis can optimize this cut-off frequency to optimize aileron use for disturbance rejection.
- Currently no data on wake wandering or movement of the wake in cruise conditions could be obtained and as a result the regions in the extremum-seeking logic controller were selected purely by reason. If more accurate wake data or models becomes available, these regions could be refined and extremum-seeking control parameters optimized to produce an extremum-seeking controller with the best possible performance.
- The perturbation frequency selection was purely based on the response time of the formation-hold controller. A deeper analysis on the extremum-seeking controller can give a better selection of perturbation frequencies, or even a range of frequencies scheduled on the level of process disturbances.

8.2 Limitations and Recommendation for Future Work

- The perturbation frequency is limited by the physical capabilities of the control actuators. For the aircraft to scan the wake at a higher perturbation frequency, and produce faster extremum seeking convergence, more powerful actuators need to be implemented in order to produce a meaningful amplitude perturbation response in the optimization objective. The current model is limited by the achievable amplitude of perturbation as the actuators saturate. This is coupled to the extremum seeking performance under turbulent conditions as the small perturbations in the optimization objective easily disappears in the noise floor, making extremum seeking with this control architecture impossible.
- The pitch angle observer plays a critical role in extracting the wake gradient information and finding the optimum separation in the wake. In this design, the observer was a state space model of the aircraft for isolated flight. This observer takes the actuator commands as inputs to estimate what the aircraft's pitch angle would be in isolated flight. This is not a realistic implementation as a highly representative state space model can be difficult to obtain in-flight. This limits the practicality of the proposed extremum-seeking controller and an alternative observer should be investigated.
- The limitations of the extremum-seeking controller is mostly caused by the application of a perturbation movement in the wake. If more advanced wake sensing technologies and sensors can be developed, such as wing distributed pressure sensors, the use of a perturbation movement to observe the wake can be omitted. This should be further investigated as it can possibly be a better solution for formation flight optimization.

References

- [1] J. Anderson, *Fundamentals of aerodynamics*. McGraw-Hill, Boston, 4th ed., 2007. [xi](#), [7](#)
- [2] N. Bizinos and C. Redelinghuys, “Passenger comfort during formation flight within atmospheric turbulence,” Master’s thesis, University of Cape Town, 2012. [xii](#), [4](#), [6](#), [46](#), [47](#), [48](#)
- [3] R. Heffley and W. Jewell, *Aircraft Handling Qualities Data*. Systems Technology Inc. NASA, 1972. [xii](#), [34](#), [40](#), [41](#), [60](#)
- [4] M. Krstić and H. Wang, “Stability of extremum seeking feedback for general nonlinear dynamic systems,” *Automatica*, vol. 36, no. 595-601, 2000. [xv](#), [130](#), [131](#), [133](#), [135](#), [150](#), [153](#)
- [5] P. Binetti, K. Ariyur, M. Krstic, and F. Bernelli, “Formation flight optimization using extremum seeking feedback,” *Journal of Guidance, Control, and Dynamics*, vol. 26, p. 132, January/February 2003. [xv](#), [4](#), [8](#), [9](#), [129](#), [130](#), [131](#), [132](#), [133](#), [135](#), [150](#), [153](#)
- [6] D. Sanders, “The effect of atmospheric turbulence on fuel consumption in formation flight.” [xix](#), [16](#), [17](#), [18](#), [27](#), [126](#), [151](#)
- [7] P. Lissaman and C. Schollenberger, “Formation flight of birds,” *American Association for the Advancement of Science*, vol. 168, no. 3934, 1970. [1](#)
- [8] M. Brodecki, K. Subbarao, and Q. Chu, “Formation flight control system for in-flight sweet spot estimation,” *AIAA Aerospace Sciences Meeting including the New Horizons Forum and Aerospace Exploration*, vol. 51, January 2013. [1](#), [8](#), [9](#)
- [9] S. Ning, T. Flanzer, and I. Kroo, “Aerodynamic performance of extended formation flight,” *Journal of Aircraft*, vol. 48, pp. 855–865, 2011. [1](#), [2](#), [4](#), [9](#)
- [10] F. A. Administration, “Faa aerospace forecast, 2013-2033,” 2013. [1](#)
- [11] J. Brachet, R. Cleaz, A. Denis, A. Diedrich, and D. King, “Reference material for a proposed formation flight system,” tech. rep., Department of Aeronautics and Astronautics, Massachusetts Institute of Technology, 2004. [2](#), [4](#)

-
- [12] C. Hanson, J. Ryan, M. Allen, and S. Jacobson, "An overview of flight test results for a formation flight autopilot," tech. rep., NASA Dryden Flight Research Center, National Aeronautics and Space Administration, Washington, DC 20546-0001, August 2002. [2](#), [7](#), [42](#)
- [13] N. Bizinso and C. Redelinghuys, "Passenger comfort during formation flight within atmospheric turbulence," *Journal of Aircraft*, 2012. [2](#), [3](#), [5](#), [6](#), [7](#), [9](#), [34](#), [42](#), [43](#), [45](#), [49](#), [50](#), [101](#), [104](#), [126](#), [130](#), [152](#), [154](#)
- [14] D. Buchner and J. Engelbrecht, "Towards automatic flight control for commercial airliners in formation flight," vol. 19, pp. 12188–12194, 2014. [2](#), [9](#), [40](#), [63](#), [101](#), [114](#)
- [15] C. Breitsamter, "Wake vortex characteristics of transport aircraft," *Progress in Aerospace Sciences*, vol. 47, pp. 89–134, 2011. [3](#)
- [16] S. Widnall, "The structure and dynamics of vortex filaments," *Annual Review of Fluid Mechanics*, vol. 7, pp. 141–165, 1975. [3](#)
- [17] H. Thien, M. Moelyadi, and H. Muhammad, "Effects of leader's position and shape on the aerodynamic performance of v flight formation," *International Conference on Intelligent Unmanned Systems*, pp. 44–49, 2007. [3](#)
- [18] Z. Bangash, R. Sanchez, and A. Ahmed, "Aerodynamics of formation flight," *Journal of Aircraft*, vol. 43, JulyAugust 2006. [4](#)
- [19] R. Ray, B. Cobleigh, M. Vachon, and C. St. John, "Flight test techniques used to evaluate performance benefits during formation flight," tech. rep., NASA Dryden Flight Research Center, Edwards, California, August 2002. [4](#)
- [20] D. Hummel, "The use of aircraft wakes to achieve power reductions in formation flight," *Advisory Group for Aerospace Research and Development, CP-584*, p. 36, 1996. [4](#), [130](#)
- [21] W. Blake and D. Gingras, "Comparison of predicted and measured formation flight interference effects," *Journal of Aircraft*, vol. 41, pp. 201–207, March-April 2004. [5](#), [6](#), [42](#), [47](#), [54](#)
- [22] J. Hansen and B. Cobleigh, "Induced moment effects of formation flight," tech. rep., NASA Dryden Flight Research Center, Edwards, California, August 2002. [5](#)
- [23] C. Lui, "Wake vortex encounter analysis with different wake vortex models," Master's thesis, Delft University of Technology, 2007. [6](#), [43](#)
- [24] W. Okolo, A. Dogan, and W. Blake, "Determination of sweet spot for trailing aircraft in formation flight," *AIAA*, vol. 6, August 2011. [8](#), [9](#)

-
- [25] M. Hemati, J. Eldredge, and J. Speyer, "Wake sensing for aircraft formation flight," *Journal of Guidance, Control and Dynamics*, February 2014. 8, 9, 129
- [26] S. Bradley, E. Mursch-Radlgruber, and S. von Hunerbein, "Sodar measurement of wing vortex strength and position," *American Meteorological Society*, June 2006. 8
- [27] F. Barbaresco, P. Brovelli, P. Currier, O. Garrouste, M. Klein, P. Juge, Y. Ricci, and J. Schneider, "Radar sensors for wind and wake vortex monitoring on airport," *European Conference on Radar in Meteorology and Hydrology*, May 2012. 8
- [28] P. Brown, "Wake vortex core profiles and stability from enroute flight data," *AIAA Atmospheric Space Environments Conference*, June 2011. 8
- [29] L. DeVries and D. Paley, "Wake estimation and optimal control for autonomous aircraft in formation flight," *AIAA Guidance, Navigation, and Control Conference*, 2013. 8
- [30] N. Brown and J. Schaefer, "Peak-seeking optimization of trim for reduced fuel consumption: Flight-test results," *AIAA Atmospheric Space Environments Conference*, 2013. 8, 9, 54
- [31] L. Jaw and J. Mattingly, *Aircraft Engine Controls: Design, System Analysis, and Health Monitoring*. AIAA Education Series, 2009. 12, 13, 14, 15, 16, 17
- [32] R. Flack, *Fundamentals of Jet Propulsion with Applications*. Cambridge Aerospace Series, 1st ed., 2005. 14
- [33] G. Development Team, *GSP 11 User Manual*, vol. 11.4. Anthony Fokkerweg 2, 1006 BM Amsterdam, The Netherlands: National Aerospace Laboratory NLR, March 2014. 16
- [34] I. Peddle, "Autonomous flight of a model aircraft," April 2005. 29, 31
- [35] J. Engelbrecht and I. Peddle, "Advanced automation - introductory course to aircraft dynamics." University Stellenbosch, April 2014. 29, 32, 33, 60
- [36] I. Peddle, *Acceleration Based Manoeuvre Flight Control System for Unmanned Aerial Vehicles*. PhD thesis, University of Stellenbosch, December 2008. 30
- [37] C. Hanke and D. Nordwall, *The Simulation of a Jumbo Jet Transport Aircraft*, vol. II, Modeling Data, D6-30643. Ames Research Center, NASA, September 1970. 30, 31, 34, 35, 36, 39, 151
- [38] D. Caughey, *Intoduction to Aircraft Stability and Control*. Sibley School of Mechanical and Aerospace Engineering, Cornell University, 1st ed., 2011. 41, 60
- [39] S. Ning, "Aircraft drag reduction through extended formation flight," 2011. 42, 104

- [40] A. Albright, C. Dixon, and M. Hegedus, “Modification and validation of conceptual design aerodynamic prediction method hasc95 with vtxchn,” tech. rep., NASA Langley Research Center, March 1996. [42](#), [54](#)
- [41] “U.s. military specification mil-f-8785c,” tech. rep. [48](#), [49](#), [146](#)
- [42] “Wind models for flight simulator certification of landing and approach guidance and control systems,” tech. rep., NASA, March 1977. [48](#)
- [43] B. Stevens and F. Lewis, *Aircraft Control and Simulation*. John Wiley and Sons, Inc., 2nd ed., 2003. [60](#), [72](#)
- [44] K. Ariyur and Krstić, “Analysis and design of multivariable extremum seeking,” *American Control Conference*, vol. 4, pp. 2903–2908, January 2002. [131](#), [133](#)

Appendix A

Model Parameters and Control Gains

A.1 Aircraft Attributes

Aerodynamic Coefficient	Value	Aerodynamic Coefficient	Value
$C_{D\alpha}$	0.426	$C_{m\alpha}$	-1.033
C_{DM}	0.0275	$C_{m\delta_e}$	-1.45
$C_{D\beta}$	0.02865	C_{mM}	0.166
$C_{D\delta_a}$	0.0183	$C_{m\dot{\alpha}}$	-6.41
$C_{L\alpha}$	4.92	C_{mq}	-24
$C_{L\delta_e}$	0.367	$C_{m\delta_r}$	0.0802
C_{LM}	0.205	$C_{m\beta}$	-0.1146
$C_{L\dot{\alpha}}$	5.91	$C_{l\beta}$	-0.277
C_{Lq}	6	C_{lp}	-0.334
$C_{Y\beta}$	-0.88	C_{lr}	0.3
C_{Yp}	0	$C_{l\delta_a}$	0.0137
C_{Yr}	0	$C_{l\delta_r}$	0.007
$C_{Y\delta_a}$	0	$C_{n\beta}$	0.195
$C_{Y\delta_r}$	0.1157	C_{np}	-0.0415
		C_{nr}	-0.327
		$C_{n\delta_a}$	0.0002
		$C_{n\delta_r}$	-0.1256

Table A.1: Boeing 747 aerodynamic coefficient parameters for isolated flight

A.1 Aircraft Attributes

Symbol	Unit	Value
Physical Data		
m	kg	288770
$\begin{bmatrix} I_{xx} & 0 & I_{xz} \\ 0 & I_{yy} & 0 \\ I_{zx} & 0 & I_{zz} \end{bmatrix}$	kg.m ²	$\begin{bmatrix} 24675878 & 0 & -2115075 \\ 0 & 44877559 & 0 \\ -2115075 & 0 & 67384129 \end{bmatrix}$
CG	m	$\begin{bmatrix} 31.75 & 0 & 0.84 \end{bmatrix}$
Wing Data		
S	m ²	510.96
\bar{c}	m	8.32
\mathcal{R}	m	6.95
b	m	59.7
Tailfin Data		
$\frac{b_f}{2}$	m	10.3
l_f	m	28.7
S_f	m ²	79.6
z_v	m	-5.9
Tailplain Data		
b_h	m	22.4
l_T	m	29.6
S_T	m ²	141
z_T	m	-5.1
a_1	rad	π
Thrust Model Data		
$\begin{bmatrix} a_{ix} & a_{iy} & a_{iz} \end{bmatrix}$	m	$\begin{bmatrix} 27.08 & 12.07 & 2.8 \end{bmatrix}$
$\begin{bmatrix} a_{ox} & a_{oy} & a_{oz} \end{bmatrix}$	m	$\begin{bmatrix} 35.71 & 21.15 & 2.23 \end{bmatrix}$
θ_e	deg	2.5
ψ_e	deg	2

Table A.2: Boeing 747 physical parameters

Symbol	Unit	Value
r_c	m	0.03b
$\frac{d\varepsilon}{d\alpha}$		0.502
h	m	0.25
h_0	m	0.25
cl_α	rad	2π

Table A.3: Boeing 747 wake characteristics

A.1 Aircraft Attributes

Actuator	Saturation Level (deg)	Rate Limits (deg/s)	Time Constant (s)
Elevator (δ_E)	+17 and -23	37	0.07
Aileron (δ_A)	+20 and -20	40	0.07
Rudder (δ_R)	+25 and -25	50	0.025

Table A.4: Aircraft actuator parameters

Appendix B

Extended Simulation Results

B.1 Conventional Control Under Turbulent Conditions

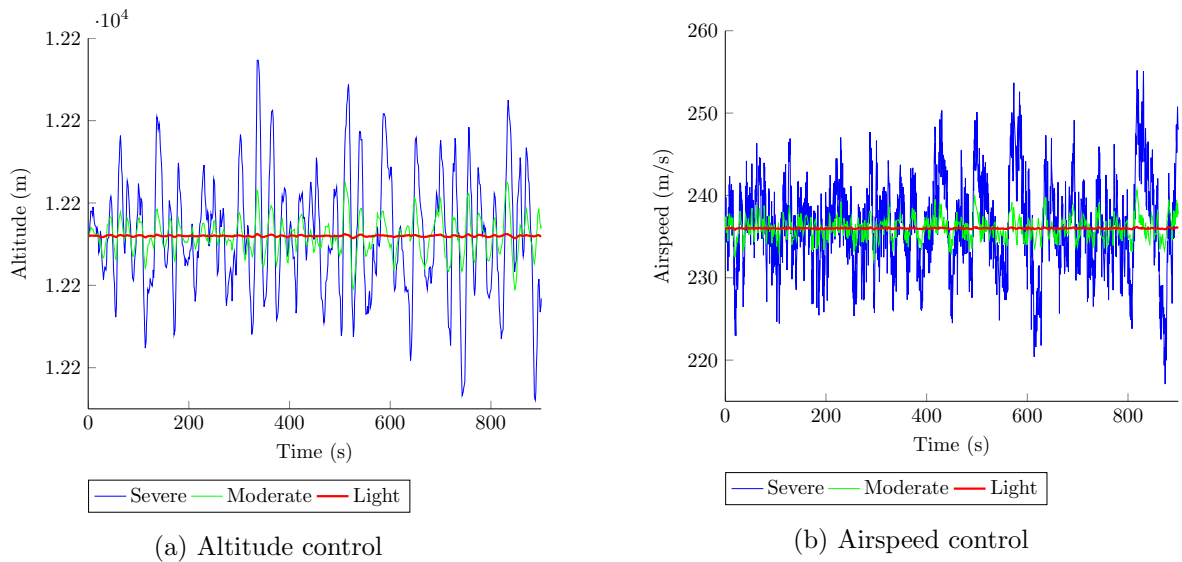


Figure B.1: Conventional controller performance under turbulent conditions

B.1 Conventional Control Under Turbulent Conditions

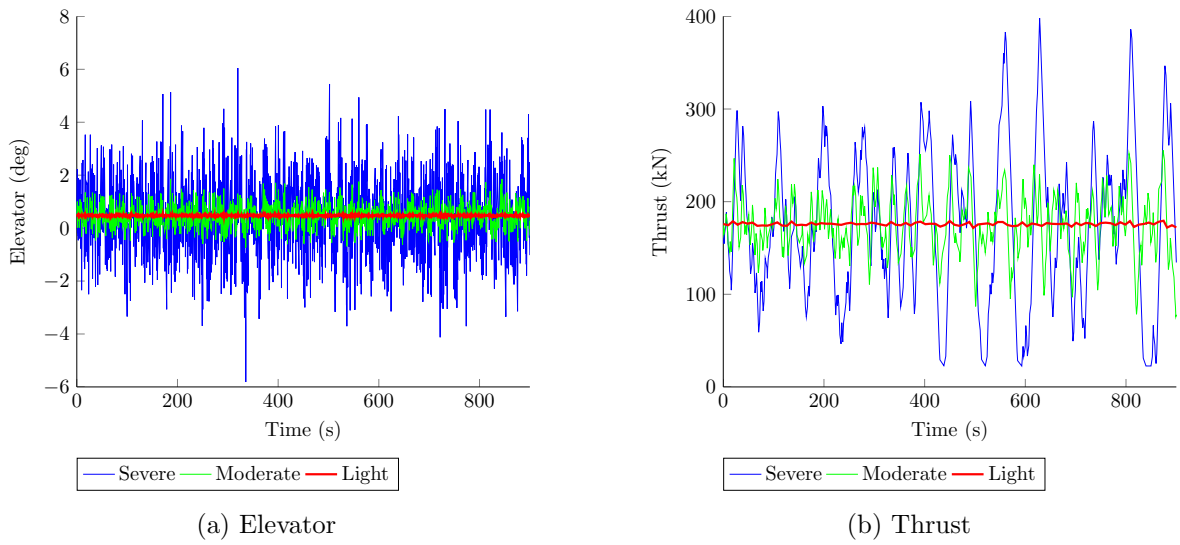


Figure B.2: Conventional controller actuator performance under turbulent conditions

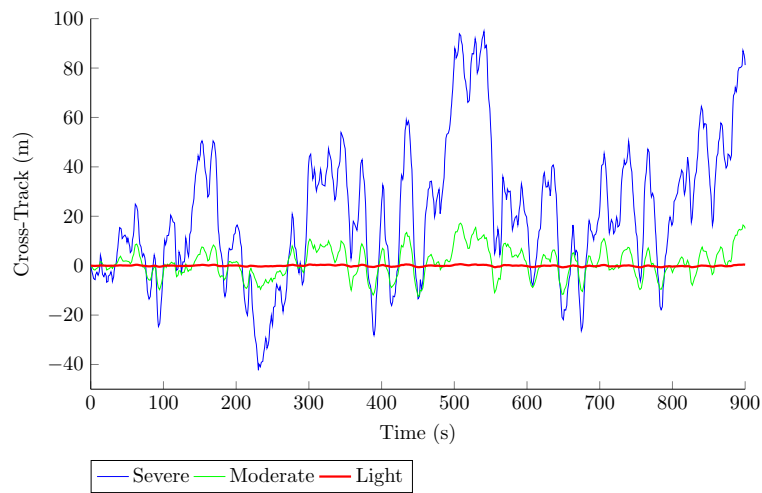


Figure B.3: Cross-track controller performance under turbulent conditions

B.2 Formation-Hold Flight Controls Under Turbulent Conditions

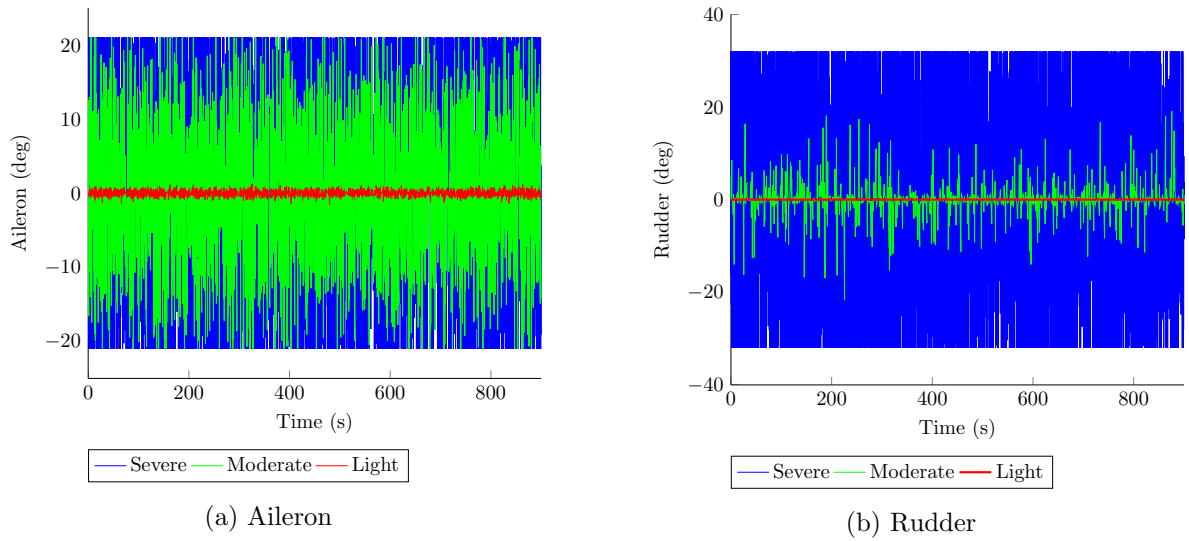


Figure B.4: Conventional controller actuator performance under turbulent conditions

B.2 Formation-Hold Flight Controls Under Turbulent Conditions

B.2.1 No Complimentary Filter Active

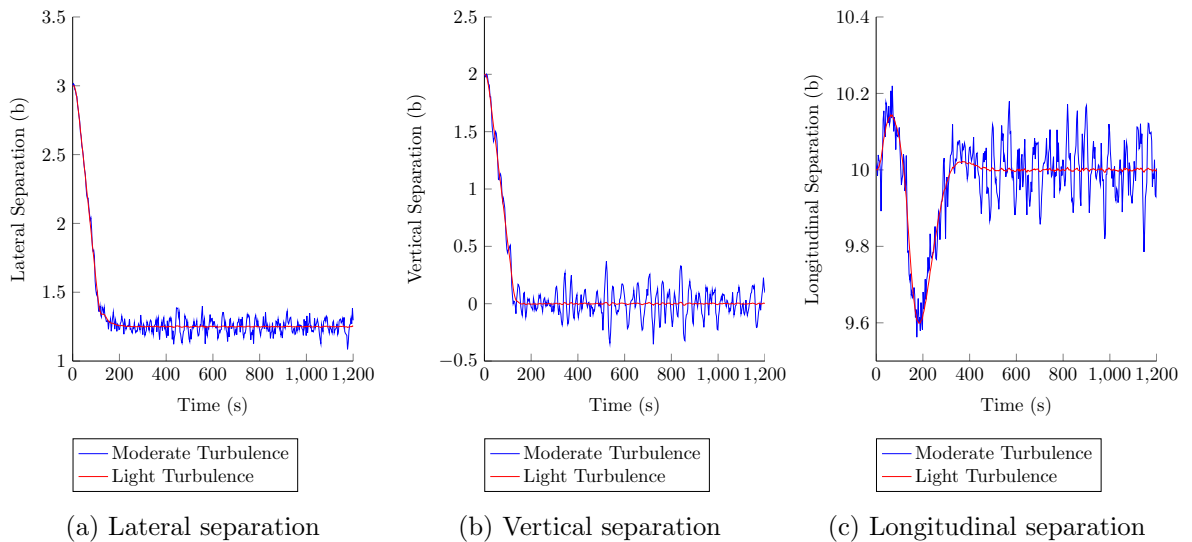


Figure B.5: Formation-hold control: a) lateral separation, b) vertical separation and c) longitudinal separation in turbulence with no complimentary filters active

B.2 Formation-Hold Flight Controls Under Turbulent Conditions

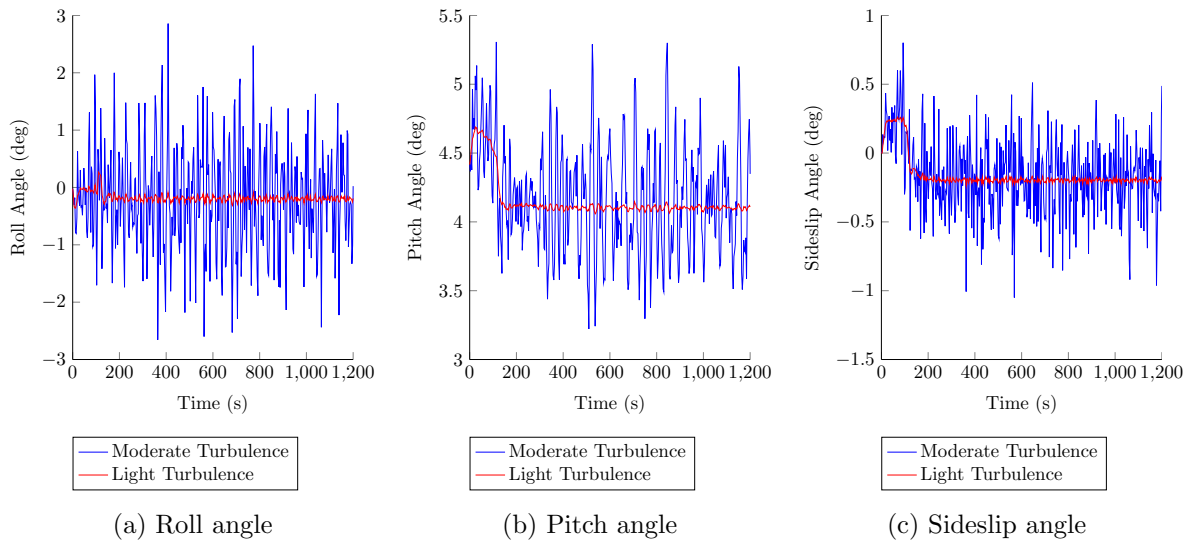


Figure B.6: Formation-hold control: a) roll angle response, b) pitch angle response and c) sideslip angle response in turbulence with no complimentary filters active

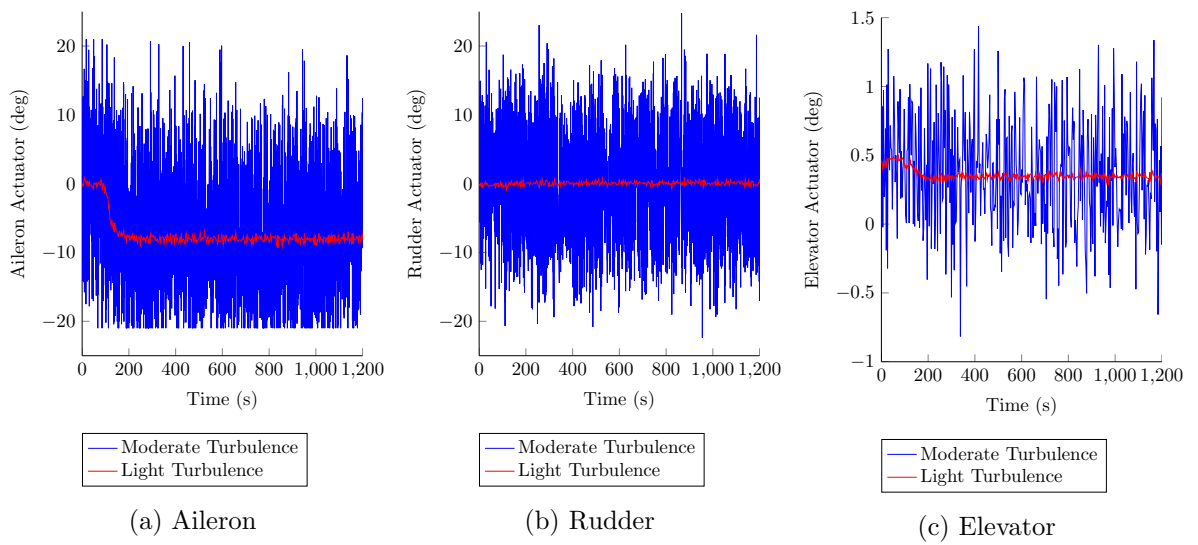


Figure B.7: Formation-hold control: a) aileron actuator response, b) rudder actuator response and c) elevator actuator response in turbulence with no complimentary filters active

B.2 Formation-Hold Flight Controls Under Turbulent Conditions

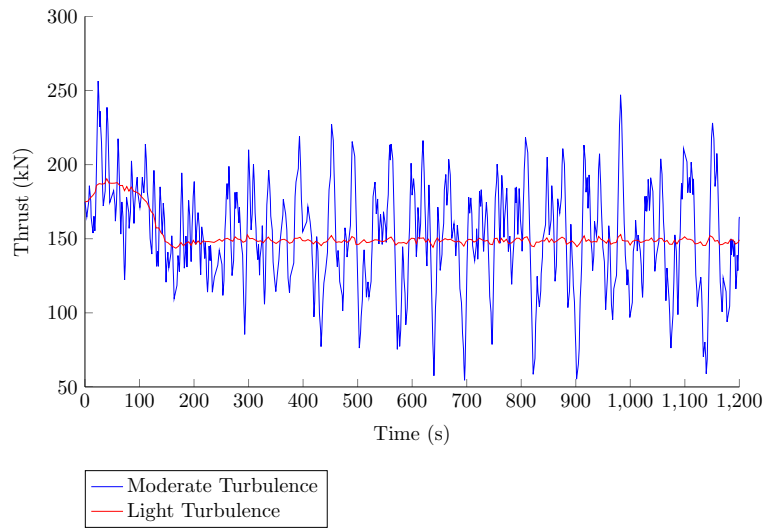


Figure B.8: Formation-hold control thrust response in turbulence with no complimentary filters active

B.2.2 Rudder Complimentary Filter Active

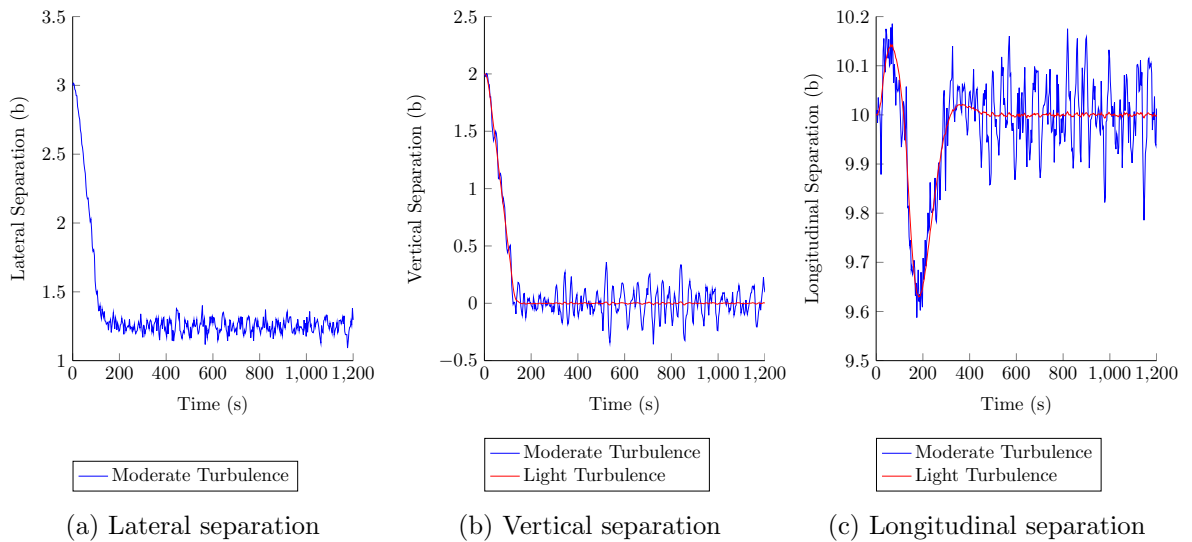


Figure B.9: Formation-hold control: a) lateral separation, b) vertical separation and c) longitudinal separation in turbulence with rudder complimentary filters active

B.2 Formation-Hold Flight Controls Under Turbulent Conditions

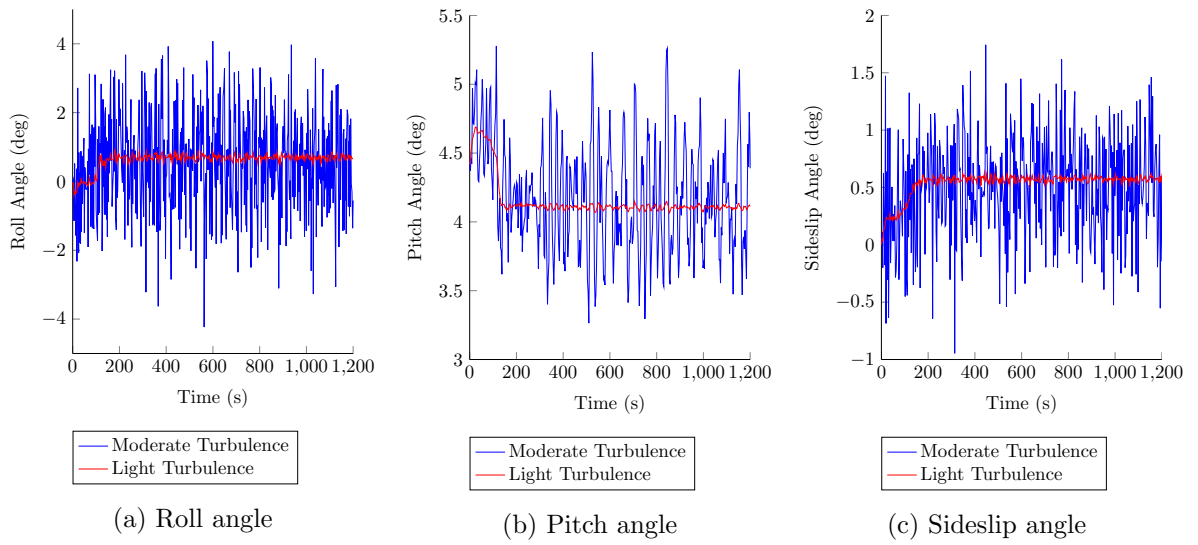


Figure B.10: Formation-hold control: a) roll angle response, b) pitch angle response and c) sideslip angle response in turbulence with rudder complimentary filters active

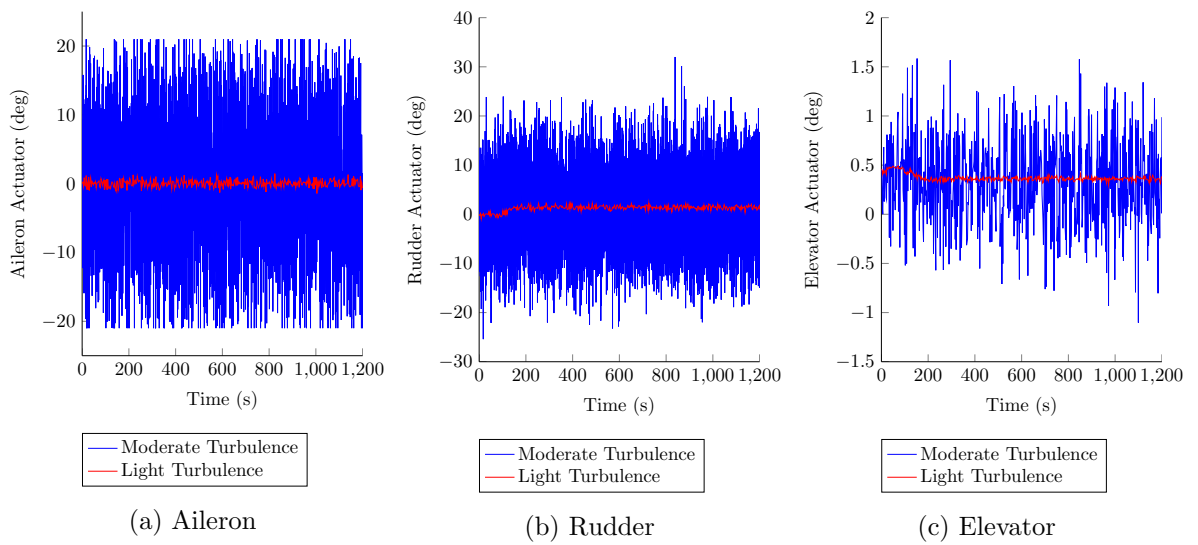


Figure B.11: Formation-hold control: a) aileron actuator response, b) rudder actuator response and c) elevator actuator response in turbulence with rudder complimentary filters active

B.2 Formation-Hold Flight Controls Under Turbulent Conditions

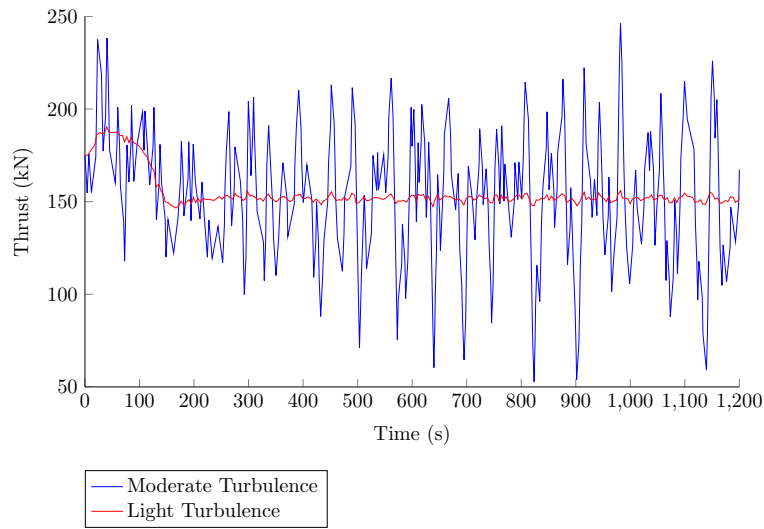


Figure B.12: Formation-hold control thrust response in turbulence with rudder complimentary filters active

B.2.3 Rudder and Differential Thrust Complimentary Filter Active

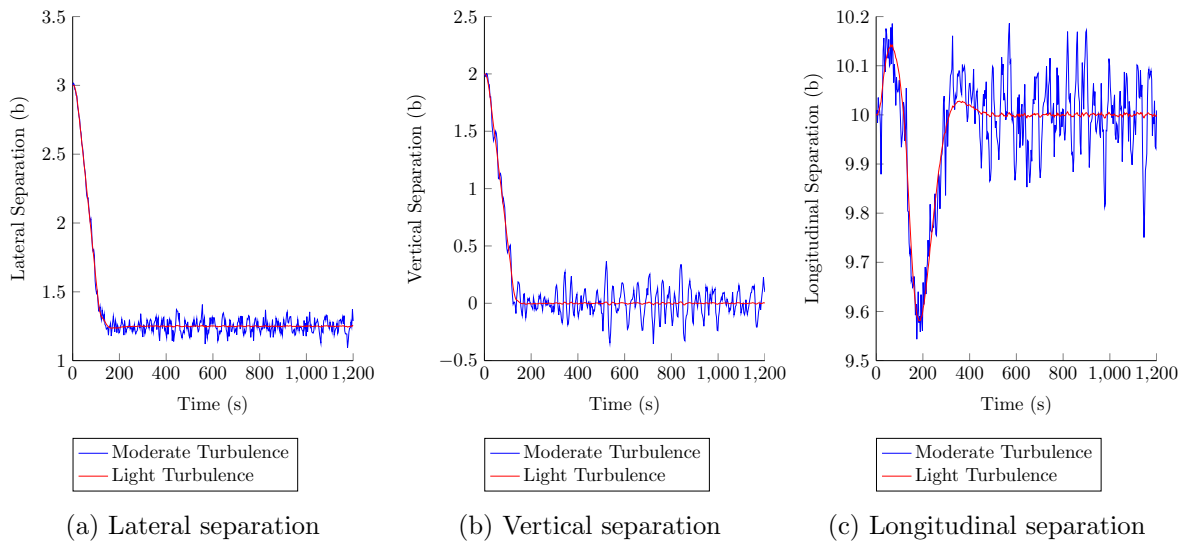


Figure B.13: Formation-hold control: a) lateral separation, b) vertical separation and c) longitudinal separation in turbulence with rudder and differential thrust complimentary filters active

B.2 Formation-Hold Flight Controls Under Turbulent Conditions

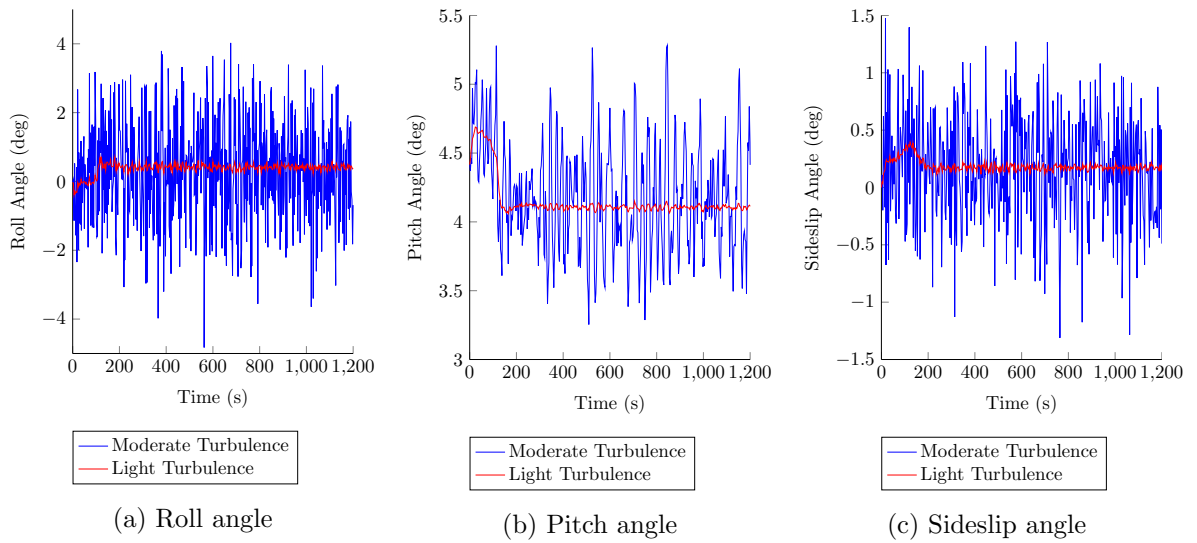


Figure B.14: Formation-hold control: a) roll angle response, b) pitch angle response and c) sideslip angle response in turbulence with rudder and differential thrust complimentary filters active

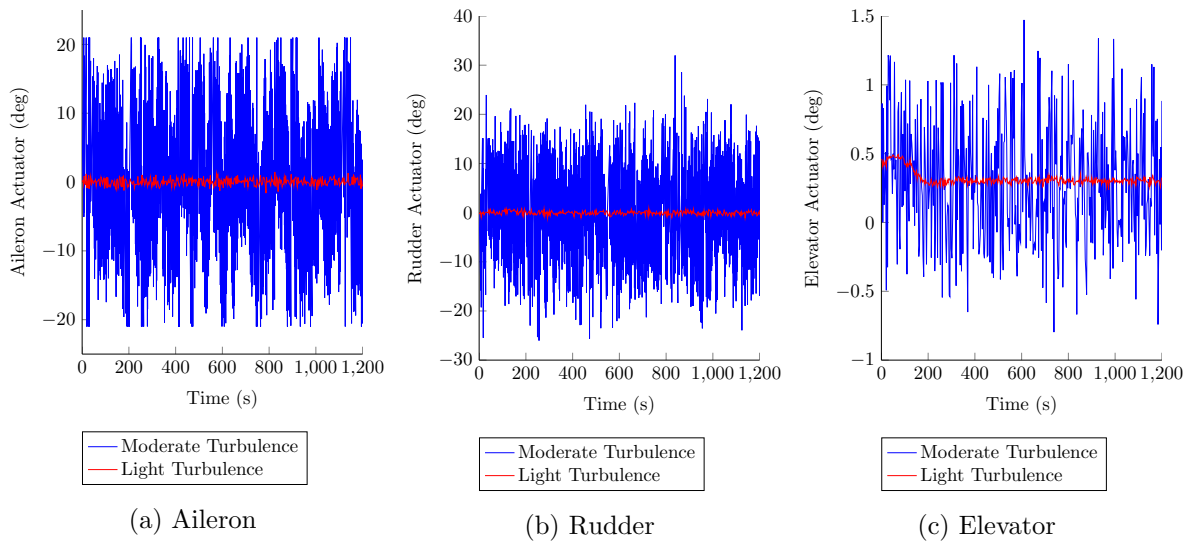


Figure B.15: Formation-hold control: a) aileron actuator response, b) rudder actuator response and c) elevator actuator response in turbulence with rudder and differential thrust complimentary filters active

B.3 Extremum-Seeking Controller

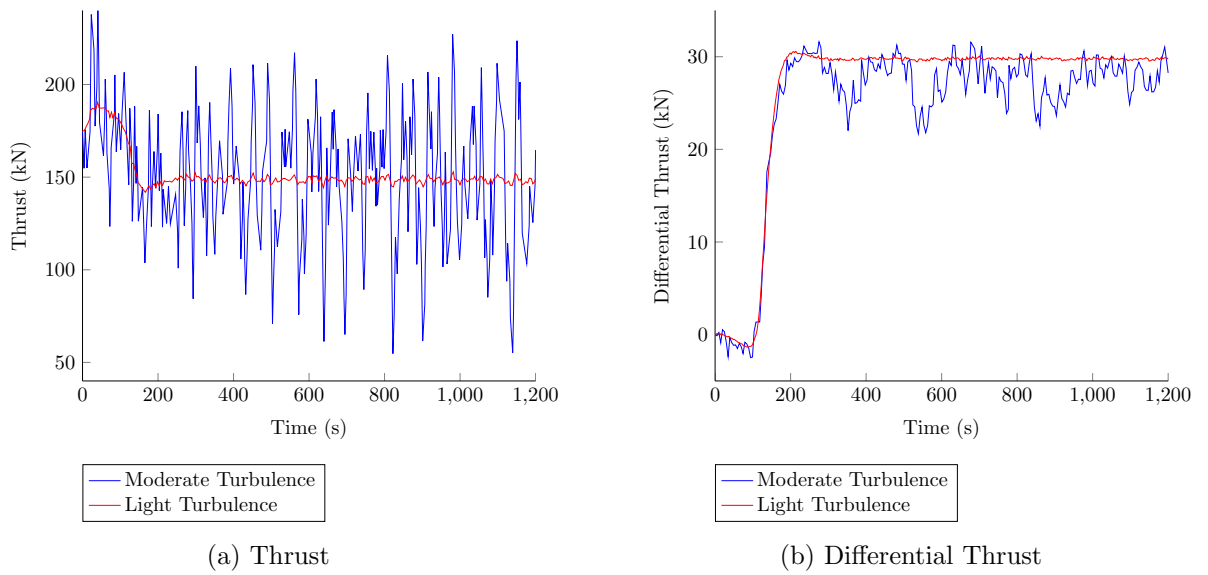


Figure B.16: Formation-hold control: a) thrust response and b) differential thrust response in turbulence with rudder rudder and differential thrust complimentary filters active

B.3 Extremum-Seeking Controller

B.3.1 Extremum-Seeking Controller With A 20s Perturbation Period

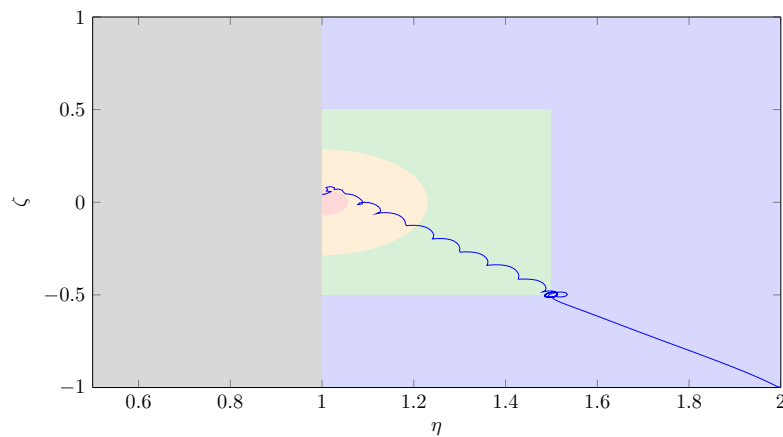


Figure B.17: Extremum-seeking control flight path with regard to lateral and vertical separation with a perturbation frequency period of 20 seconds and an amplitude of about $0.015b$

B.3 Extremum-Seeking Controller

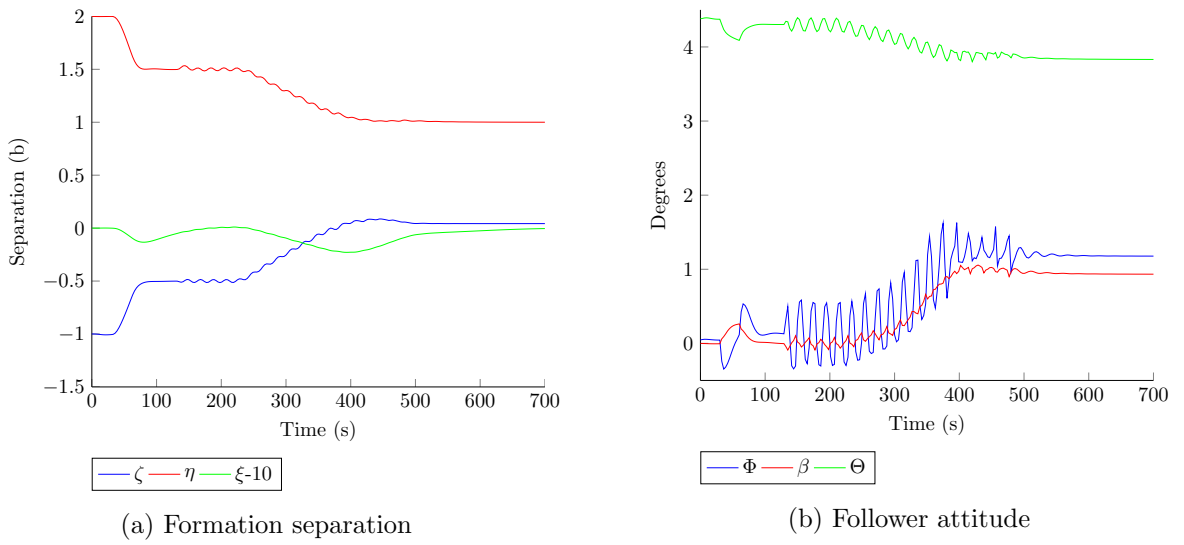


Figure B.18: Extremum-seeking controller response for formation separation and attitude with a perturbation frequency of 20 seconds and an amplitude of about $0.015b$

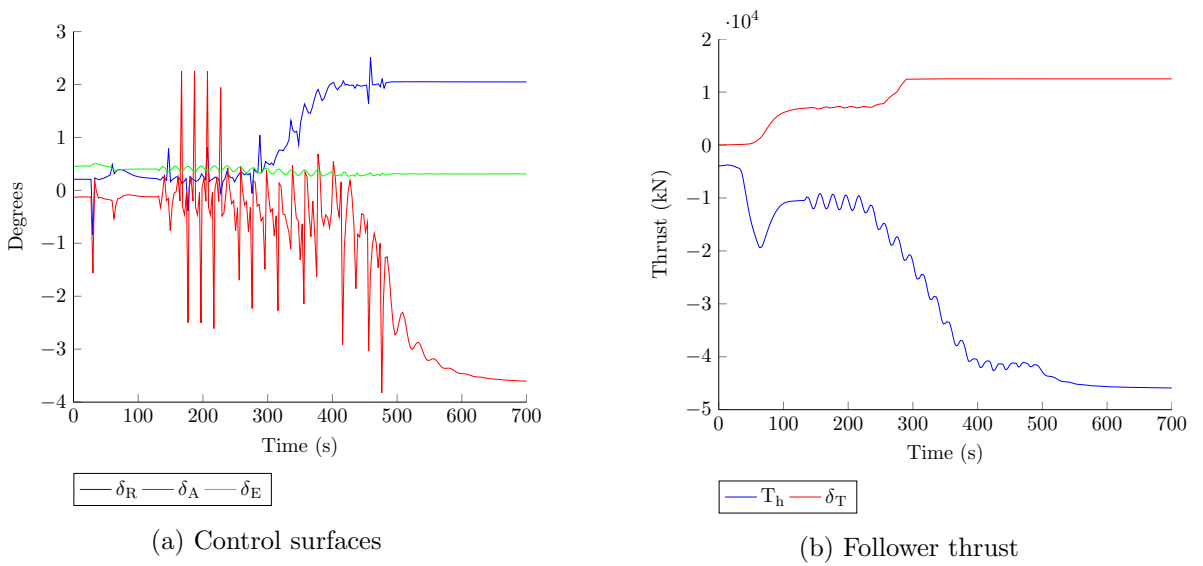


Figure B.19: Extremum-seeking controller follower inputs for the control surfaces and thrust with a perturbation frequency of 20 seconds and an amplitude of about $0.015b$

B.3.2 Extremum-Seeking Controller With A 30s Perturbation Period

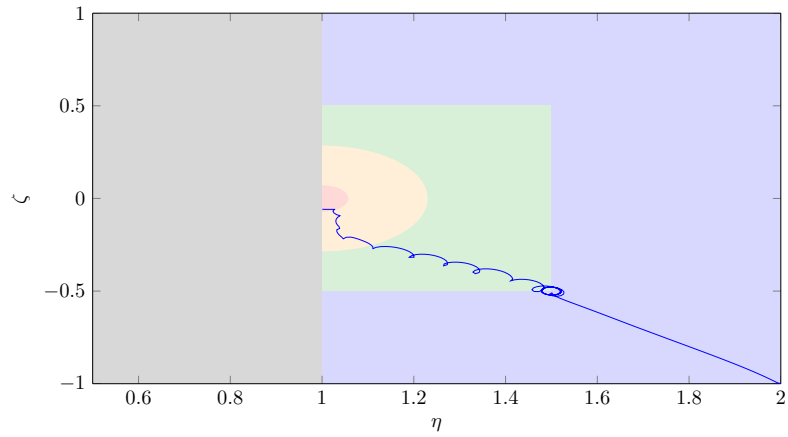


Figure B.20: Extremum-seeking control flight path with regard to lateral and vertical separation with a perturbation frequency period of 30 seconds and an amplitude of about $0.02b$

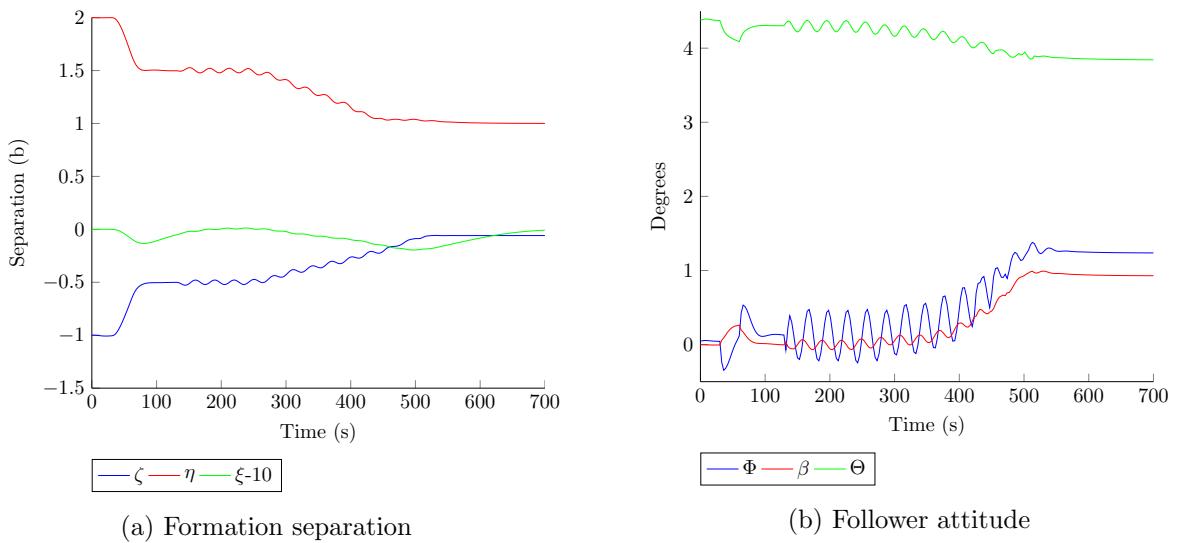


Figure B.21: Extremum-seeking controller response for formation separation and attitude with a perturbation frequency of 30 seconds and an amplitude of about $0.02b$

B.3 Extremum-Seeking Controller

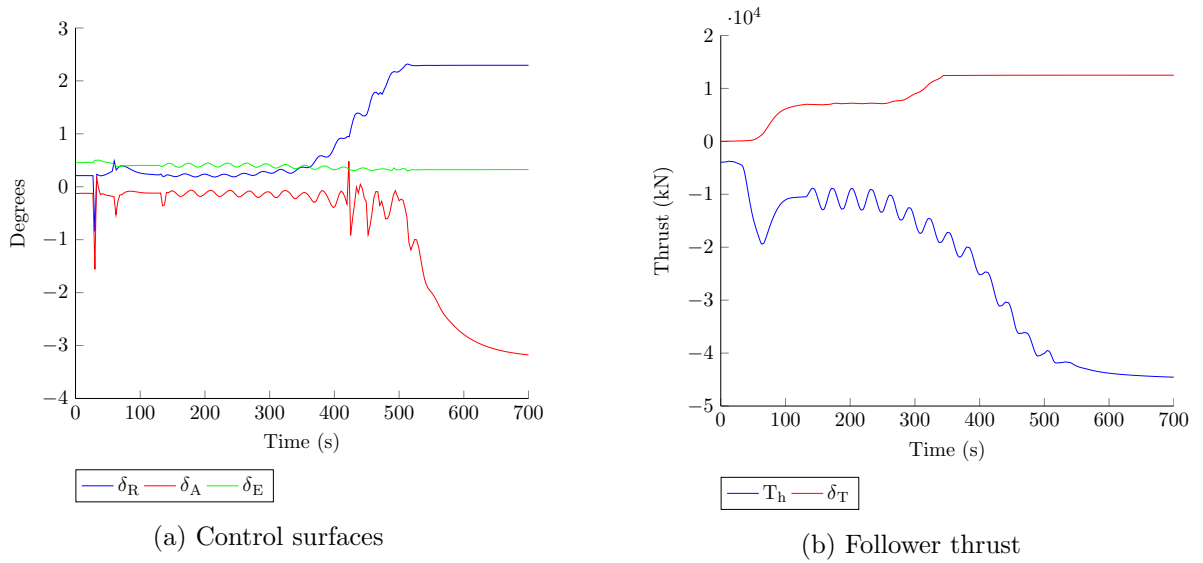


Figure B.22: Extremum-seeking controller follower inputs for the control surfaces and thrust with a perturbation frequency of 30 seconds and an amplitude of about $0.02b$

B.3.3 Extremum Seeking Control In Turbulent Conditions

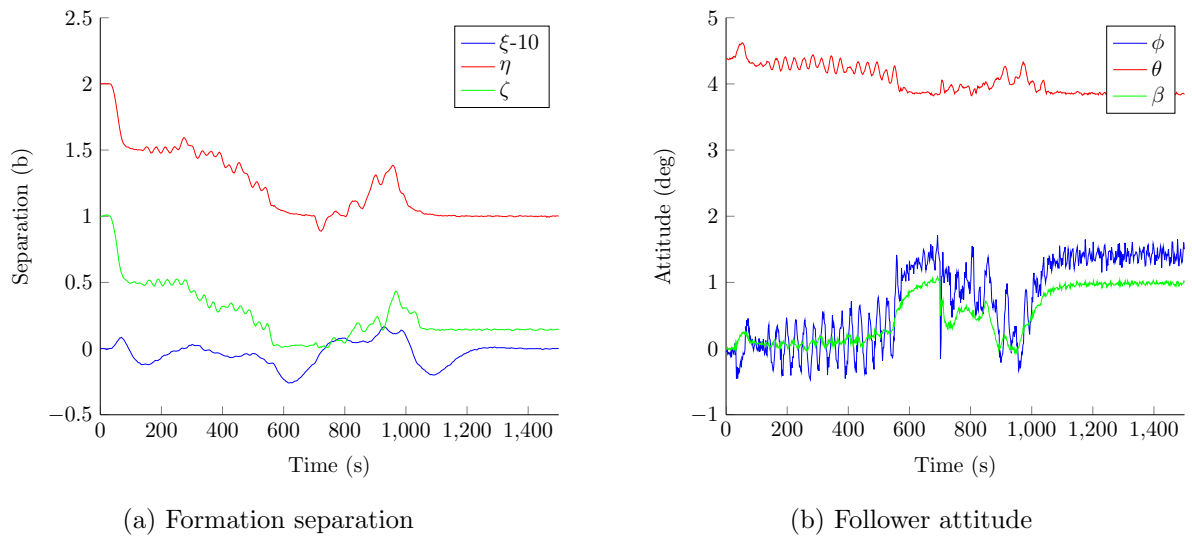


Figure B.23: Extremum-seeking controller performance under light turbulence with a perturbation period of 30 seconds and an amplitude of about $0.02b$

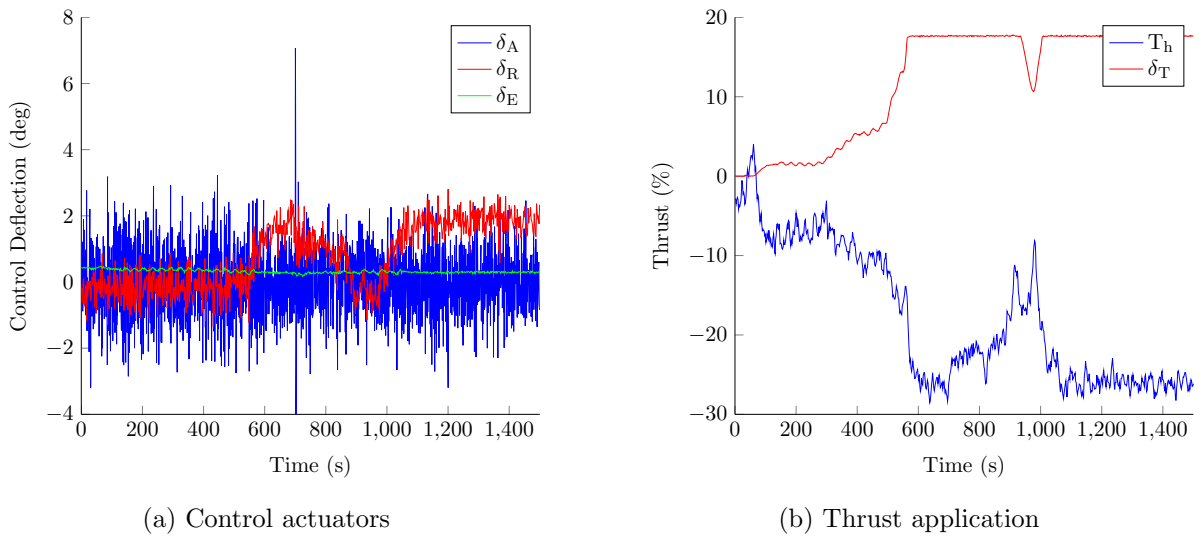
B.3 Extremum-Seeking Controller

Figure B.24: Extremum-seeking controller performance under light turbulence with a perturbation period of 30 seconds and an amplitude of about $0.02b$